

# **Magnetic X-ray Spectroscopy Studies of PLD grown Magnetolectric Hexaferrites**

**James E Beevers**

PhD

University of York  
Physics

June 2018

This thesis is dedicated to  
my wife Gemma for her unwavering support  
and encouragement

## ABSTRACT

The work here in was undertaken with two main objectives. The first has been to design and develop a bespoke pulsed laser deposition growth system to enable the growth of high quality transition metal oxide thin films. The system has been constructed to allow for the growth of multi-block or layered systems, such as the R, S and T-blocks of hexaferrites, by utilising an alternating target approach. Ultimately, the growth system's ability to grow complex oxide thin films has been tested and the successful growth of an epitaxial M-type hexaferrite, with material properties that compare well to the literature, has been realised.

Additionally, the magnetoelectric effect in M-type Ti-Co doped strontium hexaferrite,  $\text{SrCo}_2\text{Ti}_2\text{Fe}_8\text{O}_{19}$ , has been studied using a combination of magnetometry and element specific soft x-ray spectroscopies. A large increase (>30x) in the magnetoelectric coefficient is found when  $\text{Co}^{2+}$  enters the trigonal bi-pyramidal site. The 5-fold trigonal bi-pyramidal site has been shown to provide an unusual mechanism for electric polarization based on the displacement of magnetic transition metal ions. For Co entering this site, an off-centre displacement of the cation may induce a large local electric dipole as well as providing an increased magnetostriction enhancing the magnetoelectric effect.

# CONTENTS

<b>Abstract</b> .....	<b>iii</b>
<b>List of Tables</b> .....	<b>vii</b>
<b>List of Figures</b> .....	<b>viii</b>
<b>List of Symbols</b> .....	<b>xiv</b>
<b>Acknowledgements</b> .....	<b>xviii</b>
<b>Declaration</b> .....	<b>xix</b>
<b>Chapter 1: Introduction</b> .....	<b>1</b>
1.1 Motivation .....	1
1.2 Magnetoelectric Hexaferrites .....	2
1.3 Pulsed laser deposition .....	2
1.4 Summary of results and significant achievements .....	3
1.5 Structure of this thesis .....	4
<b>Chapter 2: Background and Theoretical Considerations</b> .....	<b>5</b>
2.1 Introduction .....	5
2.2 Ferromagnetism .....	5
2.2.1 The exchange interaction .....	6
2.2.2 Magnetocrystalline anisotropy .....	7
2.2.3 Magnetostatic energy and shape anisotropy .....	7
2.2.4 Magnetostriction .....	8
2.2.5 The Zeeman interaction .....	9
2.3 Antiferromagnetism and Ferrimagnetism .....	9
2.3.1 Ferrimagnetism .....	9
2.3.2 Superexchange .....	10
2.3.3 Goodenough-Kanamori-Anderson rules .....	11
2.3.4 Non-collinear magnetic order .....	11
2.4 Ferroelectricity .....	12
2.4.1 Improper ferroelectricity .....	14
2.5 Magnetoelectric Multiferroics .....	16
2.5.1 Magnetoelectric coupling coefficient .....	16
2.5.2 Composite Magnetoelectrics .....	18
2.5.3 Intrinsic Multiferroics .....	20
2.6 Hexagonal Ferrites .....	21
2.6.1 M-type hexagonal ferrites .....	23
2.6.2 Magnetoelectric Hexaferrites .....	26
2.7 Hexaferrite thin film growth .....	33
2.7.1 Hexaferrites grown by PLD .....	34
2.8 Conclusions .....	38

<b>Chapter 3: Thin Film Characterisation and Analytical Techniques .....</b>	<b>39</b>
3.1 Introduction .....	39
3.2 Structural Characterisation techniques .....	39
3.2.1 Energy-Dispersive X-ray Spectroscopy Analysis .....	39
3.2.2 X-ray Diffraction techniques .....	40
3.2.3 Raman Spectroscopy .....	46
3.3 Magnetic Characterisation techniques .....	47
3.3.1 Vibrating Sample Magnetometry .....	47
3.3.2 Ferromagnetic Resonance measurements .....	49
3.4 X-ray Magnetic Spectroscopy .....	52
3.4.1 X-ray Absorption Spectra (XAS) .....	53
3.4.2 Crystal Field Theory .....	54
3.4.3 X-ray Magnetic Circular Dichroism (XMCD) .....	57
3.4.4 Experimental setup .....	59
3.4.5 Atomic Multiplet Fitting .....	62
3.4.6 XMCD Sum Rules Analysis .....	64
3.5 Converse Magnetolectric Measurements .....	66
3.6 Summary .....	67
<b>Chapter 4: Pulsed Laser Deposition Growth System Design and Calibration .....</b>	<b>68</b>
4.1 Introduction .....	68
4.2 Design of the PLD growth system .....	68
4.2.1 Vacuum chamber design .....	68
4.2.2 Target Manipulator .....	70
4.2.3 UV laser and target ablation .....	71
4.2.4 Sample Holder and sample stage .....	74
4.2.5 Load-lock system .....	77
4.2.6 Chamber pressure and gas flow system .....	80
4.2.7 Sample heating and temperature calibration .....	82
4.2.8 The constructed PLD growth system .....	87
4.3 Calibration of the PLD system by Fe <sub>3</sub> O <sub>4</sub> thin film growth .....	87
4.3.1 Deposition time calibration at an 8 cm target-sample distance .....	87
4.3.2 Deposition time calibration at a 10 cm target-sample distance .....	93
4.3.3 Nitrogen growth pressure calibration .....	96
4.3.4 Film properties as a function of sample thickness .....	97
4.3.5 Fe <sub>3</sub> O <sub>4</sub> film grown with substrate heating .....	100
4.3.6 SrCo <sub>2</sub> Ti <sub>2</sub> Fe <sub>8</sub> O <sub>19</sub> hexaferrite thin film growth .....	104
4.4 Summary and Conclusions .....	107
<b>Chapter 5: Soft X-ray Spectroscopy Study of SrCo<sub>2</sub>Ti<sub>2</sub>Fe<sub>8</sub>O<sub>19</sub> Hexaferrite thin films .....</b>	<b>108</b>
5.1 Introduction .....	108
5.2 0.9 μm SrCo <sub>2</sub> Ti <sub>2</sub> Fe <sub>8</sub> O <sub>19</sub> single target thin film .....	108
5.2.1 EDX Analysis .....	108
5.2.2 X-ray Diffraction Measurements .....	109
5.2.3 Temperature dependent Magnetometry .....	111

5.2.4 Ferromagnetic Resonance Measurements .....	114
5.2.5 Element Specific Soft X-ray Magnetic Spectroscopy .....	116
5.3 50 nm SrCo <sub>2</sub> Ti <sub>2</sub> Fe <sub>8</sub> O <sub>19</sub> single target thin film .....	122
5.3.1 EDX Analysis .....	122
5.3.2 X-ray Diffraction Measurements .....	122
5.3.3 Temperature dependent Magnetometry .....	125
5.3.4 Element Specific Soft X-ray Magnetic Spectroscopy .....	127
5.4 Summary and Conclusions .....	130
<b>Chapter 6: Enhanced MagnetoElectric Effect in M-type Hexaferrites by Co substitution into Trigonal Bipyramidal Sites .....</b>	<b>132</b>
6.1 Introduction .....	132
6.2 EDX Chemical Composition analysis .....	133
6.3 X-ray Diffraction Measurements .....	134
6.4 Temperature dependent Magnetometry .....	135
6.5 Ferromagnetic Resonance Measurements .....	141
6.6 Magnetolectric Coupling Measurements .....	144
6.7 Element Specific Soft X-ray Magnetic Spectroscopy .....	146
6.8 Summary and Conclusions .....	149
<b>Chapter 7: Co enhancement of the magnetic-ion-induced polarisation at the hexaferrite trigonal bipyramidal sites .....</b>	<b>150</b>
7.1 Introduction .....	150
7.2 Simulation of the M-type Hexaferrite structure .....	151
7.3 Trigonal Bipyramidal site Potential Energy Calculation .....	153
7.4 Energy Potential Calculation for SrFe <sub>12</sub> O <sub>19</sub> .....	154
7.5 Calculations for Co substitutions .....	155
7.6 Calculations for Ti substitutions .....	156
7.7 Calculations for combined Co and Ti substitutions .....	157
7.8 Summary and Conclusions .....	159
<b>Chapter 8: Conclusions and Future Work .....</b>	<b>161</b>
8.1 Summary of Works .....	161
8.1.1 Summary of PLD Development .....	161
8.1.2 Summary of Soft X-ray Magnetic Spectroscopy Hexaferrite thin film Study .....	162
8.2 Future work .....	164
8.2.1 Future PLD Growth and Development .....	164
8.2.2 Hexaferrite thin film Development .....	166
<b>List of Abbreviations .....</b>	<b>167</b>
<b>References .....</b>	<b>168</b>

## List of Tables

<b>Table 4.1.</b> Table showing the XRR determined thicknesses and surface roughness of each sample as well as their measured resistances .....	89
<b>Table 4.2.</b> Table showing the XRR determined thicknesses and surface roughness of each sample, grown at a 10cm target-sample distance, as well as their measured resistances .....	94
<b>Table 4.3.</b> Table showing the XRR determined thicknesses and surface roughness of each sample, grown as a function of nitrogen partial pressure, as well as their measured resistances .....	96
<b>Table 7.1.</b> Table showing the $r_0$ and $r_1$ trigonal bipyramidal site inter-atomic distances for strontium ferrite with Co substituted to different lattice sites .....	155
<b>Table 7.2.</b> Table showing the $r_0$ and $r_1$ trigonal bipyramidal site inter-atomic distances for strontium ferrite with Ti substituted to different lattice sites .....	157

## List of Figures

<b>Figure 2.1.</b> Schematic representation of the change in length of a series of magnetic domains under the application of an external magnetic field .....	8
<b>Figure 2.2.</b> Representation of the alignment of magnetic moments in ferromagnets, anti-ferromagnets and ferrimagnets .....	10
<b>Figure 2.3.</b> Schematic representation of the Fe-O-Fe superexchange bonding .....	10
<b>Figure 2.4.</b> Three main types of the superexchange interaction: (a) anti-ferromagnetic superexchange between two half-filled d-orbitals via the same p-orbital; (b) ferromagnetic superexchange between half-filled and empty d-orbitals via the same p-orbital; and (c) ferromagnetic superexchange between two half-filled d-orbitals via different p orbitals .....	11
<b>Figure 2.5.</b> Schematic representation of the Dzyaloshinskii-Moriya interaction between two magnetic ions separated by a ligand ion .....	12
<b>Figure 2.6.</b> (a) The hysteretic relationship observed between P and E for a ferroelectric. (b) The double-well potential energy structure as a function of atomic displacement .....	12
<b>Figure 2.7.</b> The relationship among ferro-, pyro-, piezo- and dielectric materials .....	13
<b>Figure 2.8.</b> Schematic representations of different types of spiral magnetic structures. (a) Proper screw, (b) cycloidal, (c) transverse conical and (d) longitudinal conical .....	14
<b>Figure 2.9.</b> The magnetically induced electric polarisation between two magnetic ions separated by a ligand ion .....	15
<b>Figure 2.10.</b> Diagram showing the coupling relationships between the different ferroic orders .....	16
<b>Figure 2.11.</b> The three most common forms of composite multiferroics, (a) nanoparticles, (b) layered heterostructures and (c) nanocolumns .....	18
<b>Figure 2.12.</b> (a) The ferroelectric domains in PZTFT with applied magnetic field. (b) Histogram showing the change in ferroelectric phase .....	21
<b>Figure 2.13.</b> M-type structure showing Wyckoff positions, co-ordination and block of the cations .....	23
<b>Figure 2.14.</b> 3D atomistic representation of the three cation co-ordinations present with M-type hexaferrite, (a) Octahedral, (b) tetrahedral, (c) trigonal bipyramidal .....	24
<b>Figure 2.15.</b> (a) M and (b) P as a function of H for $\text{Ba}_{0.5}\text{Sr}_{1.5}\text{Zn}_2\text{Fe}_{12}\text{O}_{22}$ obtained by Kimura <i>et al</i> .....	26
<b>Figure 2.16.</b> (a) Magnetisation and (b) magnetoelectric current as a function of magnetic field for $\text{Sr}_3\text{Co}_2\text{Fe}_{24}\text{O}_{41}$ obtained by Kitagawa <i>et al</i> .....	27
<b>Figure 2.17.</b> (a) Magnetisation as a function of magnetic field for $\text{SrCo}_2\text{Ti}_2\text{Fe}_8\text{O}_{19}$ at RT for two different electric fields obtained by Mohebbi <i>et al</i> .....	30
<b>Figure 2.18.</b> The spiral spin configuration for different directions of E under the ‘slinky helix’ model .....	31
<b>Figure 2.19.</b> Illustration of $\text{Fe}^{3+}$ off-equatorial displacements in the trigonal bipyramid. The up and down displacements correspond to opposite dipoles and local minima in the energy potential .....	32
<b>Figure 2.20.</b> Schematic representation of a typical PLD setup .....	34
<b>Figure 2.21.</b> The step flow of adatoms across a terrace, with terraces labelled $T_1, T_2$ and $T_3$ .....	36
<b>Figure 3.1.</b> Schematic representation of the emission of x-rays as measured by EDX .....	39

<b>Figure. 3.2.</b> Schematic representation of the diffraction of incident x-rays by crystal planes .....	40
<b>Figure. 3.3.</b> The principle axis associated with sample movement on the XRD goniometer stage .....	40
<b>Figure. 3.4.</b> Schematic representation of the diffractometer set up .....	41
<b>Figure. 3.5.</b> The reflection and refraction of x-rays incident on a thin films surface .....	43
<b>Figure. 3.6.</b> X-ray reflectivity curve of a Fe <sub>3</sub> O <sub>4</sub> thin film on a silicon substrate .....	44
<b>Figure. 3.7.</b> XRD pole figure for an MgO sample taken at the (002) diffraction peak .....	45
<b>Figure. 3.8.</b> Energy level representation of the phonon transitions during Raman Spectroscopy .....	46
<b>Figure. 3.9.</b> Schematic representation of a typical vibrating sample magnetometer set up .....	47
<b>Figure. 3.10.</b> Representation of in and out of plane geometries during VSM measurements .....	48
<b>Figure. 3.11.</b> The damped precession of magnetisation with respect to the external magnetic field ...	50
<b>Figure. 3.12.</b> Diagram of the microwave spectrometer used to perform the FMR measurements .....	50
<b>Figure. 3.13.</b> Typical FMR spectrum measured at 10GHz using a Permalloy thin film sample .....	51
<b>Figure. 3.14.</b> Schematic representation of the K-edge (blue) and L-edge (green) transitions .....	53
<b>Figure. 3.15.</b> An example XAS spectrum, measured at the Fe L <sub>3</sub> and L <sub>2</sub> edges of an Fe <sub>3</sub> O <sub>4</sub> sample, at 300K, with vertically linear polarised x-rays .....	54
<b>Figure. 3.16.</b> Polar graphs of the probability densities for the five d orbitals .....	55
<b>Figure. 3.17.</b> The d orbitals in an octahedral, a tetrahedral and a trigonal bipyramidal crystal field .....	56
<b>Figure. 3.18.</b> (a) Schematic diagram representing the process of XMCD. (b) XAS of a SrCo <sub>2</sub> Ti <sub>2</sub> Fe <sub>8</sub> O <sub>19</sub> thin film at the Co L <sub>2,3</sub> for RCP ( $\sigma^+$ ) and LCP ( $\sigma^-$ ) x-rays, together with the XMCD .....	58
<b>Figure. 3.19.</b> Simplified schematic representation of the Diamond Light source synchrotron .....	59
<b>Figure. 3.20.</b> Schematic representation of an electrons path through an undulator array and the emission of synchrotron radiation .....	59
<b>Figure. 3.21.</b> Simplified schematic representation of the experimental XMCD setup .....	60
<b>Figure. 3.22.</b> Schematic representation of the processes of photon and Auger electron emission .....	60
<b>Figure. 3.23.</b> Simulated Ti <sup>4+</sup> XAS spectra. For an octahedral co-ordination with a 10Dq = 1.9 eV (red). For a tetrahedral co-ordination with a 10Dq = -0.9 eV (blue) .....	62
<b>Figure. 3.24.</b> Simulated Fe <sup>3+</sup> XMCD spectra. For an octahedral co-ordination with a 10Dq = 1.1 eV. Plotted for several different Gaussian-broadening parameters ( $G_B$ ) .....	63
<b>Figure. 3.25.</b> Simulated trigonal bipyramidal Co <sup>2+</sup> XMCD spectra (a) as a function of 10Dq, (b) as a function of $D\tau$ and (c) as a function of $D\sigma$ .....	64
<b>Figure. 3.26.</b> Normalised XMCD and integrated XMCD spectra for the Co L <sub>2,3</sub> edges .....	65
<b>Figure. 3.27.</b> Schematic representation of the magnetoelectric measurement setup .....	66
<b>Figure 4.2.1.</b> Diagram of the PLD vacuum chamber design (a) front view, (b) side view .....	69
<b>Figure 4.2.2.</b> Image showing the 6-target manipulator used in the PLD growth system .....	70

<b>Figure 4.2.3.</b> Image showing the Nd:YAG laser. ....	71
<b>Figure 4.2.4.</b> Graph showing the UV laser pulse energy as a function of time for a laser Q-switch delay of 360 $\mu$ s, under both manual operation and tracking mode .....	72
<b>Figure 4.2.5.</b> Schematic diagram of the UV laser optics setup .....	72
<b>Figure 4.2.6.</b> Image showing the Fused Silica lens holder, mounted onto the fused silica viewport .....	73
<b>Figure 4.2.7.</b> Image showing the plume of material created by the ablation of a Fe <sub>3</sub> O <sub>4</sub> target, with a pulsed laser energy of 100 mJ at 266 nm. In a vacuum pressure of 1x10 <sup>-7</sup> mbar .....	73
<b>Figure 4.2.8.</b> Schematic diagram of the PLD sample stage design .....	74
<b>Figure 4.2.9.</b> Schematic diagram of the PLD sample holder cradle .....	75
<b>Figure 4.2.10.</b> Schematic diagram of the sample cartridge .....	76
<b>Figure 4.2.11.</b> Image showing the top view of the PLD sample cartridge .....	78
<b>Figure 4.2.12.</b> Schematic diagram of the PLD load-lock system .....	77
<b>Figure 4.2.13.</b> Image showing the load-lock cartridge holder. Mounted on the 150 mm linear drive ...	77
<b>Figure 4.2.14.</b> Images showing the PLD load-lock sample transfer system, (a) from the left side of the chamber, (b) from the right side of the chamber .....	78
<b>Figure 4.2.15.</b> Technical diagram of the bayonet type connector, attached to the end of the magnetic transfer arm, (a) the bayonet shaft, (b) the sliding bush fitting .....	78
<b>Figure 4.2.16.</b> Image of the bayonet type connector attached to the magnetic transfer arm .....	80
<b>Figure 4.2.17.</b> Schematic diagram of the PLD gas manifold .....	80
<b>Figure 4.2.18.</b> Images showing, (a) the oxygen gas bottle, (b) the PLD chamber gas inlet .....	81
<b>Figure 4.2.19.</b> Image showing the PLD turbo throttling system .....	82
<b>Figure 4.2.20.</b> Image of the 48-2 series SYNRAD CO <sub>2</sub> laser, mounted on the cooling base .....	83
<b>Figure 4.2.21.</b> Image showing the PLD CO <sub>2</sub> laser substrate heating set up .....	83
<b>Figure 4.2.22.</b> Schematic diagram of the CO <sub>2</sub> laser substrate heating optical set up .....	84
<b>Figure 4.2.23.</b> Images showing, (a) a Silicon substrate, (b) an Al <sub>2</sub> O <sub>3</sub> substrate, heated by the CO <sub>2</sub> laser with an 80% duty cycle .....	85
<b>Figure 4.2.24.</b> The substrate temperature as a function of CO <sub>2</sub> laser duty cycle for (a) a silicon substrate, (b) an MgO substrate and (c) Al <sub>2</sub> O <sub>3</sub> substrate, measured at a pressure of 1x10 <sup>-7</sup> mbar .....	86
<b>Figure 4.2.25.</b> The complete PLD growth system with PLD chamber, load-lock, UV and CO <sub>2</sub> lasers .....	87
<b>Figure 4.3.1.</b> XRR measurement with fitted curve for the Fe <sub>3</sub> O <sub>4</sub> on silicon thin films, (a) 3 minute deposition time, (b) 5 minute deposition time .....	88
<b>Figure 4.3.2.</b> Graph showing the relationship between deposition time and thickness for the films grown at a target-sample distance of 8 cm .....	90
<b>Figure 4.3.3.</b> Graph showing the relationship between film thickness and 1/R for the films grown at a target-sample distance of 8 cm .....	91
<b>Figure 4.3.4.</b> Raman spectra of the Fe <sub>3</sub> O <sub>4</sub> thin films, grown at a target-sample distance of 8 cm .....	92
<b>Figure 4.3.5.</b> Graph showing the M(H) of the Fe <sub>3</sub> O <sub>4</sub> thin films, grown at a distance of 8 cm .....	92

<b>Figure 4.3.6.</b> XRR measurement with fitted curve for the 20-minute deposition time, Fe <sub>3</sub> O <sub>4</sub> on silicon thin film, grown at a 10 cm target-sample distance .....	93
<b>Figure 4.3.7.</b> Graph showing the relationship between deposition time and thickness for the films grown at a target-sample distance of 10 cm .....	94
<b>Figure 4.3.8.</b> Raman spectra of the Fe <sub>3</sub> O <sub>4</sub> thin films, grown at a 10 cm target-sample distance .....	95
<b>Figure 4.3.9.</b> M(H) of the Fe <sub>3</sub> O <sub>4</sub> thin films, grown at a 10 cm target-sample distance .....	95
<b>Figure 4.3.10.</b> Raman spectra of the Fe <sub>3</sub> O <sub>4</sub> thin films, grown as a function of nitrogen pressure .....	97
<b>Figure 4.3.11.</b> M(H) of the Fe <sub>3</sub> O <sub>4</sub> thin films, grown as a function of nitrogen partial pressure .....	97
<b>Figure 4.3.12.</b> Graphs showing the relationship between deposition time and thickness for (a) films grown at a target-sample distance of 8 cm (b) films grown at a target-sample distance of 10 cm .....	98
<b>Figure 4.3.13.</b> The normalised Raman intensity of the Fe <sub>3</sub> O <sub>4</sub> A <sub>1g</sub> phonon mode as a function of film thickness, for the Fe <sub>3</sub> O <sub>4</sub> films grown on silicon .....	99
<b>Figure 4.3.14.</b> XRR measurement with fitted curve for the Fe <sub>3</sub> O <sub>4</sub> film grown on MgO (001) .....	100
<b>Figure 4.3.15.</b> XRD measurement for the Fe <sub>3</sub> O <sub>4</sub> film grown on MgO (001) .....	101
<b>Figure 4.3.16.</b> XRD rocking curve taken at the (008) peak, for the Fe <sub>3</sub> O <sub>4</sub> film grown on MgO (001) .....	101
<b>Figure 4.3.17.</b> Raman spectrum measured for the Fe <sub>3</sub> O <sub>4</sub> film grown on MgO (001) .....	102
<b>Figure 4.3.18.</b> Graph showing the M(H) of the iron oxide thin film, grown on MgO (001) .....	102
<b>Figure 4.3.19.</b> The magnetoresistance (MR), at 300 K, of the Fe <sub>3</sub> O <sub>4</sub> film, grown on MgO (001) .....	103
<b>Figure 4.3.20.</b> (a) XRD measurement for the SrCo <sub>2</sub> Ti <sub>2</sub> Fe <sub>8</sub> O <sub>19</sub> film grown on Al <sub>2</sub> O <sub>3</sub> (0001). (b) Plot of I <sup>2</sup> against sin <sup>2</sup> θ for the M-type hexaferrite peak positions .....	105
<b>Figure 4.3.21.</b> (a) XRD rocking curve measurement, (b) pole figure measurement performed at the (006) diffraction peak, for the SrCo <sub>2</sub> Ti <sub>2</sub> Fe <sub>8</sub> O <sub>19</sub> film grown on Al <sub>2</sub> O <sub>3</sub> (0001) .....	106
<b>Figure 4.3.22.</b> Graph showing the M(H) of the SrCo <sub>2</sub> Ti <sub>2</sub> Fe <sub>8</sub> O <sub>19</sub> thin film grown on Al <sub>2</sub> O <sub>3</sub> (0001) .....	107
<b>Figure. 5.2.1.</b> EDX spectrum obtained for the 0.9 μm SrCo <sub>2</sub> Ti <sub>2</sub> Fe <sub>8</sub> O <sub>19</sub> thin film .....	109
<b>Figure 5.2.2.</b> (a) X-ray diffraction 2θ/ω measurement. (b) Plot of I <sup>2</sup> against sin <sup>2</sup> θ for the M-type hexaferrite peak positions of the 0.9 μm SrCo <sub>2</sub> Ti <sub>2</sub> Fe <sub>8</sub> O <sub>19</sub> film .....	110
<b>Figure 5.2.3.</b> (a) XRD rocking curve measurement, (b) pole figure measurement performed at the (008) diffraction peak, for the 0.9 μm SrCo <sub>2</sub> Ti <sub>2</sub> Fe <sub>8</sub> O <sub>19</sub> film grown on Al <sub>2</sub> O <sub>3</sub> (0001) .....	111
<b>Figure 5.2.4.</b> Graph showing the in-plane (red) and out of plane (blue) M(H) at 300 K for the 0.9 μm SrCo <sub>2</sub> Ti <sub>2</sub> Fe <sub>8</sub> O <sub>19</sub> thin film .....	112
<b>Figure 5.2.5.</b> VSM M(H) measurements performed at different temperatures for the 0.9 μm SrCo <sub>2</sub> Ti <sub>2</sub> Fe <sub>8</sub> O <sub>19</sub> thin film .....	112
<b>Figure 5.2.6.</b> (a) M(T) measured at 300 Oe for FC and ZFC conditions, (b) The derivative of the ZFC M(T) obtained for the 0.9 μm SrCo <sub>2</sub> Ti <sub>2</sub> Fe <sub>8</sub> O <sub>19</sub> thin film .....	113
<b>Figure. 5.2.7.</b> (a) In-plane FMR at 10 GHz and (b) frequency as a function of resonance field for the 0.9 μm SrCo <sub>2</sub> Ti <sub>2</sub> Fe <sub>8</sub> O <sub>19</sub> thin film .....	115
<b>Figure. 5.2.8.</b> Ti L <sub>2,3</sub> XAS measured for the 0.9 μm SrCo <sub>2</sub> Ti <sub>2</sub> Fe <sub>8</sub> O <sub>19</sub> thin film at 300 K in TEY. The blue solid line is the simulated spectra from an atomic XAS multiplet calculation of Ti <sup>4+</sup> in an octahedral co-	

ordination with $10Dq = 1.9$ eV. Equivalent calculations for octahedral $Ti^{3+}$ and $Ti^{4+}$ in a tetrahedral co-ordination with $10Dq = -0.9$ eV are also plotted .....	116
<b>Figure. 5.2.9.</b> XAS at the (a) Co and (b) Fe $L_{2,3}$ edges for $\sigma^-$ and $\sigma^+$ x-rays, measured for the $0.9 \mu m$ $SrCo_2Ti_2Fe_8O_{19}$ thin film at 300 K in TEY. The corresponding XMCD is plotted with the fit using atomic multiplet calculations .....	118
<b>Figure. 5.2.10.</b> (a) Fe and (b) Co $L_{2,3}$ edge XMCD and the corresponding integrated XMCD, measured for the $0.9 \mu m$ $SrCo_2Ti_2Fe_8O_{19}$ thin film at 300 K in TEY. The quantities p and q are illustrated .....	119
<b>Figure. 5.2.11.</b> Co $L_{2,3}$ edge XMCD spectra obtained via multiplet calculations for $O_h$ , $T_d$ and Trig in the ratios used to fit the $0.9 \mu m$ $SrCo_2Ti_2Fe_8O_{19}$ spectrum, and the corresponding integrated XMCD. The sum of the three integrated spectra is shown in black .....	120
<b>Figure. 5.2.12.</b> (a) Co and (b) Fe element specific hysteresis measurements obtained at 230 K for the $0.9 \mu m$ $SrCo_2Ti_2Fe_8O_{19}$ thin film in FY .....	121
<b>Figure. 5.3.1.</b> EDX spectrum obtained for the 50 nm $SrCo_2Ti_2Fe_8O_{19}$ thin film .....	122
<b>Figure 5.3.2.</b> (a) X-ray diffraction $2\theta/\omega$ measurement (b) Plot of $I^2$ against $\sin^2 \theta$ for the M-type hexaferrite peak positions of the 50 nm $SrCo_2Ti_2Fe_8O_{19}$ film .....	123
<b>Figure 5.3.3.</b> (a) XRD rocking curve measurement, (b) pole figure measurement performed at the (008) diffraction peak, for the 50 nm $SrCo_2Ti_2Fe_8O_{19}$ film grown on $Al_2O_3$ (0001) .....	124
<b>Figure 5.3.4.</b> M(H) measurements performed at different temperatures for the 50 nm $SrCo_2Ti_2Fe_8O_{19}$ thin film .....	125
<b>Figure 5.3.5.</b> (a) M(T) measured at 300 Oe for FC and ZFC conditions, (b) The derivative of the ZFC M(T) obtained for the 50 nm $SrCo_2Ti_2Fe_8O_{19}$ thin film .....	126
<b>Figure. 5.3.6.</b> Ti $L_{2,3}$ XAS measured for the 50 nm $SrCo_2Ti_2Fe_8O_{19}$ thin film at 300 K in TEY. The blue solid line is the simulated spectra from an atomic XAS multiplet calculation of $Ti^{4+}$ in an octahedral co-ordination with $10Dq = 1.9$ eV. An equivalent calculation for $Ti^{4+}$ in a tetrahedral co-ordination with $10Dq = -0.9$ eV is given by the green line .....	127
<b>Figure. 5.3.7.</b> XAS at the (a) Co and (b) Fe $L_{2,3}$ edges for $\sigma^-$ and $\sigma^+$ x-rays, measured for the 50 nm $SrCo_2Ti_2Fe_8O_{19}$ thin film at 300 K in TEY. The corresponding XMCD is plotted with the fit using atomic multiplet calculations .....	128
<b>Figure. 5.3.8.</b> (a) Fe and (b) Co $L_{2,3}$ edge XMCD and the corresponding integrated XMCD, measured for the 50 nm $SrCo_2Ti_2Fe_8O_{19}$ thin film at 300 K in TEY .....	129
<b>Figure. 5.3.9.</b> (a) Co and (b) Fe element specific hysteresis measurements obtained at 1.6 K, 230 K and 300 K for the 50 nm $SrCo_2Ti_2Fe_8O_{19}$ thin film in FY .....	130
<b>Figure. 6.1.</b> Perspective view of the M-type structure showing Wyckoff positions, co-ordination and block of the cations .....	132
<b>Figure. 6.2.</b> EDX spectra obtained for $\delta = 0.0$ , $\delta = 0.2$ and $\delta = 0.4$ .....	134
<b>Figure 6.3.</b> X-ray diffraction measurements for (a) $\delta = 0.0$ , (b) $\delta = 0.2$ and (c) $\delta = 0.4$ .....	135
<b>Figure 6.4.</b> VSM for (a) $\delta = 0.0$ , (b) $\delta = 0.2$ and (c) $\delta = 0.4$ measured at 300 K .....	136
<b>Figure 6.5.</b> VSM for (a) $\delta = 0.0$ , (b) $\delta = 0.2$ and (c) $\delta = 0.4$ measured at 10 K .....	137
<b>Figure. 6.6.</b> VSM as a function of temperature for $\delta = 0.0$ , $\delta = 0.2$ and $\delta = 0.4$ , showing (a) $M_s$ vs T, (b) $M_r$ vs T and (c) $H_c$ vs T .....	138
<b>Figure 6.7.</b> The derivative of $M_r$ with respect to temperature for $\delta = 0.0$ , $\delta = 0.2$ and $\delta = 0.4$ .....	139

<b>Figure 6.8.</b> $M(T)$ obtained via VSM for (a) $\delta = 0.0$ , (b) $\delta = 0.2$ and (c) $\delta = 0.4$ measured at 300 Oe for FC and ZFC conditions .....	140
<b>Figure 6.9.</b> The derivative of the ZFC $M(T)$ obtained via VSM for (a) $\delta = 0.0$ , (b) $\delta = 0.2$ and (c) $\delta = 0.4$ measured at 300 Oe .....	141
<b>Figure. 6.10.</b> In-plane FMR at 10 GHz for the (a) $\delta = 0.0$ sample, (b) $\delta = 0.2$ sample, (c) $\delta = 0.4$ .....	142
<b>Figure. 6.11.</b> Frequency as a function of resonance field measured by in-plane FMR for (a) $\delta = 0.0$ , (b) $\delta = 0.2$ and (c) $\delta = 0.4$ .....	143
<b>Figure 6.12.</b> Change in $M$ as a function of applied voltage, $V$ , for $\delta = 0.0$ , $\delta = 0.2$ and $\delta = 0.4$ . Measurements were taken with an applied bias field of 400 Oe with $E$ parallel to $M$ .....	144
<b>Figure 6.13.</b> (a) Ti $L_{2,3}$ XAS measured for $\delta = 0.0$ at 300 K in TEY. The blue solid line is the simulated spectra from an atomic multiplet calculation of $Ti^{4+}$ in an octahedral co-ordination with $10Dq = 1.9$ eV. (b) An equivalent calculation for $Ti^{4+}$ in a tetrahedral co-ordination with $10Dq = -0.9$ eV. (c) Ti $L_{2,3}$ XAS measured for $\delta = 0.2$ . (d) Ti $L_{2,3}$ XAS measured for $\delta = 0.4$ .....	146
<b>Figure 6.14.</b> Experimental XAS and XMCD spectra for (a) $\delta = 0.0$ , (b) $\delta = 0.2$ and (c) $\delta = 0.4$ at the Fe $L_{2,3}$ edges. Experimental XAS and XMCD spectra for (d) $\delta = 0.0$ , (e) $\delta = 0.2$ and (f) $\delta = 0.4$ at the Co $L_{2,3}$ edges. Atomic multiplet simulations of the XMCD are shown in black .....	148
<b>Figure 7.1.</b> Perspective view of the SrM structure as simulated using Materials Studio .....	151
<b>Figure 7.2.</b> The groundstate energy of the simulated SrM system as a function of cut off energy, calculated using CASTEP 8.0 .....	152
<b>Figure 7.3.</b> The interatomic distances $r_0$ and $r_1$ at the trigonal bipyramidal site .....	154
<b>Figure 7.4.</b> The calculated energy potentials (a) $U_{Coulomb}$ and (b) $U_{repulsion}$ as a function of off-equatorial 2b cation displacement in $SrFe_{12}O_{19}$ .....	155
<b>Figure 7.5.</b> $U_{repulsion}$ as a function of off-equatorial 2b cation displacement in $SrCo_2Fe_{10}O_{19}$ , with the Co ions substituted to (a) $4f_1$ tetrahedral, (b) 2b trigonal bipyramidal and (c) 2a octahedral sites .....	156
<b>Figure 7.6.</b> $U_{repulsion}$ as a function of off-equatorial 2b cation displacement in $SrTi_2Fe_{10}O_{19}$ , with the Ti ions substituted to (a) $4f_1$ tetrahedral, (b) 12k and (c) 2a octahedral sites .....	157
<b>Figure 7.7.</b> $U_{repulsion}$ as a function of off-equatorial 2b cation displacement, $z$ , for (a) $Fe^{3+}$ and (b) $Co^{2+}$ in the trigonal bipyramidal site and $Ti^{4+}$ in the octahedral 12k site .....	158
<b>Figure 7.8.</b> Phase diagram plot of $r_1/\rho$ against $r_0/\rho$ . In the central yellow region, the double well potential is forbidden. In the lower green region it must occur and outside these regions it is possible due to the competing interactions .....	159

## List of Symbols

$P$	Polarisation
$M$	Magnetisation
$\vec{\mu}$	Magnetic dipole moment
$\Phi$	Orbital Wavefunction
$E_{ex}$	Exchange energy
$J$	Exchange coupling strength
$\hat{S}$	Spin operator
$M_s$	Saturation magnetisation
$\vec{m}$	Reduced magnetisation
$U$	Energy density
$A$	Exchange stiffness
$a$	Nearest neighbour distance
$C$	Number of sites per unit cell
$\alpha_1, \alpha_2$ and $\alpha_3$	Directional cosines
$K$	Anisotropy coefficient
$H$	Magnetic field strength
$E_{ms}$	Magnetostatic energy
$\mu_0$	Permeability of free space
$\rho_V$ and $\rho_S$	Volume and surface charge densities
$\lambda_m$	Magnetostriction constant
$\epsilon_{ij}$	Strain tensor
$B_1, B_2, B_3$ and $B_4$	Magnetoelastic coupling constants
$c_{ij}$	Elastic constants
$D_{12}$	DM coefficient
$E$	Electric field strength
$p_i$	Pyroelectric coefficient
$T$	Temperature
$\sigma$	Stress
$d$	Piezoelectric constant
$Q$	Electrostriction coefficient
$\alpha$	Magnetoelectric coupling coefficient
$F$	Free energy
$\epsilon_0$	Permittivity of free space
$\beta_{ijk}$ $\gamma_{ijk}$	Higher order magnetolectric coefficients
$\epsilon_{ij}$	Dielectric constant tensor
$\mu_{ij}$	Permeability tensor
$\epsilon$	Strain

$H_c$	Magnetic coercivity
$M_r$	Magnetic remanence
$e$	Electron charge
$r_0$ and $r_1$	In-plane and out-of-plane TM-O distances in the 2b sites
$r_+$ and $r_-$	Cation and anion ionic radii
$C_{+-}$	Pauli's valence factor
$\epsilon$	dielectric constant
$U_{Coulomb}$	Coulomb potential
$U_{repulsion}$	Pauli repulsion potential
$\Phi_P$	Power density
$c$	Speed of light
$n_r$	Refractive index
$\mathcal{F}$	Fluence
Wt(%)	Atomic weight
At(%)	Atomic percentage
$Z$	Atomic number
$N$	Number of atoms
$d_{hkl}$	Separation of atomic planes
$\lambda$	Wavelength
$\theta$	Reflected x-ray angle
$\varphi$	XRD in-plane rotation angle
$\chi$	XRD tilt angle
$\omega$	XRD x-ray incidence angle
$h, k, l$	Lattice plane indices
$a, c$	Lattice parameters
$R_{j,j+1}$	Reflection coefficient
$\sigma_{rms}$	rms Roughness
$\rho$	Density
$I$	Intensity
$E_v$	Phonon mode energy
$\hbar$	Reduced Plank's constant
$\omega_\lambda$	Angular frequency
$\Delta w$	Wavenumber
$G$	Gilbert damping constant
$\gamma$	Gyromagnetic ratio
$g$	Lande g-factor
$\mu_B$	Bohr magneton
$H_r$	Magnetic resonance field
$\Delta H$	Ferromagnetic resonance linewidth

$\theta$	Mixing angle
$\Delta H_{pp}$	Peak to peak ferromagnetic resonance linewidth
$\chi', \chi''$	Transverse susceptibility components
$f$	Frequency
$H_A$	Magnetic anisotropy field
$\phi$	Anisotropy axis angle
$V(i;x,y,z)$	Electrostatic potential
$\Psi$	Wavefunction
$n$	Principle quantum number
$l$	Orbital angular momentum quantum number
$m_l$	Magnetic quantum number
$R_{n,l}(r)$	Radial part of the wavefunction
$Y_l^{m_l}$	Spherical harmonics
$d_{xy}, d_{xz}, d_{yz}, d_{x^2}, d_{x^2-y^2}$	d orbitals
$Dq, D\tau, D\sigma$	Crystal field parameters
$\lambda_U$	Periodic length of Undulator
$\gamma$	Einstein relativistic factor
$B$	Magnetic Induction
$m_e$	Electron mass
$k$	Magnetic deflection parameter
$L$	Electron escape depth
$I_{TEY}$	Total electron yield current
$\mu$	X-ray absorption
$\beta$	XAS x-ray incident angle
$F_{dd}, F_{pd}, G_{pd}$	Slater integral reduction parameters
$G_B$	Gaussian broadening parameter
$\langle L_z \rangle, \langle S_z \rangle$ and $\langle T_z \rangle$	Groundstate expectation values of the orbital, spin and dipole magnetic moments
$\rho^0$ and $\rho^1$	Integrated intensities of the isotropic XAS and the XMCD
$n_h$	Number of holes
$m_L$ and $m_S$	Orbital and spin magnetic moments
$C$	Capacitance
$d_s, d_f$	Substrate and film thickness
$A$	Sample surface area
$Q$	Charge
$V$	Voltage
$\xi$	Emissivity
$j^*$	Irradiance
$\sigma_B$	Steffan-Boltzmann constant

$R$	Resistance
$\rho_R$	Resistivity
$k_1$	Imaginary part of the complex refractive index
$\tau$	Mean crystallite size
$\mathcal{K}$	Crystallite shape factor
$\beta_L$	Diffraction peak broadening
$\hat{V}$	Potential energy
$V[\rho]$ and $V_{xc}[\rho]$	Density functionals
$U_k$	Arbitrary phase factor
<b>G</b>	Reciprocal lattice vector
$E_{cut}$	Cut off energy
$E_{GS}$	Groundstate energy
$F$	Force
$k_B$	Boltzmann constant
$\rho_f$	Arbitrary parameter ( $\rho_f = 0.314 \text{ \AA}$ )

## **Acknowledgements**

Firstly, I would like to express my sincere gratitude to my academic supervisor Dr S A Cavill for the continuous support of my PhD research. His guidance has proved invaluable throughout the research and writing of this thesis. Also thanks to Prof. M Probert for his advice and support with regards to the density functional calculations and to my fellow PhD candidates, namely Christopher Love, for many stimulating discussions and continuous encouragement.

Finally, my sincere thanks go to the University of York Physics department research support and mechanical workshop staff for bringing many of my growth system designs to life and the fabrication of crucial growth chamber parts.

*I declare that this thesis is a presentation of original work and I am the sole author. The work within has not previously been presented for an award at this, or any other, University. All sources are acknowledged as References.*

*Results presented in this thesis have been published in the following paper:*

J. E. Beevers, C. J. Love, V. K. Lazarov, S. A. Cavill, H. Izadkhah, C. Vittoria, R. Fan, G. van der Laan and S. S. Deshi, "Enhanced magnetoelectric effect in M-type hexaferrites by Co substitution into trigonal bi-pyramidal sites," *Appl. Phys. Lett.*, vol. 112, no. 8, 082401, 2018.



# Chapter 1: Introduction

## 1.1 Motivation

Controlling magnetism by an applied electric field would be a huge step towards creating ultra-low power, high density, magnetoresistive random access memory (MRAM). As such, magnetoelectric (ME) multiferroics are currently an intense area of research. A magnetoelectric (ME) material is one that possesses both magnetic and electric orders simultaneously, in the same phase and allow coupling between the two [1]. It is currently not well understood how the two symmetry breaking orders, of ferroelectricity and ferromagnetism, can exist in the same material as ferroelectricity usually requires empty transition metal orbitals, however ferromagnetism relies on partially filled 3d orbitals to create the spin magnetic moment. As a consequence of this most ferromagnets are metallic while ferroelectric materials must be insulating to avoid screening of the electric polarisation by mobile charge carriers. Due to this contradiction most intrinsic multiferroics reported to date have tended to be antiferromagnetic and ferroelectric, and only below room temperature with weak magnetoelectric coupling [2].

Multiferroics have potential as spintronic tunnel junctions [3], multiferroic hard drives [2], RF filters and antennas [1]. As a device application, the idea of multiferroic data storage is of particular interest. Current hard drives use the application of a magnetic field to switch the alignment of magnetic moments in order to write data bits. To apply such a magnetic field a substantial current is required. If, however, the magnetic moments could be switched by the application of an electric field, as may be possible for a multiferroic, then power consumption would be greatly reduced. For example, Ostler *et al* [4] demonstrated the energy cost to reverse a vortex core in planar structures of  $\text{Fe}_{81}\text{Ga}_{19}$  (where the polarisation of the core is used to encode logic states) via a strain coupling mechanism to be  $<1$  pJ. This is considerably smaller than the magnetic field driven case, which is  $>1$  nJ [4]. Ultimately, with the technological drive towards device minimisation, the interest in combining electronic and magnetic properties into multifunctional materials is ever increasing.

Hexagonal ferrites show potential for device applications as they have been one of the few room temperature single-phase magnetoelectrics reported and exhibit a low field large ME coupling up to and above room temperature [5]. Hexaferrites are already the most widely used magnetic material in the world due to their large anisotropy and low cost, making them ideal as permanent magnets [6]. It is believed that the discovery of the ME properties of hexaferrites will lead to a wide range of multiferroic applications such as highly sensitive magnetic field sensors for biomedicine, a new generation of smart stealth technology for military use, improved data storage solutions for IT and computing, and tuneable filters and switches for wireless communications [6]. However, if these materials are to have such device applications their properties and the mechanism governing their ME coupling need to be well understood. This is currently not the case and little is known about the mechanism governing the interaction between their ferromagnetic and ferroelectric properties. An increased understanding of the ME coupling mechanism is needed in order to optimise the amount of coupling the hexaferrites exhibit.

The work detailed in this thesis follows two main objectives. The first has been to design and develop a Pulsed Laser Deposition (PLD) growth system to enable the growth of high quality transition metal oxide thin films, such as hexaferrites. The second objective has been to characterise the structural, magnetic and magnetoelectric properties of hexaferrite thin films grown by PLD in order to gain insight into the mechanism governing their ME properties.

## 1.2 Magnetoelectric Hexaferrites

Hexaferrites are essentially iron oxides with hexagonal structures. The hexaferrite family of materials can be classified into six main types, M, Z, Y, W, X and U, according to their crystal structure and chemical composition [6]. Each structure is composed of a stacking sequence of the basic building blocks R, S and T. The S-block consists of two spinel units with formula  $\text{Fe}_6\text{O}_8$ . The R- and T-blocks are both hexagonal with compositions  $\text{MFe}_6\text{O}_{11}$  and  $\text{MFe}_8\text{O}_{14}$ , respectively, where M represents Ba, Sr or Pb [6].

Since the first hexaferrite to show ME properties was discovered in 2005 [7], ME coupling has been observed in various Z, Y, M and U-type hexaferrites [5] [8] [9] [10], however, the coupling measured for Y and U-type hexaferrites have been small and only below room temperature (RT) [9] [8]. The hexaferrite structure studied in this thesis is a cobalt and titanium doped M-type hexaferrite. M-type hexaferrites have a general composition  $\text{MFe}_{12}\text{O}_{19}$ , again where M represents Ba, Sr or Pb, and a stacking sequence  $\text{RSR}^*\text{S}^*$ , where \* indicates an  $180^\circ$  rotation about the c-axis [10].  $\text{SrCo}_2\text{Ti}_2\text{Fe}_8\text{O}_{19}$  was first shown to exhibit a large low field ME coupling at RT in 2012 [10].

The M-type structure allows for three different cation surroundings octahedral, tetrahedral and trigonal bipyramidal. It is understood that the magnetic properties in hexaferrites are primarily governed by the presence of cation-oxygen-cation bonds. Cations interact via the oxygen in a process known as superexchange [11]. The superexchange interaction between the two cations depends on bond angles, lengths and whether the ions have filled, half-filled or vacant orbitals [11]. Hence, cations in different surroundings will have different contributions to the overall magnetic properties. Understanding the contributions of these sites is crucial to understanding the mechanism governing the magnetoelectric behaviour in these materials.

In certain M, Z, W, U and Y hexaferrite structures, doping with different cations has been found to result in the formation of non-collinear magnetic arrangements [12]. Hexaferrites where these arrangements exhibit a transverse conical component, also exhibit a magnetically induced ferroelectricity. Given such hexaferrites are electrostrictive, the application of an electric field strains the material altering the magnetic configuration and vice versa. This coupling between magnetism and ferroelectricity provides a mechanism for the ME effect [13]. Interestingly, a further possible mechanism for ME coupling in hexaferrites may have been uncovered by Shen *et al* [14]. They have discovered an unusual method for electrical polarisation based on the displacement of the magnetic ion at the trigonal bipyramidal sites within the M-type structure. An effect that will be studied further in this work.

Doping strontium M-type hexaferrite with cobalt and titanium induces a non-collinear spin arrangement [15] and has been shown to exhibit strong ME coupling [10], however, the roles that the Co and Ti ions play are not well understood. Thus, this work attempts to understand which sites within the structure the Co and Ti preferentially occupy, as well as how this governs the materials magnetic and magnetoelectric properties. In order to elucidate the role of site occupancy on ME coupling, hexaferrite samples have been grown with the cobalt substituted to different sites. The affect this has on the samples magnetic and magnetoelectric properties has been investigated showing drastic results. This has allowed for an increased understanding of the magnetoelectric coupling mechanisms in M-type hexaferrite structures.

## 1.3 Pulsed Laser Deposition

The method by which the hexaferrite thin films have been grown is pulsed laser deposition and part of this project has been to develop a PLD system in order to grow high quality epitaxial thin films. PLD is unique with respect to other physical vapour deposition techniques due to the extremely high kinetic energy of the ablated particles incident on the substrate and the high deposition rate during each laser pulse. Both these factors can be controlled in order to manipulate

thin film growth [16]. The growth of ferrite films by PLD was first proposed and demonstrated by Vittoria in 1993 [17], the primary advantage being the stoichiometric transfer of complex unit cells that it is able to achieve [2] [18] [19]. No other techniques offer the same quality of reconstruction of complex unit cells, between source and film, as PLD.

PLD has previously been shown to produce high quality hexaferrite thin films [20] [21] and allows growth from multi-elemental targets, thus making the growth of complex hexaferrite structures far simpler. Multiple targets may also be incorporated into PLD systems allowing good control over the growth of multi-layer films, in a technique known as Alternating Target Laser Ablation Deposition (ATLAD) [22]. In the case of hexaferrite growth this allows for the incorporation of a different target for each of the R, S and T layers. This has enabled atomic scale chemical doping to be controlled in a block specific manner [21]. As such, a unique PLD system has been designed, with the emphasis on the growth of magnetic ferrite thin films, whilst retaining a design that is versatile enough for the growth of a wide range of materials. The PLD growth system developed in this work uses a 10Hz pulsed laser. The growth chamber itself can be used for deposition over a wide range of pressures between 1 mbar and ultra-high vacuum (UHV).

An important aspect of PLD is the heating of the substrate, which encourages crystalline growth [19]. The system has been designed to utilise a continuous wave, 35W, carbon dioxide laser, which is focussed onto the reverse of the substrate through a unique mechanism. This enables controlled heating over a wide range of substrate temperatures, including those that have previously been found optimal for the growth of epitaxial hexaferrite thin films [21] [17]. The main advantage, however, of the PLD system design is the incorporation of a 6 target manipulator. This allows the targets to be rapidly indexed during growth allowing the growth of multiple layers. These targets can also be simultaneously, individually rotated and rastered in order to maintain an even ablation pattern across the whole of a target and reduce target degradation. Being able to grow from numerous targets will allow for the use of the ATLAD technique [21]. This technique is effectively PLD but where the targets are interchanged during growth, with a different target being used to grow a different layer. Growing M-type hexaferrite films via ATLAD in this work has enabled control of the Co-Ti substitution sites within the material by only allowing the dopant to enter one of the two blocks, R and S.

#### **1.4 Summary of results and significant achievements**

In this work, a unique PLD system has been designed and constructed. The calibration and testing of the system has resulted in the design being proven to work effectively and the growth of epitaxial magnetite and hexaferrite thin films were achieved with properties comparable to those reported in the literature [23] [10] [24] [25].

As well as this, hexaferrite thin films grown via single target PLD and the ATLAD technique have been characterised both structurally and magnetically. Cobalt and titanium doped strontium M-type hexaferrite thin films have been studied that have been previously shown to exhibit large, low field magnetoelectric coupling at room temperature [24]. The co-ordinations and valences of Co and Ti dopants, in each film, have been investigated by X-ray absorption spectroscopy (XAS) and X-ray magnetic circular dichroism (XMCD). This has enabled the structure of the films to be probed to determine the contributions of given atoms and co-ordinations to the overall magnetoelectric effect observed, giving us greater understanding of a mechanism which is not yet fully understood. These studies indicate that the doping of Co to the trigonal bipyramidal sites within the hexaferrite structure act to enhance the magnetoelectric coupling observed.

Density Functional Theory (DFT) calculations have also been performed, using the CASTEP code, in order to simulate structural changes within the hexaferrite unit cell as a result of the Co and Ti doping to different atomic sites. The in and out of plane trigonal bipyramidal site bond lengths were

determined from the simulated structures and, using the phenomenological local potential energy method for the bipyramid [26], the energy profile along the c-axis has been calculated. The results show that the substitution of Co to the trigonal bipyramidal lattice sites increases the energy barrier of a double well potential. This demonstrates that a ferroelectric state is energetically favourable with ferroelectric alignment of the dipoles along the c-axis. These simulations suggest that increasing the occupation of Co into trigonal bipyramidal sites enhances the ability for the structure to polarize as well as providing a magnetoelastic ion. Therefore, it seems that the Co substitution to these sites provides a mechanism for an enhanced magnetoelectric effect.

These measurements collectively have allowed us to gain insight into the atomic structure of the magnetoelectric hexaferrite,  $\text{SrCo}_2\text{Ti}_2\text{Fe}_8\text{O}_{19}$ , and enabled the correlation between changes in structure and the magnetic and electronic properties. Thus, ultimately resulting in advances in the understanding of the possible magnetoelectric coupling mechanisms responsible for the large, low field magnetoelectric effects observed within such hexagonal ferrites.

### 1.5 Structure of this Thesis

This thesis contains eight main chapters. Following the introduction, chapter 2 provides the relevant background theory and outlines the field of magnetoelectric multiferroics, detailing the recent advances that have been made in the drive towards device applications. Additionally, the current knowledge of the structure and properties of hexagonal ferrites has been addressed and a literature review of the discovered magnetoelectric hexaferrites undertaken. Chapter 3 provides details on all of the experimental and analytical techniques performed throughout the work of this thesis. Details on the experimental set ups and equipment used are stated as are the methods and theory used in order to analyse the data obtained.

The thesis then contains four results chapters. In chapter 4 the design and construction of the PLD system is explained in detail and justified. This chapter also characterises magnetite and hexaferrite thin films that have been grown in order to calibrate and test the PLD system. Chapter 5 presents results of a polarised soft x-ray study of Co and Ti doped strontium ferrite thin films, grown via a single target PLD technique.  $\text{SrCo}_2\text{Ti}_2\text{Fe}_8\text{O}_{19}$  thin films have been shown previously to exhibit ME effects [24]. The films are characterised structurally and magnetically and the occupation sites of the Co and Ti dopants within the samples are determined using X-ray spectroscopy. This study provides insight into the preferred site of occupation by the dopants and ultimately how these substitutions affect the magnetic properties of the M-type hexaferrite structure.

Using the same X-ray spectroscopy techniques, in chapter 6,  $\text{SrCo}_2\text{Ti}_2\text{Fe}_8\text{O}_{19}$  thin films are investigated, however, this time the samples are grown using an ATLAD technique, from two targets, one to simulate the R-block and one the S-block. Three samples have been studied with an increasing amount of Co and Ti substitution to the R-block, in which the trigonal bipyramidal site resides. Using this growth technique, control over the occupation site of the Co cations is demonstrated. Measurements of the ME coupling present within these samples are correlated to the Co occupation sites observed. It is shown that cobalt occupation of the trigonal bipyramidal is important for the enhancement of the ME effect within the M-type hexaferrite.

Chapter 7 presents evidence for a mechanism responsible for the enhancement of the magnetoelectric effect as a consequence of the trigonal bipyramidal site being occupied by the cobalt cations. This study calculates the local potential of the bipyramidal sites, and shows that a double well potential, indicative of a local electric polarisation, is enhanced due to the Co substitutions. The final chapter, chapter 8, is a summary of the accomplished works and draws the conclusions from the results obtained together.

## Chapter 2: Background and Theoretical Considerations

### 2.1 Introduction

The magnetoelectric effect was first postulated by Pierre Curie over a century ago, although it was not until Dzyaloshinskii predicted the existence of ME coupling in  $\text{Cr}_2\text{O}_3$  in 1960 [12] that interest grew in the phenomenon and in discovering new materials exhibiting the effect. Furthermore, recent theoretical breakthroughs in understanding the coexistence of both ferroelectricity and magnetism, as well as the discoveries of ME coupling in materials such as  $\text{BiFeO}_3$  [27] and  $\text{TbMnO}_3$  [28], have led to a significant increase in the research of intrinsic magnetoelectric materials.

Both magnetic and electronic materials are widely used in modern technology. For example, the majority of data in consumer electronics is stored as regions of opposite magnetic polarization in ferromagnets. In addition, the sensors industry relies heavily on ferroelectrics, using them to convert sound waves into electrical signals in sonar detectors, for example, or to convert electrical pulses into motion in actuators [29]. Given this, if the two orders can be coupled, magnetoelectrics have many potential technological applications including spintronic tunnel junctions [3], multiferroic hard drives [2], tuneable RF filters and antennas [1].

In 2010 giant low field magnetoelectric effects were reported in the Z-type hexaferrite  $\text{Sr}_3\text{Co}_2\text{Fe}_{24}\text{O}_{41}$ , at 300 K [5], leading to significant investigations into the coupling mechanism within the material and the search for other hexaferrites displaying the effect. As such, one aim of this study has been to investigate the crystal and magnetic structure of the magnetoelectric hexaferrite  $\text{SrCo}_2\text{Ti}_2\text{Fe}_8\text{O}_{19}$  and correlate the Co and Ti substitutions to the materials magnetoelectric coupling mechanism. In order to place this work into context a review of the ME coupling mechanisms and the ME materials previously reported is presented. This chapter will set up the context for the experimental study of ME hexaferrites. The background properties of hexaferrite materials will be outlined as well as the discovery of the ME effect within certain M, Y and Z-type hexaferrites. Numerous growth techniques for thin film fabrication of the ME hexaferrites are discussed and the choice of the pulsed laser deposition technique justified. Ultimately, this section will outline the key theoretical concepts used as motivation and as a basis for the interpretation of the results presented within this thesis.

### 2.2 Ferromagnetism

A ferromagnetic material is one which exhibits a spontaneous magnetization in zero applied field that can be reversed by the application of a suitable external magnetic field, hence the hysteresis effect. All ferromagnets have a maximum temperature above which they no longer exhibit ferromagnetic behaviour. This is a result of thermal agitation and is known as the Curie temperature ( $T_C$ ) [30].

Only a small number of elements are ferromagnetic, most strongly are iron, cobalt and nickel, with some of the rare earth elements, such as gadolinium and terbium, also displaying ferromagnetism. The magnetic behaviour of a material depends on its electron configuration. Atoms with unpaired electrons have corresponding magnetic dipole moments,  $\vec{\mu}$ , resulting from a quantum mechanical effect but a semi-classical analogy is that the electron rotates with a quantifiable 'spin' and thus behaves as a rotating current [31]. For paramagnetic materials these moments are randomly oriented and thus produce no net magnetisation at zero field, however, in ferromagnets below  $T_C$ , the exchange interaction results in the parallel alignment of these moments, resulting in a net magnetisation, even in the absence of an applied magnetic field.

The magnetic free energy of a ferromagnetic system can be defined by the following interactions: exchange coupling, spin-orbit coupling, the magnetostatic interaction, the magnetoelastic interaction and the Zeeman interaction.

### 2.2.1. The exchange interaction

Unpaired electrons of identical nearby magnetic atoms interact via the exchange interaction. As a consequence of this interaction electrons, which repel each other, can move further apart by aligning their spins [31]. Thus, even in the absence of an applied field the magnetic moments of the electrons manage to remain aligned parallel to each other.

Exchange coupling is a quantum mechanical effect arising from the combination of Pauli's exclusion principle and the Coulomb interaction. In a two electron system the orbital part of the joint state wave-function,  $\Phi$ , is determined from the product of the two single electron wave-functions,  $\phi_a$  and  $\phi_b$ , whilst obeying the exchange symmetry between the two electrons (labelled 1 and 2). This leads to two possible orbital wave-functions, one which is symmetric,  $\Phi_S$ , and one which is antisymmetric,  $\Phi_A$ .

$$\text{symmetric} \quad \Phi_S \propto [\phi_a(\vec{r}_1)\phi_b(\vec{r}_2) + \phi_b(\vec{r}_1)\phi_a(\vec{r}_2)] \quad \text{eqn. 2.1.}$$

$$\text{antisymmetric} \quad \Phi_A \propto [\phi_a(\vec{r}_1)\phi_b(\vec{r}_2) - \phi_b(\vec{r}_1)\phi_a(\vec{r}_2)] \quad \text{eqn. 2.2.}$$

these two orbital states are not degenerate and the energy difference between them is known as the exchange energy [32]. Pauli's symmetry requirement over the complete wave-function, including both orbital and spin parts, results in the correlation between the orbital symmetry and the spin alignment. Thus, it is possible to express the exchange coupling as an effective spin-spin interaction, such that the electron exchange energy is given by:

$$E_{ex}^{el} = -2J\hat{S}_1 \cdot \hat{S}_2 \quad \text{eqn. 2.3.}$$

$\hat{S}_1$  and  $\hat{S}_2$  are the spin operators of the two electrons and  $J$  is the exchange coupling strength [32]. In a crystalline system the electronic wave-functions of nearby atoms overlap and the exchange coupling can be generalised to the Heisenberg model:

$$E_{ex} = -\sum_{ij} J_{ij} \hat{S}_i \cdot \hat{S}_j \quad \text{eqn. 2.4.}$$

Where  $J_{ij}$  is the exchange parameter between two interacting spins [33].

If we assume an isotropic exchange and only interactions between nearest neighbours are significant, eqn. 2.4 is simplified to:

$$E_{ex} = -J\sum_{\langle ij \rangle} \hat{S}_i \cdot \hat{S}_j \quad \text{eqn. 2.5.}$$

For a ferromagnet the exchange parameter is positive ( $J > 0$ ) and the exchange coupling favours the alignment of magnetic moments. This results in a non-zero value of magnetisation, even in the absence of an external magnetic field [32].

In ferromagnets, the coexistence of short-range forces, such as exchange coupling, and long-range forces, such as the magnetostatic interaction, makes the exact description of a materials magnetic behaviour difficult. To simplify the description however, a continuum model can be used to replace the atomic quantum mechanical interactions [33]. In this approximation the magnetisation is considered as a continuous field  $\vec{M}(\vec{r}) = M_s \vec{m}(\vec{r})$ , where  $\vec{r}$  is the position vector of the ferromagnetic body,  $\vec{m}$  is a dimensionless unit vector, known as the reduced magnetisation, and  $M_s$  is the saturation magnetisation. Considering the spin operators in eqn. 2.5 as classical vectors, for a crystal of uniform spins,  $S$ , the exchange energy density becomes:

$$U_{ex} = A|\nabla\vec{m}(\vec{r})|^2 \quad \text{eqn. 2.6.}$$

$A$  is the exchange stiffness and is related to the exchange parameter, such that:

$$A = \frac{JS^2}{a} C \quad \text{eqn. 2.7.}$$

where  $a$  is the nearest neighbour distance and  $C$  is the number of sites per unit cell [33].

### 2.2.2. Magnetocrystalline anisotropy

The exchange coupling explains the relative orientation of spins and therefore the magnetic moments in ferromagnets. However, there are several contributions to the anisotropy of the system that ultimately determine crystallographic orientations along which the magnetic moments preferentially align.

One source of anisotropy is magnetocrystalline anisotropy, which refers to the coupling between the lattice symmetry and the magnetic configuration of the system. The origin of magnetocrystalline anisotropy is the combination of both spin-orbit coupling and the crystal field. The spin-orbit interaction couples an electrons spin and orbital angular momenta. It arises from the electromagnetic interaction between the electron spin and the magnetic field generated by the electrons orbit around the nucleus. Additionally, a given ion within a crystal experiences an electric field due to the presence of the neighbouring ions, known as the crystal field. Depending on the crystal symmetry, the ions orbitals are arranged so as to minimise the electrostatic repulsion. As a consequence of spin-orbit coupling, the orbital arrangement results in certain spin orientations being energetically favourable. These directions are known as easy axes [32].

The symmetry of the magnetocrystalline anisotropy is dependent upon the symmetry of the crystal lattice. Consequently, a cubic crystal, such as  $\text{Fe}_3\text{O}_4$ , has a cubic anisotropy with 3 easy axes. The corresponding,  $U_{\text{cubic}}$ , energy density can be expressed as a series expansion of the directional cosines  $\alpha_1$ ,  $\alpha_2$  and  $\alpha_3$  between the magnetisation and the principle crystallographic axes  $\vec{u}_1 = [100]$ ,  $\vec{u}_2 = [010]$  and  $\vec{u}_3 = [001]$ :

$$U_{\text{cubic}} = K_{c0} + K_{c1}(\alpha_1^2\alpha_2^2 + \alpha_2^2\alpha_3^2 + \alpha_3^2\alpha_1^2) + K_{c2}\alpha_1^2\alpha_2^2\alpha_3^2 + \dots \quad \text{eqn. 2.8.}$$

$K_{c0}$ ,  $K_{c1}$  and  $K_{c2}$  are the anisotropy coefficients. As  $K_{c0}$  has no directional dependence the first order coefficient is the most important and eqn. 2.8 can be simplified to:

$$U_{\text{cubic}} = K_c(\alpha_1^2\alpha_2^2 + \alpha_2^2\alpha_3^2 + \alpha_3^2\alpha_1^2) \quad \text{eqn. 2.9}$$

with  $K_c = K_{c1}$  [32].

In hexagonal crystals, however, the crystal symmetry results in a uniaxial anisotropy with a single easy axis, coinciding with the  $\vec{u}_3$ , and any direction in the basal plane is an equally hard axis. The mathematical expression for the uniaxial anisotropy is given by eqn. 2.10:

$$U_{\text{uni}} = K_{u0} + K_{u1}\alpha_3^2 + K_{u2}\alpha_3^4 + \dots \quad \text{eqn. 2.10.}$$

Again, discarding the 0<sup>th</sup> order coefficient and making the same simplification, as in the cubic case, this becomes:

$$U_{\text{uni}} = K_u\alpha_3^2 \quad \text{eqn. 2.11.}$$

with  $K_u = K_{u1}$  [32].

### 2.2.3. Magnetostatic energy and shape anisotropy

The magnetostatic interaction is that between the magnetic field generated by the magnetic distribution of the system and the magnetisation itself [32]. In a ferromagnet, each magnetic dipole moment,  $\vec{\mu}_j$ , produces a magnetic field,  $\vec{h}_j$ , centred at the atomic position  $\vec{r}_j$ , given by:

$$\vec{h}_j = \frac{1}{4\pi} \left[ -\frac{\vec{\mu}_j}{|\vec{r} + \vec{r}_j|^3} + \frac{3}{|\vec{r} - \vec{r}_j|^5} [\vec{\mu}_j \cdot (\vec{r} - \vec{r}_j)] (\vec{r} - \vec{r}_j) \right] \quad \text{eqn. 2.12. [34]}$$

A dipole in the  $i^{\text{th}}$  lattice site,  $\vec{\mu}_i$ , interacts with the field created by the rest of the dipoles, such that the energy of  $\vec{\mu}_i$  is then:

$$E_i = -\vec{\mu}_i \cdot \sum_{j \neq i} \mu_0 \vec{h}_j \quad \text{eqn. 2.13.}$$

Summing all the individual contributions, the magnetostatic energy,  $E_{ms}$ , is then expressed as:

$$E_{ms} = -\sum_i \vec{\mu}_i \cdot \sum_{j \neq i} \mu_0 \vec{h}_j \quad \text{eqn. 2.14.}$$

Convention states that eqn. 2.14 is written as a function of the magnetostatic field,  $H_d = \sum_j \vec{h}_j$ , which is given by the total dipole field:

$$E_{ms} = -\frac{\mu_0}{2} \sum_i \vec{\mu}_i \vec{H}_d \quad \text{eqn. 2.15.}$$

The magnetostatic field is referred to as the demagnetising field inside the crystal and the stray field outside. The demagnetising field within the material opposes the local direction of magnetisation and is dependent on the magnetisation and the shape of the specimen. However, outside of the material the stray field follows the magnetic flux lines.

In the continuum approximation, the magnetostatic field can be approximated to:

$$\vec{H}_d = -\frac{1}{4\pi} \left[ \int_V \frac{\rho_V(\vec{r}')(\vec{r}-\vec{r}')}{|\vec{r}-\vec{r}'|^3} dV + \int_S \frac{\rho_S(\vec{r}')(\vec{r}-\vec{r}')}{|\vec{r}-\vec{r}'|^3} dS \right] \quad \text{eqn. 2.16.}$$

where  $\rho_V$  and  $\rho_S$  are the charge densities of the volume and surface, respectively [34]. This then leads to an expression for the magnetostatic energy density:

$$U_{ms} = -\frac{\mu_0 M_s}{2} \vec{m} \cdot \vec{H}_d \quad \text{eqn. 2.17.}$$

When a ferromagnet is uniformly magnetised the first integrand of eqn. 2.16 is zero. In this case, the magnetostatic energy depends only on the shape of the body and the magnetisation direction, resulting in the dipolar energy being referred to as shape anisotropy [32]. Within thin films, this shape anisotropy often results in keeping the magnetisation within the film plane.

First conceived by Weiss, ferromagnets are formed of ‘domains’: areas of the material within which the spin magnetic moments align along the same plane [30]. Each individual spin generates a small demagnetisation field, which favours antiparallel alignment but it is overwhelmed by the exchange energy in adjacent spin-oriented atoms, as the exchange interaction is stronger over a short range. However, defects in the crystal act to nucleate domain walls since at a defect the exchange interaction is disrupted and demagnetisation energy forces the more distant spins to align antiparallel, with the gradual rotation of spins occurring over length scales of the order of tens or hundreds of nanometres. Magnetic domains have a typical size of  $10^{12}$  -  $10^{18}$  atoms [30].

#### 2.2.4. Magnetostriction

Magnetostriction is the fractional change in length of a magnetic material as a result of an applied magnetic field [30]. The linear saturation magnetostriction,  $\lambda_s$ , is defined by eqn. 2.18, as the change in length per unit length.

$$\lambda_s = \frac{\partial l}{l} \quad \text{eqn. 2.18. [32]}$$

This is essentially a strain arising from the material being magnetised. As the atomic magnetic moments attempt to reorient along the axis of an applied field, the spins in the domains rotate. The changing shape of the domains echo through the material and consequently the shape of the material is changed [30]. A schematic representation of the process of magnetostriction is shown in fig. 2.1.

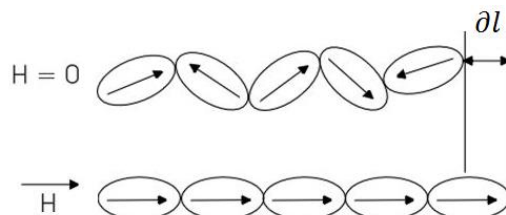


Figure 2.1. Schematic representation of the change in length of a series of magnetic domains under the application of an external magnetic field.

Magnetostriction is typically a small effect, however, the inverse effect (i.e. changes in magnetisation on the application of stress can be far more significant [32]. Governed by the magnetoelastic interaction, magnetostriction accounts for the coupling between a body's magnetisation and the strain applied to it. As such, magnetostriction is an important property to consider for magnetoelectric multiferroics. Essentially, if a strain is applied the distance between the atoms change as the lattice is distorted. Consequently, the crystal field is changed and the spin configuration of the system modified. The magnetoelastic energy is a function of the direction cosines of the magnetisation and the components of the strain tensor,  $\epsilon_{ij}$ . For a hexagonal crystal, the magnetoelastic energy density is given by eqn. 2.19.

$$U_{me}^{Hex} = B_1(\alpha_1^2 \epsilon_{xx} + \alpha_2^2 \epsilon_{yy} + \alpha_1 \alpha_2 \epsilon_{xy}) - B_2 \alpha_3^2 \epsilon_{zz} - B_3 \alpha_3^2 (\epsilon_{xx} + \epsilon_{yy}) + B_4 (\alpha_2 \alpha_3 \epsilon_{yz} + \alpha_1 \alpha_3 \epsilon_{zx}) \quad \text{eqn. 2.19. [35]}$$

Where  $B_1$ ,  $B_2$ ,  $B_3$  and  $B_4$  are the magnetoelastic coupling constants, which depend on the elastic constants,  $c_{ij}$ , and the directional saturation magnetostriction constants,  $\lambda_{100}$ ,  $\lambda_{111}$ .

### 2.2.5. The Zeeman interaction

Finally, if an external magnetic field,  $\vec{H}_{ext}$ , is applied to a ferromagnetic system, the magnetic moments inside the body tend to align with the applied field. The energy density term that describes this effect is the Zeeman term, which is given by eqn. 2.20.

$$U_Z = -\mu_0 M_s \vec{m} \cdot \vec{H}_{ext} \quad \text{eqn. 2.20. [32]}$$

## 2.3 Anti-ferromagnetism and Ferrimagnetism

If a crystal's exchange parameter is negative ( $J < 0$ ), it is favourable for the nearest neighbour magnetic moments to align anti-parallel to one another. This is Anti-ferromagnetism. One way to model this is to divide the material into two sublattices A and B, with the moments on one sublattice interacting with the moments of the other with a negative exchange coefficient, but interacting with the moments on their own sublattice with a positive exchange coefficient. This results in the magnetic moments of the two sublattices pointing in opposite directions, whilst being equal in magnitude.

There are numerous ways in which an equal number of up and down spins can be arranged in a lattice, this is dependent on the kind of crystal lattice, as such different types of antiferromagnetic order can be classified. In simple cubic lattices there are three main types, A-, C- and G-type. A-types, such as the perovskite  $\text{LaMnO}_3$ , have planes that are ferromagnetic with antiferromagnetic coupling between them. Alternatively, in C-types adjacent in-plane atoms are antiferromagnetically aligned, whilst the inter-plane atoms are aligned ferromagnetically, occurring in materials such as the manganite  $\text{Nd}_{1-x}\text{Sr}_{1+x}\text{MnO}_4$  [36]. Finally, the most common form is G-type ordering, found in the perovskites  $\text{LaFeO}_3$  and  $\text{LaCrO}_3$ , in which all nearest neighbour spins are aligned antiferromagnetically [33].

### 2.3.1. Ferrimagnetism

Ferrimagnetism is seen in some ionic compounds, such as oxides. In these materials, neighbouring electron spins align anti-parallel, much like anti-ferromagnets. However, if in the optimal geometry there is a larger magnetic moment from the sublattice that points in one direction than from the other, this results in a net magnetisation. The comparative spin alignments for the ferro-, anti-ferro- and ferrimagnetic are shown in fig. 2.2.

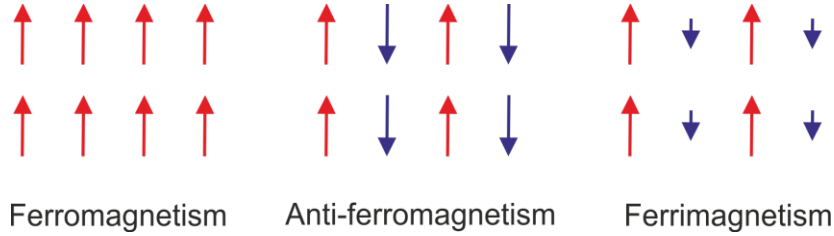


Figure 2.2. Representation of the alignment of magnetic moments in ferromagnets, anti-ferromagnets and ferrimagnets.

Ferrimagnets display all the characteristic properties of ferromagnets, such as magnetic saturation, hysteresis etc., despite the difference in magnetic ordering. The fact that most ferrimagnetic materials are oxides, they tend to have a high electrical resistivity, make them very useful for practical device applications that the typically metallic ferromagnets are unsuitable for. Such applications include inducting components in electronic circuits, like amplifiers and filters, and as components in microwave technology, allowing penetration by the high frequency fields unlike metallic materials.

### 2.3.2. Superexchange

In anti-ferromagnetic and ferrimagnetic oxides, the exchange interactions between magnetic ions are often mediated through the oxygen ions, separating the magnetic ions, in a process known as superexchange [37]. The theory governing the superexchange interaction is described in detail in [11] [38] [37], however a brief description will be given.

Superexchange can be understood by considering two transition metal ions, such as Fe, separated by an oxygen ion, as represented in fig. 2.3. The oxygen has two p electrons in its outermost occupied shell, while the Fe ions have unpaired d-shell electrons. As demonstrated in the figure, anti-ferromagnetic coupling lowers the energy of the system by allowing the electrons to become delocalised. Due to an overlap of wave functions, one of the p electrons from the O<sup>2-</sup> hops over to one of the Fe ions, as a consequence, the remaining unpaired p electron on the O<sup>2-</sup> site enters into a direct exchange with the other Fe ion.

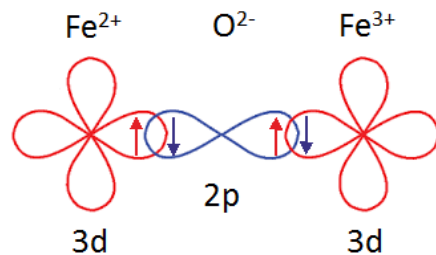


Figure 2.3. Schematic representation of the Fe-O-Fe superexchange bonding.

The spin of one of the magnetic ions ( $S_i$ ) is located on an orbit, which extends over the negative oxygen ion. This magnetic ion interacts with the magnetic ion on the other side of the mediating oxygen through an indirect exchange interaction. The exchange energy between the magnetic d-electrons, of ions i and j, is then expressed by

$$\Delta E^{ex} = -2 J_{eff} \hat{S}_i \cdot \hat{S}_j \quad \text{eqn. 2.8. [38]}$$

where the effective exchange constant is given by

$$J_{eff} = 2\zeta(J_{pd} + W_{pd}) \quad \text{eqn. 2.9. [38]}$$

Here  $J_{pd}$  is the direct exchange interaction,  $W_{pd}$  is the exchange interaction due to the charge transfer, and  $\zeta$  is an arbitrary constant. The superexchange model is complicated with the

introduction of more Fe atoms bonding to one oxygen atom and the consideration of different surroundings; however, the principle remains [38].

### 2.3.3. Goodenough-Kanamori-Anderson rules

The Superexchange interaction can result in ferromagnetic or antiferromagnetic coupling between the two cations depending on bond angles, bond lengths and whether the ions have filled, half-filled or vacant orbitals. The so-called Goodenough-Kanamori-Anderson (GKA) rules determine which of the two types of coupling is present. The rules take into account the occupation of the d orbitals involved, as well as the atomic bond angles, thus are based on the symmetry relations and electron occupancy of the overlapping orbitals [39].

The GKA rules determine, for a given environment, whether the exchange coupling is positive or negative, hence whether the coupling is ferromagnetic or antiferromagnetic. For general cases, the GKA rules can be summarised as follows [39]:

- The superexchange coupling between two half-filled d-orbitals via the same  $O^{2-}$  p-orbital is strong and antiferromagnetic for a  $180^\circ$  bond angle.
- The superexchange coupling between half-filled and empty (or filled) orbitals via the same  $O^{2-}$  p-orbital is weak and ferromagnetic for a  $180^\circ$  bond angle.
- The superexchange coupling between two half-filled d-orbitals via different  $O^{2-}$  p-orbitals, is weak and ferromagnetic.

The three cases are shown in fig. 2.4. It is clear from this that magnetic ions with different valences and in different surroundings will have a different contribution to a materials overall magnetic properties. The GKA rules are described in greater detail here [37].

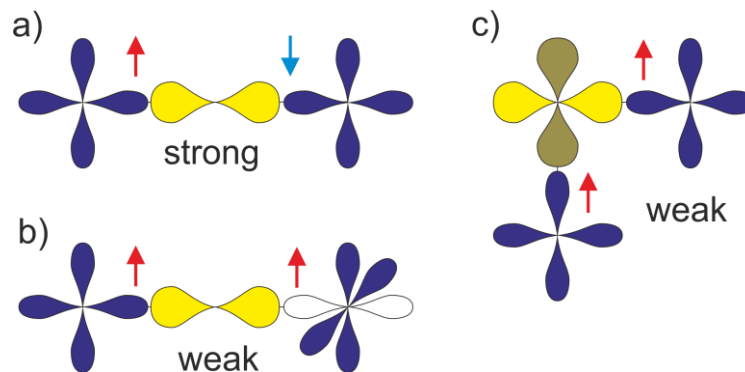


Figure 2.4. Three main types of the superexchange interaction: (a) anti-ferromagnetic superexchange between two half-filled d-orbitals via the same p-orbital; (b) ferromagnetic superexchange between half-filled and empty d-orbitals via the same p-orbital; and (c) ferromagnetic superexchange between two half-filled d-orbitals via different p orbitals. d-orbitals of the transition metal ions are shown in blue (half-filled) and white (empty), while ligand p-orbitals are in yellow.

### 2.3.4. Non-collinear magnetic order

Magnetic structures are defined as non-collinear when the spins are aligned neither parallel nor anti-parallel, and are canted at some angle with respect to each other. This can result in a long range conical or spiral magnetic ordering.

Along with the superexchange interaction certain crystal structures allows anti-symmetric spin-coupling between the spins of cations at certain sites [40]. The anti-symmetric exchange is a consequence of the Dzyaloshinskii-Moriya (DM) interaction and contributes to the overall exchange interaction between the magnetic ions. The DM interaction describes the relationship between two interacting spins,  $S_1$  and  $S_2$ , and is governed by the relation in eqn. 2.10.

$$H_{DMI} = D_{12} \cdot (S_1 \times S_2) \quad \text{eqn.2.10. [41]}$$

Here  $D_{12}$  is a constant vector, known as the DM coefficient. Considering the case where the two magnetic ions interact via a ligand ion by the superexchange mechanism, as represented in fig. 2.5, the orientation of the vector  $D_{12}$  is obtained by the relation:  $D_{12} \propto r_1 \times r_2 = r_{12} \times \mathbf{x}$ . This implies that  $D_{12}$  is oriented perpendicular to the triangle spanned by the three ions and  $D_{12}$  is zero if the ions are aligned with an  $180^\circ$  degrees bond angle.

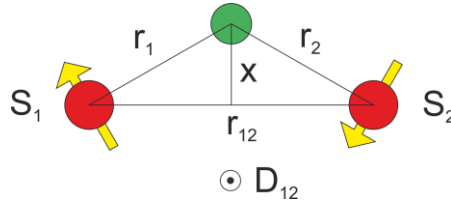


Figure 2.5. Schematic representation of the Dzyaloshinskii-Moriya interaction between two magnetic ions (red) separated by a ligand ion (green).

However, if the bond angle between the ions is not  $180^\circ$ , then the anti-symmetric exchange term has a non-zero contribution to the overall exchange. In certain sites of a crystal the superexchange may be greatly weakened due to competing interactions, or absent due to substitutions for non-magnetic ions, this can result in the canting of spins in order to minimise lattice energy. Hence, leading to the formation of a non-collinear magnetic structure. In hexaferrites the presence of sites displaying such anti-symmetric spin coupling can result in the formation of helical spin structures [40]. These spin arrangements are thought crucial to the magnetoelectric coupling discovered in such hexaferrites.

## 2.4 Ferroelectricity

A crystal is defined as ferroelectric if it has a spontaneous electric polarisation ( $P$ ) that can be reversed by the application of an external electric field ( $E$ ). It is implicit that the electric polarisation is stable without the application of  $E$  [42]. When most materials are polarized, the polarization induced increases linearly as a function of the applied electric field, this is known as dielectric polarization. For ferroelectrics however, the polarisation is not only dependent on the applied field but also on its history. Analogous to ferromagnetism, hysteresis is observed between applied electric field and electric polarisation, as displayed in fig. 2.6(a).

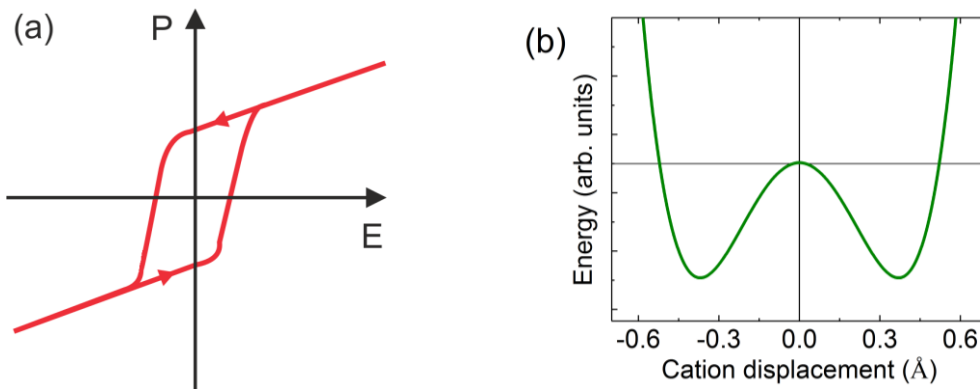


Figure 2.6. (a) The hysteretic relationship observed between  $P$  and  $E$  for a ferroelectric. (b) The double-well potential energy structure as a function of atomic displacement.

The source of this polarisation in ferroelectrics is a result of the positions of the ions in the crystal lattice; hence, the magnitude of the polarisation is highly material dependent [43]. Ferroelectric polarisation occurs due to the off centre displacement of the ferroelectric ion, within the lattice. This atomic displacement occurs because of a double-well potential energy structure, as shown in

fig. 2.6(b). The hysteresis effect observed is a consequence of the potential barrier between the two minima. At  $E = 0$  the ion will sit with an atomic displacement corresponding to the position of one minima and due to the energy barrier an electric field opposite in direction to the atomic displacement is required to move the ion to the other minima position, hence the hysteresis effect.

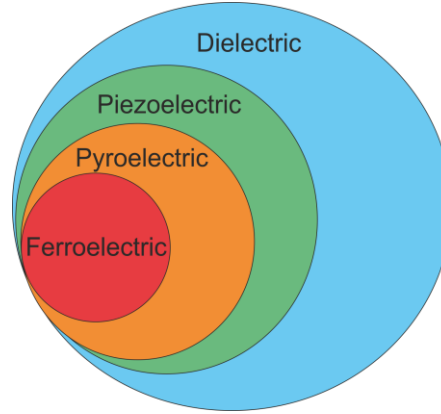


Figure 2.7. The relationship among ferro-, pyro-, piezo- and dielectric materials.

The relationships between ferroelectric, pyroelectric, piezoelectric and dielectric materials are shown in fig 2.7. All ferroelectrics are also pyroelectric. Pyroelectric materials undergo a change in polarisation as a response to a change in temperature. The temperature change modifies the atomic positions within the crystal structure, such that the materials polarisation changes. A materials pyroelectric coefficient,  $p_i$ , is defined by, eqn. 2.11, as the change in spontaneous polarisation vector with temperature, at constant stress,  $\sigma$ .

$$p_i = \frac{\partial P_{i,\sigma}}{\partial T} \quad \text{eqn.2.11. [44]}$$

All pyroelectric, hence also ferroelectric, materials are also piezoelectric, the two properties being closely related. However, some piezoelectric materials have a crystal symmetry that does not allow pyroelectricity [45]. Piezoelectrics change their shape in the presence of an applied electric field or, reversely, a change in their shape causes a change in polarisation [46]. When stress is applied to the crystal, the non-symmetric ions move closer or further apart and the separation of the charges is directly related to the net polarisation. The piezoelectric effect is also material dependent [46]. In composite multiferroics, this is exploited to change the strain on a magnetostrictive layer. When an electric field is applied to a piezoelectric, a strain is generated within the material. Where the components of the strain tensor,  $\epsilon_{ij}$ , are given by eqn. 2.12.

$$\epsilon_{ij} = d_{kij} E_k \quad \text{with } i,j,k=1,2,3 \quad \text{eqn.2.12.}$$

Here  $d_{kij}$  are the components of the third rank piezoelectric tensor and  $E_k$  are the components of the electric field vector. This can be written in 2-subscript matrix notation as:

$$\epsilon_i = d_{ki} E_k \quad \text{with } k=1,2,3 \text{ and } i=1,2,3,4,5,6 \quad \text{eqn.2.13.}$$

where the strain is now a 6-component vector:

$$\vec{\epsilon} = \begin{bmatrix} \epsilon_1 \\ \epsilon_2 \\ \epsilon_3 \\ \epsilon_4 \\ \epsilon_5 \\ \epsilon_6 \end{bmatrix} = \begin{bmatrix} \epsilon_{xx} \\ \epsilon_{yy} \\ \epsilon_{zz} \\ \epsilon_{yz} \\ \epsilon_{zx} \\ \epsilon_{xy} \end{bmatrix} \quad \text{eqn.2.14.}$$

and the piezoelectric tensor is substituted by a 6 x 3 matrix, with  $d_{ki}$ , the strain induced in the direction  $i$  per unit electric field applied along the direction  $k$  [44].

Another mechanism known to change the shape of a material as a result of an applied electric field is electrostriction. Electrostriction is exhibited by all insulators, or dielectrics, and causes them to change shape under influence of an electric field [47]. Electric polarisation results in a strain ( $\epsilon$ ) within the material. Unlike piezoelectricity, which is a linear effect, electrostriction is a second order effect; hence the strain increases quadratically with polarisation,  $\epsilon = QP^2$ , where  $Q$  is the electrostriction coefficient [47]. The reason electrostriction is not more important than piezoelectricity in terms of device applications is due to the coupling coefficient being much smaller than piezoelectric coefficients, resulting in electrostriction effects often being negligibly small [48]. The origin of electrostriction is that under the influence of an external electric field positive and negative ions within the lattice are displaced in opposite directions. This displacement is replicated throughout the material resulting in an overall strain [47].

Although, generally, ferroelectric materials are not oxides, oxide ferroelectrics have become the most commonly used as they display the strongest properties [45]. Lead zirconate titanate (PZT) and barium titanate ( $BaTiO_3$  / BTO) are among the most interesting due to having strong piezoelectric responses [42]. The origin of ferroelectricity can be different for different materials. AlN typically has a wurtzite structure. This results in the aluminium and nitrogen ions being slightly separated along the x,y and z axis', the origin of the net polarisation in wurtzites [42]. BTO, on the other hand, was the first complex perovskite found to exhibit ferroelectricity [43]. Below its Curie temperature ( $120^\circ C$ ) the BTO lattice does not have enough energy to minimise the free energy caused by the electric fields of the ions, this change breaks the charge symmetry of the lattice creating a spontaneous dipole moment. The sum of these dipole moments gives a net polarisation in the material, which results in the ferroelectric effect [43]. The most commonly used piezoelectric however, is PZT ( $PbZr_xTi_{1-x}O_3$ ). PZT like BTO has a perovskite structure with the Zr and Ti ions octahedrally co-ordinated at the centre of the unit cell. The ratio of Zr-Ti is influential in changing the lattice parameters. For a chemical composition such as  $PbZr_{0.52}Ti_{0.48}O_3$  an increased piezoelectric response is seen due to its position at a boundary between structural phases [49].

### 2.4.1. Improper ferroelectricity

In certain materials, ferroelectricity can be induced by complex internal arrangements of magnetic moments, such as spin spirals. These materials, where the ferroelectricity is induced by magnetic order are known as improper ferroelectrics. This mechanism is important for several of the materials discovered displaying strong magnetoelectric coupling, including hexaferrites [12].

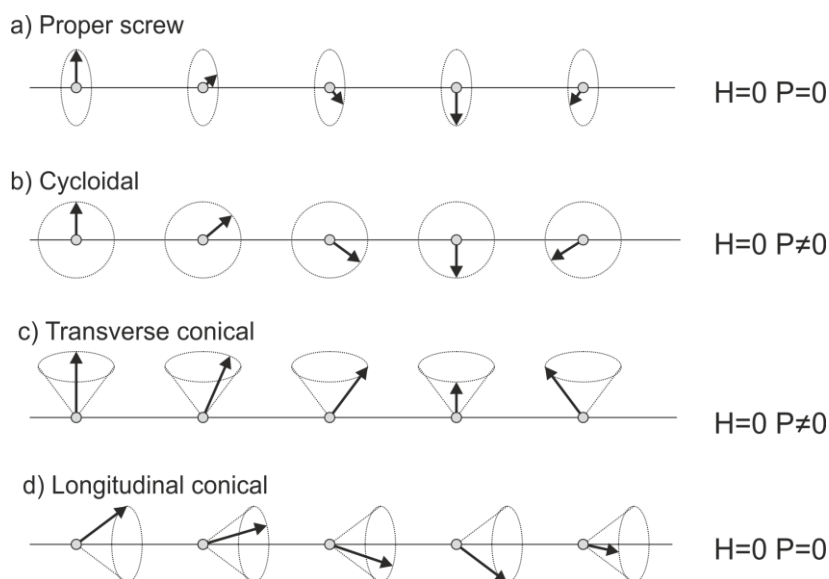


Figure 2.8. Schematic representations of different types of spiral magnetic structures. (a) Proper screw, (b) cycloidal, (c) transverse conical and (d) longitudinal conical.

The non-collinear spin states in materials, such as hexaferrites, arise due to the mechanism discussed in section 2.3.4. Helical magnetic structures can take several different forms, depending on the crystal structure being considered, four of which can be seen in fig. 2.8. The classification of the magnetic spiral type is critical for understanding the spiral-spin-driven ferroelectricity observed. If the spin rotation axis is parallel to the propagation vector of the spiral, the arrangement gives a screw spiral structure, as in fig. 2.8(a). Alternatively, if the spin rotation axis is perpendicular to the propagation vector, the resulting arrangement is termed a cycloidal spiral structure, fig. 2.8(b). A more complicated system is a conical spiral in which a ferromagnetic component coexists with a cycloidal or screw component for transverse or longitudinal conical structures, fig. 2.8(c) and (d) respectively [50].

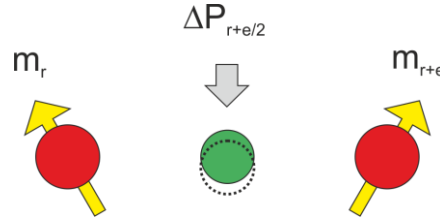


Figure 2.9. Schematic representation of the magnetically induced electric polarisation between two magnetic ions (red) separated by a ligand ion (green).

Jia *et al* [51] [52] systematically investigated the magnetically induced ferroelectricity for various electron configurations of transition metal oxides and classified the origins of ferroelectric polarisation into three mechanisms: exchange-striction, inverse Dzyaloshinskii-Moriya and the d-p hybridisation. If we consider the model where two magnetic ions at positions  $r$  and  $r+e$ , hybridized through a ligand ion at  $r+e/2$ , as shown in fig. 2.9, resulting in a polarisation,  $\Delta P_{r+e/2}$ . This magnetically induced improper ferroelectricity can be expressed by eqn.2.15, [12] where  $m_r$  and  $m_{r+e}$  are the local magnetic moments of magnetic ions.

$$\Delta P_{r+e/2} = P^{ms}(m_r \cdot m_{r+e}) + P^{sp}e \times (m_r \times m_{r+e}) + P^{orb}[(e \cdot m_r)m_r - (e \cdot m_{r+e})m_{r+e}] \quad \text{eqn. 2.15.}$$

In eqn.2.15, the 1<sup>st</sup> term is attributed to magnetostriction (exchange-striction). This mechanism was originally developed to explain the ME coupling observed in  $\text{Cr}_2\text{O}_3$  and has since been applied to other systems such as  $\text{HoMnO}_3$  with E-type antiferromagnetic ordering [12]. Here the ferroelectricity is attributed to a symmetric interaction between the magnetic ions. The combination of the spin arrangement and crystallographic symmetry makes the local polarisations align uniformly, resulting in ferroelectricity. For materials governed by this mechanism, a non-collinear spin arrangement is not needed to invoke ferroelectricity, thus is not thought to be the mechanism responsible for the ME properties of hexaferrites [12].

The 2<sup>nd</sup> term is the spin-current or inverse Dzyaloshinskii-Moriya mechanism, in which the electrical polarisation is induced by a non-collinear spiral magnetic structure with a cycloidal component. This mechanism was proposed by Katsura *et al* [53] and can be regarded as an inverse effect of the DM interaction in which non-collinearly coupled magnetic moments displace the ligand ion between them, hence producing a local polarisation. The small shifts of the ligand ions can be induced by the magnetic ordering, as the system finds it favourable to enhance the magnetic interaction energy at the cost of lattice energy. In certain non-collinear spiral magnetic structures, all ligand ions are shifted in the same direction leading to a net electric polarisation.

The 3<sup>rd</sup> term is associated with the variation of the metal-ligand d-p hybridization with spin-orbit interaction. This can be a source of ferroelectricity in certain low symmetry structures with non-collinear magnetic orders, this includes structures with a proper-screw magnetic ordering and low crystallographic symmetries such as triclinic or monoclinic [12].

Both the spin-current and the d-p hybridisation mechanisms have been found to both be

responsible for the induction of polarisation in structures with a non-collinear magnetic ordering. The spin-current mechanism is thought to be the dominant mechanism for the magnetically induced polarisation in hexaferrites with a non-collinear magnetic structure. In hexaferrite materials, displaying non-collinear magnetic ordering, a cycloidal component in the spin structure is required in order to induce a spontaneous polarisation due to the inverse DM mechanism; as the net polarisation due to this mechanism is cancelled out for a proper screw magnetic ordering. Hence, materials with either the cycloidal or transverse conical magnetic structure, fig. 2.8(b) and (c), allow for a magnetically induced ferroelectricity. Both the proper screw and longitudinal conical arrangements, fig. 2.8(a) and (d), however, do not exhibit a spontaneous polarisation. Although, in these helical magnetic states with no cycloidal component, applying weak in-plane magnetic fields can induce such a transverse component resulting in a polarisation [12] [13].

## 2.5 Magnetolectric Multiferroics

Multiferroic materials are those in which the two ferroic orders, namely ferroelectricity, ferroelasticity and ferromagnetism, are present, with a coupling mechanism existing between them [29]. Magnetolectricity, on the other hand, refers specifically to the coupling between the ferromagnetic and ferroelectric properties of a material that is both magnetically and electronically polarisable. A diagram showing the coupling relationships between polarisation (P), magnetisation (M) and strain ( $\epsilon$ ) is displayed in fig. 2.10.

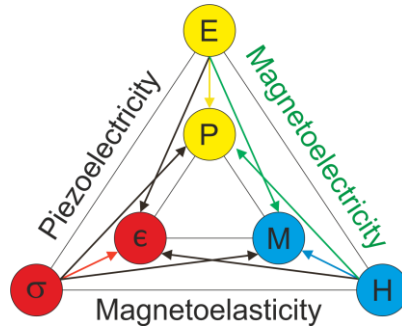


Figure 2.10. Diagram showing the coupling relationships between the different ferroic orders.

The magnetolectric effect can take two main forms. Direct magnetolectric coupling is the mechanism in which the application of a magnetic field results in a change in the electrical polarisation of the material. Alternatively, converse magnetolectric coupling is the change in magnetisation due to the application of an electric field [54].

Most ferromagnets are metallic but for ferroelectricity the material must be an insulator to avoid screening of the electric field by the mobile charge carriers. As such, few materials exhibit both ferroelectricity and ferromagnetism in the same phase and at the same temperature. Those that do often rely on a complex internal mechanism. However, as an alternative way of overcoming the problem created by the two symmetry breaking orders, composite multiferroics have been developed and pursued [54] that potentially allow the combination of a ferroelectric and a ferromagnetic phase through a strong coupling at the interface between the two materials.

### 2.5.1. Magnetolectric Coupling coefficient

The strength of the ME effect in given materials can be compared by their magnetolectric coupling coefficient,  $\alpha$ . This coefficient is derived from the adiabatic magnetolectric tensor,  $\tilde{\alpha}_{ij}$ . To gain a better understanding of ME coupling, first we must consider the free energy of the system,  $F$ , which may be represented in an infinite, homogeneous and stress free medium, by eqn. 2.16. [55]

$$-F(E, H) = \frac{1}{2}\epsilon_0\epsilon_{ij}E_iE_j + \frac{1}{2}\mu_0\mu_{ij}H_iH_j + \tilde{\alpha}_{ij}E_iH_j + \frac{\beta_{ijk}}{2}E_iH_jH_k + \frac{\gamma_{ijk}}{2}H_iE_jE_k + \dots \quad \text{eqn. 2.16.}$$

where  $\epsilon_0$  and  $\mu_0$  are the permittivity and permeability of free space,  $\mathbf{E}$  is the electric field and  $\mathbf{H}$  the magnetic field. Additionally, other important thermodynamic quantities include the dielectric constant tensor, defined by eqn. 2.17.

$$\epsilon_{ij} = 1 + 4\pi \left( \frac{\partial \mathbf{P}}{\partial \mathbf{E}} \right)_{s, \mathbf{H}, \sigma} \quad \text{eqn. 2.17. [13]}$$

and the adiabatic permeability tensor, defined by eqn. 2.18.

$$\mu_{ij} = 1 + 4\pi \left( \frac{\partial \mathbf{M}}{\partial \mathbf{H}} \right)_{s, \mathbf{E}, \sigma} \quad \text{eqn. 2.18. [13]}$$

The third rank tensors,  $\beta_{ijk}$  and  $\gamma_{ijk}$ , represent higher order ME coefficients; however, they are much smaller in magnitude than the linear coupling,  $\alpha$  [56]. Differentiation of the free energy leads to the order parameter of polarisation,  $\mathbf{P}$ , and magnetisation,  $\mathbf{M}$ , given by eqns. 2.19 and 2.20, respectively.

$$P_i(\mathbf{E}, \mathbf{H}) = -\frac{\partial F}{\partial E_i} = P_i^s + \epsilon_0 \epsilon_{ij} E_j + \tilde{\alpha}_{ij} H_j + \frac{\beta_{ijk}}{2} H_j H_k + \gamma_{ijk} H_i E_j + \dots \quad \text{eqn. 2.19. [56]}$$

$$M_i(\mathbf{E}, \mathbf{H}) = -\frac{\partial F}{\partial H_i} = M_i^s + \mu_0 \mu_{ij} H_j + \tilde{\alpha}_{ij} E_i + \beta_{ijk} E_i H_j + \frac{\gamma_{ijk}}{2} E_j E_k + \dots \quad \text{eqn. 2.20. [56]}$$

Here the intrinsic ME coefficient is defined by eqn. 2.21 and holds the strain ( $\epsilon$ ) and temperature ( $T$ ) constant.

$$\tilde{\alpha}_{ij} = \left( \frac{\partial \mathbf{M}}{\partial \mathbf{E}} \right)_{T, \mathbf{H}, \epsilon} = \left( \frac{\partial \mathbf{P}}{\partial \mathbf{H}} \right)_{T, \mathbf{E}, \epsilon} \quad \text{eqn. 2.21. [57]}$$

Subsequently it was shown by Brown *et al* [58] that the intrinsic magnetoelectric coupling,  $\tilde{\alpha}_{ij}$ , is bound by the relative permittivity and permeability tensors  $\epsilon_{ii}$  and  $\mu_{jj}$ , such that;

$$\tilde{\alpha}_{ij}^2 \leq \epsilon_0 \mu_0 \epsilon_{ii} \mu_{jj} \quad \text{eqn. 2.22. [55]}$$

Eqn. 2.22 is obtained from analysis of the free energy disregarding the higher order coupling terms. It represents a stability condition in  $\epsilon_{ij}$  and  $\mu_{ij}$ . This then suggests that in order to have a strong ME coupling  $\epsilon_{ij}$  and  $\mu_{ij}$  must be large [55]. The conventional intrinsic ME coupling assumed for eqn. 2.22, however, has not considered the effects of strain, although, such indirect coupling effects may be significant or even dominant. The inclusion of either magnetostriction or piezoelectricity would generate additional terms in the free energy proportional to strain. In such materials, the ME coupling is not limited by eqn. 2.22. These strain-coupled effects are important in the composite multiferroics and other intrinsic magnetoelectrics with more complex coupling mechanisms. In fact, the total ME coefficient,  $\alpha_{ij}$ , is given by the sum of the intrinsic ME coefficient in eqn. 2.21 and an additional contribution  $\Delta\alpha_{ij}$ .

$$\alpha_{ij} = \tilde{\alpha}_{ij} + \Delta\alpha_{ij} \quad \text{eqn. 2.23. [57]}$$

The total adiabatic magnetoelectric tensor is defined independently as;

$$\alpha_{ij} = \left( \frac{\partial \mathbf{M}}{\partial \mathbf{E}} \right)_{T, \mathbf{H}, \sigma} = \left( \frac{\partial \mathbf{P}}{\partial \mathbf{H}} \right)_{T, \mathbf{E}, \sigma} \quad \text{eqn. 2.24. [57]}$$

where  $\sigma$  is the tensor stress.

Through mathematical analysis of the difference between the definitions of both the intrinsic and total ME coefficients, Vittoria *et al* [57] showed that if a crystal were absolutely rigid when fields were applied (i.e. zero strain), then the intrinsic ME coupling would be equal to the total ME coupling, hence  $\Delta\alpha_{ij}$  would be zero. Furthermore, it is shown that the  $\Delta\alpha_{ij}$  term is a function of both the piezoelectric and magnetostriction constants,  $d$  and  $\lambda_m$ , respectively [57].

Based on the definition of  $\alpha_{ij}$  in eqn. 2.24, the direct magnetoelectric coupling coefficient is given to be  $dP/dH$  [59] and according to the Maxwell relation  $dP/dH = \mu_0 dM/dE$ , for a single phase, the converse magnetoelectric coupling coefficient is defined as  $\mu_0 dM/dE$  [59].

Measurements of a materials ME coupling constant are typically performed by either recording a magnetic response to an applied electric field or an electrical response to an applied magnetic field. A variety of methods have been developed to measure the converse ME coupling constant [60] [61]. One such method uses a vibrating sample magnetometer (VSM) to measure the change in the samples  $M(H)$  characteristics due to the application of an electric field [60]. Alternatively, for materials considered for tuneable microwave applications, the ME coupling has been measured through electric field induced changes in the ferromagnetic resonance (FMR) [61].

To measure the direct ME effect on the other hand the dynamic change in voltage or charge induced by the application of a magnetic field is often recorded. This can be achieved in several ways. One method is to record the polarisation hysteresis in the presence of different external magnetic fields, for which the change in  $P$  as a result of  $H$  can be determined [54]. Alternatively, Kitagawa *et al* [5] measured the direct ME coupling of a hexaferrite sample by measuring the ME current as a function of applied magnetic field. The  $P(H)$  of the sample was obtained through integration of the ME current in order to reveal the ME coupling. Here the magnetoelectric current is defined as the current induced in the sample as a result of the applied magnetic field [5].

### 2.5.2. Composite Magnetolectrics

A composite magnetoelectric is a multi-phased material in which neither of the phases possess the magnetoelectric effect individually, however, if one phase is piezoelectric whilst the other is magnetic, for example, the properties of one can be indirectly changed via strain/stress, or several other mechanisms, by the other [54].

For composite magnetoelectrics, there are two main criteria which need to be met before their potential applications, such as multiferroic hard drives can be realised [1]; the coupling mechanism must be strong, and this coupling mechanism must have a fast dynamic response. This is a particular challenge for composites due to the nature of coupling across phases. Whereas for intrinsic multiferroics the ME response can often be significantly faster due to the direct coupling and single-phase nature [55]. As such, the ideal magnetoelectric material would be one with a strong intrinsic ME coupling at and above RT. Given that few materials of this nature have been found, the concept of composite multiferroics has been significantly investigated throughout the past 20 years [62].

The three main methods for producing composite multiferroics have been discussed by Wang *et al*

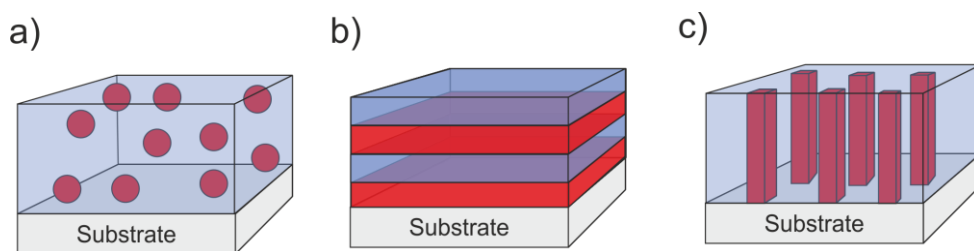


Figure 2.11. The three most common forms of composite multiferroics, (a) nanoparticles, (b) layered heterostructures and (c) nanocolumns.

[54]. As is shown in fig. 2.11, one form of composite multiferroic structure uses ferromagnetic nanoparticles embedded in a ferroelectric thin film, another uses ferromagnetic or ferroelectric nanopillars embedded in a film of the opposite phase. Perhaps the most common however is a '2-2 heterostructure', consisting of alternate ferromagnetic and ferroelectric layers deposited on a substrate. The ferroelectric phase is often chosen to be a material displaying strong, controllable piezoelectric properties, such as BTO, PZT or lead magnesium niobate - lead titanate (PMN-PT), and the ferromagnetic phase is often chosen to be a ferrite material, decided upon according to its properties [62].

### **2.5.2.1. Composite Magnetolectric coupling mechanisms**

There have been two primary magnetolectric coupling mechanisms exploited in composite multiferroics. The coupling mechanisms [1] [18] are based on; strain applied between the piezoelectric and magnetostrictive phases and by charge coupling, where the electric field can be used to alter the density of charge carriers in the ferromagnetic layer.

#### **2.5.2.1.1. Strain Coupling**

Strain mediated ME coupling is a result of piezoelectric and magnetostrictive interaction across the interface between ferroelectric and ferromagnetic phases [1]. When a composite multiferroic is constructed the phases can be engineered with a minimal lattice mismatch between layers in order to allow the expansion (or constriction) of one material to be enforced on the other via interfacial strain. For a multiferroic heterostructure, in the absence of an external electric or magnetic field the ferromagnetic and ferroelectric layers will sit in equilibrium. However, applying an electric field causes the electrical domains in the ferroelectric layer to re-orient with the field. Thus, a converse piezoelectric effect will induce the ferroelectric layers to grow or shrink. This strains the ferromagnetic layer and the magnetostrictive properties of ferromagnetic layer will cause its domains to re-orient.

The strain coupling mechanism has been extensively studied in the last decade [1] but problems remain. Layered thin film structures suffer from a clamping effect of the substrate on the lattice. This effect damps the piezoelectric strain of the ferroelectric component, thus the overall ME coupling. It was reported by Opel [2] that clamping can lead to a decrease in the ME coupling by a factor of 5. However, the effect is interface dependent and a result of chemical, structural and electromagnetic parameters [63]. It has been shown [54] that by the inclusion of a buffer layer at the substrate interface, clamping effects can be reduced.

An alternative solution to the clamping problem has been demonstrated in the growth of self-assembled nanopillars [64]. Zheng *et al* [1] deposited  $\text{CoFe}_2\text{O}_4$  with  $\text{BaTiO}_3$  using PLD on a  $\text{SrTiO}_3$  substrate and found that nanopillars self-assembled on the surface. Subsequent experiments have measured ME coupling effects in such structures. Vaz [54] reported that these nanostructures minimize the clamping problems discussed. However, self-assembled nanostructures such as these pillars remain difficult to synthesise.

#### **2.5.2.1.2. Charge Coupling**

More recently, charge coupling across the interface has been discovered as a magnetolectric coupling mechanism in composite heterostructures [1]. At the interface between the phases, the different lattices co-exist and automatically create a non-symmetric structure. In addition, as one of the phases is ferromagnetic, it follows that the interface will also be ferromagnetic. Rondinelli *et al* [65] suggested that the interface could be modelled as that of a capacitor. They found the electric field induces a change in the magnetisation at the interface. This results in a magnetic response in the ferromagnetic layer by accumulating spin-polarised charge in the atomic layers closest to the interface. As a result, the magnetism and charge polarisation coexist at the interface between films. In the last decade, ME effects in many composite multiferroics have been reported. Perhaps the most notable of which has been in a ferromagnetic 40nm  $\text{La}_{0.67}\text{Sr}_{0.33}\text{MnO}_3$  film on a 0.5mm ferroelectric  $\text{BaTiO}_3$  substrate. In this composite a large ME coupling of  $2.3 \times 10^{-7} \text{ s m}^{-1}$  has been observed, near RT with low magnetisation [66]. Ni –  $\text{BaTiO}_3$  composite materials have also shown promise as room temperature magnetolectrics. Castel *et al* [67] successfully measured a change in the permittivity of the  $\text{BaTiO}_3$  phase with applied magnetic field. The effect is due to ME coupling at the interface between the magnetostrictive Ni and the Piezoelectric  $\text{BaTiO}_3$ , with Geprags *et al*

[68] measuring a ME coupling of  $5 \times 10^{-10} \text{ s m}^{-1}$ . Parkes et al [69] reported the development of Galfenol ( $\text{Fe}_{81}\text{Ga}_{19}$ ) thin films displaying high magnetostriction. Investigating  $\text{Fe}_{81}\text{Ga}_{19}$  deposited on piezoelectric PZT, they demonstrated voltage controlled modifications to the magneto-crystalline anisotropy within the composite. This demonstrates the possibility for using voltage induced strain in low-power voltage tuneable magnetic devices.

Numerous other heterostructures with various combinations of piezoelectric and ferromagnetic have been investigated and found to display ME coupling by both strain and charge coupling mechanisms [1]. Combinations of ferrite layers, such as  $\text{CoFe}_2\text{O}_4$ ,  $\text{Fe}_3\text{O}_4$  and  $\text{Zn}_{0.1}\text{Fe}_{2.9}\text{O}_4$ , with piezoelectrics like BTO and PMN-PT have been characterised with several showing significant ME coupling. For example,  $\text{Fe}_3\text{O}_4/\text{PMN-PT}$  has one of the largest coupling constants found of  $1 \times 10^{-7} \text{ s m}^{-1}$  [1]. Additionally, one of the most promising combinations studied has been Terfenol-D/PZT. Terfenol-D ( $\text{Tb}_x\text{Dy}_{1-x}\text{Fe}_2$ ) as a material is strongly magnetostrictive and PZT piezoelectric. As a combination, they display a direct magnetoelectric coupling of  $1 \times 10^{-9} \text{ s m}^{-1}$  [70]. The strain and charge coupling mechanisms demonstrate how an electric field, in principle, switches the orientation of the ferromagnetic domains in a composite multiferroic. This has driven extensive research into composite multiferroics [1] [54] [2].

### 2.5.3. Intrinsic Multiferroics

Ultimately, finding an intrinsic magnetoelectric material with a strong ME coupling at RT, would be the ideal solution to realising large scale ME device applications. Unfortunately, most intrinsic magnetoelectrics reported to date tend to be antiferromagnetic and ferroelectric, and only below RT. As previously mentioned, the reason for this is that ferroelectrics have to be insulators, as free electrons would screen the electrical polarisation; ferromagnets need to have unfilled orbital shells to create the spin magnetic moment. Thus, intrinsic multiferroics typically have a very weak ME coupling [3].

The first intrinsic multiferroic to be discovered and extensively studied was  $\text{Cr}_2\text{O}_3$ . This may have potential for device applications due to its relatively high Néel temperature of 307 K. It has a coupling coefficient of  $4.1 \times 10^{-12} \text{ s m}^{-1}$  at 307 K, which is a small effect, orders of magnitude smaller than that observed in some ME hexaferrites or composite multiferroics.  $\text{Cr}_2\text{O}_3$  is both ferroelectric and antiferromagnetic at RT [60].

One group of materials which also exhibit the ME effect are perovskite based ferroelectrics, such as  $\text{BiMO}_3$ , where M may represent Mn, Fe or Cr and  $\text{PbVO}_3$  [71]. The mechanism for the ferroelectricity in these materials is due to the displacement of cations with respect to the oxygen octahedral cage. Thus, the hopping of an electron can occur between the d-shell of the transition metal and the p-shell of the oxygen. This mechanism requires a transition metal with an empty d-shell where ferromagnetism requires the d-shell to be partially filled. Hence, these materials are ferroelectric and antiferromagnetic. In the case of  $\text{BiFeO}_3$ , these two orders can coexist as the lone pair of electrons in  $\text{Bi}^{3+}$  tries to displace the d-shell in the Fe atom contributing to the magnetism [71].  $\text{BiFeO}_3$  has a high Curie temperature of  $\sim 1100 \text{ K}$ . Until 2010 the only single phase, multiferroic thin films produced had been Bi and Pb based perovskites, such as  $\text{BiFeO}_3$  and  $(\text{Bi}_{0.5}\text{Pb}_{0.5})(\text{Fe}_{0.5}\text{Zr}_{0.5})\text{O}_3$ , as well as some hexagonal manganites [56]. However, the coupling observed has been small. For example, the ME effect in thin films of  $\text{BiFeO}_3$  was observed to be  $\sim 3 \times 10^{-11} \text{ s m}^{-1}$  [72]. Another well-researched intrinsic multiferroic is  $\text{LuFe}_2\text{O}_4$  [73]. This is a compound containing ions of mixed valence, which form a polar arrangement. Due to this charge order, it exhibits improper ferroelectricity. The structure of  $\text{LuFe}_2\text{O}_4$  is triangular with Fe/O double layers, with the ferroelectricity originating from the arrangement of  $\text{Fe}^{2+}$  and  $\text{Fe}^{3+}$  with respect to

the oxygen atoms. However, it only exhibits the ME effect far below RT as, although this ferroelectricity is seen below 330 K, its ferrimagnetism is only present below 240 K [73].

One intrinsic multiferroic with potential for device applications may be CuO [74]. CuO is a candidate for exhibiting the ME effect at close to RT, having magnetic transitions at 213 K, 229 K and 230 K, although investigations have only seen ME coupling at temperatures of 213 K to date [75]. CuO forms a monoclinic crystal system and exhibits non-collinear spiral magnetic order, which breaks inversion symmetry, thus inducing ferroelectricity [74]. Other multiferroics showing this spiral spin structure are TbMnO<sub>3</sub> and MnWO<sub>4</sub>, although both have Curie temperatures around 20 K [74].

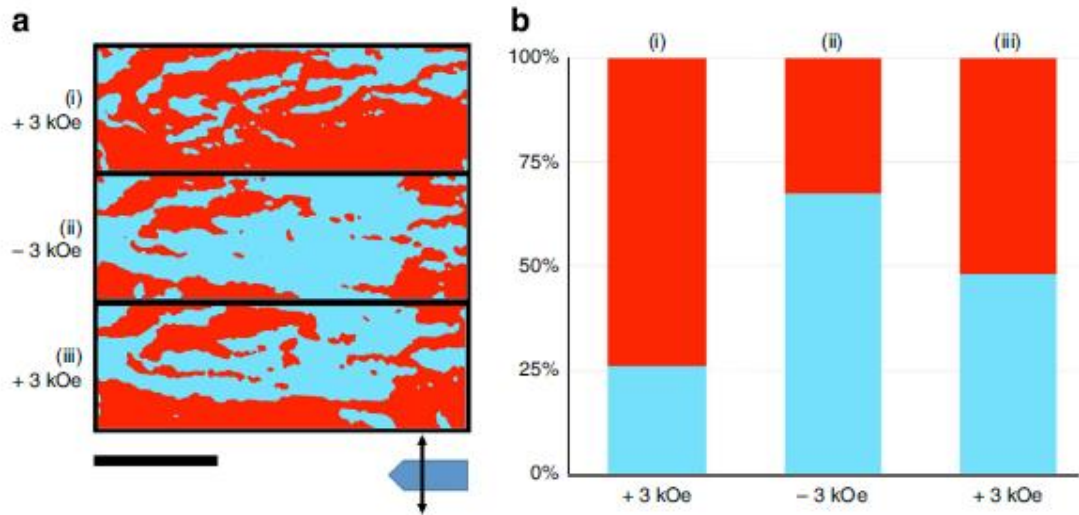


Figure 2.12. (a) The ferroelectric domains in PZTFT with applied magnetic field. (b) Histogram showing the change in ferroelectric phase [76].

Recently, a newly-discovered single-phase multiferroic,  $[\text{Pb}(\text{Zr}_{0.53}\text{Ti}_{0.47})\text{O}_3]_{0.6}[\text{Pb}(\text{Fe}_{0.5}\text{Ta}_{0.5})\text{O}_3]_{0.4}$  or PZTFT has been shown to exhibit significant ( $\sim 60\%$  change in polarization) direct ME coupling at room temperature ( $\sim 1 \times 10^{-7} \text{ s m}^{-1}$ ) [76]. Evans *et al* [76] measured this effect by observing the change in the orientation of ferroelectric domains as the direction of an applied magnetic field was reversed, as shown in fig. 2.12. This demonstrates that with careful material design, the development of room temperature multiferroic materials can be achieved, although few materials have as yet been discovered displaying strong ME coupling at RT.

## 2.6 Hexagonal ferrites

Magnetoplumbite was the first hexaferrite to be studied, with the pure form having the composition  $\text{PbFe}_{12}\text{O}_{19}$  [6]. However, it was not until the 1950's that Phillips technical laboratories led the way in developing hexaferrites for device applications. Since this period there has been an exponential growth in the studies of such materials to the point where they now account for a vast part of the total magnetic materials manufactured globally. Hexaferrites have a wide range of currently applied technological applications, for example as permanent magnets and as microwave devices such as antennas, circulators and isolators [6].

In digital data storage a material with a square hysteresis loop is required, as well as a relatively low coercivity so that small fields can be used in order to re-write data. As such, M-type hexaferrites are commonly used for magnetic recording being both mechanically strong and chemically stable. Cobalt and titanium doped M-type hexaferrites have been found to be particularly suited to use in recording media, as the grain size and coercivity can be lowered without significant loss in magnetisation, due to the Co and Ti substitutions [6].

In the past few years, several compositions of hexaferrite have been discovered displaying a strong magnetoelectric coupling at room temperature [12] [5]. This has opened up a resurgence of interest

into their properties, with hexaferrites becoming a leading contender for magnetoelectric device applications. Kitagawa *et al* [5], in 2010, showed that the Z-type hexaferrite,  $\text{Sr}_3\text{Co}_2\text{Fe}_{24}\text{O}_{41}$ , possesses low-field ME coupling at room temperature. Even more recently, in 2012,  $\text{SrCo}_2\text{Ti}_2\text{Fe}_8\text{O}_{19}$  was found to exhibit a spontaneous polarization at zero magnetic field, which enabled electric-field control of magnetism at RT, in the absence of a magnetic field [10]. Such a spontaneous polarisation was unexpected in the M-type structure, as the M-types reported had been shown to have either a ferrimagnetic, screw or longitudinal conical spin structure, at  $H = 0$ . None of which result in an improper ferroelectricity under the inverse Dzyaloshinskii-Moriya mechanism [12].

There are six main types of Hexaferrite, M, Z, Y, W, X and U, classified according to their crystal structure and chemical composition. The general compositions of each type are:

- M-type –  $\text{BaFe}_{12}\text{O}_{19}$
- Z-type –  $\text{Ba}_3\text{Me}_2\text{Fe}_{24}\text{O}_{19}$
- Y-type –  $\text{Ba}_2\text{Me}_2\text{Fe}_{12}\text{O}_{22}$
- W-type –  $\text{BaMe}_2\text{Fe}_{16}\text{O}_{19}$
- X-type –  $\text{Ba}_2\text{Me}_2\text{Fe}_{28}\text{O}_{46}$
- U-type –  $\text{Ba}_4\text{Me}_2\text{Fe}_{36}\text{O}_{60}$

where Me represents a small 2+ ion such as cobalt, iron, nickel or zinc. Additionally, the Ba can be substituted for either Sr or Pb within each structure. The Z, W, X and U-types can be seen as different combinations of the M-type, Y-type and a spinel unit ( $\text{MeFe}_2\text{O}_4$ ), for example  $Z = M + Y$ ,  $U = 2M + Y$  and  $W = M + 2$  spinel units [6].

Each Hexaferrite structure is composed of a stacking sequence of the basic S-, R-, and T-blocks [5]. The S-block represents a  $\text{Me}_2\text{Fe}_4\text{O}_8^{2+}$  unit, the R-block  $\text{BaFe}_6\text{O}_{11}^{2-}$  and the T-block  $\text{Ba}_2\text{Fe}_8\text{O}_{14}^{2-}$  [77]. Different repeating sequences of these blocks make up the different hexaferrite types, for example the Z-type consists of a STRSS\*T\*R\*S\* sequence, where the \* represents a  $180^\circ$  rotation about the c-axis [6]. The S-block consists of two spinel units, with two layers of four oxygen atoms and three metal ions between each layer. Four of the metal ions within the S-block are in octahedral sites and two in tetrahedral sites. The R-block is made up of three layers of four hexagonally packed oxygen's, with one of the oxygen's replaced by a similarly sized barium ion. This barium ion results in an asymmetry in some of the cation sites, producing five octahedral and a trigonal bipyramidal cation site. Finally, the T-block is made of four oxygen layers, with a barium atom replacing an oxygen in each of the two middle layers, resulting in six octahedral and two tetrahedral cation sites [6].

Hexaferrites are typically ferrimagnetic materials, with their magnetic properties intrinsically linked to their crystal structures. The hexagonal structure allows for various ionic substitutions, which in turn alter their magnetic properties, such as anisotropy, coercive field and saturation magnetisation, ultimately extending the range of their possible applications by allowing the tailoring of their properties through ionic substitutions. The origin of the magnetic properties in hexaferrites is primarily governed by the presence of the Fe-O-Fe bonds. In Hexaferrites, iron atoms interact with each other via the oxygen in a process known as superexchange, described in section 2.3.2. The GKA rules determine the type of magnetic coupling present. Hence Fe in different surroundings will have a different contribution to the hexaferrites overall magnetic properties. Understanding the contributions of these sites is crucial to understanding the mechanism governing the magnetoelectric behaviour of certain hexaferrite materials.

Along with the superexchange interaction the hexaferrite crystal structure allows anti-symmetric spin-coupling between the spins of cations at certain sites, first shown by Moriya [41] [78]. This anti-symmetric exchange contributes to the overall exchange interaction between the magnetic ions. In hexaferrites antisymmetric spin coupling can be observed in sites of the lattice where the superexchange is greatly weakened due to competing superexchange interactions or is absent due to substitutions for non-magnetic ions [78]. For certain M, Z, W, U and Y hexaferrite structures the

presence of sites displaying such anti-symmetric spin coupling results in the formation of helical spin structures [78], some of which lead to the presence of an improper ferroelectricity, as discussed in section 2.4.1.

### 2.6.1. M-type hexagonal ferrites

The particular hexaferrite structure studied in this work will be the M-type. M-type hexaferrites have a general composition  $MFe_{12}O_{19}$ , where M represents a Ba, Sr or Pb atom. The molecular unit of an M-type hexaferrite is made of one S and one R-block, with an overlap of hexagonally and cubically packed layers. They have a stacking sequence  $RSR^*S^*$ , where \* indicates an  $180^\circ$  rotation about the c-axis [79]. The S layer represents a spinel structure ( $S = Fe_6O_8^{2+}$ ) and the R layer a hexagonal structure ( $R = MFe_6O_{11}^{2-}$ ) [77].

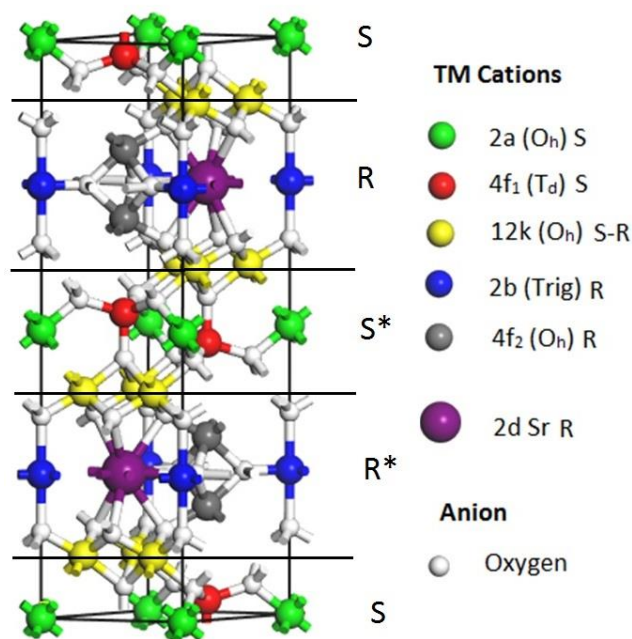


Figure 2.13. M-type structure showing Wyckoff positions, co-ordination and cation block.

M-type hexaferrites have a structure belonging to the  $P63/mmc$  space group [6]. A schematic representation of the structure of the M-type unit cell can be seen in fig. 2.13. Here the unit cell consists of two formula units. In the figure, the different Wyckoff positions are shown in different colours. The M atom, whether it be Ba, Sr or Pb, substitutes for an oxygen and occupies the 2d position in the R-block. Each cation within the structure is surrounded by a cage of oxygen atoms. There are three different cation co-ordinations within the M-type structure, octahedral, tetrahedral and trigonal bipyramidal. A unit cell contains 18 octahedral sites, 2 at the 2a positions, located in the S-block, 4 at the R-block 4f<sub>2</sub> positions and 12 at the 12k Wyckoff positions at the boundary between R and S-blocks. Likewise, there are 4 tetrahedral sites, all located at the 4f<sub>1</sub> positions within the S-block and finally, there are 2 cations in a trigonal bipyramidal site per unit cell, which are at the 2b positions of the R-block [77].

The three different co-ordinations present within the M-type structure are shown in fig. 2.14. In an octahedral surrounding, the cations are enclosed by 6 oxygen atoms that form an octahedra, resulting in  $90^\circ$  bond angles between all ligands. For a tetrahedral co-ordination the cation is surrounded by 4 oxygens forming a tetrahedra, or triangular based pyramid, with a  $109.47^\circ$  bond angle [37]. Finally, a trigonal bipyramidal co-ordination is formed when the cation is surrounded by 5 oxygen atoms. This structure forms with three equatorial ligands, with  $120^\circ$  bond angles, and axial ligands, above and below the cation.

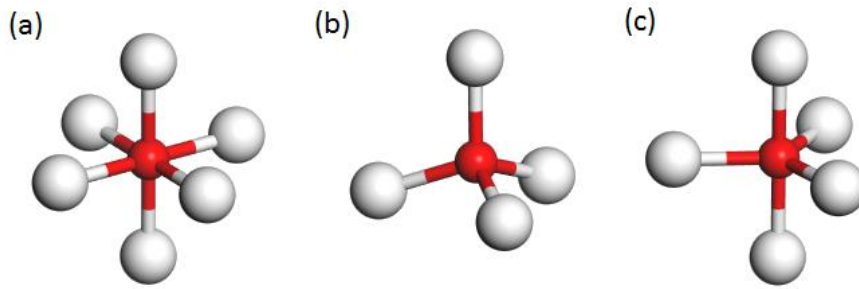


Figure 2.14. 3D atomistic representation of the three cation co-ordinations present with M-type hexaferrite, (a) Octahedral, (b) tetrahedral, (c) trigonal bipyramidal.

As the magnetism and magnetic interactions in such ferrite materials are mediated through the oxygen bonds via superexchange, the co-ordinations of the cations are an important consideration when substituting different cations into the structure [80]. Thus, the site of substitution should have a significant effect on the materials magnetic properties.

#### 2.6.1.1. Barium ferrite

The archetype M-type structure is barium ferrite (BaM),  $\text{BaFe}_{12}\text{O}_{19}$ , within which the barium ion is located at the 2d site and all cation sites are occupied by Fe ions with a 3+ valence [37]. BaM has lattice constants of  $a = 5.89 \text{ \AA}$  and  $c = 23.17 \text{ \AA}$  [6]. The presence of the  $\text{Ba}^{2+}$  ion causes a perturbation in the lattice, due to its size difference with respect to the oxygen atoms. This results in a uniaxial anisotropy, with a preferred axis of magnetisation along the c-axis [6].

As a consequence of the superexchange interactions within the BaM structure, the 12k and 2a octahedral sites as well as the 2b trigonal bipyramidal all have magnetic moments that are parallel to each other along the c-axis. However, the tetrahedral  $4f_1$  and octahedral  $4f_2$  sites have moments that are antiparallel to these. These orientations of magnetic moments are governed by the GKA rules in accordance with the relative bond angles at each site. This results in 8 moments pointing up and 4 moments pointing down, resulting in a net total of 4 up. As all the magnetic ions within the structure are  $\text{Fe}^{3+}$ , each with a magnetic moment of  $5.92 \mu_B$ , the theoretical magnetisation per formula unit is equal to  $4 \times 5.92 = 23.68 \mu_B$  [80]. This structure results in a relatively high saturation magnetisation ( $M_s$ ) of  $72 \text{ emu/g}$  (or  $382 \text{ emu/cc}$ ) at room temperature, as well as a Curie temperature of  $723 \text{ K}$  [80] [6]. It also has a large crystalline anisotropy field of  $17 \text{ kOe}$  along the c-axis [6]. This uniaxial anisotropy gives BaM a large theoretical maximum coercivity ( $H_c$ ) of  $7.5 \text{ kOe}$ . The experimental  $H_c$  values tend to be significantly smaller than this, with Went *et al* [81] observing coercivities of the order of  $2 \text{ kOe}$  for bulk samples prepared by standard ceramic methods and Geiler *et al* [21] observing coercivities as low as  $150 \text{ Oe}$  for epitaxial BaM thin films.

In recent years, M-type Ba-hexaferrite ( $\text{BaFe}_{12}\text{O}_{19}$ ) thin films have shown potential for microwave devices due to their excellent electromagnetic performance, high chemical stability and mechanical durability [82].

#### 2.6.1.2. Strontium ferrite

The M-type hexaferrite structure can be readily modified by replacing the Ba with Sr to form strontium ferrite (SrM), with chemical composition  $\text{SrFe}_{12}\text{O}_{19}$ .  $\text{Ba}^{2+}$  has a radius of  $1.36 \text{ \AA}$  and the radius of  $\text{Sr}^{2+}$  is smaller at  $1.16 \text{ \AA}$  [37], hence replacing the Ba ion with the smaller Sr ion creates local distortions in the crystal lattice. The Fe-O-Fe bond angle in the vicinity of the Sr ion is changed from  $116^\circ$  (with Ba) to  $123^\circ$  (with Sr) [83], resulting in a change in lattice constants from  $a = 5.89 \text{ \AA}$ ,  $c = 23.17 \text{ \AA}$  to  $a = 5.86 \text{ \AA}$  and  $c = 23.03 \text{ \AA}$  [6]. This also affects the superexchange between local Fe ions, producing changes in the materials magnetic properties. Typically, the magnetic properties of

SrM are slightly higher than those of BaM. Strontium ferrite has a Curie temperature of 743 K [6], as well as a uniaxial anisotropy along the c-axis with  $H_A = 20$  kOe [6]. The saturation magnetisation has been reported to be as high as 74.3 emu/g (400 emu/cc) for single crystal SrM at RT, with a maximum coercivity of 6.7 kOe [6]. Again, the values reported for polycrystalline samples or thin films are typically much lower [6].

### 2.6.1.3. Co and Ti substituted Hexaferrites

The substitution of the Fe ions for other elements has long been investigated as a means to modify the magnetic properties of the M-type hexaferrite, in order to suit specific device applications [6]. The technologically most important of which are the Co and Ti substituted M-type, namely,  $\text{BaCo}_x\text{Ti}_x\text{Fe}_{12-2x}\text{O}_{19}$  and  $\text{SrCo}_x\text{Ti}_x\text{Fe}_{12-2x}\text{O}_{19}$ . They are of major commercial interest as magnetic recording media and for their microwave properties and were first studied in the 1960's as a way of lowering grain size and coercivity without any significant loss to  $M_s$ . These materials were then commercially developed in the 80's by Toshiba, producing nanoparticles 50 nm wide with a coercivity of 2 kOe [84]. Since then, the coercivity has been reduced greatly, through investigation of the  $\text{BaCo}_x\text{Ti}_x\text{Fe}_{12-2x}\text{O}_{19}$  series of hexaferrites, and the properties can be tuned with the variation of  $x$ . Kojima *et al* [85] observed a minimum in coercivity with a value of  $x = 1.2$ .

Doping barium or strontium ferrite with Co and Ti has been found to weaken multi-block spin interactions, inducing non-collinear magnetic structures, above a critical  $x$  value. The non-magnetic  $\text{Ti}^{4+}$  cations are believed to substitute to the 12k octahedral sites [10]. This is thought to interrupt the magnetic interactions in such a way that the two blocks  $RS$  and  $R^*S^*$ , within the unit cell become magnetically decoupled [10] [15]. As for the cobalt, above a critical doping concentration, it is proposed that occupation of trigonal bipyramidal sites by  $\text{Co}^{2+}$  are partly responsible for the induction of a cone of magnetisation due to non-collinearity, the formation of which also has an effect in further reducing  $H_c$  [86] [6]. However, there are contradictions in the literature as to whether the  $\text{Co}^{2+}$  cations prefer to occupy the octahedral ( $O_h$ ) [10] [87] or tetrahedral ( $T_d$ ) [15] [88] [86] lattice sites initially. Wang *et al* [10] have observed the occupation of the  $4f_2$   $O_h$  sites by Co in polycrystalline  $\text{SrCo}_2\text{Ti}_2\text{Fe}_8\text{O}_{19}$ , using Reitveld refinement of X-ray diffraction analysis. Alternatively, Cabanas *et al* [86] observed occupation of  $T_d$  sites by Co using neutron diffraction, as did Kreisel *et al* [15], with Batlle *et al* [89] determining by Reitveld refinement that Co substitutes initially into both the  $O_h$   $4f_2$  and  $T_d$   $4f_1$  sites.

Kreisel *et al* [15] performed a detailed neutron diffraction study on  $\text{BaCo}_x\text{Ti}_x\text{Fe}_{12-2x}\text{O}_{19}$  single crystals, with  $x$  ranging between 0 and 1.1. They determined that the uniaxial anisotropy is weakened with increased substitution, forming a conical magnetic structure above  $x = 0.8$  and for  $x = 1$  at RT a cone angle of  $61^\circ$  from the c-axis was determined. The induction of the conical spin configuration in Co-Ti doped M-type hexaferrites is a consequence of the combined effects of the Co and Ti on the crystal and magnetic structure [15]. The ionic substitution and formation of such a spin arrangement, allows for the tailoring of magnetic properties due to dopant concentration. Studies also show a change in the temperature dependence of magnetisation due to doping, for  $\text{BaCo}_x\text{Ti}_x\text{Fe}_{12-2x}\text{O}_{19}$  the Curie temperature reduces with increased  $x$ , as does  $M_s$  [80].

### 2.6.1.4. Other substituted M-type Hexaferrites

Many other doped M-type hexaferrites have been investigated, in order to tailor their magnetic and electronic properties. Cobalt and zirconium doped M-types have been reported to show a large drop in  $H_c$  whilst maintaining  $M_s$ , with bulk samples producing a  $H_c$  as low as 150 Oe [90]. Whilst increasing substitution of Zn and Ti has been shown to reduce both  $H_c$  and grain size, by Wang *et al* [91], however this was also combined with a reduction in  $M_s$ . Co and Sn doping also results in a reduced  $H_c$  whilst maintaining a high  $M_s$  and  $M_r/M_s$ , with a grain size smaller than BaM [92]. The

design of Phase shifter microwave devices requires a low  $H_c$  as well as a high Néel temperature, high remanence and  $M_s$ . To this end, Harris *et al* [93] investigated Sc doped  $BaFe_{12-x}Sc_xO_{19}$  thick films which showed, for  $x = 0.3$ , a  $H_c$  of 250 Oe and a high squareness ratio of 0.9. They also observed a reduction in  $M_s$  for an increase in Sc substitution. It was also shown that doping with In as opposed to Sc increased  $M_s$  and the squareness, however, also dramatically increased  $H_c$  [94]. Numerous combinations of doped M-type hexaferrites have been studied, each displaying different magnetic properties that can be tailored by doping to suit specific device applications, a review of such materials has been produced by Pullar [6].

## 2.6.2. Magnetolectric Hexaferrites

In recent years, several forms of Y, Z, U and M-type hexaferrites, all displaying non-collinear magnetic structures, have been found to exhibit magnetolectric effects, some of which have been measured up to and above room temperature.

### 2.6.2.1. Y-type Magnetolectric Hexaferrites

The first hexaferrite discovered to be a single-phase multiferroic material was the Y-type  $Ba_{2-x}Sr_xZn_2Fe_{12}O_{22}$  by Kimura *et al*, in 2005 [7]. It was found that within this structure the partial substitution of the Ba for Sr affects the superexchange interactions in such a way to induce a non-collinear magnetic structure. Further investigation showed that this helical spin structure could be modified by the application of a magnetic field perpendicular to the c-axis, resulting in a transition through several magnetic spin phases before becoming collinear at a field of 2.2 T. Kimura *et al* reported that these phase changes additionally coincided with changes in the electrical polarisation, demonstrating the direct magnetolectric effect, fig. 2.15. However, although the magnetic phase transitions were found to occur to above RT, the induced polarisation can only be observed up to 110 K, above which the conductivity of the material became too great [7].

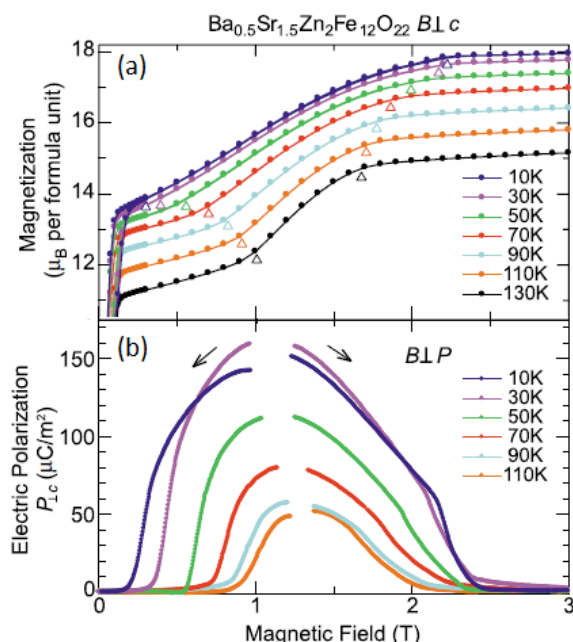


Figure 2.15. (a)  $M$  and (b)  $P$  as a function of  $H$  for  $Ba_{0.5}Sr_{1.5}Zn_2Fe_{12}O_{22}$  obtained by Kimura *et al* [7]. To pole the crystal  $E = 220$  kV/m was applied initially.

It was subsequently found, by Chun *et al* [95] that the ME properties of this Y-type hexaferrite could be enhanced by Al substitution to the octahedral cation sites, resulting in a reduction in the magnetic field required to induce polarisation to as little as 1 mT. They determined this to be as a consequence of the Al reducing the magnetocrystalline anisotropy, producing a large direct ME

coupling. Chai *et al* [96] then measured a converse ME coupling in single crystals of the same Y-type structure, with composition  $\text{Ba}_{0.5}\text{Sr}_{1.5}\text{Zn}_2(\text{Fe}_{0.92}\text{Al}_{0.08})_{12}\text{O}_{22}$ , below 170 K and without any external magnetic field.

Another form of Y-type hexaferrite was discovered to display multiferroic properties in  $\text{Ba}_2\text{Mg}_2\text{Fe}_{12}\text{O}_{22}$ , by Taniguchi *et al* [97]. They reported the coexistence of ferroelectric polarisation and spontaneous magnetisation at zero applied magnetic field, however, only up to 200 K. Below this temperature, a reversal in magnetisation was also accompanied by a reversal in polarisation for magnetic fields as low as 200 Oe. This effect was attributed to the formation of a non-collinear helical-spiral spin structure, below 200 K, in which the spins rotate about the c-axis [97].

More recently, both converse and direct ME effects have been observed in the Co, Al and Zn doped Y-type,  $\text{BaSrCoZnFe}_{11}\text{AlO}_{22}$  single crystals [98]. Shen *et al* [98] demonstrated that the electrical polarisation induced in the material due to its conical magnetic structure, at low temperature, can be reversed by small magnetic fields and conversely the in-plane can be controlled by electric fields. Relatively large ME coupling constants have been measured for this material, as high as  $6 \times 10^{-9} \text{ s m}^{-1}$  at 100 K, but still only at temperatures far below RT.

### 2.6.2.2. Z and U-type Magnetolectric Hexaferrite

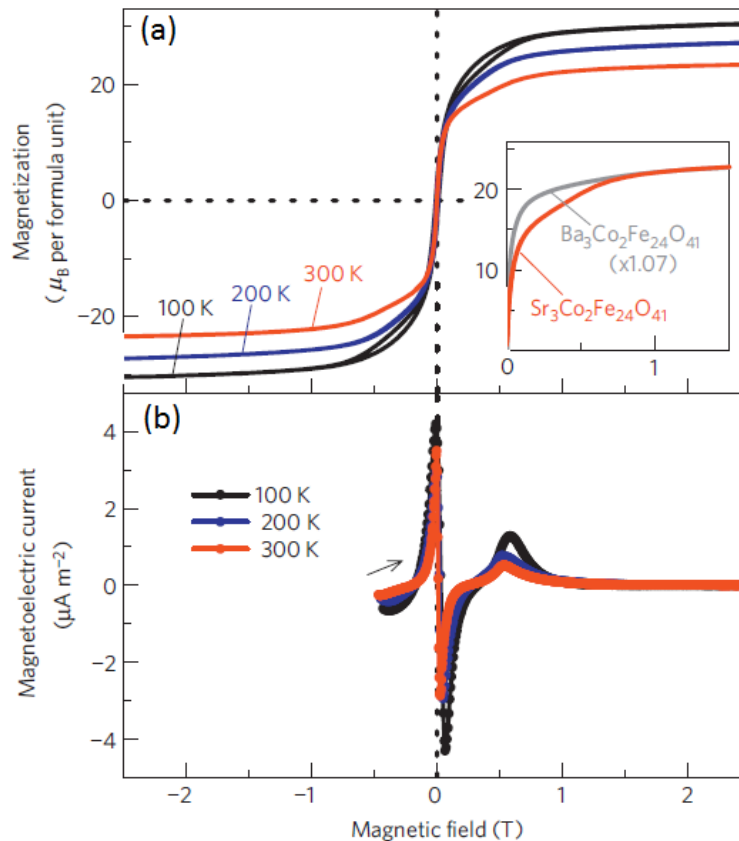


Figure 2.16. (a) Magnetisation and (b) magnetolectric current as a function of magnetic field for  $\text{Sr}_3\text{Co}_2\text{Fe}_{24}\text{O}_{41}$  obtained by Kitagawa *et al* [5].

Perhaps the most significant breakthrough for ME hexaferrites came in 2010, as up until this point none of the existing single-phase magnetoelectrics had combined large and robust electrical and magnetic polarisations at RT, when Kitagawa *et al* [5] reported a large, low-field ME effect in the Z-type,  $\text{Sr}_3\text{Co}_2\text{Fe}_{24}\text{O}_{41}$ . Studies on  $\text{Ba}_3\text{Co}_2\text{Fe}_{24}\text{O}_{41}$  had suggested that it undergoes a magnetic transition at 230 K and has a cone of easy magnetisation below this temperature. It has been shown that the replacement of Ba with Sr modifies the superexchange interaction of nearby Fe-O-Fe bonds and increases the bond angle to stabilise a spiral magnetic order [5]. Pullar *et al* [99] had noticed a

strange double step in the magnetic hysteresis of  $\text{Sr}_3\text{Co}_2\text{Fe}_{24}\text{O}_{41}$  at RT, suggesting that it was a consequence of a helical magnetic order.

This then led Kitagawa *et al* [5] to investigate the multiferroic properties of the Z-type  $\text{Sr}_3\text{Co}_2\text{Fe}_{24}\text{O}_{41}$ . They discovered that  $\text{Sr}_3\text{Co}_2\text{Fe}_{24}\text{O}_{41}$  sintered in oxygen exhibits a low field ME effect at RT. Samples sintered in oxygen showed a six order of magnitude increase in resistivity compared to those prepared in air. They postulate that this is due to a decrease in the presence of  $\text{Fe}^{2+}$  reducing the hopping conduction between the  $\text{Fe}^{2+}$  and  $\text{Fe}^{3+}$  sites within the hexaferrite structure. High resistivity is required for large ME effects as the presence of any leakage current significantly suppresses the ferroelectricity. It was shown, fig. 2.16, that for the polycrystalline  $\text{Sr}_3\text{Co}_2\text{Fe}_{24}\text{O}_{41}$  samples the magnetisation increased in two stages with applied magnetic field up to their saturation magnetisation. As the field is increased from 0 to 0.1 T the magnetisation shows a rapid increase, with a more gentle increase observed between 0.1 and 0.7 T, and saturation achieved at fields  $>1$  T. These anomalies in the magnetisation accompany large ME effects at the same values of applied field which indicates a strong coupling between the magnetic and ferroelectric properties [5]. An applied field of 300 Oe was enough to observe a direct ME coupling of  $2.5 \times 10^{-10} \text{ s m}^{-1}$  at RT, more than 50 times larger than in  $\text{Cr}_2\text{O}_3$  [5].

Ebnabbasi *et al* [100] backed up the work of Kitagawa, reporting the observation of converse ME effects on Sr doped Z-type hexaferrite,  $\text{Sr}_3\text{Co}_2\text{Fe}_{24}\text{O}_{41}$ , at RT. They measured a change of  $\sim 18\%$  in remanence magnetisation as a consequence of the application of an electric field of 5 kV/cm. A similar change was also observed in the dielectric constant in a magnetic field as small as 320 Oe. Ebnabbasi *et al* [101] also published further measurements on the material, reporting ME effects at microwave frequencies, achieved by measuring permeability as a function of frequency via an FMR method outlined in their work. The ME coupling coefficient for a bulk polycrystalline  $\text{Sr}_3\text{Co}_2\text{Fe}_{24}\text{O}_{41}$  sample was measured to be  $7.6 \times 10^{-10} \text{ s m}^{-1}$  at RT [102]. At RT a ME coupling of  $2.3 \times 10^{-6} \text{ s m}^{-1}$  was also observed in single crystal  $\text{Sr}_3\text{Co}_2\text{Fe}_{24}\text{O}_{41}$  by Ebnabbasi *et al* [60]. In an electric field equivalent to 3.75 V/cm a 14% change in  $M_r$  was observed. This is promising for device applications in terms of being able to induce magnetisation changes with as little as 0.15 V compared to polycrystalline materials requiring hundreds of volts to induce the same change.

In the study of Z-type ME hexaferrites, the most recent development has been the observation of giant magnetoresistance due to ME currents in  $\text{Sr}_3\text{Co}_2\text{Fe}_{24}\text{O}_{41}$  by Wang *et al* [103]. Their work has indicated that an induced ME current in a transverse conical spin structure not only presented a nonlinear behaviour with magnetic and electric field but also depended on the sweep rate of the applied magnetic field. At RT a giant magnetoresistance of 32.2% was measured for low magnetic fields (125 Oe). This discovery takes the ME hexaferrites a step closer to device applications e.g. detecting the magnitude and frequency of an alternating magnetic field and generating a magnetically controllable pulse signal, important for applications such as medical imaging.

Given the structural similarities between the Z and U-types,  $\text{Sr}_4\text{Co}_2\text{Fe}_{36}\text{O}_{60}$  has also been reported as a room temperature magnetoelectric, governed by a very similar mechanism to that of the Z-type [104]. However, the ME effect in the U-type hexaferrite has only been observed as a small effect to date, suggesting that perhaps the Z- and M-type hexaferrites show the greatest promise in terms of practical multiferroic applications.

### 2.6.2.3. M-type Magnetoelectric Hexaferrites

Sc and Mg doped M-type hexaferrites were also shown to be magnetoelectric by Tokunaga *et al* [105]. They studied single crystal Sc doped M-type Barium Hexaferrites ( $\text{BaFe}_{12-x}\text{Sc}_x\text{O}_{19}$ ) and showed that by altering the Sc concentration a longitudinal conical state is stabilised up to above RT. In the longitudinal conical state, spins collinearly align within each block while the inter-block coupling is non-collinear, forming a “block-type” conical structure. As discussed in section 2.4.1, the

longitudinal conical state does not generate a spontaneous polarisation. However, ME measurements showed that with the application of a transverse magnetic field an electric polarization can be induced at low temperatures. They also demonstrated its electrically fixed and magnetically controllable spin helicity to be robust against varying magnetic-field and temperature up to RT. Suggesting that M-type hexaferrites with Fe-site substitutions inducing a conical spin structure are promising candidates for RT multiferroics. Although it was found that this particular M-type Hexaferrite exhibits low resistivity at around RT, which is a problem to be overcome [105]. None the less, this opened the door for M-type hexaferrites to be investigated, with regards to magnetoelectric coupling.

#### 2.6.2.4. M-type Magnetoelectric Hexaferrite $\text{SrCo}_2\text{Ti}_2\text{Fe}_8\text{O}_{19}$

A large converse magnetoelectric effect at room temperature was observed in Co-Ti doped strontium ferrite,  $\text{SrCo}_2\text{Ti}_2\text{Fe}_8\text{O}_{19}$  by Wang *et al* [10]. They reported a large magnetisation and electric polarisation were present simultaneously at RT and the control of magnetisation by the application of an electric field. They achieved this at room temperature and without the application of an external magnetic, which has not been the case for several other of the ME hexaferrites reported, that require the presence of an external magnetic field to induce the electrical polarisation. Again, they attributed the ME coupling mechanism present within this structure to the existence of a conical spin arrangement. The resistivity of the polycrystalline  $\text{SrCo}_2\text{Ti}_2\text{Fe}_8\text{O}_{19}$  sample was measured to be  $4.4 \times 10^{10} \Omega \cdot \text{cm}$ , high enough to support an electric field. Subsequently, measuring the magnetisation in a magnetic field of 460 Oe they observed a 6.3% reduction in M due to the application of a 22 kV/cm electric field perpendicular to H. Furthermore, a similar effect was also seen with no applied magnetic field and the time dependence of M under the influence of a square wave electric field demonstrates that M decreases with applying or removing E, respectively, indicating a stable response to the electric field. Although Wang *et al* [10] did not directly determine the presence of a non-collinear spin arrangement within the  $\text{SrCo}_2\text{Ti}_2\text{Fe}_8\text{O}_{19}$  sample, they observed an anomaly in the M(T) measurements at 420 K, which coincided with a sudden decrease in polarisation an effect that has been attributed to a transition from a conical magnetic structure to a collinear ferrimagnetic phase. The spontaneous room temperature polarisation at zero magnetic field may indicate that its spin structure has a cycloidal component [72]. This is unusual for M-type hexaferrites. As previously discussed, the M-types reported have been shown to have either a ferrimagnetic, screw or longitudinal conical spin structure, at  $H = 0$ . None of which result in an improper ferroelectricity under the inverse Dzyaloshinskii-Moriya mechanism [12]. As such, it may be possible that the spontaneous polarisation is induced via an alternative mechanism and not by the presence of a transverse conical spin structure. One possible mechanism is discussed in chapter 7 of this work, and was proposed by Shen *et al* [14] as a displacive electric polarisation induced by the magnetic ion at the trigonal bipyramidal site of the M-type hexaferrite structure.

Ebnabbasi *et al* [102] were also able to measure converse ME effects in bulk poly-crystalline M-type  $\text{SrCo}_2\text{Ti}_2\text{Fe}_8\text{O}_{19}$  at RT. For an electric field of 13 kV/cm they observed a 3% change in magnetic remanence. This same effect was seen for samples sintered in both air and oxygen. The ME coupling coefficient for the sample sintered in oxygen was found to be  $2.4 \times 10^{-10} \text{ s m}^{-1}$  while that for the sample sintered in air was reduced to  $1.7 \times 10^{-10} \text{ s m}^{-1}$ . Subsequently, it was concluded that the absence of oxygen in local oxygen sites lowers resistivity and modifies the magnetic structure. Therefore sintering in air reduces the ME effect as had been previously predicted [102].

Mohebbi *et al* [24] reported the first observation of the magnetoelectric effect in M-type hexaferrite thin films, prior to which it had only been observed in bulk polycrystalline hexaferrites. The  $\text{SrCo}_2\text{Ti}_2\text{Fe}_8\text{O}_{19}$  films had been grown on sapphire (0001) via PLD and exhibited an  $M_s$  of 100

emu/cc and  $H_c$  of 20 Oe. They observed a change in the magnetic remanence of 12.8% as a result of the application of 1 V (DC voltage) at RT, as shown in fig. 2.17, producing a magnetoelectric coupling of  $6.07 \times 10^{-9} \text{ s m}^{-1}$  [24]. The realisation of the converse ME effect within hexaferrite thin films is a significant step towards practical device applications. Naturally, the thinner the sample the lower the voltage required to apply a given electric field. Additionally, thin films are far more compatible with modern technologies due to the drive towards miniaturisation. The thin films measured by Mohebbi *et al* [24] were polycrystalline, meaning that there should be further scope for increasing the ME coupling with the growth of epitaxial thin films.

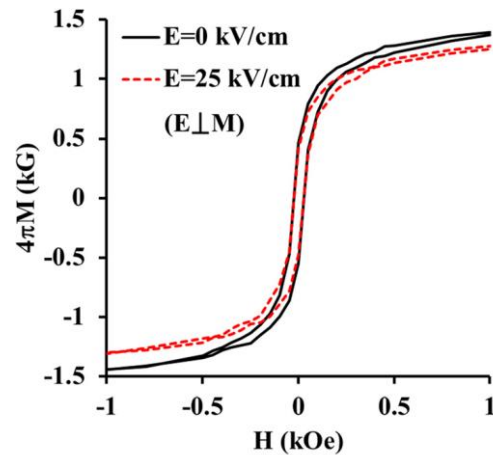


Figure 2.17. (a) Magnetisation as a function of magnetic field for  $\text{SrCo}_2\text{Ti}_2\text{Fe}_8\text{O}_{19}$  at RT for two different electric fields obtained by Mohebbi *et al* [24].

Both Mihalik *et al* [106] and Zentkova *et al* [23] investigated the physical and magnetic properties of single crystal  $\text{SrCo}_2\text{Ti}_2\text{Fe}_8\text{O}_{19}$  samples. They determined a Curie temperature of 768 K, which is higher than that reported for undoped SrM. In agreement with Wang *et al* [10] they observe a sharp increase in the magnetisation at around 400 K and again associate this behaviour to a transition between a collinear and a non-collinear magnetic structure [23]. For  $\text{SrCo}_2\text{Ti}_2\text{Fe}_8\text{O}_{19}$  a significant reduction in coercivity is observed compared to SrM at RT, with Mihalik *et al* [106] measuring values as low as 20 Oe and the  $M_s$  is also reduced compared to SrM, as a consequence of the Co-Ti substitutions, with Wang *et al* [10] measuring an  $M_s$  of 160 emu/cc for bulk polycrystalline samples [10]. Studies of  $\text{SrCo}_2\text{Ti}_2\text{Fe}_8\text{O}_{19}$  also only show small changes in the structures lattice constants with respect to SrM. Wang *et al* [10] determined values of  $a = 5.88 \text{ \AA}$  and  $c = 23.10 \text{ \AA}$  [10].

Izadkhah *et al* [107] experimentally investigated the correlation between the ME coupling and the amount of Co substitutions into Co-Ti doped strontium ferrite. They measured the ME coupling constant in polycrystalline  $\text{SrCo}_x\text{Ti}_{3-0.5x}\text{Fe}_8\text{O}_{19}$  thin films, grown on  $\text{Al}_2\text{O}_3$ , varying  $x$  between 1.2 and 3.5. The ME measurements were performed with  $M$  measured in the plane of the film whilst the electric field was applied perpendicular to the film plane, across both film and substrate. Their work showed a maximum value of  $\alpha = 1.0 \times 10^{-8} \text{ s m}^{-1}$ , measured for a Co substitution of  $x = 1.65$ . It is suggested that the optimal amount of Co may be related to the value of magnetostriction as a consequence of the cobalt site occupancies [107].

Recently, in an attempt to make  $\text{SrCo}_2\text{Ti}_2\text{Fe}_8\text{O}_{19}$  thin films compatible with device applications, Zare *et al* [108] [109] have investigated the ME properties of films grown on Si with an intermediate conductive oxide layer of indium-tin oxide (ITO). Compatibility with Si is a significant advantage in terms of technological applications and the ITO buffer layer was shown to make this possible by reducing the lattice mismatch between film and substrate. Additionally, the conductive ITO layer allows the electric field to be applied solely across the film, lowering the voltage required to observe the ME effect at RT. They measured a room temperature ME coupling of  $1.4 \times 10^{-9} \text{ s m}^{-1}$ , in

the absence of an applied magnetic field, with a voltage as low as 0.5 V. This voltage is over 1000 times smaller than that required to observe the effect without the ITO buffer layer [108].

As mentioned in section 2.6.1.3, the preferred substitution sites of the Co and Ti in the M-type hexaferrite structure are not well understood, with contradictions in the literature as to whether the  $\text{Co}^{2+}$  cations prefer to initially occupy the  $\text{O}_h$  [10] [87] or  $\text{T}_d$  [15] [88] [86] lattice sites. Due to the effects of superexchange, and how the Co occupation of the different sites affects the magnetostriction of the hexaferrite, it is expected that the co-ordination of the Co within the structure has a significant impact on the materials magnetoelectric properties.

To model the effect that the Co-Ti substitutions have on the magnetic interactions in  $\text{SrCo}_2\text{Ti}_2\text{Fe}_8\text{O}_{19}$ , with respect to SrM, Feng *et al* [87] performed a density functional study of the simulated structure. They calculated the exchange integrals of the structure based on the assumption that the  $\text{Ti}^{4+}$  ions occupy the 12k and the  $\text{Co}^{2+}$  ions occupy solely the  $4f_1$  tetrahedral sites. Their exchange energy calculations in this case indicated that the interaction between the R and S blocks is reduced significantly due to the occupation of the 12k sites [87].

### 2.6.2.5. Magnetoelectric coupling mechanisms in Hexaferrites

In hexaferrites anti-symmetric spin-coupling can be observed in sites of the lattice where the superexchange is greatly weakened due to competing interactions, or is absent due to substitutions for non-magnetic ions such as Ti. In certain M, Z, W, U and Y hexaferrite structures, this results in the formation of non-collinear magnetic structures. These spin states can take several different forms, depending on the specific hexaferrite structure being considered. The classification of the spiral type is critical for understanding the spiral-spin-driven ferroelectricity observed in such hexaferrites, as discussed in section 2.4.1. In hexaferrites with non-collinear magnetic structures, exhibiting a cycloidal component, the application of a magnetic field alters the magnetic arrangement, thus inducing a change in the electric polarisation, resulting in the direct ME effect.

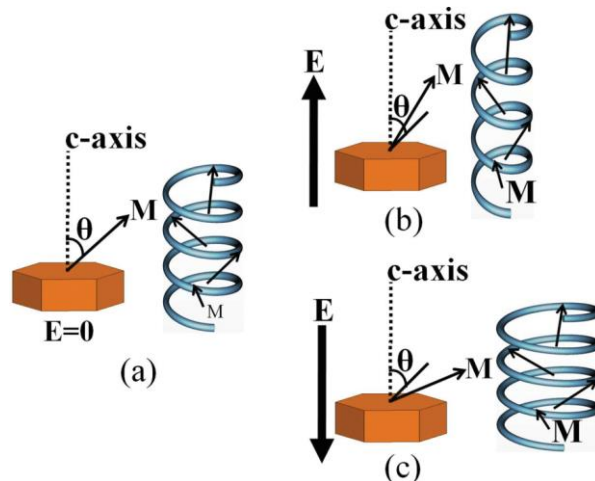


Figure 2.18. The spiral spin configuration for different directions of  $E$  under the 'slinky helix' model [13].

Vittoria and Ebnabbasi, in 2012, developed a complementary model for the converse magnetoelectric effect observed in certain hexaferrites due to the spin spiral configuration [13]. They refer to the model as the 'slinky helix model'. Their work has revealed that such hexaferrites are electrostrictive. Hence, the application of an electric field strains the material altering the spiral spin configuration. This physical motion alters the Fe-O-Fe bond angles, inducing changes in the magnetisation via superexchange. Fig. 2.18 gives a physical representation of the 'slinky helix model'. It demonstrates that with the application of  $E$  the angle of the magnetic moment within the cone is affected by the direction of  $E$ . The angle varies with  $E$ , thus the spin 'slinky' is either stretched or compressed depending on the electric field direction. Changes in the spin helix result

in a net change in internal magnetisation [13]. This model of magnetoelectric coupling then is not a conventional intrinsic magnetoelectric effect and must be attributed as contributing to the  $\Delta\alpha_{ij}$  term discussed in section 2.5.1.

A further possible mechanism for ME coupling in hexaferrites may have been uncovered by Shen *et al* [14]. They have discovered an unusual mechanism for electrical polarisation based on the displacement of the magnetic ion at the trigonal bipyramidal sites within the M-type structure. In conventional ferroelectric oxides, such as BaTiO<sub>3</sub>, the local electric dipole usually requires the off-centre displacement of transition metal ions with an empty d-shell due to the hybridisation between the empty d orbital and the filled oxygen 2p orbital. Hence, the simultaneous presence of ferroelectricity and magnetism has typically required an improper mechanism of ferroelectricity. However, simulations performed by Shen *et al* [14] suggest that the competition between the long-range Coulomb interaction and short-range Pauli repulsion in the FeO<sub>5</sub> bipyramidal unit of (Ba,Sr)Fe<sub>12</sub>O<sub>19</sub> favours an off-centre displacement of the Fe<sup>3+</sup> ion.

It was found experimentally that the temperature dependence of the dielectric constant  $\epsilon(T)$ , for both BaFe<sub>12</sub>O<sub>19</sub> and SrFe<sub>12</sub>O<sub>19</sub> strongly resembles quantum paraelectric behaviour [14]. Quantum paraelectricity being a form of ferroelectricity in which the ferroelectric order is suppressed by quantum fluctuations. This behaviour can only be explained by the existence of local electric dipoles whose origin must be related to the magnetic Fe<sup>3+</sup> ions. Investigating this Shen *et al* [10] suggested an explanation in the existence of off-equatorial displacements of Fe<sup>3+</sup> ions at the 2b trigonal bipyramidal sites, resulting in two adjacent 4e sites. They show that the off-equatorial displaced Fe<sup>3+</sup> has a lower energy than the symmetric 2b sites, suggesting that a local dipole along the c-axis would be favoured, as illustrated in fig. 2.19.

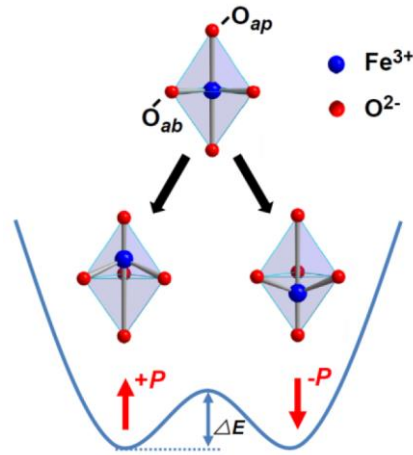


Figure 2.19. Illustration of Fe<sup>3+</sup> off-equatorial displacements in the trigonal bipyramid. The up and down displacements correspond to opposite dipoles and local minima in the energy potential [14].

They calculated the local potential energy profile along the c-axis,  $U_{total}(z)$ , for the trigonal bipyramidal site, using the phenomenological local potential energy, defined by eqn. 2.25.

$$\begin{aligned}
 U_{total}(z) &= U_{Coulomb}(z) + U_{repulsion}(z) \\
 &= \left[ -\frac{18e^2}{4\pi\epsilon\sqrt{r_0^2+z^2}} - \frac{6e^2}{4\pi\epsilon(r_1+z)} - \frac{6e^2}{4\pi\epsilon(r_1-z)} \right] \\
 &+ \left[ 3\beta c_{\pm} \exp\left[\frac{(r_+ + r_- - \sqrt{r_0^2+z^2})}{\rho_f}\right] + \beta c_{\pm} \exp\left[\frac{r_+ + r_- - (r_1+z)}{\rho_f}\right] + \beta c_{+-} \exp\left[\frac{r_+ + r_- - (r_1-z)}{\rho_f}\right] \right] \quad \text{eqn. 2.25.}
 \end{aligned}$$

where  $r_0$  and  $r_1$  are the in-plane and out-of-plane TM-O distances in the bi-pyramid for 2b sites,  $\beta$  is a constant (taken to be  $1.35 \times 10^{-19}$  J),  $c_{+} = 1$  is Pauling's valence factor,  $\epsilon$  is the hexaferrites permittivity and  $\rho_f = 0.314 \text{ \AA}$  [26].  $r_{+} = 0.58 \text{ \AA}$  is the ionic radius of  $\text{Fe}^{3+}$  with a co-ordination number of 5 and  $r_{-} = 1.4 \text{ \AA}$  is the ionic radius of  $\text{O}^{2-}$  [110]. The total potential energy is the sum of the Coulomb potential,  $U_{Coulomb}(z)$ , between the  $\text{Fe}^{3+}$  and  $\text{O}^{2-}$  and the short-range Pauli repulsion potential,  $U_{repulsion}(z)$ . The calculated potential shows a double well feature, as seen in fig. 2.19, due to the repulsion term. For SrM at RT, however, such a local electric dipole may average to an equatorial position, due to effects such as thermal excitation, providing no net polarisation. In principle if the amplitude of the electric dipoles and the energy barrier could be increased, either through strain or the substitution of cations into the structure for example, this mechanism may result in a stabilisation of polarisation, hence, providing an alternative mechanism for ferroelectricity and magnetoelectric coupling.

## 2.7 Hexaferrite thin film growth

Bulk M-type hexaferrite samples have been grown by several techniques, such as co-precipitation, solid-state, ceramic and sol-gel methods. Each of these growth methods have proved effective at producing high quality single-phase bulk M-type hexaferrite samples [111] [112] [113] [88]. However, as has been previously discussed, for many technological applications it is desirable to miniaturise the hexaferrite material into thin film form. This would be essential for the integration into electronic and semiconductor devices. Additionally, for magnetoelectric hexaferrites, it would allow for the control of magnetism under the application of a lower voltage. The challenge presented for such minimisation is often to maintain the materials bulk properties. Typically, interface effects can inhibit a film's magnetic properties, for example. Numerous techniques have been pursued for the growth of hexaferrite thin films including sputtering, plasma assisted Molecular Beam Epitaxy (MBE), liquid phase epitaxy and PLD [114] [115] [82] [24].

Liu *et al* [115] demonstrated the growth of epitaxial BaM thin films on sapphire (0001) substrates by a plasma-assisted MBE technique. They observed the natural formation of a  $\text{Fe}_2\text{O}_3$  buffer layer that acts to assist in accommodating the lattice mismatch between film and substrate. The films were grown at  $750^\circ\text{C}$  in an oxygen partial pressure of  $5 \times 10^{-6}$  mbar, using Ba, Fe and oxygen-plasma sources. Difficulties remain however, with the growth of oxides by MBE with achieving the desired stoichiometry due to the multiple sources having different oxygen affinities [116]. Alternatively, liquid phase epitaxy has been used to grow high quality M-type hexaferrite films, however, BaM seed layers are typically required, which need to be grown by another method, usually PLD [94].

Sui *et al* [114] grew BaM thin films, via RF magnetron sputtering, exhibiting saturation magnetisation 90% of that of bulk single crystals and perpendicular uniaxial anisotropy 60% of the bulk value. Additionally, they observed good c-axis orientation perpendicular to the film plane. Growing M-type Ba hexaferrite thin films on  $\text{Al}_2\text{O}_3$  (0001) substrates Zhiyong Xu *et al* [117] have shown that the crystallographic and magnetic properties of such films are strongly dependent on film thickness. Between 150 and 550 nm, they show that  $M_s$  decreases gradually with thickness, as does the perpendicular magnetocrystalline anisotropy. They postulate that these changes are due to an increase in random nucleation sites and strain relaxation in the films with increased thickness, as the  $M_s$  of BaM films is greatly influenced by the c axis alignment of the grains [117]. Additionally, other studies have reported that the orientation of substrate [118] and the process parameters such as atmosphere of growth [119], substrate temperature [120] and annealing process [121] directly govern the structure and magnetic properties of the M-type Hexaferrite thin films.

The method used for the growth of hexaferrite thin films in this work has been PLD. This growth method, and variations of it, have been shown to be effective at growing high quality hexaferrite thin films with stoichiometric transfer of material between target and film [24] [21]. Most

importantly for this work, it allows for atomic cation substitutions into specific blocks of the hexaferrite structure [122].

### 2.7.1 Hexaferrites grown by PLD

PLD as a method for thin film growth is a well-studied process. The basic set up of a typical PLD system can be seen in fig. 2.20. Inside a chamber, where the pressure and gas composition is controlled, a high energy pulsed laser is focussed onto a target causing the target material directly under the focus of the laser to evaporate. This results in a plume of material being ejected from the target surface after every laser pulse. The vaporized material, containing neutrals, ions and electrons, expands rapidly away from the target surface. If a substrate is placed in its path, the plume material will re-condense on the substrate surface, eventually forming a thin film [22]. However, the situation is not this simple, as there are a large number of variables affecting a films properties; such as laser fluence, background gas pressure and substrate temperature [22].

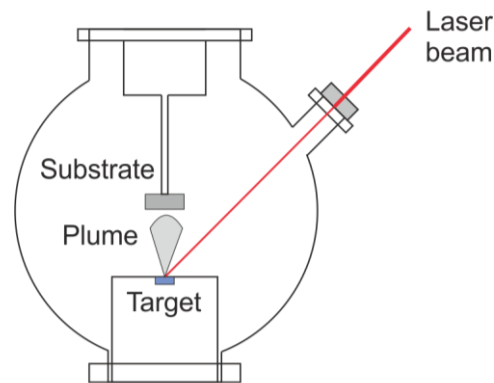


Figure 2.20. Schematic representation of a typical PLD setup.

PLD allows for the manipulation of such variables to control the film properties to suit individual applications. Optimization of the growth conditions can require a considerable amount of time and effort [22]. The physical concepts governing PLD are now outlined.

#### 2.7.1.1. Laser-Target Interaction

The interactions between the pulsed laser beam and the target material are of a complex nature. Firstly, the laser pulses must have high enough energy to trigger dielectric breakdown on the target surface. The electric field amplitude ( $E$ ) of an electromagnetic wave can be expressed as [19];

$$E = \left( \frac{2\Phi_P}{cn\epsilon_0} \right)^{\frac{1}{2}} \quad \text{eqn. 2.26.}$$

where  $\Phi_P$  is the power density of the wave,  $c$  is the speed of light,  $n_r$  is the refractive index and  $\epsilon_0$  is the permittivity of free space. Dielectric breakdown in the target occurs when the electric field exceeds the dielectric field strength of the material,  $E_{crit}$ ;

$$E > E_{crit} \quad \text{eqn. 2.27.}$$

The power density of the laser is directly related to the laser fluence ( $\mathcal{F}$ ) by the inverse of the pulse duration ( $t$ ) [19];

$$\Phi_P = \frac{\mathcal{F}}{t} \quad \text{eqn. 2.28.}$$

Therefore, the laser fluence is directly related to the amplitude of its electric field. Thus, dielectric breakdown occurs when the laser fluence exceeds a threshold value [19].

Opel [2] concluded that a  $45^\circ$  angle of incidence on target appears to be optimal as this minimises the number of macroscopic particles reaching the film. He also emphasises the importance of a

uniform beam shape for encouraging uniform ablation, which is important for maintaining stoichiometric transfer of target material. This is a key advantage of PLD. In other deposition techniques, such as MBE, the lightest elements in the source are evaporated first; hence, the chemical composition of the film is different to that of the source material [18].

#### **2.7.1.2. Target Ablation and Plasma Formation**

Regarding target ablation and plume formation, while some secondary mechanisms involved with PLD remain unclear, there are four primary mechanisms of ablation. These are stated to be collisional (momentum transfer from the beam), thermal (heating from the nascent plasma), electronic (processes involving electronic excitation of the target atoms) and hydrodynamic (splashing or exfoliation) [123].

A 'nascent plasma' forms close to the surface of the target, immediately after evaporation by the laser pulse [19]. Due to its proximity to the target, it is coupled, both mechanically and thermally, to its surface. It has also been observed that the plasma can act to shield the target surface from further laser ablation and as a result of the thermal coupling it can also cause re-sputtering of the target surface. Christen *et al* [124] established that the dense plasma near the surface of the target acts to generate collisions and keep different elemental components expanding on similar trajectories; thus, helps to maintain stoichiometry.

Macroscopic particulates, which are unwanted for high quality film growth, can be ejected from the target by three mechanisms [19]. The first is subsurface boiling which is a consequence the explosive pressure of the laser beam causing 'splashing' in the target below the focus of the laser beam. The second mechanism 'recoil ejection' is similar to subsurface boiling in that it is also 'splashing' as a result of a pressure on the transient melt under the surface at the laser focus. However, in this case the pressure is caused by the plasma plume expanding away from the target surface. The third is exfoliation, exfoliation is caused by repeated freeze melt cycles on the target surface, causing surface roughening leading to macroscopic outgrowths. These outgrowths eventually detach and can be sent towards the substrate in the plume. Methods to reduce particulates tend to be material dependent [123].

#### **2.7.1.3. Plasma Expansion and Chamber Atmosphere**

The dense plasma after ablation of the target surface is forced to expand, converting the thermal energy of the plume into kinetic energy. Due to its high density, the plasma is not a collision-less environment so collisions lower the energy of the high energy particles [19]. The vacuum chamber is often backfilled either with an inert gas or, in the case of reactive PLD, a reactive gas such as O<sub>2</sub>. This atmosphere acts to thermalize the plume species, as, during collisions, the kinetic energy of the plume particles becomes equalised with that of the background gas particles. Thus the particles reaching the substrate surface will have a much reduced energy, typically in the range 5-50 eV [19], which, if the substrate is placed a sufficient distance from the target, prevents re-sputtering from the substrate surface [18].

#### **2.7.1.4. Film Growth Models**

Upon reaching the substrate, the plume of material begins to form a thin film on the substrate surface. Layer-by-layer growth; where a new monolayer will not nucleate until the previous monolayer is complete, is the ideal way in which to grow a thin film. The simplest growth model is one in which adatoms deposited onto a surface become immobile on the site on which they fall [18]. However, in reality, the adatoms remain mobile until they occupy an energetically favourable

site. For general deposition, three established thin film growth models exist [18] [123] [2]; these are the Frank-van der Merwe, Volmer-Weber and Stranski-Krasnov models.

The Frank-van der Merwe growth model is a step flow model, where the energetically favourable site is adjacent to a step edge. As demonstrated in fig. 2.21, the adatom diffuses across a terrace until it reaches the end of the terrace where it settles. With the deposition of further adatoms, the edge of the terrace ‘flows’ across the terrace below [18]. Assuming the adatoms are equally likely to land on any site, the growth rate of each terrace will depend on the size of the terrace. Thus, larger terraces will grow faster, creating step bunching. Ehrlich and Hudda [125] showed that at low temperatures adatoms could be reflected away from the edge of a terrace. This effect became known to result from an ‘Ehrlich-Schwoebel Barrier’. It has been shown that the presence of this Ehrlich-Schwoebel barrier acts to prevent step bunching [18].

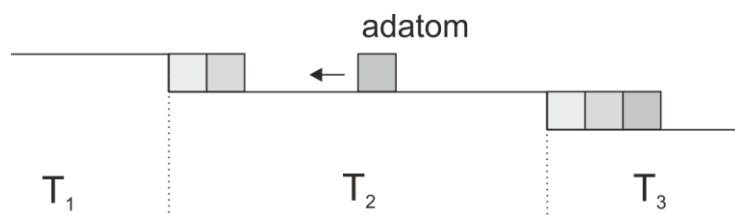


Figure 2.21. The step flow of adatoms across a terrace, with terraces labelled  $T_1$ ,  $T_2$  and  $T_3$ .

The Volmer-Weber growth model instead of the previous model of step growth introduces island growth. It is possible for two adatoms to meet on a terrace. Upon meeting, the adatoms stop diffusing as these sites become energetically favourable. These sites are known as ‘nucleation sites’ and are the starting point for island growth [18]. The model states that step flow is prevented when the nucleation site separation is smaller than the step terrace length. In this case, growth is completely by island formation. With increased size, islands coalesce to form a layer and new islands grow on the next layer. However, islands do not grow uniformly and can form fractals [126]. Finally, Stranski-Krasnov growth is a combination of step flow and island growth. Whereby adatoms form islands but only after 1 – 5 monolayers have been deposited by a step growth process. After the initial deposition, island growth is enabled due to a change in the lattice parameters as a result of deposition [123]. The dominant growth mode for any thin film depends on the thermodynamics at the growth surface, as such is dependent on many parameters including laser fluence, growth temperature, growth pressure, the condensing material and substrate properties.

#### 2.7.1.5. Advantages and Disadvantages of PLD

The Primary advantage of PLD for the growth of Hexaferrite thin films is the stoichiometric transfer of complex unit cells that it is able to achieve [18] [2] [19]. No other techniques offer the same quality of reconstruction of complex unit cells as PLD. PLD operates in a non-thermal equilibrium regime. This is unlike MBE, Sputtering and Chemical Vapour Deposition, which tend to evaporate the lightest elements from the surface first. However, for certain materials ‘incongruent ablation’ may occur. This can often be resolved by replacing the elemental component of the target (such as oxygen) lost during ablation with a background gas [19]. As well as this, the background gas acts to thermalise the ablated species, which reduces surface damage and surface-to-bulk diffusion [19] thus creating high quality thin films. PLD is a versatile technique and can be operated over a wide range of pressures between UHV and 1 mbar [123]. The simplicity of the experimental setup of a PLD system gives the technique flexibility; as long as the laser fluence exceeds the dielectric constant of the target, almost any material can be evaporated stoichiometrically.

The primary issue observed with PLD is the growth of macroscopic particulates. As discussed previously there is no simple solution that can be implemented, several things can be done

however to reduce the number of particulates present in a PLD grown thin film. One such way is to place the substrate at an optimal distance from the target and displaced from the centre of the plume. Likewise, the heating of the substrate will encourage crystalline growth and any particulates may be encouraged to dissolve into the bulk. R. Eason's group in Southampton have discovered that pulsing a gas jet, at a delay from the laser pulses, across the path of the plume also greatly reduces the number of particulates [127].

#### 2.7.1.6. M-type films grown by PLD

PLD is already a well-established technique for growing ferrite films and was first proposed as a suitable technique for the growth of hexaferrites by Vittoria in 1991 [128]. The first M-type hexaferrite film successfully grown by PLD was then reported by Carosella *et al* [129], who demonstrated the growth of BaM films on Al<sub>2</sub>O<sub>3</sub> (0001) substrates. These films were grown from a target of BaFe<sub>12</sub>O<sub>19</sub> incident by a wavelength of 246 nm pulsed at 10 Hz, with a substrate temperature of 900°C and an oxygen partial pressure of 1x10<sup>-2</sup> mbar. The films grown were determined to be single phase and epitaxial in nature with magnetic properties close to bulk values observed by VSM and FMR spectroscopy [129]. Dorsey *et al* [20] then also demonstrated the growth of BaM on Al<sub>2</sub>O<sub>3</sub> (1100), however could not achieve epitaxial growth. They discovered that even on a sapphire substrate with (0001) orientation that above a critical film thickness only polycrystalline growth could be achieved.

In the years following this initial work, the PLD growth parameters were developed and optimised for the growth of hexaferrite films, again many of these conditions are specific to the individual growth systems used. Among the highest quality BaM films grown are those by Song *et al* [130], who achieved epitaxial films with a perpendicular magnetic anisotropy and a narrow FMR linewidth of 16 Oe. The growth temperature of these films were again optimised at 900°C and an oxygen partial pressure of 5x10<sup>-1</sup> mbar was found to produce the narrowest FMR linewidth.

A long-term goal of the hexaferrite community has been to integrate hexaferrite devices with semiconductor electronics. This has been complicated by the poor lattice matches, high temperatures required for growth and the formation of other oxides at the substrate surface obstructing epitaxial growth. However, Liu *et al* [131] reported the growth of BaM on Si through the use of an MgO buffer layer and Chen *et al* [132] reported the oriented growth of BaM films directly on to 6H-SiC substrates but with magnetisation compared to bulk.

Besides BaM many other M-type hexaferrite films have been grown by PLD including PbM and SrM [133] as well as numerous doped variations of BaM and SrM. For example, Sc doped BaM films were deposited to control magnetic anisotropy [134] and Co-Ti doped BaM films have been grown to optimise the magneto-optical properties [135]. Mohebbi *et al* [24] demonstrated the growth of SrCo<sub>2</sub>Ti<sub>2</sub>Fe<sub>8</sub>O<sub>19</sub> by PLD on a sapphire (0001) substrate at a temperature of 600°C and in an oxygen partial pressure of 2x10<sup>-1</sup> mbar. After deposition, it was also found that the films magnetic properties were improved through post-annealing at 1050°C in an oxygen atmosphere for 40 minutes. Due to the thickness of the film however, its structure remained polycrystalline, with a (00n) preference, which is consistent with the work of Dorsey *et al* [20] demonstrating a relaxation to polycrystalline ordering for thicker films.

#### 2.7.1.7. ATLAD Growth of Hexaferrites

As a way to further control the substitution sites of the dopants within the hexaferrite structure, Geiler *et al* [136] have developed an Alternating Target Laser Ablation Deposition (ATLAD) technique. This is essentially PLD but makes use of multiple targets that are interchanged rapidly to grow layer by layer, each from a different target.

This technique for the growth of hexaferrites was first demonstrated by Geiler *et al* [136] in which a combination of two targets, with compositions  $\text{Fe}_2\text{O}_3$  and  $\text{PbO}$  were used to deposit  $\text{PbFe}_{12}\text{O}_{19}$  thin films. Using an Excimer laser pulsed at 10 Hz, they obtained the best results by depositing 3 shots from the  $\text{PbO}$  target before rapidly indexing to the  $\text{Fe}_2\text{O}_3$  target to deposit 33 shots, then repeating this process 500 times, resulting in a thickness of 0.6  $\mu\text{m}$ . The atomic ratio of  $\text{Pb}^{2+}$  and  $\text{Fe}^{3+}$  ions deposited approximately follows that of the M-type unit cell. The films were deposited on  $\text{MgO}$  (111) substrates in an oxygen partial pressure of  $3 \times 10^{-1}$  mbar at  $700^\circ\text{C}$ . X-ray diffraction and VSM showed epitaxial growth with the presence of a cubic secondary phase and magnetic properties comparable to films grown from single target PLD [136].

Geiler *et al* [21] [137] also demonstrated that high quality BaM thin films could be grown using an ATLAD technique, with magnetic properties comparable with single crystal Bulk Hexaferrites. In this work, targets of  $\text{BaFe}_2\text{O}_4$  and  $\text{Fe}_2\text{O}_3$  were used to grow the R and S blocks, respectively. The films were grown on  $\text{Al}_2\text{O}_3$  substrates at  $925^\circ\text{C}$ , with a target substrate distance of 5 cm. The rotation of the target carousel was also synchronised with the laser trigger signal to allow the targets to be alternated during film growth. Finally, the films were post-annealed in oxygen at  $1050^\circ\text{C}$  for 20 minutes, it was noted that further annealing drastically reduced the magnetic properties of the films, an effect that was attributed to diffusion between the film and substrate [137].

Further studies by Geiler *et al* [122] built on their pioneering ATLAD technique by tailoring the positions of the Mn substitutions in Mn-doped BaM films. The films were grown with the aim of directing the Mn substitutions solely into the S-block of the M-type structure. This was achieved through the combined use of 3 targets, with the deposition routine consisting of 3 laser pulses on a  $\text{BaFe}_2\text{O}_4$  target, 11 pulses on the  $\text{Fe}_2\text{O}_3$  target and then 11 pulses on the  $\text{MnFe}_2\text{O}_4$  target followed by another 11 pulses on the  $\text{Fe}_2\text{O}_3$  target. Thus, the sequence in which the targets were deposited was intended to force the Mn ions into the S-block. EXAFS measurements performed on the films then supported this, with fitting showing that 75% of the Mn ions occupy the 12k sites and the remaining 25% in the tetrahedral  $4f_1$  sites, both of which are located within or on the boundary of the S-block. The films were found to be epitaxial in nature and characterisation showed also that placing Mn cations at these interstitial sites in  $\text{BaFe}_{12}\text{O}_{19}$  thin films  $M_s$  was increased by 12-22%, depending on the site selection with respect to uncontrolled Mn substitution in bulk BaM. An increase in the Néel temperature by 40-60 K, compared to bulk was also observed. This work by Geiler *et al* [122] has demonstrated that the growth of thin films via a variation of PLD can achieve selective cation substitution at the atomic scale.

By allowing the control over the cation distribution within the structure, the ATLAD growth technique enables the processing of a new class of hexaferrite materials in which the magnetic, microwave and possibly magnetoelectric properties can be engineered towards specific applications beyond what is attainable by conventional deposition methods.

## 2.8 Conclusions

The mechanisms governing the magnetoelectric effects observed in ME materials have been discussed and the current state in the development of magnetoelectrics has been outlined. Hexaferrites have been identified in recent work as a prominent candidate for the realisation of room temperature magnetoelectric devices. The properties of these materials and their device applications have then been discussed, as have the growth procedures for the production of hexaferrite thin films. The particular growth method of pulsed laser deposition has been demonstrated to be the most significant method for the growth of high quality hexaferrite films. Additionally, the use of the ATLAD variation of PLD growth has been shown in the literature to be capable of tailoring the substitutions of dopants to specific sites within the hexaferrite structure, allowing for the tailoring of their magnetic and therefore their magnetoelectric properties.

## Chapter 3: Thin Film Characterisation and Analytical Techniques

### 3.1 Introduction

This chapter will aim to explain and outline the techniques used to analyse the samples studied in this work. As well as detailing, the experimental set up used for the different methods of characterisation the processes used to analyse the data obtained is explained and justified.

### 3.2 Structural Characterisation techniques

#### 3.2.1 Energy-Dispersive X-ray Spectroscopy Analysis

A powerful tool incorporated into a Scanning Electron Microscope (SEM) is the ability to perform Energy-Dispersive X-ray spectroscopy (EDX) measurements. EDX enables the chemical analysis of a sample, thus was used to determine the composition of the hexaferrite films grown. Critically, this technique enabled the verification of doping levels within the hexaferrite films by giving the ratio of elements within a film.

Essentially an SEM works by scanning a focussed electron beam over a surface to create an image. The electrons in the beam interact with the sample via several different mechanisms and the products of which are detected to obtain information about the sample surface and composition. As represented in fig. 3.1, within the SEM, x-rays are produced by inelastic collisions of the incident electrons from the beam with electrons in discrete atomic orbitals of the atoms in the sample [138]. Electrons from higher orbitals fill the hole left, emitting x-rays of fixed wavelengths related to the electronic transition in filling the core hole [138]. Thus, characteristic x-rays are produced for each element and the spectrum of these x-rays is detected and used to determine the ratio of elements present within the sample [138].

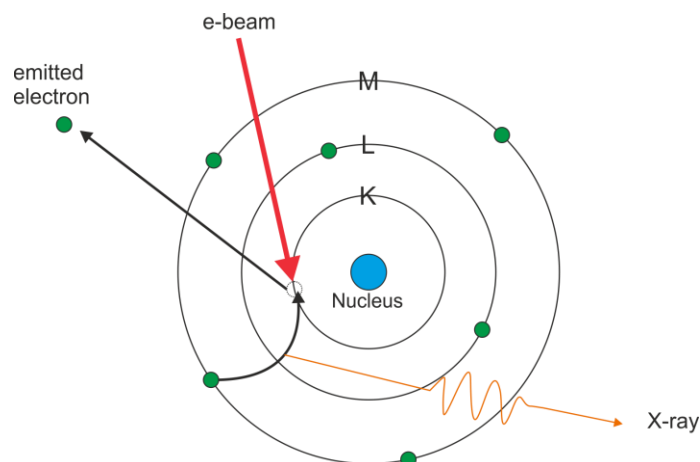


Figure. 3.1. Schematic representation of the emission of x-rays as measured by EDX.

The SEM used in this work was fitted with an Oxford Instruments, Model 7274, EDS x-ray detector and the EDX spectra obtained were processed and analysed using the INCA software package. The samples were mounted on aluminium stubs through the use of carbon tabs and the film surface was contacted to the stub by silver conducting paint. All EDX measurements were taken at a magnification of 1000x in order to cover a relatively broad area of the sample and for all samples observed, measurements were taken at three different sites across each sample to ensure the chemical composition of the films were consistent and not just a localised representation. All the EDX measurements were performed with an acceleration voltage of 15 kV.

The EDX analysis software outputs the atomic weight ( $Wt_i(\%)$ ) of a given element,  $i$ . This is the percentage of the total mass measured to be of that element. Equation 3.1 is used to convert the atomic weight to atomic percentage ( $At_i(\%)$ ).

$$At_i(\%) = \frac{\frac{Wt_i(\%)}{Z_i}}{\left(\frac{Wt_a(\%)}{Z_a} + \frac{Wt_b(\%)}{Z_b} + \frac{Wt_c(\%)}{Z_c} + \dots\right)} \quad \text{Eqn. 3.1.}$$

where  $Z_i$  is the atomic number of the element,  $i$ . Having now used this equation to calculate the atomic percentage for each element present equation 3.2 was then used to calculate the number of  $i$  atoms ( $N_i$ ), knowing the total number of atoms present ( $N_{total}$ ). For example for  $SrCo_2Ti_2Fe_8O_{19}$ ,  $N_{total} = 32$ .

$$N_i = \frac{At_i(\%) \times N_{total}}{100} \quad \text{Eqn. 3.2.}$$

It is noted that for the  $SrCo_2Ti_2Fe_8O_{19}$  films grown on  $Al_2O_3$ , oxygen is present in both film and substrate; as such, the ratio of the other film elements was calculated excluding oxygen.

### 3.2.2 X-ray Diffraction techniques

X-ray diffraction (XRD) has been used to determine the crystal structure of the thin film samples studied throughout this work and has been used to identify the presence of any secondary faces as well as to determine whether the samples have polycrystalline or epitaxial ordering. Different x-ray crystallography measurements have been performed, such as x-ray reflectivity and rocking curve measurements, to determine film thickness, roughness and to gain information on the film quality.

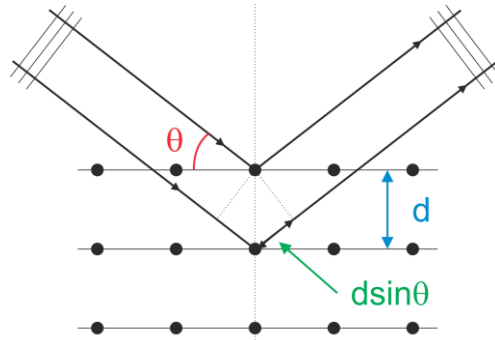


Figure. 3.2. Schematic representation of the diffraction of incident x-rays by crystal planes.

Crystals are formed from regular repeating arrays of atoms. These periodic structures of atoms act to scatter incident x-rays [139]. As is shown in fig. 3.2, the incident x-rays cause each scatterer to re-radiate some of its intensity as a spherical wave. If the scattering points are arranged with a separation ( $d_{hkl}$ ) these waves will be in phase and add constructively only in directions where their path-length difference ( $2d_{hkl} \sin \theta$ ) equals an integer multiple of the wavelength ( $\lambda$ ). In that case, part of the incoming beam is deflected by an angle  $2\theta$ , producing a peak in the diffraction pattern. This relationship is known as Bragg's law [139].

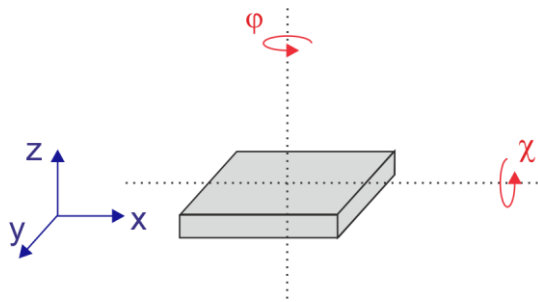


Figure. 3.3. Diagram showing the principle axis associated with the XRD goniometer stage.

The x-ray diffractometer used for all XRD measurements presented in this work was a Rigaku SmartLab diffractometer. This consists of a  $Cu \text{ K}\alpha_1$  x-ray source that produces x-rays with a wavelength of  $1.54059 \text{ \AA}$ . The x-ray beam produced is parallelised through the use of a multilayer mirror and the incident beam width is limited by the insertion of slits, that for the thin film sample

studied in this work were set to 2mm. For many of the measurements the incoming beam was monochromated by a 2-bounce Ge(220)x2 monochromator to improve the diffractometers resolution and remove the presence of any  $L_{\alpha}$  and  $K_{\beta}$  reflections. The x-ray beam is then incident on the sample that is placed on a goniometric stage that can be adjusted in  $x$ ,  $y$ ,  $z$ ,  $\varphi$  and  $\chi$ . Where  $\varphi$  is the in-plane rotation axis and  $\chi$  is the tilting axis. The axis of sample movement by the goniometer stage are shown in fig. 3.3.

The intensities of the x-rays, at a given  $2\theta$  angle, diffracted by the sample are measured by a detector after passing through several receiving optics. This includes a mechanical receiving slit, known as a Parallel Slit Analyser (PSA), to maintain a constant resolution even for x-rays spreading over a wider area [140]. The detector used is a scintillation counter that can measure x-ray intensities varying over a wide range, from 0.1cps to greater than  $10^7$  cps. An attenuator is also used in front of the detector to prevent detector damage. A schematic representation of the diffractometer set up is shown in fig. 3.4.

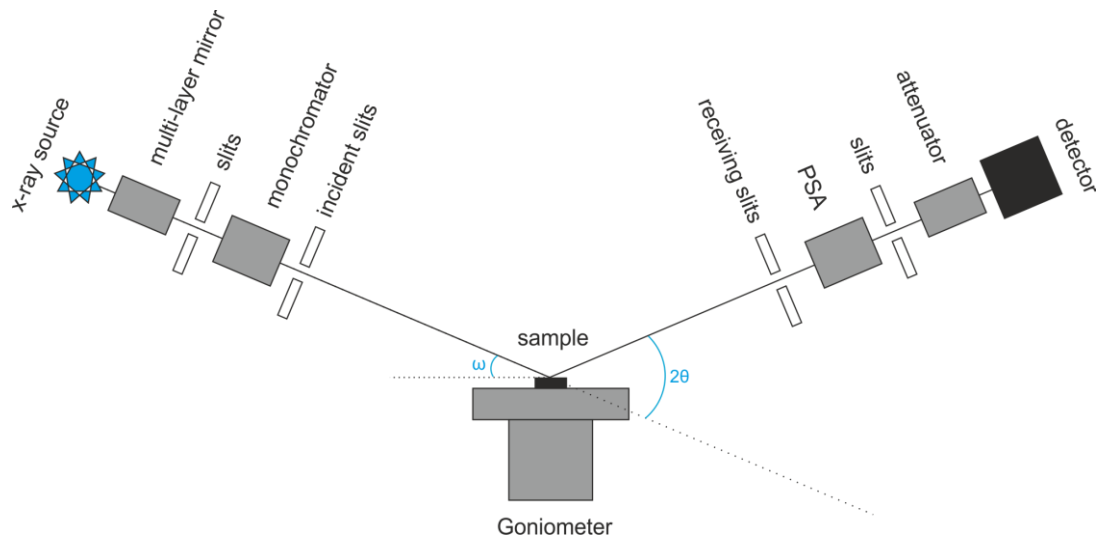


Figure. 3.4. Schematic representation of the diffractometer set up.

The diffractometer control programme has an automated optics alignment procedure that was run each time the diffractometer was used or the optics changed. The procedure for the optics alignment consists of a height reference plate being placed on the sample stage. Following this, both the stage height and incident x-ray angle ( $\omega$ ) are adjusted so that the height reference plate is aligned at zero degrees and at the centre of rotation. Additionally, the heights of both the incident and receiving slits are optimised. The diffractometer also has an automated sample alignment procedure, which was used each time a sample was placed on the stage. This procedure optimises the sample height ( $z$ ) and zeros the incident x-ray angle. The alignment was checked manually by running a rocking curve on a substrate peak with a known peak position. If the  $\omega$  peak position corresponds to half that of the  $2\theta$  angle then the sample is well aligned. If however there was an offset between the substrate and film planes running rocking curves on the most prominent film peak and adjusting the offset ensured alignment to the film planes.

### 3.2.2.1. $2\theta/\omega$ measurements

The most widely used x-ray diffraction measurement is a  $2\theta/\omega$  scan. This scan is a direct measurement of both crystal structure and phase. Determination of the crystallinity of the film and extraction of lattice constants was essential in this work. For the  $2\theta/\omega$  measurement the angles of both the incident and diffracted x-rays are kept equal, i.e.  $\omega = \theta$ , and this angle is scanned relative to the sample surface plane. The resulting plot of intensity against  $2\theta$  displays peaks corresponding to reflections from specific crystal planes with indices  $h$ ,  $k$  and  $l$ . Hence, by observing the peaks

present in the  $2\theta/\omega$  data and indexing to the crystal planes of the appropriate structure and as the peak positions only depend on the dimensions of the crystal lattice, the films lattice parameters can be determined.

The  $2\theta/\omega$  measurements in this work were performed with a step size of  $0.01^\circ$  and over a range that was determined by the positions of the peaks of interest determined from theoretically predicted reflections. Initially all peaks, from both film and substrate, were indexed to their (hkl) plane using the INDX software [141]. For this, the materials space group and lattice constants were taken from accepted values in the literature. However, when a peak had more than one possible assignment a more thorough analytical procedure was required that would also allow for the determination of the samples lattice constants by their peak separations. Starting from the Bragg equation [139];

$$\lambda = 2d_{hkl} \sin \theta \quad \text{Eqn. 3.3.}$$

where  $\lambda$  is the x-ray wavelength, which for the Cu  $K\alpha_1$  x-ray source used is  $1.54056 \text{ \AA}$  and the inter-planar spacing is given by  $d_{hkl}$  for each peak. Using the hkl values as assigned by INDX, the standard formula for the specific crystal system can be applied to determine the lattice constants. For a hexagonal crystal system, such as a hexaferrite, eqn. 3.4 is used [142].

$$\frac{1}{d_{hkl}^2} = \left( \frac{4(h^2+hk+k^2)}{3a^2} \right) + \left( \frac{l^2}{c^2} \right) \quad \text{Eqn. 3.4.}$$

Here  $a$  and  $c$  are the lattice constants of the hexagonal structure. To determine these lattice constants equations 3.3 and 3.4 are equated. For the peaks assigned to the (00l) reflections this then becomes;

$$\sin^2 \theta = \left( \frac{\lambda}{2c} \right)^2 l^2 \quad \text{Eqn. 3.5.}$$

Thus plotting  $\sin^2 \theta \nu l^2$  and performing a linear fit, the gradient can be used to determine the out of plane lattice constant,  $c$ . Whether a peak has been miss-assigned is immediately obvious with this plot, as it does not fit with the linear relationship of the rest. Having found the value of  $c$  from this method it is now possible to determine values for  $a$  by equating equations 3.3 and 3.4, this time in their full form. It again becomes immediately apparent if the hkl values for a peak have been assigned incorrectly by whether the value determined for that peak is within a reasonable margin of the literature value. The in plane lattice constant values calculated for each peak were collated and a mean value taken and the error associated with this value taken to be the standard error of the distribution.

For structures studied that were not hexagonal in nature, such as the  $\text{Fe}_3\text{O}_4$  thin films, the equation relating  $d$  to  $h$ ,  $k$  and  $l$  for the appropriate crystal system was used, in place of eqn. 3.4, and the same method applied. Given that  $\text{Fe}_3\text{O}_4$  has a cubic structure [143] eqn. 3.6 was used [142].

$$\frac{1}{d_{hkl}^2} = \frac{(h^2+k^2+l^2)}{c^2} \quad \text{Eqn. 3.6.}$$

### 3.2.2.2. Rocking curve measurements

A rocking curve is essentially a plot of x-ray intensity as a function of  $\omega$  for a fixed  $2\theta$  position. This measurement was performed by setting and fixing  $2\theta$  to the angle associated with the reflection of interest, this reflection's peak position will have already been determined from the  $2\theta/\omega$  measurement. With  $2\theta$  set,  $\omega$  is scanned about the  $\omega = \theta$  angle to determine the angular distribution of the crystal planes. The degree of orientation is an important factor that can strongly affect the physical properties of a thin film. Insight into the distribution in orientations can be gained from a rocking curve measurement typically by taking the full width at half maximum

(FWHM) of the rocking curve profile [140]. This FWHM parameter is one that can be compared between samples as a measure of the quality of a thin film sample.

In a rocking curve measurement, a perfect crystal will produce a very sharp peak, observed only when the crystallographic direction is perfectly aligned in angle. This peak will have some width purely due to instrument broadening. However, for imperfect crystals defects such as mosaicity, dislocations or film curvature create a distribution in the angles of the atomic planes, this is observed as a broadening of the rocking curve [140]. Hence the smaller the FWHM of the rocking curve, typically the fewer of these defects the thin film has. The FWHM of a rocking curve is also sensitive to the strain accumulation and tensile stress in the material, with an increased tensile stress increasing the FWHM [144].

For the rocking curve measurements performed, on the samples studied in this work,  $2\theta$  was set as determined from the previously run  $2\theta/\omega$  scan. Initially  $\omega$  was scanned over a 5-degree range centred on the expected peak position. After this initial measurement, the measurement range and step size was adjusted appropriately for the distribution observed.

### 3.2.2.3. Reflectivity measurements

X-Ray Reflectivity (XRR) is not a technique that evaluates diffraction phenomena, however it can be performed with the same optics and set up used for XRD [140]. XRR measurements can be used to determine parameters such as film thickness or surface and interface roughness [145]. In this work, it has been used primarily to determine the thicknesses of the samples grown in order to calibrate growth rates of the pulsed laser deposition system.

Upon setting up the reflectivity measurement, the incident slits were reduced to a width of 0.1 mm, in order to ensure the beam footprint was not significantly larger than the 5mm sample, and the receiving slits were set to 0.2 mm. The measurement then carried out is simply a  $2\theta/\omega$  scan at low angles, typically between  $2\theta$  values of 0.1 and  $10^\circ$ . All XRR measurements carried out in this work were taken with a step size of  $0.01^\circ$ . For the same set up as that used for the XRD measurements, at low incident angles, the x-rays incident on the films surface generate a specularly reflected wave, a refracted wave and a series of diffuse reflections [145] as represented in fig. 3.5.

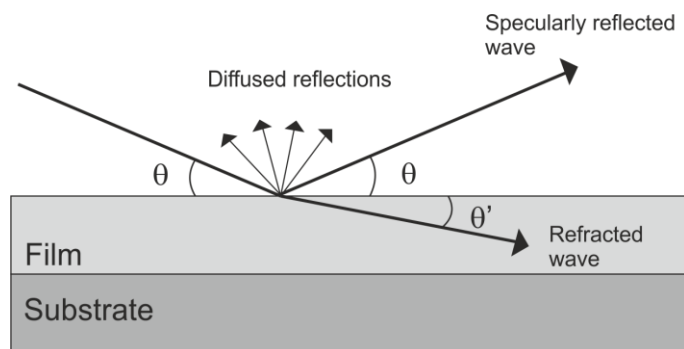


Figure 3.5. The reflection and refraction of x-rays incident on a thin films surface.

Below a critical angle ( $\theta_c$ ), the x-ray beam is completely reflected by the thin film surface. For a fixed x-ray wavelength, this critical angle is a function of the films refractive index and can be fitted to determine the sample's density [140]. As the incident angle is increased above  $\theta_c$  the measured x-ray reflectivity decreases rapidly at a rate that is proportional to  $\theta^4$  [140], consequently XRR measurements are typically plotted on a log scale, fig. 3.6.

At incident angles above  $\theta_c$  interference fringes are created in the reflectivity measurement by the phase difference between x-rays reflected from the different surfaces of the film and substrate [146]. These fringes, known as Kiessig fringes, are used to determine the thickness of the thin film as the distance between the fringes is inversely proportional to the film thickness [146]. There is a limit, of the order of a 100 nm, to how thick of a sample can still be measured and produce visible

Kiessig fringes. This limit depends on both the sample density and surface roughness [140]. The amplitude of the Kiessig fringes is dependent on the difference between the densities of the film and substrate. With the smaller the difference in film and substrate densities the lower the fringe amplitude [140]. As such, the closer match the two densities are the harder it is to determine film thickness from XRR. It is also known that the film surface roughness acts to decrease the reflectivity more rapidly with increase angle of incidence [140]. Thus, for a thin film with a rougher surface the signal drops off much faster, again making the observation and accurate fitting of Kiessig fringes more difficult. The roughness of the film-substrate interface also plays a key role in that the higher the interface roughness the lower the amplitude of the Kiessig fringes [140].

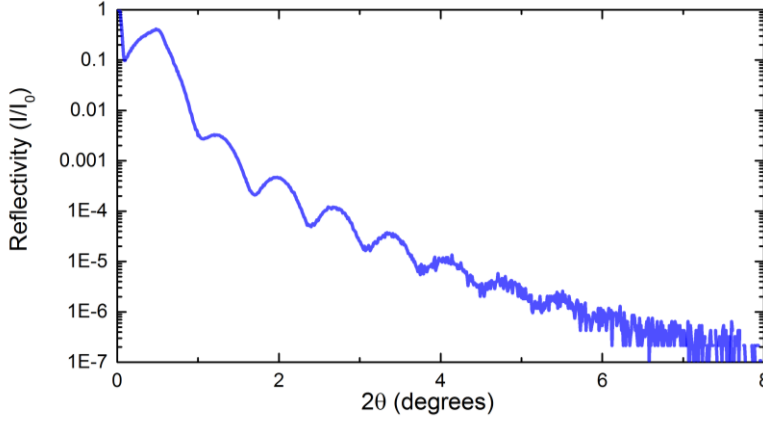


Figure. 3.6. X-ray reflectivity curve of a  $\text{Fe}_3\text{O}_4$  thin film on a silicon substrate.

Given the dependence of the reflectivity curve on the above-mentioned parameters, fitting software can be used to graphically fit the XRR data in order to determine density, roughness and film thickness. For the measurements taken in conjunction with this work, two independent fitting software packages were used and it was ensured that the fitting parameters they both produced were in good agreement. The fitting software packages used were Globalfit [147] and GenX [148]. The reflectivity fitting is primarily based on a non-linear least squares fitting method [140] and uses algorithms [148] to prevent the fitting process become stuck in local minima, when optimising values for the density, roughness and thickness parameters. Firstly the structure is simulated by inputting expected values for the structures thickness, roughness etc. The programme uses these parameters to simulate the reflectivity curve, based on the recurrence eqn. 3.7 [140].

$$R_{j,j+1} = \frac{R_{j+1,j+2} + F_{j,j+1}}{R_{j+1,j+2} \times F_{j,j+1} + 1} a_j^4 \quad \text{Eqn. 3.7.}$$

In eqn. 3.7 the air above the film surface is regarded as the  $j = 1$  layer and the substrate is the  $j = n+1$  layer.  $R_{j,j+1}$  is define as the reflection coefficient at the interface between the  $j$  and  $j+1$  layers [140]. Where  $F_{j,j+1}$  and  $a_j$  are defined by eqn. 3.8 and eqn. 3.9, respectively [140].

$$F_{j,j+1} = \frac{g_j - g_{j+1}}{g_j + g_{j+1}} \exp\left(\frac{-8\pi^2 g_j g_{j+1} \sigma_{rms,j+1}^2}{\lambda^2}\right) \quad \text{Eqn. 3.8.}$$

$$a_j = \exp\left(\frac{-i\pi g_j t_j}{\lambda}\right) \quad \text{Eqn. 3.9.}$$

Given that  $\sigma_{rms}$  is the rms roughness of the layer and  $g_j$  is related to  $\theta$  such that  $g_j = \sqrt{n_{rj}^2 - \cos^2 \theta}$  where  $n_{rj}$  is the refractive index of the layer and is a function of the density ( $\rho$ ) [149]. Once the reflectivity for all subsequent layers has been calculated this allows for the calculation of the total x-ray reflectivity,  $I/I_0 = R_{1,2}$  [140]. After the initial simulation, the software performs numerous iterations until the fit converges on the experimental data.

When fitting the XRR data the fits were run until the convergence parameters remained the same for more than 30 minutes and the limits on the convergence values of density, thickness and

roughness were set to prevent unreasonable values being converged upon. This ensured that all the XRR data was fit as reliably as possible.

#### 3.2.2.4. Pole Figure measurements

For several of the thin film samples XRD pole-figure measurements were performed. These measurements are used for the analysis of textural information averaged over a large area of the sample [140]. In the pole-figure technique,  $2\theta$  is fixed and the diffracted intensity is measured as a function of two geometric parameters. The pole-figure measurements were performed by measuring the diffracted beam intensity of the specific Bragg reflection of interest as a function of sample rotation angle ( $\varphi$ ) at various tilt angles of the sample surface normal ( $\chi$ ). The intensity is plotted as a 2-dimensional map. It is this map that is known as a pole-figure and is essentially a representation of the distribution of a crystallographic orientation in space [140].

In pole-figure representation, the tilt angle ( $\chi$ ) varies radially and the rotation angle ( $\varphi$ ) varies circularly as shown in fig 3.7, an example pole-figure plot. As seen in fig. 3.7, a sharp, narrow distribution at the centre of a pole figure indicates a high degree of orientation of this direction parallel to the surface normal [150]. A line profile, taken across the pole-figure, at a fixed rotation angle shows the intensity distribution as a function of tilt angle with respect to the film surface normal. On the other hand, a profile taken as a ring, at a fixed tilt angle shows the intensity as a function of rotation angle.

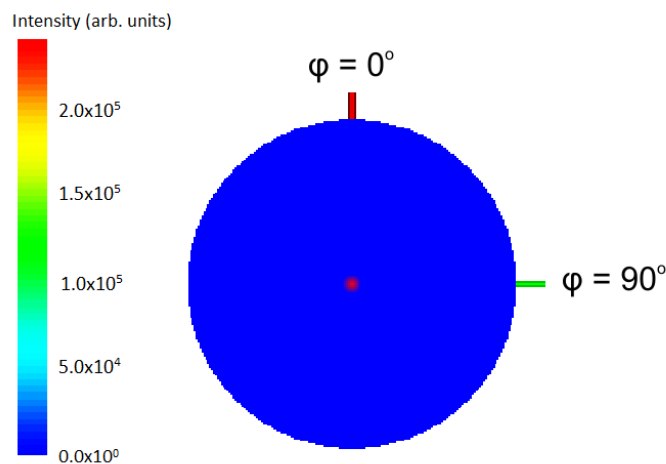


Figure. 3.7. XRD pole figure for an MgO sample taken at the (002) diffraction peak.

Pole-figure analysis provides valuable information on the crystallographic texture that may be related to physical, chemical and mechanical properties of materials [140]. Pole-figures are useful for visualising the orientation distribution (texture) of grains in polycrystalline materials. Texture is the distribution of crystallographic orientations of a sample. A sample in which these orientations are random is said to have a random texture. If the crystallographic orientations are not random, but have some preferred direction, then the sample is said to have a weak, strong, or moderate texture. The degree of texture is dependent on the percentage of crystals that have the preferred orientation. Texture can have a great influence on material properties [151].

The Pole-figure measurements were performed, once the  $2\theta$  angle of interest was set, by setting the tilt angle ( $\chi$ ) and scanning the rotation ( $\varphi$ ). Then  $\chi$  was stepped and  $\varphi$  scanned again. The measurements were taken at  $1^\circ$  intervals in both  $\varphi$  and  $\chi$ , with  $\varphi$  measured between 0 and  $360^\circ$  and  $\chi$  between 0 and  $90^\circ$ . Each individual  $\varphi$  scan was performed with a scan speed of  $100^\circ$  per minute.

### 3.2.3 Raman Spectroscopy

The samples have also been investigated in terms of their vibrational spectra in order to gain further insight into their structural characteristics. Raman spectroscopy has been used as a technique to investigate this as it does not necessitate long-range order as is the case for XRD. Additionally it can be used to identify between materials, such as magnetite and maghemite, that cannot be easily distinguished from one another using XRD [152] [153] [154].

The energy of a lattice vibration is quantised, where each quantum of energy is called a phonon [155]. Phonons are essentially quantised lattice vibrations in which the lattice of atoms uniformly vibrates at a single frequency [156]. The energy ( $E_v$ ) of a given phonon mode of angular frequency ( $\omega_\lambda$ ) is given by eqn. 3.10.

$$E_v = \left( n + \frac{1}{2} \right) \hbar \omega_\lambda \quad \text{Eqn. 3.10.}$$

when the mode is occupied by  $n$  phonons. The  $\frac{1}{2}\hbar\omega_\lambda$  is the zero point energy of the mode and occurs in equivalence to a quantum harmonic oscillator [155]. A crystal's dispersion relation shows two different branches of phonon mode, characterised as acoustic and optical modes. Both modes can be categorised further into longitudinal and transverse modes [155]. However, typically, Raman spectroscopy only probes the Raman active optical modes. Phonon modes are often described by using Mulliken symbols, the nomenclature of which is described in detail in [157] [158]. Different crystal structures have different phonon modes and hence different vibrational spectra. As such, characterising the phonon modes observed within a given sample can be used to gain insight into its composition and structure.

Raman Spectroscopy works by focussing a laser, of visible wavelength, onto the sample's surface. The photons of the laser interact with the molecular vibrations and phonons, within the sample structure, with the energy of the re-emitted photons providing information on the vibrational modes of the system. As depicted in fig. 3.8, an incident photon excites a phonon in a vibrational energy state to a virtual energy state, which then de-excites back to a vibrational state causing the re-emission of a photon [159]. The energy difference between initial and final states is measured as the difference between the incident and emitted photon energy, by the Raman spectrometer [159]. These energy differences correspond to the energies of the vibrational and phonon modes of the structure and are typically measured in terms of wavenumber ( $\Delta w$ ) and is given by eqn. 3.11.

$$\Delta w = \left( \frac{1}{\lambda_0} - \frac{1}{\lambda_1} \right) \quad \text{Eqn. 3.11.}$$

where  $\lambda_0$  is the wavelength of the laser and  $\lambda_1$  the wavelength of the re-emitted light [159].

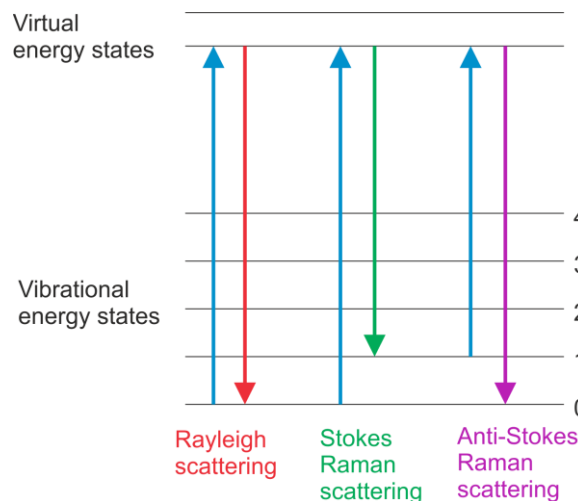


Figure. 3.8. Energy level representation of the phonon transitions during Raman Spectroscopy.

As depicted in fig. 3.8, if the phonon de-excites back to its original energy state, this elastic scattering is known as Rayleigh scattering [159]. However, when the scattering is inelastic, a peak is seen in the Raman spectrum corresponding to a vibrational or phononic mode transition. If the final vibrational energy state is higher than the initial, this is defined as Stokes Raman scattering. Alternatively, if the final vibrational energy state is lower than the initial state this is anti-Stokes Raman scattering [159]. Additionally, in order for a given phonon mode to be Raman active, it must cause a change in molecular polarizability [159], where the polarizability is the tendency of the molecules electron cloud to be distorted by an external magnetic field i.e. electromagnetic radiation. As such, each molecules polarizability depends on its rotational and vibrational state. If we consider the rotational and vibrational states to be numbered  $J$  and  $v$ , according to their energy, the specific selection rule for rotational transitions is that  $\Delta J = \pm 2$ . Similarly for a vibrational state, only  $\Delta v = \pm 1$  transitions are Raman active [159].

The Raman spectra of the iron oxide films studied were measured using an HORIBA XPLORA Raman spectrometer, with a 532 nm wavelength laser and using a 50x objective lens. Before each time the spectrometer was used a calibration was performed to a silicon reference sample. For each measurement the optics were at first focused visually onto the sample surface, this was then checked by focussing the laser spot to a minimum diameter. Spectra were acquired each time with an acquisition time of 20 seconds for 5 accumulations and for the iron oxide films between  $100\text{ cm}^{-1}$  and  $1600\text{ cm}^{-1}$ , to cover all significant Raman modes possible. The spectrometer used had a resolution of  $0.5\text{ cm}^{-1}$ , which allowed for the observation of small shifts in peak position between samples, and a beam size of approximately  $1\text{ }\mu\text{m}$  meaning that the Raman spectra measured were representative of that given area of the film. To ensure that the spectra were typical of the film in general, measurements were taken for each sample at five different locations across the film. The spectrum at one chosen area was then taken 3 times and averaged to aid noise reduction.

### 3.3 Magnetic Characterisation techniques

#### 3.3.1 Vibrating Sample Magnetometry

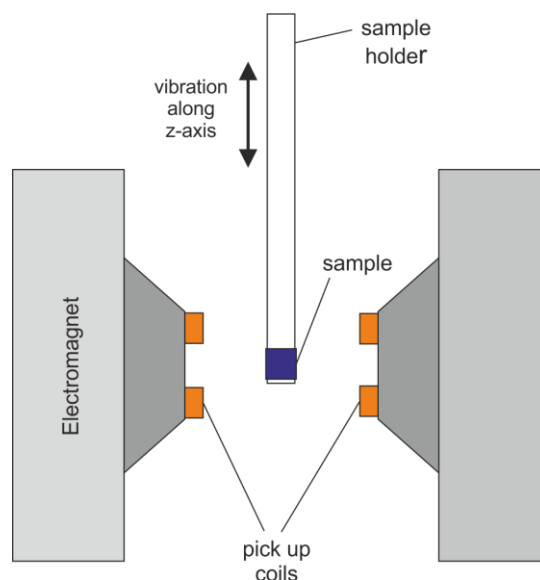


Figure. 3.9. Schematic representation of a typical vibrating sample magnetometer set up.

Throughout this work, Vibrating Sample Magnetometry (VSM) has been used to measure the magnetic properties of the ferrite and hexaferrite samples. In VSM, the sample to be investigated is placed inside a uniform magnetic field, created by an electromagnet. This field acts to magnetise the sample being investigated. The sample is then vibrated sinusoidally, through the use of a piezoelectric material. Detection coils are located close to the sample, within the uniform magnetic

field. Typically, the changing magnetic flux due to the vibration of the sample induces a voltage in the detection coils, which is measured through a lock-in-amplifier, using the piezoelectric signal as the reference signal. From the voltage induced in the coils the magnetic moment of the sample material can be determined, hence, also the magnetisation. Consequently, measuring this magnetisation ( $M$ ) as a function of the magnetic field ( $H$ ) makes it possible to produce a  $M(H)$  curve. Additionally, the magnetisation can be measured as a function of sample temperature ( $T$ ). A sample's  $M(T)$  characteristics can allow insight into the magnetic phase transitions present. The basic VSM set up is shown in fig. 3.9.

To study the ferrite samples at room temperature a MicroSense Model 10 VSM magnetometer was used. For these measurements, the samples were mounted on a quartz rod through the use of a small amount of GE varnish. Both in and out of plane measurements at RT were performed using this magnetometer. Where the orientations of the two measurements are shown in fig. 3.10, and are defined by the orientation of the applied field with respect to the sample. Switching between the two orientations was achieved by the rotation of the electromagnet.



Figure. 3.10. Representation of in and out of plane geometries during VSM measurements.

The temperature dependent measurements on the hexaferrite samples were performed using a Quantum Design Vibrating Sample Magnetometer (VSM-SQUID), Magnetic Property Measurement System. A Superconducting Quantum Interference Device (SQUID) is a highly sensitive form of magnetometer and allows for the measurement of extremely small magnetisation and magnetic field changes, based on superconducting tunnel junctions [30]. The use of this more sensitive magnetometer for the temperature dependent measurements, allows for any subtle changes in magnetisation to be picked up as the temperature is swept. For these measurements taken using the SQUID magnetometer the samples were again mounted on a quartz rod sample holder and all samples were measured with the magnetic field applied in the plane of the sample.

### 3.3.1.1. $M(H)$ measurements

$M(H)$  measurements were performed on all samples at RT.  $M$  was measured as a function  $H$  with all measurements starting at a positive saturating field, sweeping to negative saturation and then returning to the positive saturation point. These measurements allowed magnetic hysteresis loops to be observed and for the determination of key magnetic parameters. Namely, saturation magnetisation ( $M_s$ ), magnetic remanence ( $M_r$ ) and coercive field ( $H_c$ ). Magnetisation was always measured in electromagnetic units (emu) and converted to emu/cc when the sample thickness and dimensions were known. The coercivity was always measured as half of the full opening of the hysteresis loop, in magnetic field units of Oersteds (Oe).

For each sample, an initial measurement was performed over a wide field range with a broad step size, typically 500 Oe. This then allowed an appropriate saturating field and step size to be chosen for the specific sample before running the measurement again. For the hexaferrite thin films studied, in plane  $M(H)$  were also taken at a range of temperatures between 10 K and 300 K, as mentioned previously these were performed using a Quantum Design VSM-SQUID. When measuring a sample using this magnetometer, a  $M(H)$  measurement was performed at RT initially and compared to measurements taken using the Model 10 VSM, to ensure consistency between

the two magnetometers. It is worth noting that the  $M(H)$  measurements were performed, for each sample, in order of ascending temperature.

For all  $M(H)$  measurements taken there was a diamagnetic background contribution due to the sample holder and substrate. As such, each time a sample was measured, a measurement was also taken of purely the sample holder and a plane substrate, of the same size and composition. This was then subtracted from the sample measurement.

### 3.3.1.2. $M(T)$ measurements

All  $M(T)$  measurements were performed using the Quantum Design VSM-SQUID. For a fixed magnetic field value, magnetisation was measured as a function of temperature between 10 K and 500 K. These measurements have been performed to gain insight into the magnetic structure of the samples as the shape of the temperature dependence relationship can provide insight into the magnetic ordering within a sample [80]. Magnetic phase transition temperatures can also be determined from the turning points within the  $M(T)$  relationship.

The  $M(T)$  measurements were performed starting at low temperature and measuring to high. Due to the nature of ferrimagnetic materials the  $M(T)$  measurement produced is dependent on the pre-measurement conditions. For each sample, measurements were performed under both Zero Field Cool (ZFC) and Field Cool (FC) conditions. The FC and ZFC measurements produce different  $M(T)$  relationships due to magnetic anisotropy, which acts to align the magnetic moments in a preferred direction [160]. In the ZFC case, since no magnetic field is applied while cooling, the moments are locked in random directions for a polycrystalline sample. When a small magnetic field is applied at the starting measurement temperature (10 K), the magnitude of the resultant magnetization will depend on the anisotropy of the system. If the system is highly anisotropic, the small applied field will not be sufficient to rotate the unordered moments in the direction of the applied field hence the magnetization measured will be small [160]. However, for the FC process, the sample is cooled in the presence of a high magnetic field. Therefore the moments will be aligned and have less chance of disorientation, remaining aligned during cooling. Producing a larger magnetisation at low temperature compared to the ZFC case [160]. The difference between the FC and ZFC measurements can then provide insight into magnetic structure [160].

In the ZFC measurements, the samples were cooled from room temperature in the absence of an applied magnetic field to 10K and for the FC measurements, saturating field of 30 kOe was applied during cooling. For all measurements the samples were cooled at a rate of 5 K/min. At 10 K an un-saturating magnetic field was then applied, typically, this field was 300 Oe but measurements using different values were also taken. Magnetisation was then measured at 0.1 K intervals, as the temperature was increased at a rate of 5 K/min. For consistency, the FC measurement was always performed first. For all  $M(T)$  measurements an offset, to account for the contribution of the substrate, was subtracted. This effect was typically small compared to the sample signal however, it was determined by measuring the  $M(T)$  of a blank substrate.

### 3.3.2 Ferromagnetic Resonance measurements

Ferromagnetic Resonance (FMR) spectroscopy is a well-established technique used to probe the magnetisation dynamics of ferro and ferrimagnetic materials [161]. FMR occurs in the microwave range of frequencies, in magnetic samples, and has been used in this thesis to study the samples magnetic properties. Some of the most important magnetic parameters can be deduced from FMR spectroscopy such as the Lande  $g$ -factor ( $g$ ), the FMR linewidth ( $\Delta H$ ) and the anisotropy field ( $H_A$ ) [162]. Additionally the microwave properties of the hexaferrites are of significant interest for microwave device application, with hexaferrites being a widely used material in the microwave industry [6] [82].

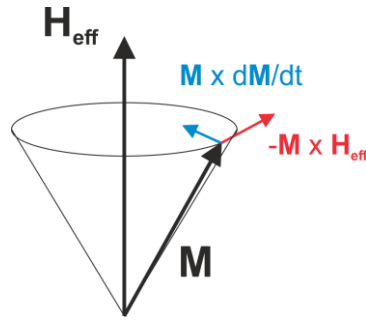


Figure. 3.11. Schematic representation of the damped precession of magnetisation ( $M$ ) with respect to the external magnetic field ( $H$ ) direction.

FMR arises from the precessional motion of magnetisation ( $M$ ). If a magnetic field is applied to the magnetic moments within a magnetic sample, they will tend to line up parallel to the field in order to minimise magnetostatic energy. If the magnetic moments are displaced from the external field direction, they will precess back to it, as shown in the schematic diagram of fig. 3.11 [162].

The motion of the magnetisation is a damped precession and can be described by the Landau-Lifshitz-Gilbert equation, eqn. 3.12 [161].

$$\frac{dM}{dt} = -\gamma(M \times H_{eff}) + \frac{G}{\gamma M_s^2} \left( M \times \frac{dM}{dt} \right) \quad \text{Eqn. 3.12.}$$

Here  $H_{eff}$  is the effective magnetic field, which is a combination of the applied field, the microwave magnetic field, the demagnetising field and the magnetocrystalline anisotropy field.  $G$  is the Gilbert damping constant and  $\gamma$  is the gyromagnetic ratio and is related to the  $g$ -factor by eqn. 3.13 [161].

$$\gamma = g \frac{\mu_B}{\hbar} \quad \text{Eqn. 3.13.}$$

where  $\mu_B$  is the Bohr magneton. In eqn. 3.12, the initial term in the equation describes the precession motion and the second is essentially a damping term. If a transverse Radio Frequency (RF) field is applied to the sample, and if this RF frequency coincides with the precessional frequency of the magnetisation, magnetic resonance occurs and the RF power is absorbed by the sample [162]. In the FMR measurements performed, a fixed RF frequency is applied to the sample through a waveguide and the applied bias field is swept. The sample absorption of the RF power is measured by a lock-in amplifier. As the magnetic sample absorbs the RF signal when the frequency corresponds with the precessional frequency of  $M$ , a peak is seen in the absorption at a resonance field ( $H_r$ ).

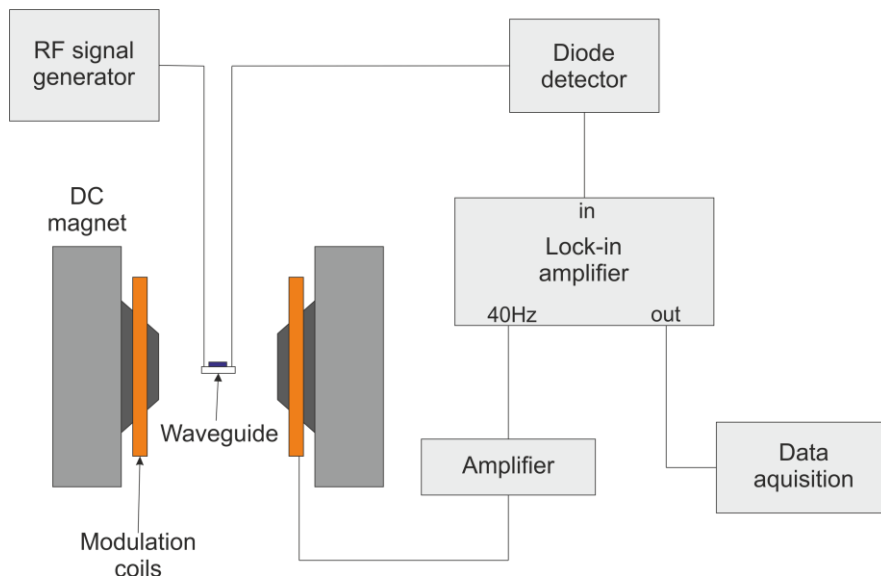


Figure. 3.12. Diagram of the microwave spectrometer used to perform the FMR measurements.

The set up of the modulation FMR system used is shown in fig. 3.12. The sample is placed on a coplanar waveguide (CPW) in a DC magnetic field. A small pair of Helmholtz coils applies a small modulating AC field, at 40 Hz, allowing for lock-in detection [163]. A Rohde and Schwarz SMB 100A signal generator outputs a 10dBm RF signal, of fixed frequency, through the CPW, which generates a RF H field at the sample. The RF power transferred through the CPW is detected by an AtlanTec BZD diode detector, which converts the RF signal to a voltage that can be measured by the lock-in amplifier. Measurements have been performed in this work by measuring the microwave absorption, at a fixed frequency, as a function of applied magnetic field. Typically, the absorption derivative is plotted, an example of which is displayed in fig. 3.13.

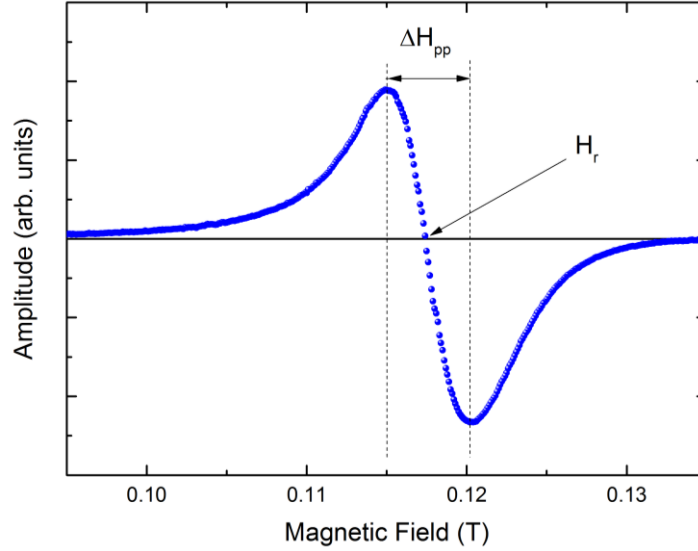


Figure. 3.13. Typical FMR spectrum measured at 10GHz using a Permalloy thin film sample. The resonance field ( $H_r$ ) and peak-to-peak linewidth ( $\Delta H_{pp}$ ) are indicated in the diagram.

Two important parameters are determined from an FMR spectrum: the resonance field ( $H_r$ ) and the linewidth ( $\Delta H$ ) [161]. The resonance field position  $H_r$  depends on the anisotropy parameters, g-factor, and magnetization of the sample. The linewidth  $\Delta H$  is connected to the damping processes and, in this case, is defined as the half width at half maximum of the absorption line. To extract the resonance field and linewidth values the FMR data was fitted using the derivative of an asymmetric Lorentzian, as detailed by eqn. 3.14 [161].

$$\frac{d[\chi'' \cos \Theta + \chi' \sin \Theta]}{dH} = -\frac{2(H-H_r)\Delta H \cos \Theta}{[\Delta H^2 + (H-H_r)^2]^2} - \frac{[\Delta H^2 - (H-H_r)^2] \sin \Theta}{[\Delta H^2 + (H-H_r)^2]^2} \quad \text{Eqn. 3.14.}$$

Where  $[\chi'' \cos \Theta + \chi' \sin \Theta]$  is the asymmetric absorption function and  $\Theta$  denotes the mixing angle between the dispersive and absorptive components.  $\chi''$  and  $\chi'$  are the imaginary and real parts of the susceptibility. The resonance field and linewidth given by this equation can also be determined by inspection of the plotted data, provided that the lineshape is fairly symmetric. The resonance field is given by the zero crossing, as shown in fig. 3.13 and the linewidth is related to the peak to peak linewidth by eqn. 3.15 [161].

$$\Delta H = \frac{\sqrt{3}}{2} \Delta H_{pp} \quad \text{Eqn. 3.15.}$$

FMR measurements were performed for all hexaferrite thin film samples studied in this work. The measurements were classified as in-plane due to the geometry of the measurement, meaning that the bias field ( $H$ ) was applied in the plane of the samples being studied. The field step size used was dependent on the linewidth observed for a given sample, to ensure enough data points were present across the resonance peak to produce reliable fitting of the data. Typically, for the hexaferrite samples a step size of 50 Oe was used, taking 7000 averages at each point. The lock-in

sensitivity was also chosen dependent on the strength of the FMR response for a given sample, to obtain a signal as large as possible without saturation.

For each sample, a measurement was initially taken at an RF frequency of 10 GHz, with the DC magnetic field applied perpendicular to the RF H-field. To remove any magnetic contribution from the measurement system itself, in terms of FMR response, background measurements were taken and subtracted from the data. The data could then be fitted with eqn. 3.14 and the  $H_r$  and  $\Delta H$  values extracted. These values were then checked to be reasonable by comparing to the zero crossing point and the  $\Delta H_{pp}$  from the graphical plot of the data.

If a good FMR response was observed, at 10 GHz, then the frequency dependence of the FMR was measured between 3 GHz and 18 GHz. Based on the work of Kittel [164], applied to hexaferrite thin films [165] [162], the frequency dependence can be used to deduce g-factor values and anisotropy field ( $H_A$ ) values, assuming the  $M_s$  values obtained from VSM. By plotting frequency as a function of  $H_r$  insight can also be gained into the magnetic structure of the samples, as the relationship between  $H_r$  and frequency will be different depending on whether the uniaxial anisotropy is normal to the film plane and whether it is a hard or easy axis [165]. The general frequency relation for the in plane FMR geometry is given by eqn. 3.16 [165]

$$f = 1.4 \times 10^6 g \sqrt{((H_r + H_A \cos^2 \phi)(H_r + H_A \cos 2\phi + 4\pi M_s))} \quad \text{Eqn. 3.16.}$$

where  $\phi$  is the angle of the anisotropy axis relative to the film plane. If this axis lies in the plane of the sample, then this relation simplifies to the following [165]

$$f = 1.4 \times 10^6 g \sqrt{((H_r + H_A)(H_r + H_A + 4\pi M_s))} \quad \text{Eqn. 3.17.}$$

Alternatively, if the sample has a uniaxial axis of anisotropy that lies out of plane, as is the case for BaM with large c-axis anisotropy, then the frequency,  $H_r$  relationship will be different and governed by eqn. 3.18. [165]

$$f = 1.4 \times 10^6 g \sqrt{(H_r(H_r - H_A + 4\pi M_s))} \quad \text{Eqn. 3.18.}$$

By fitting of the experimental data it is made apparent which relationship holds, indicating whether the presence of a cone of magnetisation is possible within a given sample.

Measurements were also taken as a function of angle between the DC magnetic field and the [1120] crystallographic axis of the substrate. The angular dependence of the resonance field provides information on the magnetic anisotropy of the samples [161].

### 3.4 X-ray Magnetic Spectroscopy

X-ray absorption spectroscopy (XAS) and x-ray magnetic circular dichroism (XMCD) have been performed at the cobalt, iron and titanium L-edges (2p→3d) of the hexaferrite samples studied in this thesis. The measurements were performed on the I06 magnetic spectroscopy beamline at the Diamond Light Source synchrotron facility.

XAS was developed in the early 1970's [166], and is a widely used technique at synchrotron facilities today. The utilisation of tuneable synchrotron based x-ray sources has allowed for spectra with extremely high signal to noise ratios. As such, XAS has become a useful tool for identifying the local structure and oxidation states of a specific element within a vast range of materials.

A variation of the XAS technique is XMCD, which is the difference spectrum between XAS spectra taken with right and left circular polarised x-rays, in the presence of a magnetic field. From the XMCD spectrum, information can be gained on the magnetic properties of the atoms being probed [167]. A key advantage of XMCD is the element specific nature of the magnetic measurements, which allows for the investigation of the magnetic contributions of individual elements in different co-ordinations, giving insight into how substitutions to different sites affect the magnetic structure and properties of the hexaferrite thin films.

### 3.4.1 X-ray Absorption Spectra (XAS)

XAS measurements are obtained by scanning the energy of the x-rays incident upon a given sample and measuring the absorption. X-ray absorption occurs when an x-ray photon is absorbed by an atom with the excess energy transferred to an electron. As a result of this photoelectric absorption, the energy is used to either excite the electron into a higher unoccupied orbital, or into the continuum where it is no longer associated with the atom. X-ray absorption spectra of any material, be it atomic or molecular, are characterized by sharp increases in absorption at specific x-ray energies. These energies are characteristic of the absorbing element. The sudden increases in absorption observed are known as absorption edges, and correspond to the energy required to excite a core electron into a higher unoccupied state or into the continuum.

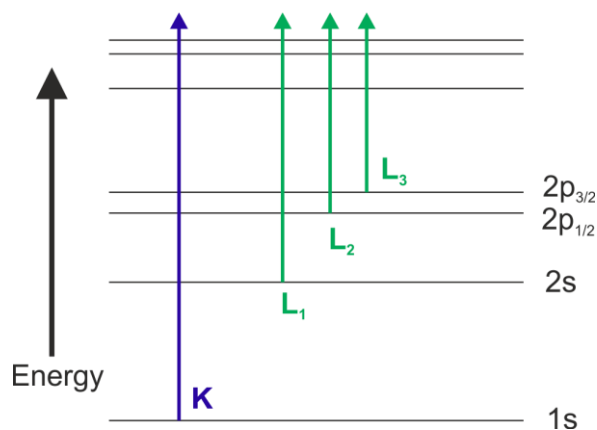


Figure. 3.14. Schematic representation of the K-edge (blue) and L-edge (green) transitions.

The name of the edge depends upon the core electron that is excited. The principle quantum numbers  $n = 1, 2$  and  $3$  are represented by the K, L and M edges, respectively. Thus, the K-edge features arise from the excitation of electrons from the 1s orbital. The L-edge from the excitation of 2s and 2p electrons [168]. The electronic transitions associated with both the K and L-edges are shown in fig. 3.14. As can be seen, in the energy level diagram of fig. 3.14, the L-edge transitions are categorised further into the L<sub>1</sub>, L<sub>2</sub> and L<sub>3</sub> edges. These are defined according to the initial electron energy level, with L<sub>1</sub> from the 2s state, L<sub>2</sub> from the 2p<sub>1/2</sub> and L<sub>3</sub> from the 2p<sub>3/2</sub> [167].

The electron transitions are bound to follow the quantum mechanical selection rules. These select the symmetry of the final states of the excited electrons. As such, the most intense features in the absorption spectra are due to electric-dipole allowed transitions (i.e.  $\Delta l = \pm 1$ ) to unoccupied final states. Hence, for the K-edge transitions the most prominent features in the spectra arise from the core transitions from 1s to p-like final states. Where the most intense features of the L<sub>2</sub> and L<sub>3</sub> edges are due to transitions from 2p to final states of d-character [169].

The energy at which an absorption edge appears depends upon the transition involved as well as the element measured. For a given element, the K-edge occurs at a higher energy than the L-edge. In the case of the 3d transition metals such as Fe, this results in the K-edge occurring in the hard x-ray range of the spectrum. The L-edge occurs at a lower energy than the K-edge, between 400-1,000 eV, in the soft x-ray region [169]. Of particular interest for their magnetic properties are the L<sub>2</sub> and L<sub>3</sub> edges of 3d metals such as Fe and Co as the magnetism in these elements arise from the 3d orbitals. An example XAS spectrum at the Fe L<sub>2,3</sub> edges can be seen in fig. 3.15, two pronounced peaks are seen in the absorption spectrum corresponding to the L<sub>3</sub> and L<sub>2</sub> edges, respectively. The spectrum presented is that obtained at 300 K from a Fe<sub>3</sub>O<sub>4</sub> thin film sample. It is evident from fig. 3.15, that there is a finer structure present in the spectra at both edges, as seen by the shoulders on the absorption peaks. These shifts in energy are as a consequence of Fe ions in different coordinations and valences. The effects these have on the XAS spectra can be understood through the consideration of crystal field theory.

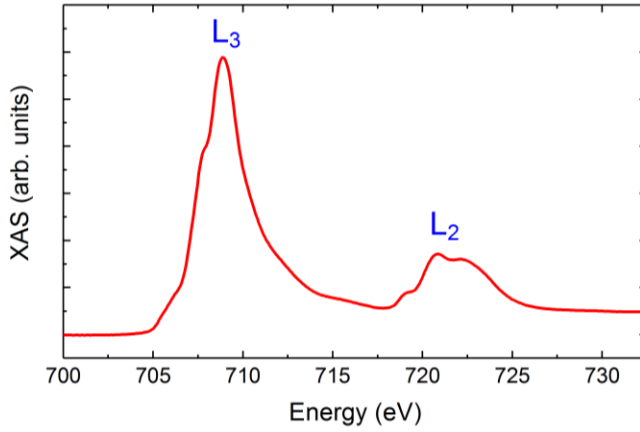


Figure. 3.15. XAS measured at the Fe  $L_3$  and  $L_2$  edges of a  $Fe_3O_4$  sample, at 300 K, with vertically linear polarised x-rays.

### 3.4.2 Crystal Field Theory

Crystal field theory is a model that describes the breaking of degeneracies of the electron orbital states. This splitting of electron orbitals is due to a static electric field produced by the surrounding charge distribution. The static electric field produced is known as the crystal field. The charge distribution creating the crystal field is that of the atoms anion neighbours within the specific crystal structure being studied [170].

The basic concept of a crystal field was first developed by Bethe [171], who studied the effect of the surrounding ions on the electron distribution within a NaCl lattice. He modelled the interactions between ions as due to electrostatic potentials. In the specific example of NaCl, the Na atom was considered to be surrounded by 6 negative point charges. Each of the negative charges is known to create an electrostatic potential [170]

$$V_{(i;x,y,z)} = \frac{e}{r_{(i;x,y,z)}} \quad \text{Eqn. 3.19.}$$

where  $V_i$  is the potential of the  $i$ th ion, at the point  $(x,y,z)$  and  $r_{(i;x,y,z)}$  is the distance from the from the  $i$ th ion to the point  $(x,y,z)$ . The origin of the co-ordinate system is located on the central transition metal ion. The total potential at any point is then given by eqn. 3.20 [170].

$$V_{(x,y,z)} = \sum_i V_{(i;x,y,z)} \quad \text{Eqn. 3.20.}$$

The process of performing this summation, for a given ion environment, and examining the effect of the potential on the electron orbitals of the central ion is mathematically complex. As the edges studied in this work are typically the  $L_3$  and  $L_2$  edges, the most important final states are the d-orbitals, and in the case of the Fe and Co studied, more specifically the 3d orbital states. To define the d orbitals it is necessary to consider the one electron hydrogen like wavefunctions [170].

$$\Psi_{n,l,m_l} = R_{n,l}(r)Y_m^{m_l}(\theta, \varphi) = R_{n,l}(r)\Theta_{l,m_l}(\theta)\Phi_{m_l}(\varphi) \quad \text{Eqn. 3.21.}$$

where  $n$  is the principle quantum number,  $l$  is the orbital angular momentum quantum number and  $m_l$  is the magnetic quantum number.  $R_{n,l}(r)$  is the radial part of the wavefunction and describes the time averaged probability of finding an electron in the specified orbital at a distance  $r$  from the nucleus. The spherical harmonics  $Y_m^{m_l}$  describe the directional properties of the orbital defined by the wavefunction; these are functions of the angles  $\theta$  and  $\varphi$ , in spherical polar co-ordinates [170]. The crystal field due to point charges can be described by a linear combination of spherical harmonics,  $Y_m^{m_l}$ , which allows the matrix elements to be calculated purely in the language of

spherical tensor algebra, as shown by Racah [172]. The probability density of the 5 d orbitals  $d_{yz}$ ,  $d_{xz}$ ,  $d_{x^2-y^2}$  and  $d_{xy}$  can be represented graphically [170], as shown in fig. 3.16.

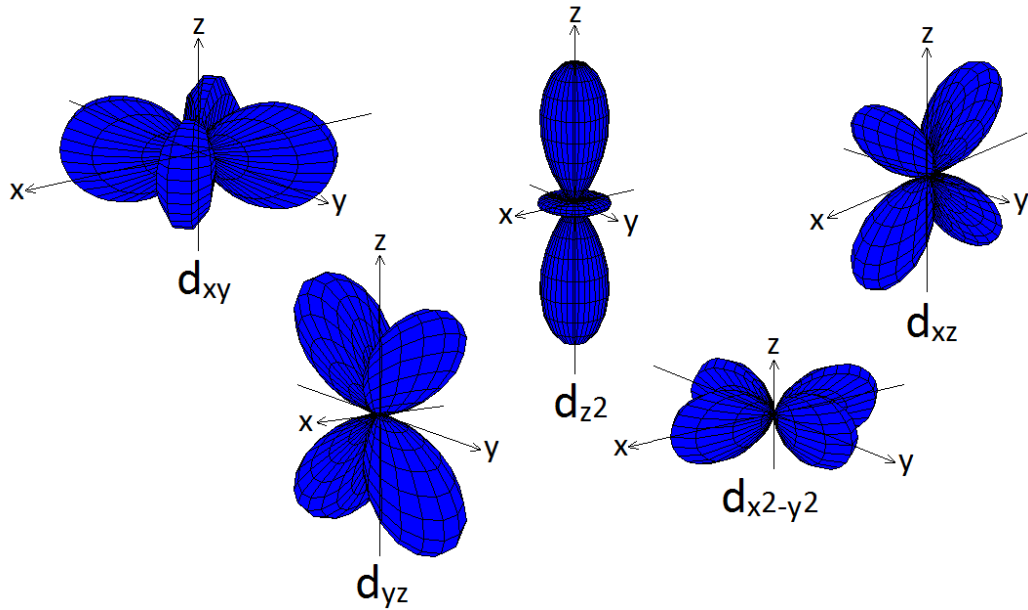


Figure. 3.16. Polar graphs of the probability densities for the five d orbitals.

In the absence of a crystal field, i.e. with no surrounding anions, all 5 d orbitals are degenerate. However, the presence of surrounding ligands and hence crystal field acts to cause a splitting in the energies of the orbitals. This energy level splitting is different depending on the arrangement of ligands around the cation, hence the co-ordination. The species of the cation and that of the surrounding ligands also affects the splitting, as does the cations oxidation state. Typically, the higher the oxidation state the larger the splitting of the orbitals, for a given co-ordination [170]. The  $d_{xy}$ ,  $d_{xz}$  and  $d_{yz}$  orbitals lie in the x-y, x-z and y-z plane, respectively. Each of these orbitals has four lobes, as shown in fig. 3.16, pointing between the two axes. Conversely, the lobes of the  $d_{x^2-y^2}$  and  $d_{z^2}$  orbitals point along the co-ordination axes. As a consequence of this, the crystal field affects the two sets of orbitals differently [170].

Let us consider the case of an octahedral co-ordination, remembering that the three co-ordinations present within the hexaferrite structure are octahedral, tetrahedral and trigonal bipyramidal. The six surrounding negative charges of magnitude,  $Ze$ , are situated on the x, y and z-axes at a distance  $\pm a$ . For a general point, A, the potential experienced due to charge 1 is given by eqn. 3. 22 [173].

$$V_1 = + \frac{Ze^2}{d} \quad \text{Eqn. 3.22.}$$

$d$  being the distance from charge 1 to A, and can be expressed as  $d = \sqrt{a^2 + r^2 - 2ar \cos \theta}$ . Hence, an expression for potential due to all 6 ligands can be given by eqn. 3.23 [173].

$$\begin{aligned} V &= \sum_{i=1}^6 V_i = \frac{6Ze^2}{a} + \frac{35Ze^2}{4a^5} \left( x^4 + y^4 + z^4 - \frac{3}{5}r^4 \right) \\ &= \frac{7Ze}{3a^5} \pi^{1/2} r^4 \left[ Y_4^0 + (5/14)^{1/2} (Y_4^4 + Y_4^{-4}) \right] \end{aligned} \quad \text{Eqn. 3.23.}$$

This is the form of the of the crystal field potential perturbing the central ions d electrons. The perturbation energy of the d states is then given as; [173]

$$\int \Psi^* V \Psi d\tau = \langle \Psi | V | \Psi \rangle \quad \text{Eqn. 3.24.}$$

Thus, by calculating this quantity for the five d states (five values of  $m_l$ : -2, -1, 0, 1, 2) the perturbations on the energies of the states due to the octahedral co-ordination are determined.

The  $6Ze^2/a$  term, in eqn. 3.23, is spherically symmetric and does not cause any splitting of the levels. It simply acts to raise the whole set of the d orbital energies by the factor of  $6Ze^2/a$ . The mathematical derivations of the energy level perturbations are shown in several textbooks, including that by Figgis [173]. It is found that the d orbitals split into a doublet and a triplet. The doublet,  $e_g$ , contains the  $d_{x^2-y^2}$  and  $d_{z^2}$  orbitals, both of which are degenerate. The triplet,  $t_{2g}$ , contains the degenerate  $d_{xy}$ ,  $d_{xz}$  and  $d_{yz}$  orbitals. A diagram of this splitting in an octahedral crystal field is shown in fig. 3.17. It is noted that the  $d_{x^2-y^2}$  and  $d_{z^2}$  orbitals are affected more than the rest by the octahedral field due to having electron density maxima located in the plane of the axis and hence closer to the nearest anion. Consequently, the d electrons of the central ion prefer to occupy the lower energy triply degenerate  $d_{xy}$ ,  $d_{xz}$  and  $d_{yz}$  states. It is seen that the  $e_g$  states are shifted positively by a factor of  $6Dq$  and the  $t_{2g}$  states are shifted negatively by  $4Dq$ . This results in a splitting between the double and triplet by a factor of  $10Dq$ , where  $Dq$  is a crystal field parameter, defined by eqn. 3.25.

$$Dq = \frac{Ze^2\bar{r}^4}{6a^5} \quad \text{Eqn. 3.25.}$$

where  $\bar{r}^4$  is the mean fourth power radius of the d electrons of the central ion [173].

Through applying the same principles it can be shown that a tetrahedral crystal field results in the same form of splitting of the d orbitals but with the opposite sign to that produced for the octahedral case. The four surrounding anions are considered as point charges at the points  $(\pm \frac{a}{\sqrt{3}}, \mp \frac{a}{\sqrt{3}}, \frac{a}{\sqrt{3}})$  and  $(\pm \frac{a}{\sqrt{3}}, \mp \frac{a}{\sqrt{3}}, -\frac{a}{\sqrt{3}})$ . The reversal in the splitting can now be pictured as the  $d_{xy}$ ,  $d_{xz}$  and  $d_{yz}$  orbitals having electron density maxima closer to the anions. As the ligand electrons are not orientated directly towards the d orbitals, however, the energy splitting will be lower than in the octahedral case. Indeed, the splitting is  $4/9$  that of the octahedral [170].

$$Dq_{tet} = -\frac{4}{9}Dq_{oct} \quad \text{Eqn. 3.26.}$$

The tetrahedral crystal field still splits the d orbitals into the  $e_g$  doublet and  $t_{2g}$  triplet. However, in this case the  $t_{2g}$  is shifted positively by  $4Dq$  and the  $e_g$  negatively by  $6Dq$ , depicted in fig. 3.17.

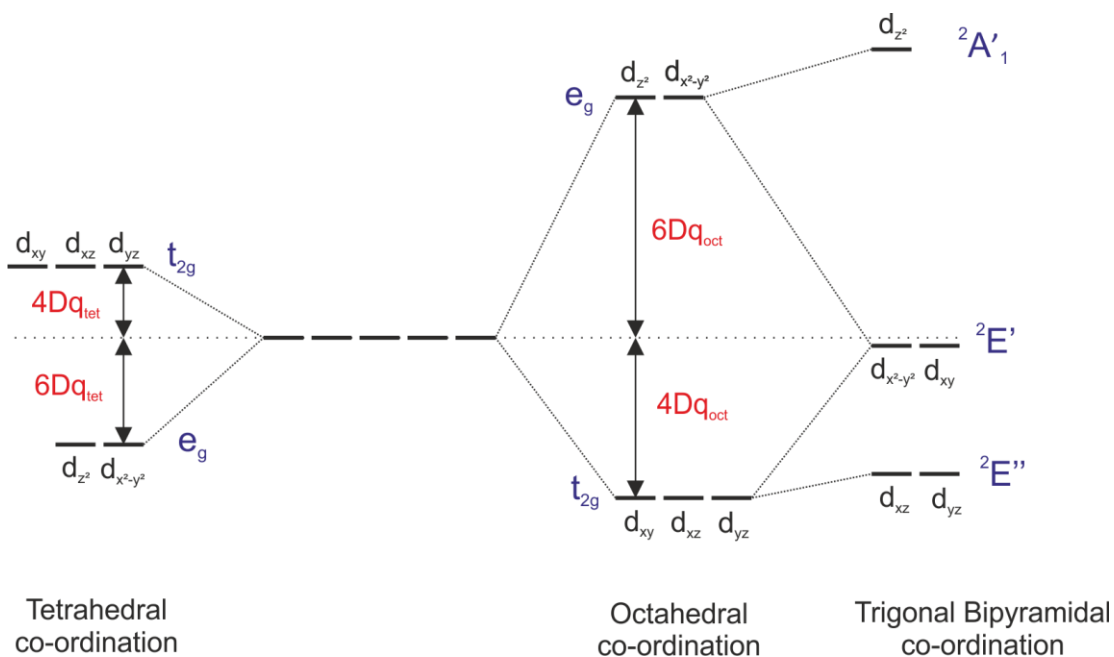


Figure. 3.17. The d orbitals in an Octahedral, Tetrahedral and Trigonal Bipyramidal crystal field.

The final co-ordination to consider for a hexaferrite structure is a trigonal bipyramidal co-ordination. This consists of five ligands, three of which are equally spaced in the xy plane of the cation, with one above and one below. This arrangement can be considered as a distortion of an

octahedral arrangement. Consequently, a further splitting occurs to the  $e_g$  and  $t_{2g}$  states, resulting in two doublets  ${}^2E''(d_{zx}, d_{yz})$  and  ${}^2E'(d_{x^2-y^2}, d_{xy})$  plus a singlet  ${}^2A'_1(d_{z^2})$  [174]. It is seen from fig. 3.17, that the singlet has the highest energy and the  ${}^2E''$  doublet has the lowest energy. The splitting for the trigonal bipyramidal crystal field can be characterised by the introduction of two new crystal field parameters  $D\tau$  and  $D\sigma$ . The  ${}^2A'_1$  has an energy of  $2D\sigma + 6D\tau$ , the  ${}^2E'$  doublet an energy of  $-2D\sigma + D\tau$  and the  ${}^2E''$  doublet an energy of  $D\sigma - 4D\tau$  [174]. For a trigonal bipyramidal arrangement,  $|D\tau|$  is known to be larger than  $|D\sigma|$ , with both parameters defined in eqns. 3.27 and 3.28 [175].

$$D\sigma = \frac{e}{14} \left[ \frac{4q}{R_c^3} - \frac{3q}{R_a^3} \right] \overline{r^2} \quad \text{Eqn. 3.27.}$$

$$D\tau = \frac{e}{168} \left[ \frac{16q}{R_c^5} + \frac{9q}{R_a^5} \right] \overline{r^4} \quad \text{Eqn. 3.28.}$$

Here  $q$  is the ligands charge,  $R_a$  is the distance to the three ligand ions in the  $xy$ -plane and  $R_c$  the distance to the two ligands along the  $z$ -axis.

As well as the co-ordination, the oxidation state of the cation also has an effect of the degree of splitting of the  $d$  orbitals. Typically, the higher the oxidation state the larger the splitting, with  $V^{3+}$  having a larger splitting than  $V^{2+}$ . This is as the difference in charge density allows the ligands to be closer to a  $V^{3+}$  than a  $V^{2+}$ , resulting in a stronger crystal field and therefore larger splitting off the orbitals [170]. Additionally, in complexes with a strong crystal field splitting it can be unfavourable for the electrons to occupy the higher energy orbitals. Therefore, in this case, the lower energy orbitals fill completely before the upper sets become occupied. Instances where this ordering occurs are called low spin states and do not follow Hund's rules. Alternatively, for ligands, which only cause a weak splitting of the  $d$  orbitals, it remains energetically favourable to fill the orbitals according to Hund's rules. This is known as high spin splitting. Whether the crystal field cause high spin or low spin splitting has a large effect on the cations magnetic properties, due to the change in  $d$ -shell configuration [176].

As has been shown, the crystal field produced due to different co-ordinations, result in differences in the splitting of the  $d$  orbitals. Additionally, the valence of the cation also affects the extent of this splitting. Hence, differences will be observed in the XAS spectra due to the changes in the electronic transitions as the  $d$  orbitals are shifted.

### 3.4.3 X-ray Magnetic Circular Dichroism (XMCD)

The effect of X-ray Magnetic Circular Dichroism (XMCD) was predicted in 1985 and was first observed just one year later [177]. A sum rule was derived in 1992 that related the integrated intensity of the XMCD spectrum over the x-ray absorption edge to the ground state orbital magnetic moment [178]. This has helped turn XMCD into a powerful technique for the determination of spin and orbital magnetic moments. It can provide insight into the element specific microscopic origins of a material's bulk magnetic properties. Such properties include magnetic hysteresis, coercivity, magnetostriction and the easy direction of magnetisation [167]. XMCD is the difference spectrum of two XAS taken in a magnetic field, one spectrum measured with right circular polarised (RCP) x-rays and the other with left circular polarised (LCP). The effect arises from the excitation of core electrons into the unoccupied conduction states [179]. As stated previously for the  $L_2$  and  $L_3$  edges, the electrons are most notably excited to the  $3d$  states. Thus, for magnetic transition metal ions such as Fe, with partially filled  $3d$  orbitals, a difference is seen between the two spectra due to the spin-up spin-down hole imbalance.

As depicted by fig. 3.18(a), the  $d$  shell of the ion being measured is initially partially filled up to the fermi level. For a magnetic material the  $d$  shell has a spin moment, which is given by the imbalance of spin-up and spin-down electrons (or holes). To measure the difference in the number of  $d$  holes

with up and down spin, the x-ray absorption process is made spin dependent by using circular polarised x-rays. RCP photons transfer the opposite momentum to the electron as left circular LCP photons, and hence photoelectrons with opposite spins are created in the two cases. Since the  $p_{3/2}$  ( $L_3$ ) and  $p_{1/2}$  ( $L_2$ ) levels have opposite spin-orbit coupling, the spin polarization will be opposite at the two edges. As spin flips are forbidden in electric dipole transitions, spin-up photoelectrons from the p core shell can only be excited into spin-up d hole states. With the same being true for the spin-down electrons. Thus, the absorption cross-section for a given polarisation is proportional to the number of empty d-states of the given spin [179].

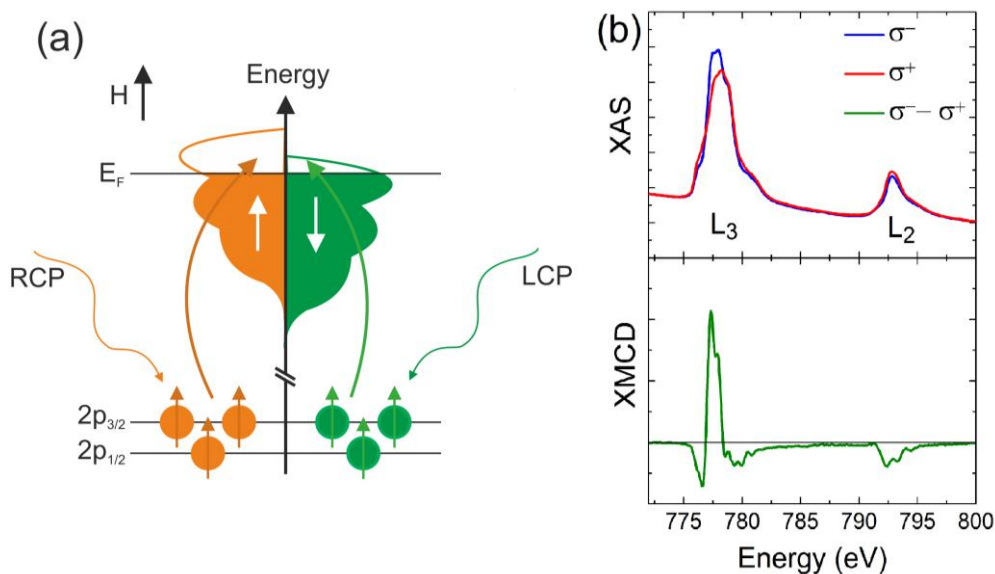


Figure. 3.18. (a) Schematic diagram representing the process of XMCD. (b) XAS of a  $\text{SrCo}_2\text{Ti}_2\text{Fe}_8\text{O}_{19}$  thin film at the Co  $L_{2,3}$  for RCP ( $\sigma^+$ ) and LCP ( $\sigma^-$ ) x-rays, together with the difference spectrum: the XMCD.

If a magnetic field is applied in the positive direction, this aligns the valence electron spins along the same direction and hence leaving more hole states in the negative direction. Thus, the x-ray absorption becomes sensitive to the magnetic polarisation of the atoms, which offers a method for element specific magnetometry [179]. Essentially, the hole density of states is split when the sample is magnetised. Because of the density of states difference between spin-up and spin-down holes in the 3d band, the absorption of LCP and RCP x-rays will be different, as depicted in fig. 3.18. Additionally, as is the case for all XAS spectra, the XMCD is sensitive to the co-ordinations of the cations involved, with the effects of the crystal field splitting the d orbitals in energy, resulting in changes to the x-ray absorption. As such, the XMCD can be simulated and fitted using atomic multiplet calculations, providing insight in to the magnetic contributions of cations in different sites, to the overall magnetic properties of the material. This technique is especially useful in ferrimagnets, such as hexaferrites, where the different magnetic cation sites can be distinguished using their opposite magnetic alignments [167].

For consistency, XMCD is defined as LCP-RCP for a positively defined magnetic field and thus, if there are more spin-up than spin-down holes available, the XMCD spectrum has a net positive  $L_3$  and negative  $L_2$  peak, as is the case in fig. 3.18(b). For the  $L_3$  ( $l+s$ ) transition ( $2p_{3/2} \rightarrow 3d$ ) RCP x-rays are more likely to excite spin-down electrons than spin-up and for the  $L_2$  ( $l-s$ ) transition ( $2p_{1/2} \rightarrow 3d$ ), the spin-orbit coupling is opposite, so the excitations spin sensitivity is opposite. In a more sophisticated picture, the polarization dependent selection rules give rise to a multiplet structure, which can serve as a fingerprint for the ground state electronic and magnetic structure [179].

The dependence of the XMCD signal on the strength and direction of the applied magnetic field can enable element specific hysteresis measurements. Element-specific hysteresis can be recorded by measuring the magnitude of the XMCD, at a specific energy, whilst sweeping the applied magnetic

field. These measurements are important for the understanding of composite magnetic structures and their magnetic interactions [167]. As well as in the case of cobalt doped hexaferrites can allow insight into the contributions of the Fe and Co to the overall magnetic properties.

### 3.4.4 Experimental setup

The x-ray energies required to cover the transition metal L-edges are in the soft x-ray range of the spectrum, 100 eV – 5 keV [179]. As such, an intense, tuneable x-ray source is required, meaning XMCD is a synchrotron based technique performed using a specialised experimental setup for x-ray magnetic spectroscopy. As such, the XMCD measurements performed in this work were carried out on the I06 magnetic spectroscopy beamline at the Diamond Light Source synchrotron facility.

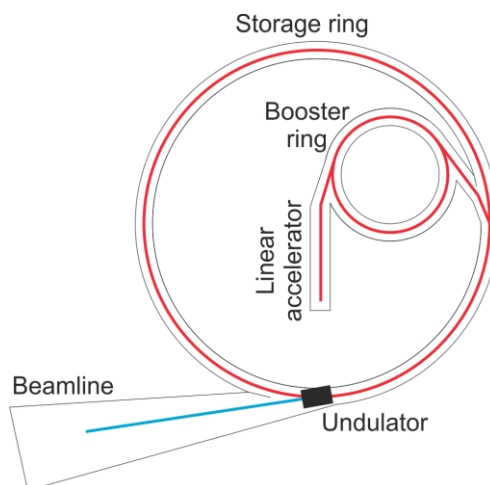


Figure. 3.19. Simplified schematic representation of the Diamond Light source synchrotron.

A simplified diagram of the synchrotron set up is shown in fig. 3.19. Within the synchrotron high-energy electrons are accelerated first by a linear accelerator and then, on a circular trajectory through the use of bending magnets, in the booster synchrotron up to an energy of 3 GeV [180]. Having been accelerated, the electron beam is maintained and circulated through a storage ring, 562 m in circumference [180], within the facility. To maintain electrons lost in the storage ring, the beam is topped up every 10 minutes. As the electron beam passes the front end of the I06 beamline, insertion devices, known as undulators, cause the electron beam to undulate resulting in the synchrotron radiation [179].

The I06 beamline uses APPLE-II undulators, to produce x-rays in the energy range 106-1300 eV. These undulators consist of a periodic array of dipole magnets, which create a static magnetic field alternating along their length. A representation of the magnetic arrays in the undulator, and their effect on the electrons, is shown in fig. 3.20.

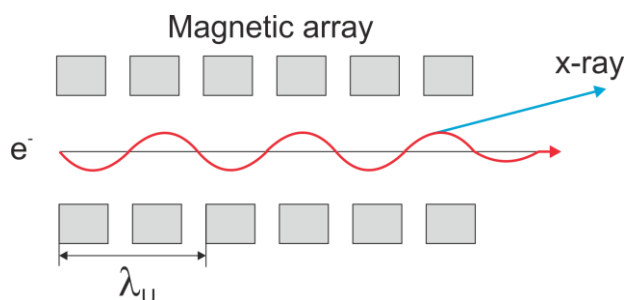


Figure. 3.20. Schematic representation of an electrons path through an undulator array and the emission of synchrotron radiation.

Electrons passing through the array are forced to oscillate resulting in the radiation of energy. This radiation is concentrated at a set of discrete energies, or harmonics, which are dependent on the periodic length of the magnetic array ( $\lambda_U$ ). By changing the magnetic field strength of the undulator

the wavelength of the emitted x-rays ( $\lambda$ ) can be tuned. This is governed by the undulator equation, eqn. 3.29 [181].

$$\lambda = \frac{\lambda_U}{2\gamma^2} \left( 1 + \frac{k^2}{2} + \gamma^2 \theta^2 \right) \quad \text{Eqn. 3.29.}$$

where  $\gamma$  is the Lorentz factor,  $\theta$  is the deflection angle, and  $k$  is the magnetic deflection parameter, given by  $eB_0\lambda_U/2\pi m_e c$ . Here,  $e$  and  $m_e$  are the electron charge and mass, respectively, and  $B_0$  is the field applied by the undulator [181]. The APPLE-II undulator is an elliptical polarisation type undulator, consisting of four magnetic arrays. The manipulation of these four arrays allows the polarisation of the emitted x-rays to be controlled by manipulating their relative positions [179]. The polarised x-rays produced by the undulator travel down the beamline towards the experimental end station. As soft x-ray wavelengths are absorbed easily in air [179], the beamline is entirely under UHV conditions. The x-ray beam is passed through several apertures and grazing incidence mirrors before being monochromatised by diffraction gratings. The beam is then focused onto the sample in the experimental chamber by a toroidal mirror to a spot size of  $20 \mu\text{m}$  by  $200 \mu\text{m}$ . A schematic representation of the experimental setup is shown in fig. 3.21.

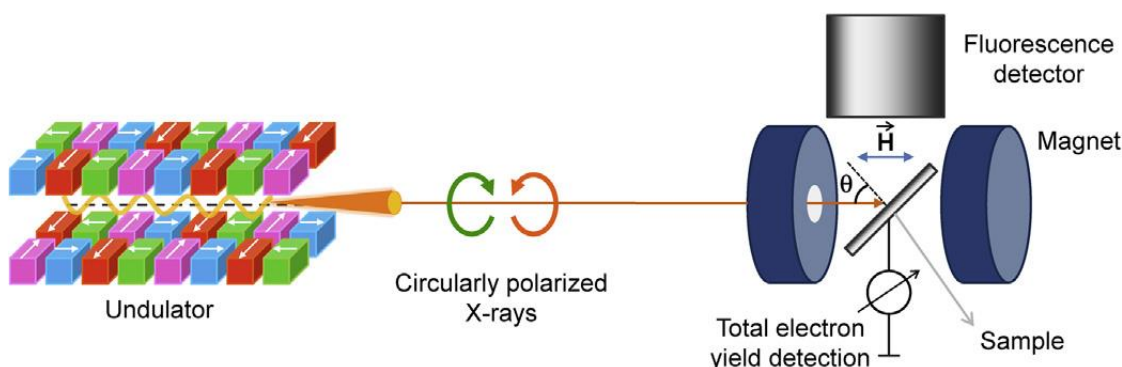


Figure. 3.21. Simplified schematic representation of the experimental XMCD setup [179].

The sample is placed in a 6 T vector superconducting magnet. The split coil design of the magnet allows the x-ray beam to pass through the centre of the magnet. This provides a magnetic field, which can be increased up to 6 T along the x-ray beam direction and anywhere in a sphere of 2 T radius. A cryostat also allows a 1.6 K to 400 K sample temperature range.

There are several methods that can be used for the detection of x-ray absorption. The decay of the core holes created results in an avalanche of electrons, with photons and ions being emitted from the sample surface [179]. The detection of any of these processes or emitted particles can be used to measure x-ray absorption. Typically, the electrons decay to the core holes, created due to x-ray absorption, with the energy difference emitted in two ways. Either the emission of Auger electrons or the emission of photons [182]. A representation of these decay processes is shown in fig. 3.22.

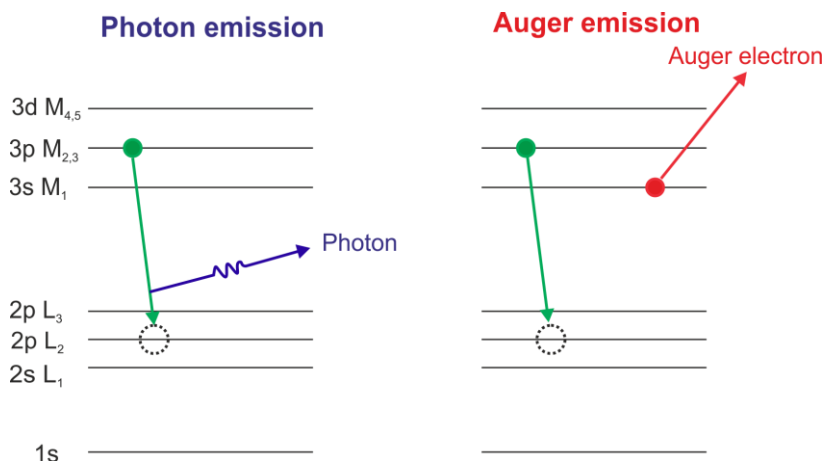


Figure. 3.22. Representation of the processes of photon and Auger electron emission.

For photon emission, as electrons decay photons are emitted with energies corresponding to the electron transitions. These photons are detected and measured as the Fluorescence Yield (FY). Alternatively, the extra energy resulting from an inward electron transition may be used to reorganise the electron distribution within the atom resulting in the emission of an Auger electron from the outer shell [182]. Total Electron Yield (TEY) detection measures the total number of electrons emitted from the sample, including Auger, secondary and photoelectrons, where the secondary electrons are the electrons emitted due to interactions of the atoms with any of the initial x-ray absorption products, such as the primary Auger electrons, photoelectrons or emitted photons. As such the number of emitted electrons is proportional to the number of core holes created by the incident x-rays absorbed by the sample [179]. Therefore TEY is proportional to the absorption coefficient. Transmission detection, which detects the intensity of the x-rays transmitted through the sample, is the only detection method from which the absolute absorption cross-section can be determined. However, due to the short absorption depths of soft x-rays, samples are required to be very thin for transmission detection [179]. Hence, transmission measurements have not been performed for the samples considered here in.

Both FY and TEY detection have been used in this work to measure x-ray absorption. FY and TEY were recorded simultaneously for each measurement taken. The data analysed and fitted was the TEY due to self-absorption effects in the FY signal, however, it was always checked that the fluorescence data agreed with the results of the TEY. TEY is measured by measuring the drain current flowing from ground to the sample to compensate the electron emission current. The TEY current ( $I_{TEY}$ ) is related to the x-ray absorption ( $\mu$ ) by eqn. 3.30 [179].

$$I_{TEY} = \frac{X\mu(\omega)L}{\mu(\omega)L + \cos \beta} \quad \text{Eqn. 3.30.}$$

where  $X$  is a constant factor,  $\beta$  is the x-ray incidence angle and  $L$  is the electron escape depth, which is typically of the order of 3-5 nm [179]. Hence, the TEY measurements are surface sensitive.

As the TEY signal is proportional to the absorption coefficient, sum rules can be applied. The FY however, unlike the TEY, is not proportional to the absorption coefficient and hence sum rules analysis cannot be performed using the FY signal [179]. As such in this work any sum rules analysis performed has been done so on the TEY data. As the FY probes deeper than the TEY [179], it is used as a check that the TEY is a true representation of the bulk of the thin film samples. As mentioned previously self-absorption is an issue with FY detection due to the emitted photons being re-absorbed before exiting the sample. Hence, due to this and the resulting emissions of secondary electrons, in the soft x-ray region, for the L-edges TEY is the dominant detection method [179].

The hexaferrite samples studied were fixed to the sample holder by copper clamping plates, which also acted to ground the samples. Each time a new sample was inserted to the experimental chamber to be measured, the x-ray beam was repositioned onto the centre of the sample by adjusting the beamline mirrors. The sample height was scanned while the x-ray energy was fixed on the iron  $L_3$  peak, to find the sample position relative to the beam and then the sample height adjusted to centre the beam on the sample.

For each sample investigated, measurements were taken at a grazing x-ray incidence angle of  $65^\circ$ , at a number of different temperatures between 1.6 K and 300 K. All XMCD measurements being performed with a positive saturating magnetic field of 6T and the x-ray polarisation was changed between RCP and LCP through the use of the undulators. XAS measurements were performed at the titanium, cobalt and iron L-edges over the ranges 445-490 eV, 770-810 eV and 695-745 eV, respectively. Oxygen K-edge XAS spectra were also measured over the range 520-565 eV. At the Ti and O edges only XAS measurements were taken for a fixed polarisation. However, for the magnetic Co and Fe XMCD, measurements were acquired by measuring both RCP and LCP XAS spectra. To remove the effect of drift in the measurements, four spectra were measured consecutively; the

first RCP followed by two LCP then a final RCP measurement. These measurements were repeated at each edge until consistent, repeatable spectra were obtained. To analyse the spectra, each data set was interpolated to produce 800 data points over the given energy range. The RCP spectra, taken at a given temperature, could then be averaged, as could the LCP spectra. These averaged spectra were normalised to the first data point taken. The XMCD could then be calculated.

As well as performing the element specific XAS and XMCD measurements for the magnetic elements within each sample, element specific hysteresis loops were obtained providing further insight into the role of each magnetic element. The element specific hysteresis was performed by measuring the XMCD on the  $L_3$ -edge, relative to a pre-edge position, as a function of the applied magnetic field, by FY detection, as the ramping magnetic field is known to affect the TEY signal. The magnetic field was swept from positive saturation to negative and then back again, with a step size appropriate for the coercivity measured in each individual case.

### 3.4.5 Atomic Multiplet Fitting

The titanium XAS and cobalt and iron XMCD, once normalised and interpolated, were fitted using simulated spectra. This has allowed the co-ordinations, valences and crystal field energies of the specific elements within the samples to be determined, thus, giving insight into the substitution sites of the co and Ti dopants. The simulated spectra were generated based on crystal field effects and atomic multiplet theory, discussed in section 3.4.2, using the CTM4XAS software [183].

The CTM4XAS software code incorporates a combination of atomic multiplet theory and crystal field theory to simulate XAS and XMCD spectra for transition metal ions [183]. The programme simulates the spectra based on several input parameters. The parameters were chosen to simulate spectra of the correct valence and co-ordination with the co-ordination being controlled by the selection of the symmetry and crystal field parameters,  $10Dq$ ,  $D\sigma$  and  $D\tau$ . Other input parameters were the Slater integral reduction parameters,  $Fdd$ ,  $Fpd$  and  $Gpd$ , which describe the two electron integrals defined by Cowan [184], with a parameter value ranging between 0 and 1, where a factor of 1 uses atomic values, which are 80% of the Hartree-Fock values [183]. The peaks in the simulated spectra can be broadened through a combination of Gaussian and Lorentzian broadening. The broadening was adjusted, using trial and error, to best match the broadness of the peaks in the experimental data. For experimental spectra containing contributions from several different co-ordinations and or valences, the simulated spectra were combined and the relative contribution of each adjusted to fit experiment, providing a relative proportion of each valence and co-ordination present for each element.

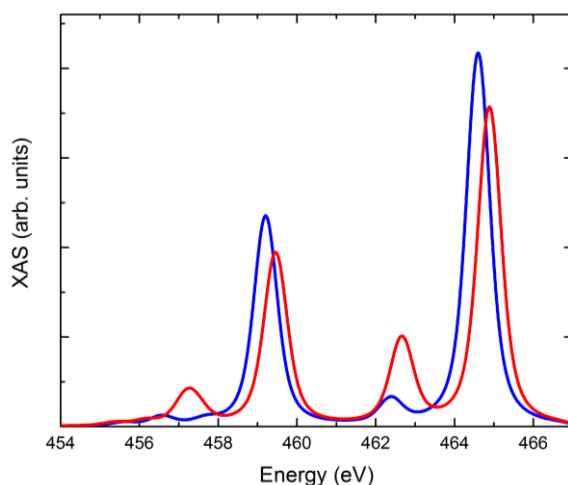


Figure. 3.23. Simulated  $Ti^{4+}$  XAS spectra. For an octahedral co-ordination with a  $10Dq = 1.9$  eV (red). For a tetrahedral co-ordination with a  $10Dq = -0.9$  eV (blue).

As an example of the simulated spectra, fig. 3.23 compares the octahedral and tetrahedral XAS spectra for  $\text{Ti}^{4+}$ . The octahedral spectrum is simulated with a  $10Dq$  of 1.9 eV and the tetrahedral a  $10Dq$  of -0.9 eV. These values are consistent with crystal field theory, which states that the d-orbital splitting due to a tetrahedral surrounding is  $-4/9$  of the octahedral splitting [176]. Both spectra are simulated with Slater integral reduction parameters of 1.0. In octahedral symmetry, the crystal field splits the degenerate 3d orbitals into an  $e_g$  and a  $t_{2g}$  configuration, where the  $t_{2g}$  consists of the  $d_{xy}$ ,  $d_{xz}$ , and  $d_{yz}$  orbitals and the  $e_g$  configuration, the higher energy  $d_{z^2}$  and  $d_{x^2-y^2}$  orbitals [176]. Thus, two peaks are expected for each spin orbit split initial state ( $2p^{3/2}$ ,  $2p^{1/2}$ ). In the tetrahedral case, the orbitals are split into the same triplet and doublet but the triplet now has the higher energy and the splitting is reduced [176].

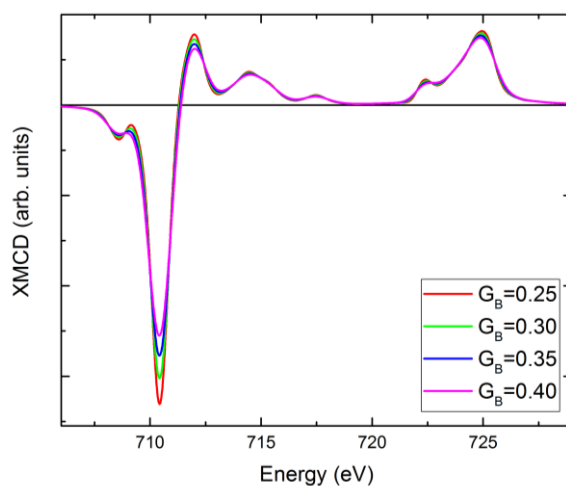


Figure. 3.24. Simulated  $\text{Fe}^{3+}$  XMCD spectra. For an octahedral co-ordination with a  $10Dq = 1.1$  eV. Plotted for several different Gaussian-broadening parameters ( $G_B$ ).

For all spectra the Slater parameters and broadening of the peaks adjusted to best fit the experimental data. The effect of adjusting the broadening parameters can be seen in fig.3.24, where the octahedrally co-ordinated  $\text{Fe}^{3+}$  XMCD is plotted as a function of the Gaussian broadening parameter ( $G_B$ ), for a fixed Lorentzian broadening of 0.25. It is seen that increasing the broadening of the spectra decreases the magnitude of the XMCD peaks, whilst broadening the spectral line. To simulate the trigonal bipyramidal site the  $S_6$  symmetry was used with  $10Dq = 0.8$  eV,  $D\tau = 0.08$  eV and  $D\sigma = 0.01$  eV. None zero  $D\tau$  and  $D\sigma$  values result in a further splitting of the d orbitals. For these values of the crystal field parameters, used for the trigonal bipyramidal, the five d-orbitals break up into two doublets  ${}^2E''(d_{zx}, d_{yz})$  and  ${}^2E'(d_{x^2-y^2}, d_{xy})$  plus a singlet  ${}^2A'_1(d_{z^2})$  with  ${}^2A'_1 > {}^2E' > {}^2E''$  as expected for this co-ordination [176].

Before settling on the crystal field parameters used for the trigonal bipyramidal site, the effects of varying the  $10Dq$ ,  $D\tau$  and  $D\sigma$  values were investigated. As shown in fig. 3.25, simulated XMCD data was produced over a range of  $10Dq$  for fixed  $D\tau$  and  $D\sigma$ , a range of  $D\tau$  with fixed  $10Dq$  and  $D\sigma$  as well as over a range of  $D\sigma$  values. Comparing the simulations, it is apparent that the  $10q$  value has a large effect on the spectral lineshape, as does  $D\tau$ . The effect of the  $D\sigma$  value has less significance in terms of the XMCD lineshape. In fig. 3.25(a), it is evident that for increased  $10Dq$ , the main XMCD peaks reduce in magnitude and the initial  $L_3$  peak, at 777 eV, becomes increasingly positive.

For both the Fe and Co simulated spectra of both 2+ and 3+ valences were considered for all three co-ordinations possible and a combination of spectra used to best fit the experimental data. Whilst primarily fitting to the XMCD of the Co and Fe, comparisons were also made between the simulated and experimental XAS spectra. The fitted XMCD spectra for each sample could then be used to determine the valence and co-ordination of the elements responsible for the magnetic contributions within the sample. Where fitting of the Ti XAS shows the valence and co-ordination of the substituted Ti ions within the hexaferrite structure. Hence, the fitting of the XAS and XMCD

with atomic multiplet calculations have been used to provide insight into the role of the Co and Ti substitutions within the magnetoelectric Co-Ti doped strontium ferrite.

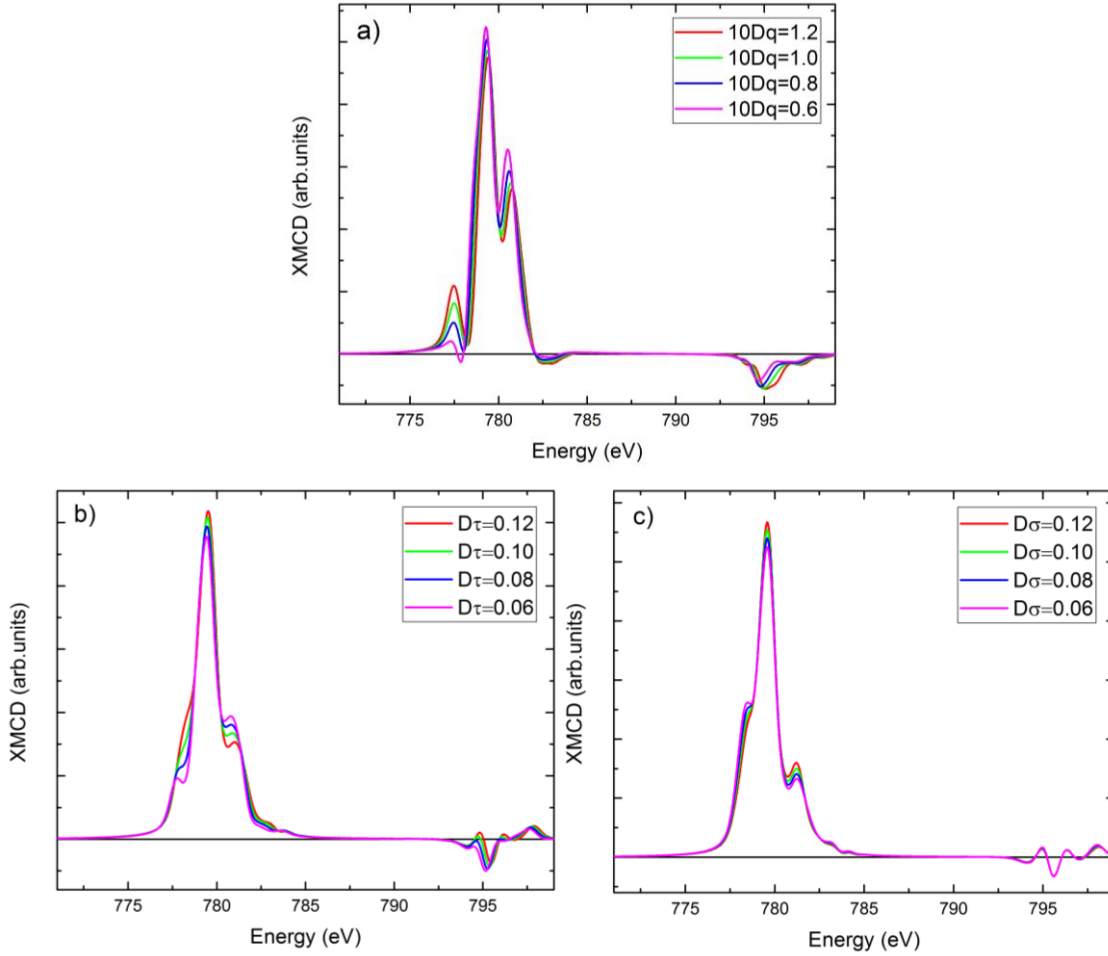


Figure. 3.25. Simulated trigonal bipyramidal  $\text{Co}^{2+}$  XMCD spectra (a) as a function of  $10Dq$  for  $D\sigma = D\tau = 0.0$  eV, (b) as a function of  $D\tau$  for  $10Dq = 0.8$  eV and  $D\sigma = 0.06$  eV and (c) as a function of  $D\sigma$  for  $10Dq = 0.8$  eV and  $D\tau = 0.15$  eV.

### 3.4.6 XMCD Sum Rules analysis

As the x-rays only interact with the orbital and not the spin part of the electrons wavefunction, XMCD can be used to distinguish between the spin and orbital part of the magnetic moment [167]. In the early 1990's, a set of sum rules were derived relating the integrated XMCD spectrum to the ground state spin and orbital momentums. Sum rules provide a method for obtaining ground state properties; hence, the discovery of these sum rules has transformed XMCD into a powerful standard technique. In 1992, Thole *et al* [178] derived the sum rule which relates the integrated XMCD signal to the ground state expectation value of the orbital magnetic moment,  $\langle L_z \rangle$ . Subsequently, Carra *et al* [185] derived a second XMCD sum rule, which relates the XMCD branching ratio to the spin magnetic moment,  $\langle S_z \rangle$ , and the magnetic dipole term,  $\langle T_z \rangle$ , in the ground state. The derivations of the sum rules can be found in [178] [185] and a more detailed description has been provided by van der Laan and Figueroa [179]. For the  $L_2$  and  $L_3$  edges of d-metals, the sum rules are defined in eqns. 3.31 and 3.32. These relate the integrated intensities of the two edges to the ground state expectation values.

$$\frac{\rho_{L_3}^1 + \rho_{L_2}^1}{\rho_{L_3}^0 + \rho_{L_2}^0} = \frac{\langle L_z \rangle}{2n_h} \quad \text{Eqn. 3.31.}$$

$$\frac{\rho_{L_3}^1 - 2\rho_{L_2}^1}{\rho_{L_3}^0 + \rho_{L_2}^0} = \frac{2\langle S_{z,eff} \rangle}{3n_h} = \frac{2\langle S_z \rangle}{3n_h} + \frac{7\langle T_z \rangle}{3n_h} \quad \text{Eqn. 3.32.}$$

where  $\rho^0$  and  $\rho^1$  are the integrated intensities of the isotropic XAS and the XMCD, respectively, over the  $L_3$  and  $L_2$  edges [179] and the isotropic XAS is defined as the sum of both the RCP and LCP spectra. The number of holes,  $n_h$ , is often unknown but can be estimated for example using band structure calculations. However,  $n_h$  is cancelled out when considering the ratio of the orbital to spin moment, as given by eqn. 3.33 [179].

$$\frac{\langle L_z \rangle}{\langle S_{z,eff} \rangle} = \frac{4}{3} \frac{\rho_{L_3}^1 + \rho_{L_2}^1}{\rho_{L_3}^1 - 2\rho_{L_2}^1} \quad \text{Eqn. 3.33.}$$

For the simplification of the sum rules analysis, Chen et al [186] introduced an alternative notation in terms of the orbital and spin magnetic moments  $m_L$  and  $m_{S_{eff}}$ , by which;  $m_L = -\langle L_z \rangle$  and  $m_{S_{eff}} = -2\langle S_{z,eff} \rangle$ . They also define the parameters  $p = \rho_{L_3}^1$ ,  $q = \rho_{L_3}^1 + \rho_{L_2}^1$  and  $r = 2/3\rho^0$ . This then allows the sum rules to be written as follows;

$$m_L = -\frac{4}{3} \frac{q}{r} n_h \quad \text{Eqn. 3.34.}$$

$$m_{S_{eff}} = -\frac{6p-4q}{r} n_h \quad \text{Eqn. 3.35.}$$

$$\frac{m_L}{m_{S_{eff}}} = \frac{1}{(9/2)(p/q)-3} \quad \text{Eqn. 3.36.}$$

Given that the number of holes is often unknown, eqn. 3.36 is most commonly applied. This equation enables the orbital to spin magnetic moment ratio to be determined from the branching ratio of the XMCD,  $p/q$ . An example of an integrated XMCD spectrum can be seen in fig. 3.26, in which the parameters  $p$  and  $q$  are illustrated. Thus, by extracting  $p$  and  $q$  from the XMCD integral the orbital to spin moment ratio of the metal ion within the sample can be determined.

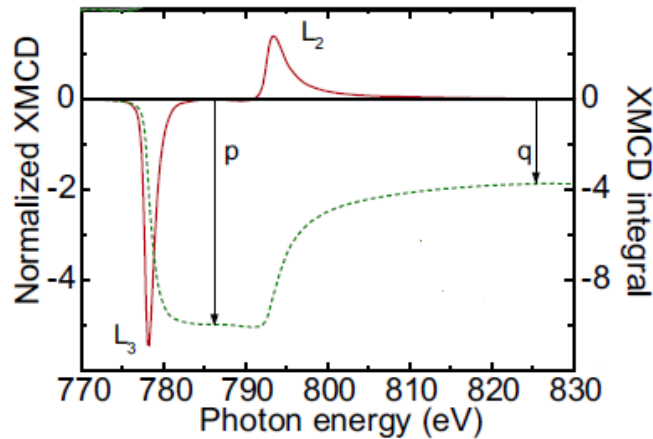


Figure. 3.26. Normalised XMCD (red) and integrated XMCD (green) spectra for the Co  $L_{2,3}$  edges, with the quantities  $p$  and  $q$  illustrated [179].

The magnetic moment of an ion has contributions from both the spin and orbital angular momentum. Non-spherical environments can lead to a quenching of the contribution from the orbital moment [43]. This manifests itself as a reduction in  $q$ , which as can be seen from eqn. 3.34 is directly proportional to  $m_L$ . However, the spin magnetic moment is dependent on both  $p$  and  $q$  so survives in all cases. The spin moment is related to the number of unpaired electrons in the ion, thus, is sensitive to the oxidation state. The orbital to spin magnetic moment ratio determined through XMCD sum rules analysis can then be used to gain insight into the magnetic properties of specific elements within a sample and their environment. The ratio is also a useful value to be compared between samples as a comparison of their magnetic structure. The orbital to spin

moment ratio can also be used to determine the element specific form of the g-factor, discussed in section 3.3.2.  $g$  is given by eqn. 3.37 [187].

$$g = 2 \left( \frac{m_L}{m_{S_{eff}}} + 1 \right) \quad \text{Eqn. 3.37.}$$

Transition metals typically have g-factor values close to 2 and the values determined from the sum rules analysis can be used to compare between samples as well as to evaluate the g-factors determined through ferromagnetic resonance measurements [187].

In this work, XMCD sum rules analysis has been performed on the XMCD spectra obtained for the hexaferrite thin films studied. The orbital to spin moment ratios have been extracted by measuring the parameters  $p$  and  $q$  from the integrated XMCD spectra. To ensure consistency between samples the  $p$  and  $q$  values were all extracted at the same photon energies. For measurements taken at the iron edge, these were 715 eV and 735 eV for  $p$  and  $q$ , respectively, and at the cobalt edge 785 eV and 805 eV. The extraction of reliable  $p$  and  $q$  values relies upon the baselines of both the RCP and LCP spectra aligning with each other so it was insured that a matching set of normalised spectra were obtained before the integration was performed.

### 3.5 Converse Magnetolectric Measurements

The converse magnetolectric coupling measurements, shown in this thesis, were carried out by collaborators at Northeastern University, Boston, USA. The magnetisation of the samples was measured, using a VSM, as a function of applied electric field. The measurements were performed in a fixed magnetic field of 400 Oe, applied parallel to the applied electric field. To apply the electric field ( $E$ ) across the thin film samples, a voltage ( $V$ ) was applied across both film and substrate, by contacting both the underside of the substrate and the thin film surface, as shown in fig. 3.27.

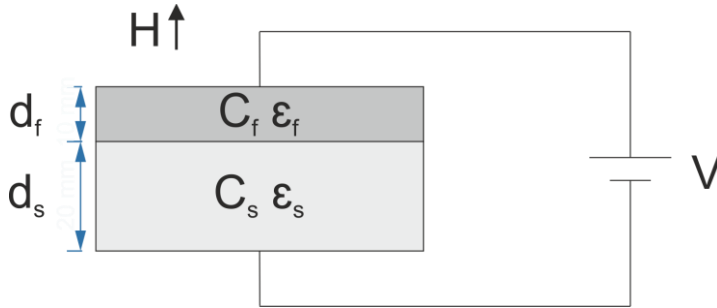


Figure. 3.27. Schematic representation of the magnetolectric measurement setup.

If the film and substrate have dielectric constants  $\epsilon_f$  and  $\epsilon_s$ , respectively, with thicknesses  $d_f$  and  $d_s$ , the film and substrate can be modelled as two capacitors in series. The capacitance of the film is  $C_f$  and the substrate  $C_s$ , then the total capacitance of the sample ( $C_{total}$ ) is given by; [188]

$$\frac{1}{C_{total}} = \frac{1}{C_s} + \frac{1}{C_f} \quad \text{Eqn. 3.38.}$$

For a given capacitor, the capacitance can be expressed as; [188]

$$C_{f,s} = \frac{\epsilon_{f,s} \epsilon_0 A}{d_{f,s}} \quad \text{Eqn. 3.39.}$$

Where  $A$  is the capacitors surface area, in this case the area of the thin film surface, and  $\epsilon_0$  is the permittivity of free space. Through the combination of equations, 3.38 and 3.39, an expression is obtained for the total capacitance.

$$C_{total} = \frac{\epsilon_0 A \epsilon_f \epsilon_s}{d_f \epsilon_s + d_s \epsilon_f} \quad \text{Eqn. 3.40.}$$

The charge stored by a capacitor (Q) is related to the capacitance such that  $Q = C_{total}V$  [188]. Consequently, the potential difference across the film ( $V_f$ ) can be expressed as;

$$V_f = \frac{Q}{C_f} = \frac{C_{total}V}{C_f} = \frac{\epsilon_s d_f V}{d_f \epsilon_s + d_s \epsilon_f} \quad \text{Eqn. 3.41.}$$

So that the electric field applied across the thin film ( $E_f$ ) is given by; [188]

$$E_f = \frac{V_f}{d_f} = \frac{\epsilon_s V}{d_f \epsilon_s + d_s \epsilon_f} \quad \text{Eqn. 3.42.}$$

Making the assumption that  $d_s \epsilon_f \gg d_f \epsilon_s$ , which is reasonable given that the substrate thickness is many times larger than the thin films, eqn. 3.42 can be simplified further.

$$E_f = \frac{\epsilon_s V}{d_s \epsilon_f} \quad \text{Eqn. 3.43.}$$

Eqn. 3.43 has then been used to calculate the electric field applied across the film for a given applied voltage, using the substrate thickness and the dielectric constants of the film and substrate that are determined from the literature.

At each electric field value, magnetisation was measured for 1-second intervals and an average value taken over 50 measurements. The absolute change in magnetisation is then plotted as a function of electric field applied to the thin film. Using eqn. 3.44 [55], the linear magnetoelectric coupling coefficient ( $\alpha$ ) was then calculated from the gradient of the M(E) relationship.

$$\alpha = \mu_0 \frac{\partial M}{\partial E} \quad \text{Eqn. 3.44.}$$

Where  $\mu_0$  is the permeability of free space.

It is worth noting, some contribution to the change in magnetisation may occur due to the heating of the samples due to the voltage being applied. It was ensured that the total change in magnetisation observed for a given sample, was not as a consequence of the heating due to the applied electric field. In each case the change in M measured was much larger than that observed in the M(T) over the given temperature range that the sample would heat up over. Thus, the changes in M due to temperature change during the measurements were deemed to be much smaller than the magnetoelectric effects and hence not significant.

### 3.6 Summary

The experimental and analytical techniques discussed and explained in this chapter will be used throughout the rest of this thesis to obtain structural, magnetic and magnetoelectric information, regarding the samples studied.

## Chapter 4: Pulsed Laser Deposition Growth System Design and Calibration

### 4.1 Introduction

One of the main aims of this work has been to develop an effective method for the growth of oxide, more specifically hexaferrite, thin films. For future practical device applications of multiferroics, thin films have numerous advantages. For example, the thinner the sample the smaller the voltage required to apply a given electric field across it. To grow high quality oxide thin film structures, a pulsed laser deposition (PLD) system has been developed and tested. PLD is well suited for the growth of hexaferrite films, as it allows for stoichiometric growth of complex unit cells. It has previously been demonstrated as a technique to produce high quality hexaferrite films allowing for cation substitution on the atomic scale due to non-equilibrium growth [133] [21] [24].

In this chapter, the design of the PLD growth system is detailed and justified. The system developed is catered towards the growth of complex oxides, such as hexaferrites, whilst remaining a versatile system, enabling the growth of a wide range of thin film materials. Briefly, the PLD system incorporates a specifically designed target manipulator, allowing for up to 6 targets, which all rotate individually and can be indexed rapidly. This allows for the growth of hexaferrite thin films with the R and S-block layers grown from separate targets. Using this ATLAD method, the composition of the targets could be controlled in such a way that dopant ions can be positioned in just one of the R or S blocks. Target ablation is achieved with a frequency quadrupled Neodymium-doped: Yttrium Aluminium Garnet (Nd:YAG) laser, pulsed at 10 Hz, and sample heating is achieved using a unique 35 W CO<sub>2</sub> laser setup. The system design also means that the samples can be grown and annealed safely in an oxygen partial pressure. This is important for the growth of oxide films in order to control the stoichiometry [19].

Following the design and construction of the PLD, the system has been tested and calibrated. Thin films have been grown as a function of time, target to substrate distance and growth partial pressure. The films grown have been characterised magnetically using VSM and structurally, using XRD and Raman spectroscopy. Calibration of the substrate heating system has also been performed, using a pyrometer to measure the substrate temperature, for a given laser power. Substrate temperatures in excess of 900°C have been achieved, showing that the substrate heating mechanism is capable of attaining the conditions required for the formation of M-type hexaferrite [21] [24] [6]. Using the substrate heating system the growth of an epitaxial magnetite thin film has also been achieved. Demonstrating that the PLD system developed is effective for the growth of high quality oxide thin films. Given this achievement, efforts were made to grow M-type hexaferrite thin films. This was ultimately achieved, as detailed in this chapter.

### 4.2 Design of the PLD growth system

#### 4.2.1 Vacuum chamber design

The first component of the PLD growth system to be designed and constructed was the main vacuum chamber. Much care and deliberation was taken over the design process to ensure that enough ports were available and appropriately placed for the mounting of all the possible instruments to be used. Schematic diagrams of the design are shown in fig. 4.2.1. Once designed, the chamber itself was constructed by an external vacuum chamber specialist, to the specifications required. The ports fig. 4.2.1 are numbered and are from here referred to by their number.

Port 6, located at the bottom of the chamber, has been specifically designed to mount the target manipulator. The centre of the port is offset from the centre of the chamber, such that the centre of the exposed target lines up with point B, as shown in fig. 4.2.1(b). Ports 2 and 3 are designed to be used for entrance points of the target ablating, Ultra-Violet (UV) laser. They are fitted with fused

silica viewports, to allow the transmission of the UV light. Both ports are centred on the PLD target located at point B, but at different inclination angles. Port 3 at an angle of  $45^\circ$  and port 2 at an angle of  $60^\circ$ . By aligning the ablating laser through one or other of the ports, the target ablation angle of incidence can be changed. For all the samples grown in this chapter port 3 was used, hence a target ablation angle of  $45^\circ$ . Ports 9 and 10 mirror ports 2 and 3 on the other side of the chamber. These two ports have been included with the intent of being used for diagnostics of the UV laser beam and or the ablated target plume.

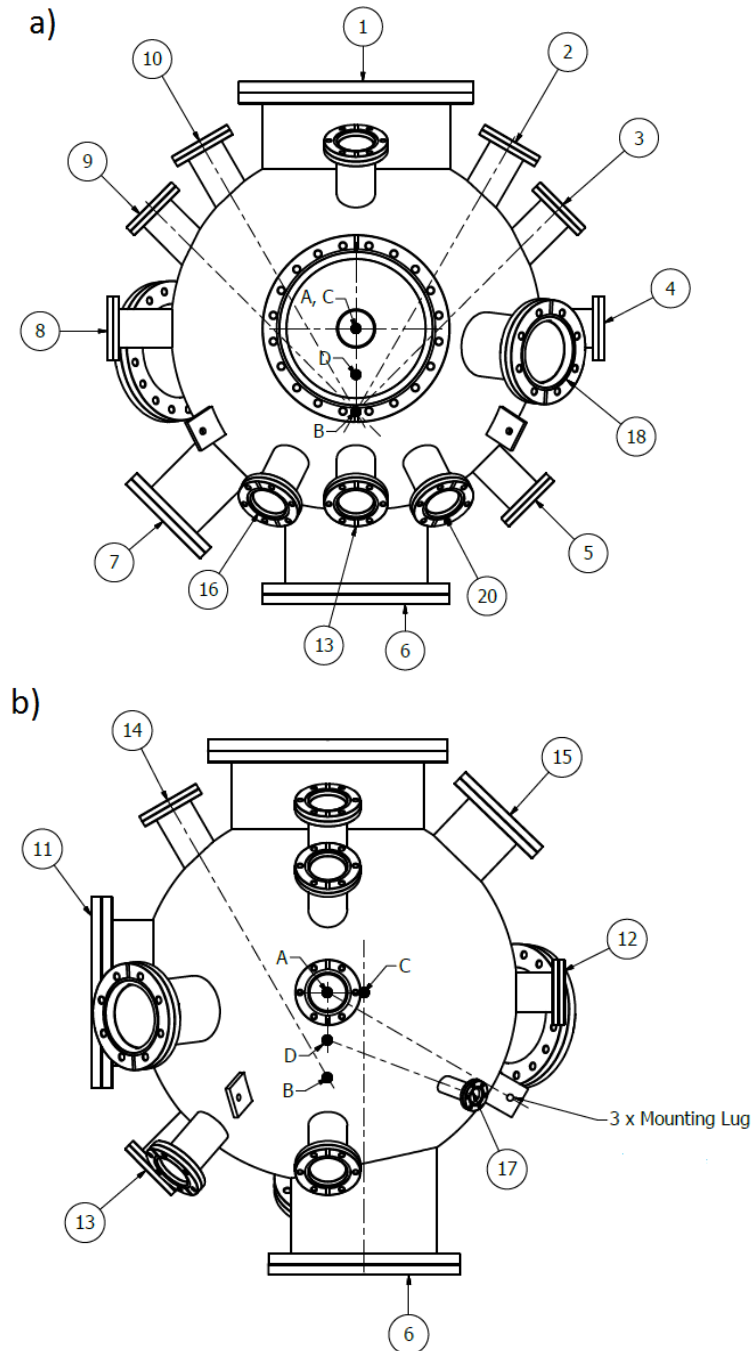


Figure 4.2.1. Schematic diagram of the PLD vacuum chamber design (a) front view, (b) side view.

The DN200CF port 1, is used to mount a specifically designed flange that enables the mounting of the sample stage and shutter. The sample stage allows the position of the sample to be centred on point A but the stage allows its height and position to be moved relative to this point. The shutter is used to mask the sample from the target plume during pre-ablation. The front and central, port 11, is designed to mount a large viewport, to view the whole of the inner chamber, making it easier for tasks such as sample transfer and the replacement of the PLD targets. The load-lock sample transfer system is extended from port 12. Through this, the sample is transferred to and from the

sample stage. Port 5 is used as the gas inlet into the chamber and port 8 is attached to the vacuum pumping system, comprising of a turbo backed by a scroll pump that can be throttled by a valve system to control the pumping rate. Port 18 and the unlabelled DN100CF port 19, are both centred on the sample position A. They are inclined at an angle of  $5^\circ$  below the chamber centre line. These ports have been designed for the future incorporation of a Reflection High-Energy Electron Diffraction (RHEED) screen and gun. RHEED will allow for the in-situ surface characterisation of the thin film during growth.

The three ports aligned along the front of the chamber, 13, 16 and 20, are centred on the sample position of point A. These three ports are designed for the attachment of E-beam evaporators with the aim of being able to deposit metal capping layers, in-situ, to the oxide thin films grown. This will be advantageous in preventing over oxidation or reduction of the films post-growth and additionally allow the samples surface to be contacted, as would be necessary for many electrical and magnetoelectric measurements. As yet, however, no evaporators have been used in the PLD growth system and port 13 has been used as a window for a pyrometer to measure sample temperature. Both ports 14 and 15 are designed to be viewports. Port 14 is centred on the target and is used to view target motion and degradation, while Port 15 is centred on the sample position to view the sample and sample stage during sample transfer.

Two different gauges, mounted on ports 4 and 17, measure the pressure of the vacuum chamber. On port 4, an ion gauge measures the pressure below  $1 \times 10^{-3}$  mbar and a pirani gauge is mounted onto port 17, measuring pressures above  $1 \times 10^{-4}$  mbar. Port 17 has also been designed to be centred on point D, which is situated in front of the sample surface position. This was done with the possibility of using this port in the future to mount a pulsed valve. Eason and his group at Southampton have used such a pulsed valve to send intense pulses of gas across the target plume and have shown that this is effective in removing unwanted particulates from the plume and hence the thin film grown [189]. This has not yet been replicated in this work but the chamber design allows for its future incorporation.

#### 4.2.2 Target Manipulator

The target manipulator was constructed by PVD products and enables the mounting of up to 6 targets that can be rapidly indexed as well as individually rastered and rotated. An image of the target manipulator is shown in fig. 4.2.2.

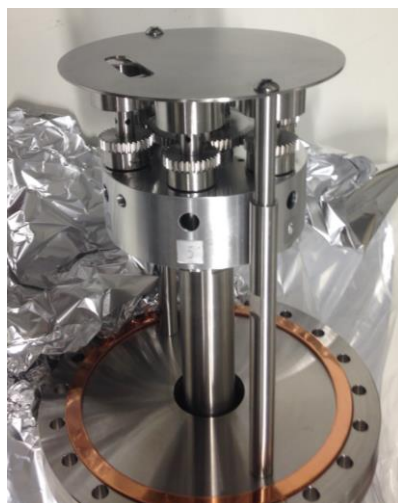


Figure 4.2.2. Image showing the 6-target manipulator used in the PLD growth system.

The target manipulator is controlled through the use of a labView based software programme. This programme was written and provided by PVD products. The targets are indexed about the carousel using this programme with the target chosen to grow from being positioned in the centre of the

slot in the protective plate, as seen in fig. 4.2.2. The UV laser pulses are incident on this target creating the growth plume. In order to prevent degradation of just one point on the target and ensure that the full target was utilised, the target was simultaneously rastered and rotated during growth. It was found that, to ablate the entire target surface, rastering the target between 300 and -300 steps from its zero position, at a rate of 200 steps per second, was optimal. Here a single step is defined as the smallest unit of movement of the target position. In addition, a target rotation speed of 17 rpm was used, as a prime number meaning that this would not synchronise with the pulse rate of the UV laser. These conditions were then used for the growth of all subsequent thin films grown with this PLD system.

The PLD targets used, for the growth of thin films in this system, were purchased from Testbourne Ltd. The targets were specified to be disc shaped, with a diameter of 25 mm and a thickness of 5 mm, in order to fit the target holders. The targets had been prepared to a purity of greater than 99.9%. It was also ensured that the density of the targets was greater than 90% of the accepted theoretical value. This was checked by measuring the mass of the targets prior to use, for their known dimensions and atomic composition. Using a high-density target has been shown to be important in reducing the size and number of particulates in the films grown [127].

#### 4.2.3 UV laser and target ablation

To ablate the PLD targets a frequency quadrupled Nd:YAG laser is used. The laser is a LPY674-10 model laser produced by Litron Lasers. The laser outputs pulses of energy, optimised in the UV region of the spectrum with a wavelength of 266 nm.

The pulses are produced with a repetition rate of 10 Hz and a pulse duration of 2 ns. The power output or energy of the laser pulses can be controlled by adjusting the Q-switch delay. This is the delay between triggering the laser flash lamp and triggering the Q-switch. The peak output of the laser was found to be 200 mJ per pulse at a Q-switch delay of 240  $\mu$ s. However, for target ablation the laser power was reduced and a pulse energy of 100 mJ was decided optimal for a controlled growth rate. This pulse energy was achieved with a Q-switch delay of 360  $\mu$ s.

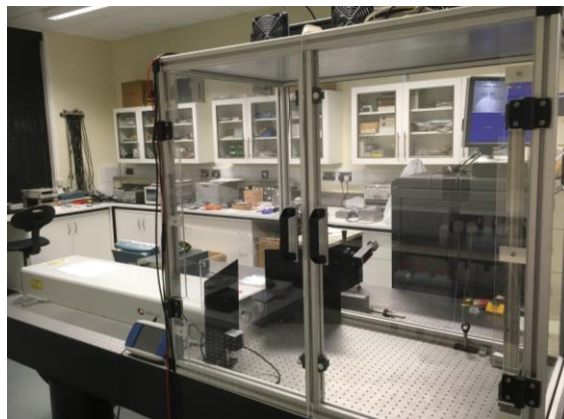


Figure 4.2.3. The Nd:YAG laser mounted on an optical bench surrounded by safety enclosure.

The laser itself is mounted on a 2.4 m by 1.2 m optical bench, as can be seen in fig. 4.2.3. The power output of the laser was measured using a gentec UP19K power-meter. Before operating the laser, it is ensured that the laser crystal is up to operating temperature and the power-meter is aligned with the beam path before opening the shutter. The laser output is then peaked up to a maximum manually. The laser then has two options for operation; one is on manual mode with constant set laser conditions. The other is to use the auto-tracking mode, in which the laser output is monitored and the laser setup adjusted to maintain a constant output power. For the two modes of operation, the laser pulse energy was measured as a function of time, to compare, as shown in fig. 4.2.4.

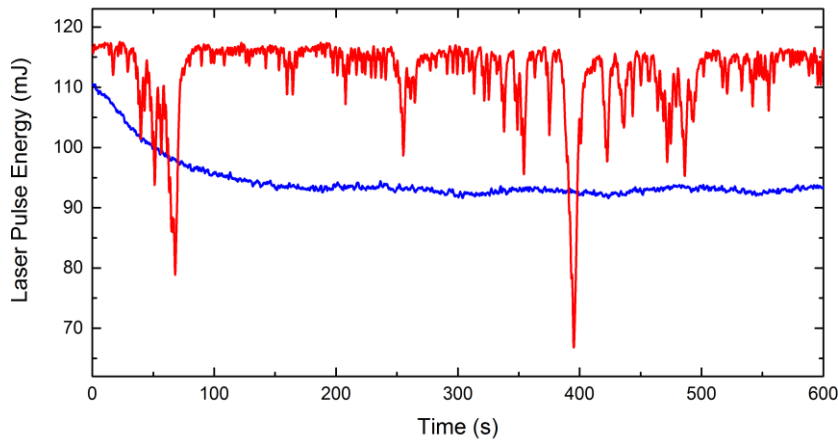


Figure 4.2.4. Graph showing the UV laser pulse energy as a function of time for a laser Q-switch delay of  $360\mu\text{s}$ , under both manual operation (blue) and tracking mode (red).

It is seen that in the auto-tracking mode the laser output is much less stable than in the manual mode. For auto-tracking the laser power repeatedly drops off before being recovered, whereas in manual operation the laser output decays initially before becoming stable after approximately 3 minutes. Given this, it was found that to produce the most stable beam output, the laser should be run on auto-track for 5 minutes before being switched to manual operation, at which point the power-meter was removed and the laser readied for target ablation. The profile of the beam produced by the laser was observed using burn paper. The beam shape was found to be approximately spherical and at a distance of 300 mm from the laser beam output has a diameter of 8 mm.

In order to direct and focus the pulsed laser beam onto the PLD target, the optical set up shown in the schematic diagram of fig. 4.2.5 was used. Two 266 nm laser line mirrors are used in a periscope system to direct the beam up and then back down through port 3 towards the PLD target. The port is fitted with a fused silica viewport to allow the transmission of the UV laser beam. The inside of this viewport is fitted with a stainless steel cone, to protect the viewport from deposition of the ablated target material.

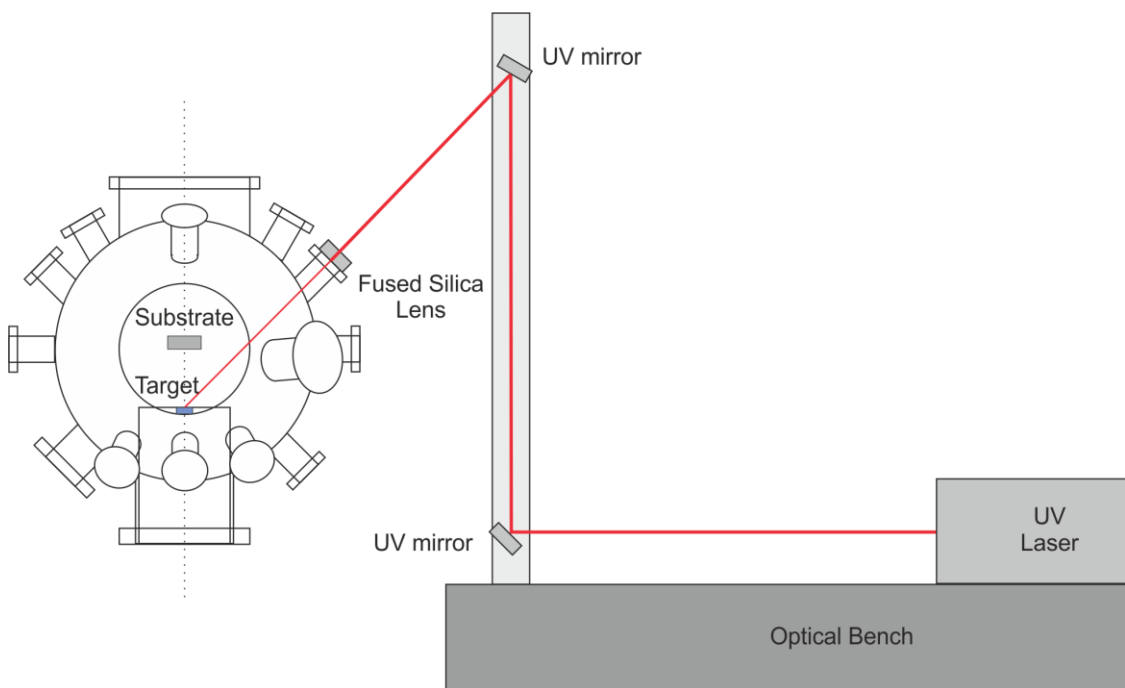


Figure 4.2.5. Schematic diagram of the UV laser optics setup. Showing the Laser beam, in red, passing through a periscope set up before being focussed onto the PLD target.

Upon reaching the viewport, the beam was found to have diverged to a diameter of 9mm. To focus the beam onto the target a plano-convex fused silica lens was positioned in front of the viewport. This lens was chosen to have a focal length of 300 mm producing a focussed beam with diameter 1 mm incident on the target. This spot size could be adjusted by adjusting the lens to target distance, allowed for by an adjustable lens mount. An image of the adjustable lens holder mounted on the fused silica viewport is displayed in fig. 4.2.6.



Figure 4.2.6. Image of the Fused Silica lens holder, mounted onto the fused silica viewport.

After the laser was aligned and the warm up procedure, discussed previously, completed, the pulsed beam was allowed to ablate the PLD target in position. The initial target used was a  $\text{Fe}_3\text{O}_4$  target. An image taken of the plume created by the ablation of this target is shown in fig. 4.2.7. This image was taken at a vacuum pressure of  $1 \times 10^{-7}$  mbar with a laser pulse energy of 100 mJ. In fig. 4.2.7, no sample is present but the sample holder can be seen in the centre of the chamber. The sample shutter is also closed, preventing the plume reaching the sample position. For the growth of a sample, the target was always pre-ablated for 1 minute with the shutter closed. The pre-ablation of the target has been shown as an effective method for the cleaning of the target and for achieving the stoichiometric removal of target material [190].

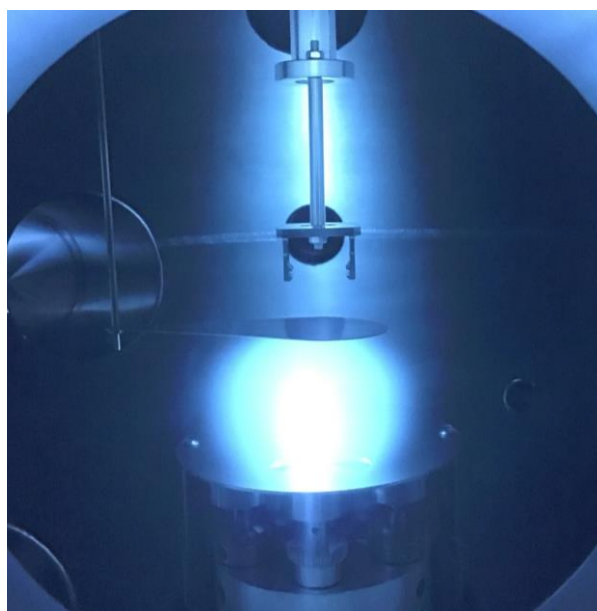


Figure 4.2.7. Image showing the plume of material created by the ablation of a  $\text{Fe}_3\text{O}_4$  target, with a pulsed laser energy of 100 mJ at 266 nm. In a vacuum pressure of  $1 \times 10^{-7}$  mbar.

The laser system is cooled through the flow of de-ionised water and, for safety and to prevent damage to the laser; several interlocks are in place, which shut the laser down if the interlocks are broken. The interlocks are on the de-ionised water level and temperature, on the laser case and shutter, as well as on several other parts of the laser system and the laboratory door. All in the laboratory also wore safety goggles during laser operation and importantly the entire laser path,

up unto the chamber is enclosed by a Perspex safety enclosure, shown in fig. 4.2.4. The enclosure has access doors to the side, which are used for the adjustment of optics and beam diagnostics.

#### 4.2.4 Sample Holder and sample stage

The design of the PLD system means that the sample must be mounted above the target in or around the centre of the vacuum chamber, with the surface of the substrate facing down towards the target. In order to heat the substrate an Infrared CO<sub>2</sub> laser system was used with the laser illuminating the back of the substrate from above. To meet these requirements the design presented in fig. 4.2.8 was implemented.

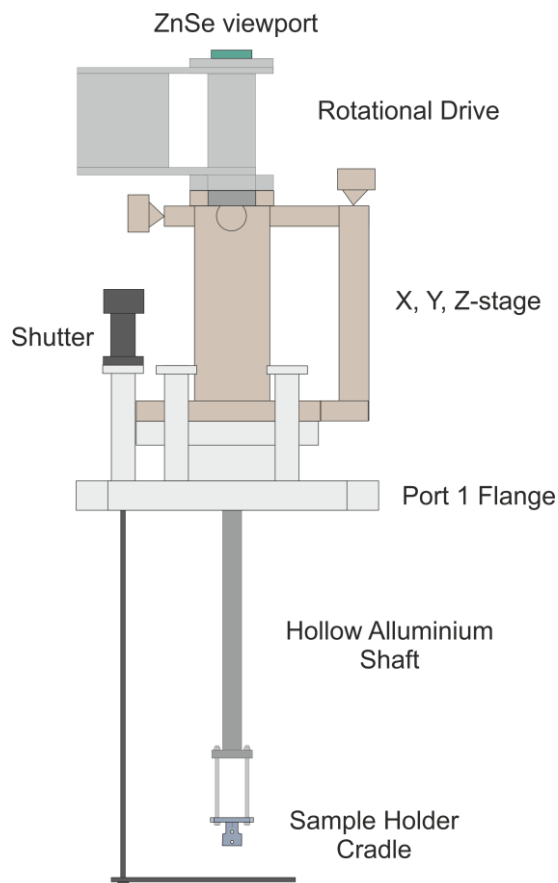


Figure 4.2.8. Schematic diagram of the PLD sample stage design.

Fitted to port 1 of the PLD chamber a specially designed port adapting flange was made. This port adapter on the underside has a DN200CF flange to mount to port 1 of the chamber. On the top side of the adapter, is a DN100CF flange, enabling the mounting of an x, y, z-manipulation stage. Surrounding this flange and protruding higher than it are three DN16CF flanges. The shutter is mounted on the flange to the left hand side of the stage and is made from an oval shaped piece of stainless steel sheet, mounted on a stainless steel rod, attached to a manual rotational drive. The other two DN16CF flanges were designed in order to provide alternate positions for the shutter and also allow for other components to be added, such as crystal deposition monitors.

The x, y, z manipulation stage, mounted on the top of the port adapter, enables motion of the sample stage relative to the target. In the plane of the sample, the x and y motion both allow 25 mm of movement about the centre of the chamber. The sample height, and hence target to sample distance, is controlled by the z position, enabling 90mm of movement about the chamber centre.

As is shown in fig. 4.2.8, on top of the x, y, z-stage a rotational drive is mounted. This is a UHV Design Motorised MagiDrive, which allows for the rotation of the sample stage, to achieve an even film distribution across the entirety of the sample surface. The sample stage rotation is also important for the substrate heating mechanism to provide an even distribution of heating across

the substrate, which is illuminated by the infrared laser from above. The rotation is driven by a 24 V DC motor, with a 25:1 ratio gearbox, which, on maximum output, produces a rotation speed of 33 rpm. However, for sample deposition, a slower rotation speed of 10rpm was found to be more suitable. To allow the transmission of the infrared laser beam through the sample stage system to the sample, the interior of the rotational drive is a hollow tube, sealed by a DN16CF zinc selenide (ZnSe) viewport. To allow transmission of the 10600 nm infrared laser beam.

The inside of the rotational drive has a flange for the fixing of the remainder of the sample stage. Fixed to this is a specifically designed hollow aluminium shaft to allow the IR laser beam to pass down its centre. As seen in fig. 4.2.8, the shaft passes down through the x, y, z-stage, the port adapter and into the chamber. To mount the sample holder cradle to the aluminium shaft, two stainless steel rods are fixed to its end. This aids the access of the area above the sample holder, which is beneficial for the beam alignment of the CO<sub>2</sub> substrate heating laser.

The design of the cradle for the mounting of the sample cartridge is shown in fig. 4.2.9. The cradle is made from a high-grade stainless steel. In the top plate of the cradle, two holes 25 mm apart are designed for mounting to the stainless steel rods above. The larger hole in the centre of the top plate, with a diameter of 16 mm, is for the laser beam to access the sample below. The sample cartridge itself is designed to slide into the slots, such that the sample at the centre of the cartridge sits in the centre of the cradle. The cradle has been designed with the emphasis on minimising the contact between sample cartridge and cradle. This is important when the sample is to be heated to high temperatures, in order to reduce thermal dissipation.

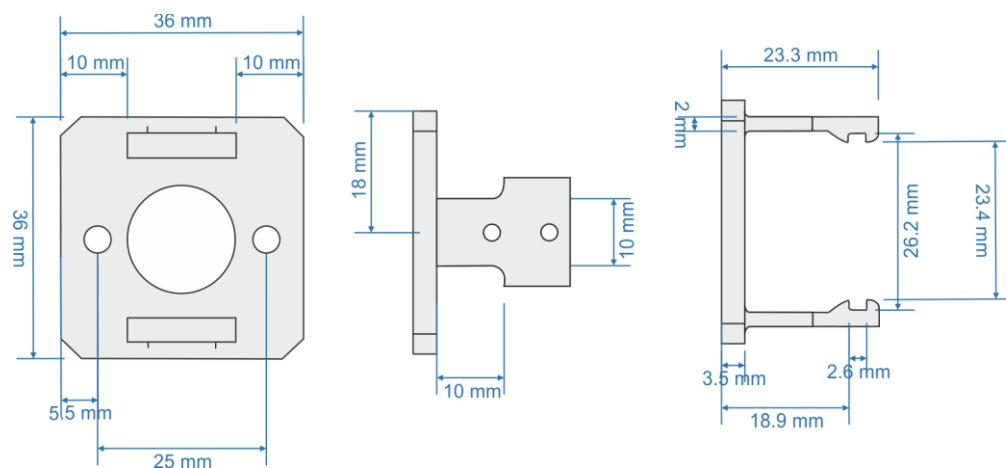


Figure 4.2.9. Schematic diagram of the PLD sample holder cradle.

2.5 mm holes have been designed in the stems of the cradle. The lowest hole is positioned level with the centre of the sample cartridge slot and the other 8.5 mm above this. These holes were designed with the intention of mounting a ball bearing in the lower hole supported by a spring loaded attachment in the upper. This ball bearing would then position itself within the groove in the side of the sample cartridge, seen in fig. 4.2.10, and would act to hold the cartridge in place. It was found however, when testing the system that this was not needed to hold the sample cartridge in position, as friction alone was sufficient. The cartridge is made from titanium to withstand the high temperatures at which the sample is heated.

The titanium cartridge itself is 2.5 mm thick, with chamfered front edges to aid its sliding insertion into the cradle. The front of the cartridge is radial in shape for the same purpose also. The sides of the cartridge are flat so to be compatible with the slots in the cradle, up to a point 7 mm back from the centre of the cartridge. Where a step in the edge of the cartridge prevents it sliding further into the cradle, such that the centre of the sample sits in the centre of the sample stage.

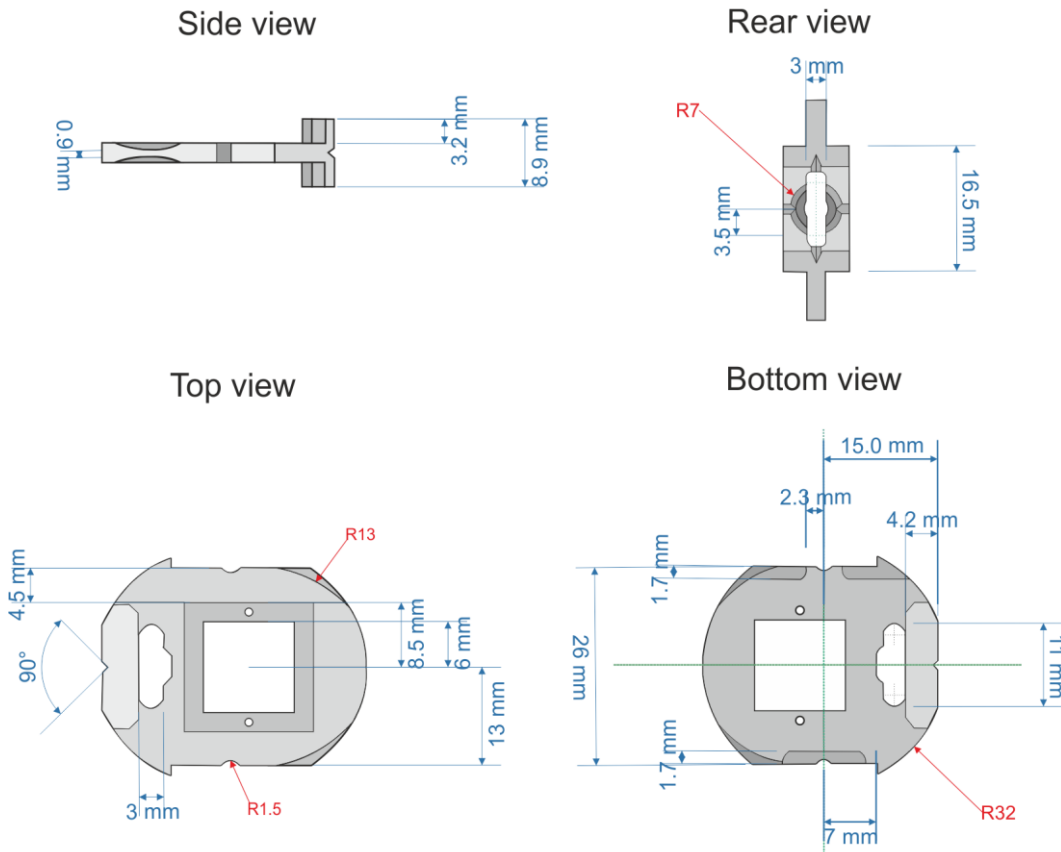


Figure 4.2.10. Schematic diagram of the sample cartridge. Showing views from the side, rear, top and bottom.

To hold a substrate, the sample cartridge has a hole, 12 mm square, with a 17 mm square recess around it. Within this recess, a piece of macor ceramic has been designed to hold a 5 mm x 5 mm substrate. The 1 mm tapped holes in the recess of the sample cartridge allow the ceramic inset to be fixed in position. This system is versatile enabling the ceramic inset to be changed if damaged and for the insertion of different ceramic insets designed to hold substrates of different sizes. The ceramic inset is shown, mounted in the PLD cartridge, in fig. 4.2.11. The sample cartridge inset is made from Macor ceramic, chosen due to its good thermal insulating properties, in order to minimise the conduction of heat away from the sample through the sample holder. At the centre of the ceramic inset is a 5.5 mm square indent, into which a substrate is placed face down. In order to stop the substrates falling straight through, the corners of the square are left 0.5 mm thick, thin enough to prevent significant shadowing of the sample.



Figure 4.2.11. Image showing the top view of the PLD sample cartridge. The image was taken after several hours of deposition with substrate heating.

An image of the sample cartridge is shown in fig. 4.2.11, after it had been used to grow numerous samples. The sample cartridge is transferred into the chamber from the load-lock system using a

magnetic transfer arm, on the end of which is a specially designed bayonet type connector. This connector is spring loaded and is designed to slot into the end of the PLD cartridge. Rotating the magnet by 90°, rotates the bayonet pin in the hole in the cartridge, locking the cartridge to the connector.

#### 4.2.5 Load-lock system

To transfer samples in and out of the PLD chamber, fast and effectively, without breaking the vacuum of the chamber, a load-lock system has been designed. A schematic diagram of the load-lock assembly is shown in fig. 4.2.12.

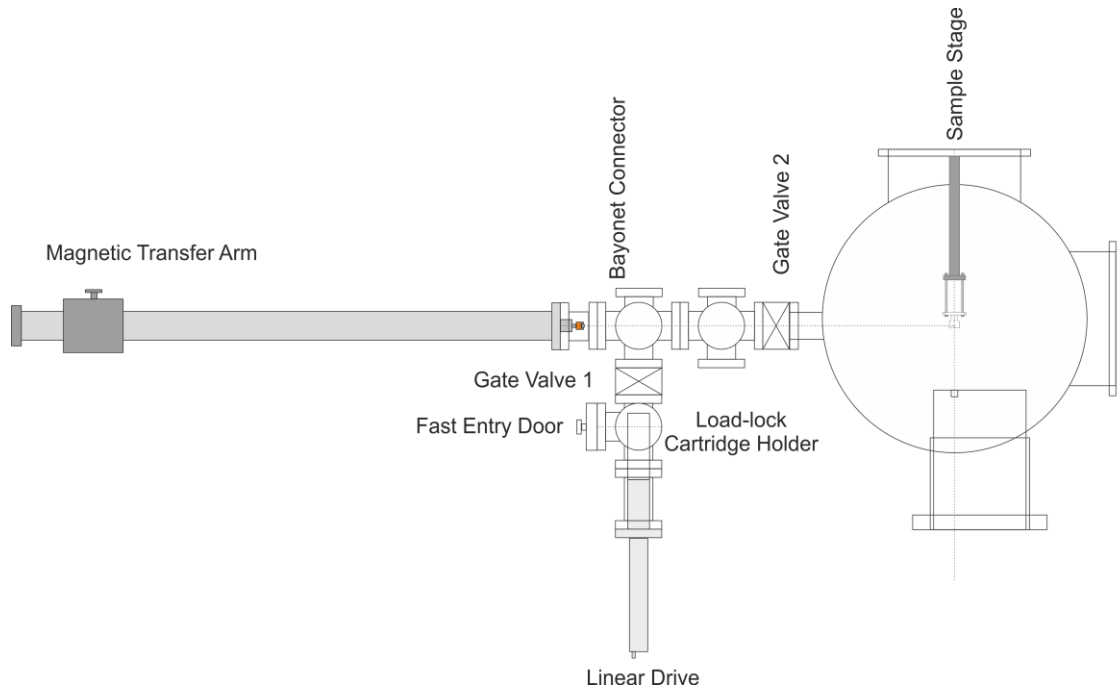


Figure 4.2.14. Schematic diagram of the PLD load-lock system.

The lower part of the load-lock system, below gate valve 1, consists of a 5- way DN40CF cross, on the bottom of which is mounted a 90 mm extension nipple with a 150 mm linear drive. On the front of the 5-way cross is a viewport to see into the fast entry lock, on the side is a fast entry door and to the rear an Edwards EXT 75DX turbo pump is mounted, to rapidly evacuate the fast entry lock. The fast entry door can be opened and the sample cartridge, loaded with a new cleaned substrate, is mounted in the load-lock cartridge holder, as shown in fig. 4.2.13, attached to the head of the linear drive. This piece is made from aluminium and has been specifically designed to house the sample cartridge and transport it to the second part of the load-lock system.



Figure 4.2.13. Image showing the load-lock cartridge holder. Mounted on the 150 mm linear drive.

With the sample cartridge secure in the load-lock holder, the fast entry lock is evacuated by the connected turbo. After a sufficient vacuum pressure of  $<1 \times 10^{-5}$  mbar, is reached, gate valve 2 is closed before gate valve 1 is opened and the sample is moved up into the top part of the load-lock

using the linear drive. The top part of the load-lock system consists of two connected 6-way DN40CF crosses. The linear drive moves the sample cartridge into the first of these crosses to a height level with the magnetic transfer arm. The transfer arm can move the sample cartridge a distance of 600 mm, which is sufficient to transfer the sample into the centre of the PLD chamber.

Fig. 4.2.14(a) shows the load-lock system as viewed from the left hand side of the PLD chamber. This view is the same as that detailed in fig. 4.2.12. In this image, it can be seen that attached to the end of the magnetic transfer arm is a supporting brace. This effectively supports the magnetic transfer arm and indeed the rest of the load-lock system.

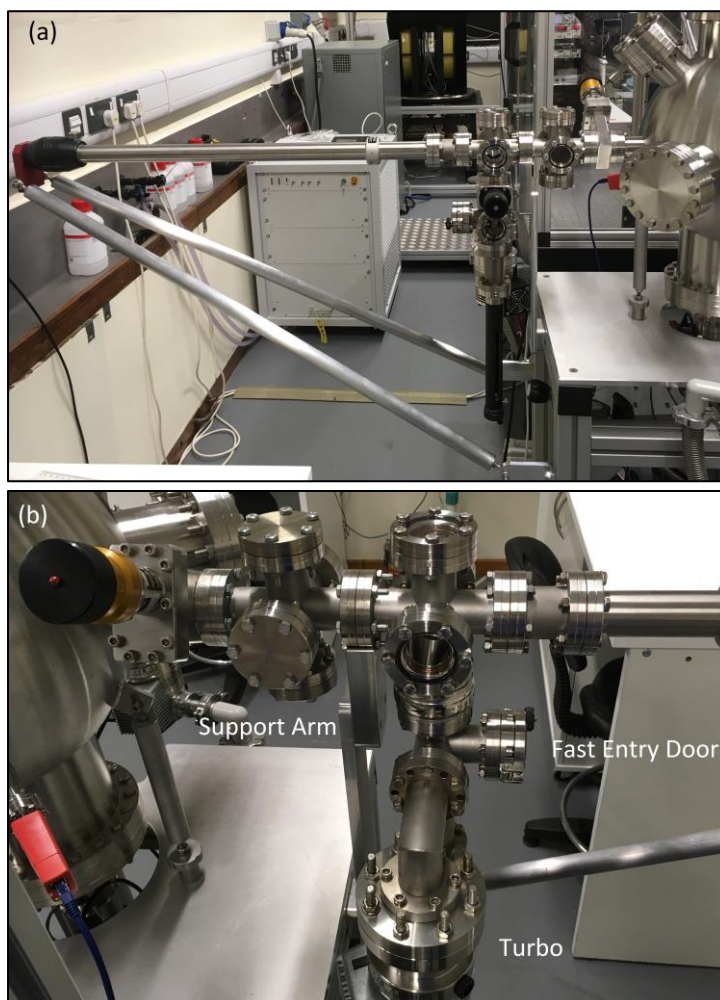


Figure 4.2.14. Images showing the PLD load-lock sample transfer system, (a) from the left side of the chamber, (b) from the right side of the chamber.

Fig. 4.2.14(b) shows the load-lock system from the opposite side. The first 6-way cross has 3 viewports, mounted on the front back and top flanges. These viewports allow the load-lock holder and magnetic transfer arm connector to be seen, when transferring the sample cartridge. A second 6-way cross with a viewport on its front flange, allows the sample cartridge to be viewed during transfer. The purpose of the inclusion of this second 6-way cross was for the mounting of a sample storage column. This has not yet been included on the system but it is planned at a later date, allowing several samples to be loaded into the load-lock at once.

One important consideration in the design of the load-lock system was the design of the bayonet style connector attached to the end of the magnetic transfer arm. This connector locks on to the sample cartridge and remains fixed as the cartridge is transported between the load-lock and the sample stage before being easily detachable. The designs of the two main parts of the bayonet connector are shown in fig. 4.2.15. In fig. 4.2.15(a), the bayonet shaft is attached to the magnetic transfer arm by the M6 thread. The flats on the side of the broadest part of the shaft allow the

thread to be tightened to the transfer arm with a spanner. The shaft narrows to a stretch that is 4mm long and has a radius of 6.1 mm, upon which a spring is mounted. The other end of this spring fits into the 7.5 mm recess in copper sliding bush fitting, shown in fig. 4.2.15(a). This copper bush is mounted on the 6 mm square part of the shaft. This part of the shaft is 13 mm in length, allowing the spring-loaded movement along it. The bush is held in place by a 9 mm long pin that is inserted into the 1 mm cylindrical hole at the end of the shaft, with the pin tight enough to be fixed in place. The square design of the shaft prevents the bush from rotating. Two shorter pins, 5 mm in length, are fixed into the 2.5 mm holes in the copper bush; these are to aid the alignment of the bayonet and the cartridge, when transferring the sample. The shaft is made from stainless steel and the bush copper. Copper was chosen as the bush material as this is a softer metal than the shaft [191] and would ease the sliding of the bush along the shaft.

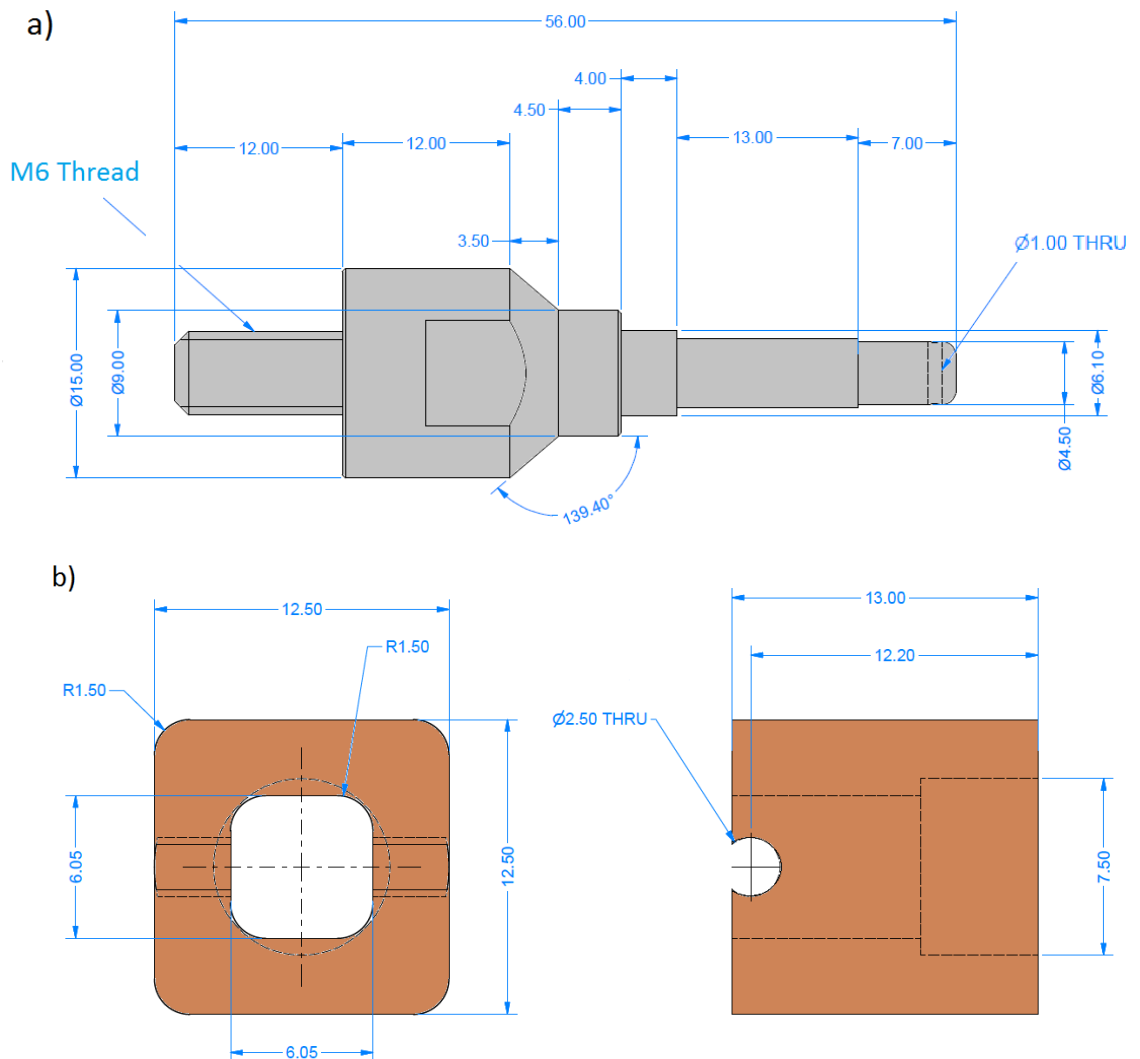


Figure 4.2.15. Technical diagram of the bayonet type connector, attached to the end of the magnetic transfer arm, (a) the bayonet shaft, (b) the sliding bush fitting. All measurements shown in this figure are in mm.

In fig. 4.2.16 the assembled bayonet connector can be seen, attached to the end of the magnetic transfer arm. The connection is made with the sample cartridge by the pin at the end of the shaft, in its horizontal position, sliding into the slot at the end of the cartridge. This forces the spring to compress as the copper bush is slid along the shaft. When the pin reaches the clearing 4.2 mm into the cartridge, it is rotated 90 degrees and the tension of the spring pushes the bush up to the cartridge locking it in place. The pins extruding from the copper bush fit into the slots in the face of the cartridge, shown in fig. 4.2.10, preventing the cartridge from spinning on the bayonet.

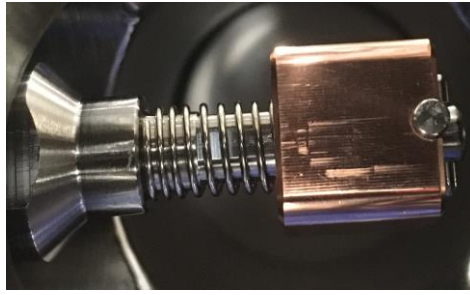


Figure 4.2.16. Image of the bayonet type connector attached to the magnetic transfer arm.

#### 4.2.6 Chamber pressure and gas flow system

As previously mentioned, the chamber and load-lock system are evacuated through the use of two Edwards EXT 75DX turbo pumps. These two turbos are both connected to the same backing pump. The backing pump is an Edwards nXDS6i rotary pump, which was chosen for its ability to safely pump oxygen gas. Both turbo pumps can be isolated from the backing pump by Edwards speedi valves that are placed between the turbo and the backing pump. This allows the load-lock pump to be isolated from the pumping system and spun down in order to remove a sample. The PLD chamber, without being baked can readily achieve pressures as low as  $1 \times 10^{-8}$  mbar. This is significantly lower than the pressures need for the PLD growth. However, if E-beam evaporators were to be added to the system lower pressures would be required and could be achieved through the baking out of the chamber.

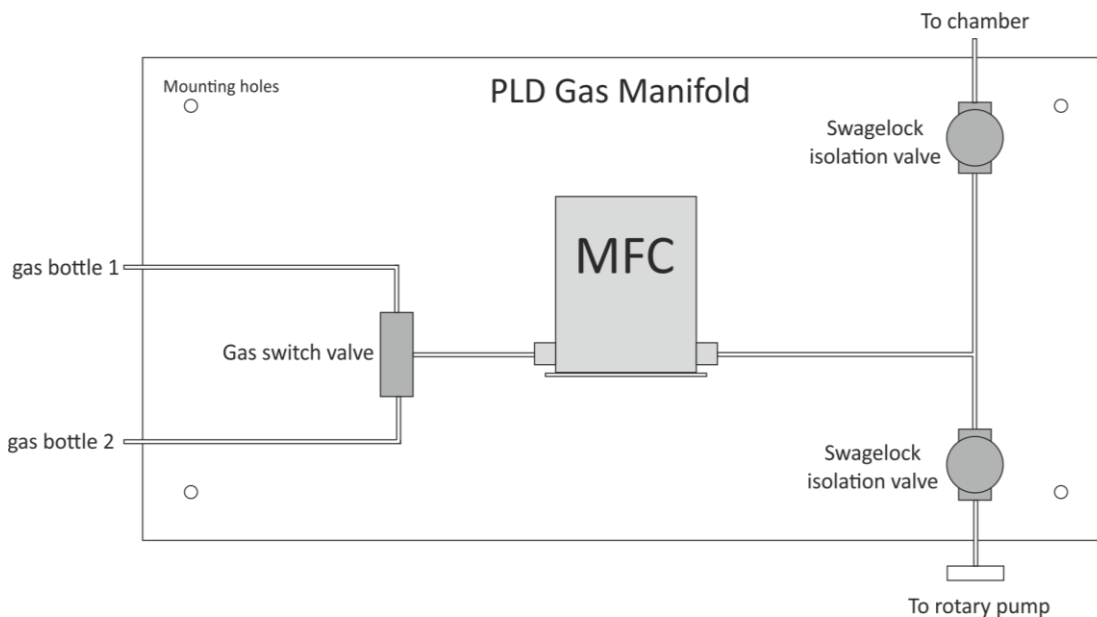


Figure 4.2.17. Schematic diagram of the PLD gas manifold.

An important aspect of PLD growth is the ability to control the pressure of the chamber during growth as well as the gas mixture [22] [127]. For the growth of oxides and more specifically ferrites, a controlled oxygen partial pressure is often required to maintain stoichiometry, with the oxygen in the chamber replacing any of that lost from the target [22] [190]. As such, to control the gas pressure within the chamber, systems to manipulate both the inflow and outflow of gas have been designed. A gas manifold has been built, fig. 4.2.17, incorporating a Mass Flow Controller (MFC), which controls the rate at which gas is leaked into the system to create a partial pressure. The manifold allows the option of two different input gasses. The fine control of the MFC enables the partial gas pressure within the growth chamber to be reliably controlled. Additionally, as a second mechanism for controlling the pressure of the chamber, a gas throttling system has been constructed to control the rate at which the turbo pump evacuates the chamber. A combination of

both the gas manifold and throttling system have been used to control the flow of gas through the system and achieve settled partial gas pressures within the chamber. This has been achieved over a wide range of pressures and the system is adaptable to incorporate a wide range of gasses. A schematic diagram detailing the gas manifold is shown in fig. 4.2.17. The manifold is mounted to the side of the PLD chamber stand. Two gas bottles are mounted to the legs of the stand; this set up is shown in fig. 4.2.20(a). The two gasses used initially were nitrogen and high purity oxygen, nitrogen chosen due to its inert properties and oxygen for its previously mentioned advantages when growing ferrite films. These gasses could be readily swapped for other appropriate gasses to achieve specific growth conditions. The gas bottles are fitted with regulators and stop valves to regulate the pressure in the gas line, as can be seen in fig. 4.2.18(a). All fittings and connections made in the gas manifold system are made using Swagelok fittings. The incoming pipelines from the two gas bottles are connected to a 3-way gas-switching valve, with the valve pointing upwards gas from bottle 1 can flow along the pipeline towards the MFC. When the valve is turned down gas from bottle 2 flows to the MFC. The MFC then controls the gas flow into the rest of the system. The MFC used is an Alicat Scientific MCE series, which was chosen as it controls the flow rate between 0.1 and 100 sccm, allowing adjustment over a wide range of PLD chamber pressures. With an appropriate flow rate set for the desired growth pressure, the gas flows further down the manifold system where a t-piece splits the line. One direction leads to a KF connector that has been designed to be connected up to the rotary pump and used to purge the pipeline before a different gas is used. The other direction leads to the vacuum chamber itself. As can be seen in the diagram of fig. 4.2.17, both directions can be closed off by Swagelok isolation valves.

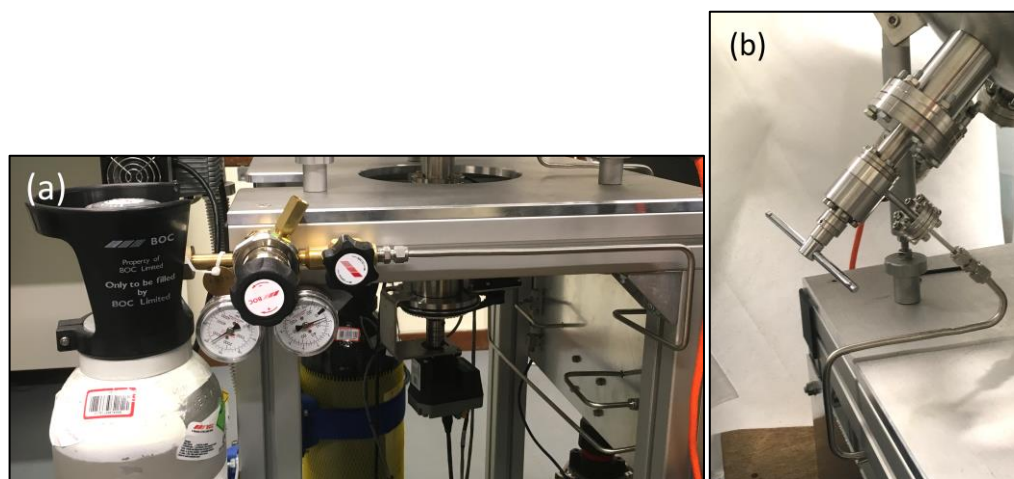


Figure 4.2.18. Images showing, (a) the oxygen gas bottle, with regulator piped up to the PLD gas manifold, (b) the PLD chamber gas inlet, with leak valve and pipe leading to the gas manifold.

The gas line is connected to the chamber at port 5, as shown in fig. 4.2.18(b), via a VG Scienta manual leak valve. The leak valve enables a further mechanism for the fine control of the gas flow in to the chamber and allows the gas manifold system to be completely isolated for when pumping down the chamber or when high vacuum conditions are required.

A specifically designed gas throttling system can also control the evacuation of the gas from the chamber. This system is shown in fig. 4.2.19. The image shows the turbo pump attached to the PLD chamber through the throttling system. Attached to port 8 of the chamber is a double sided DN40CF flange, welded through the bottom of which is a pipe, with a 4 mm inner diameter and on the end of the flange is attached a VG Scienta right-angled gate valve. On the other end of this right-angled valve is a t-piece, on the side of which a DN16CF flange is connected to a leak valve, which is in turn connected to the 4 mm pipe. The remaining flange of the t-piece is connected to the turbo pump. With the right-angled valve opened, the turbo is able to pump on the chamber to its full capacity. However, in order to effectively throttle the turbo and reduce the pumping speed

to the chamber the valve can be turned to a fraction of its fully opened position. Additionally, for even further throttling of the turbo, the right-angled valve can be closed completely and the leak valve opened. This allows for a very fine control of the pumping speed. Controlling the pumping speed, in addition to the fine control available for the inflow of gas, allows the pressure within the chamber to be manipulated reliably, producing a stable partial pressure for the growth of thin films. Ultimately, the gas flow system has been used to effectively control the partial pressure of the PLD chamber over a wide range, between  $1 \times 10^{-7}$  mbar and  $1 \times 10^{-2}$  mbar.

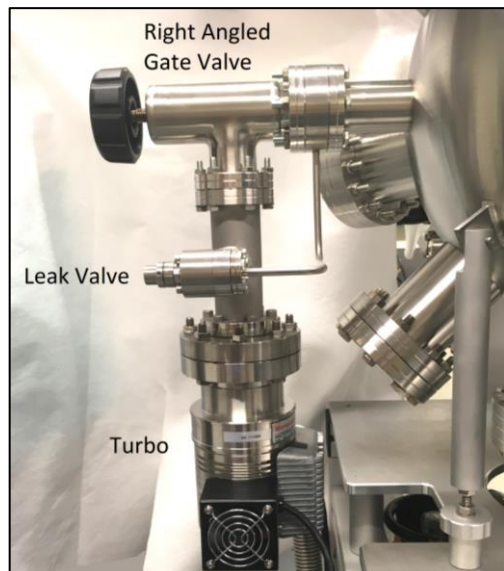


Figure 4.2.19. Image showing the PLD turbo throttling system.

#### 4.2.7 Substrate heating and temperature calibration

As discussed in section 4.2.4, the sample stage is designed with a hollow centre and a ZnSe viewport mounted at its top, to allow the back of the sample to be heated by an Infrared CO<sub>2</sub> laser beam. The beam enters the chamber through the ZnSe viewport and passes through the hollow sample stage while the sample is rotated.

CO<sub>2</sub> laser substrate heating has been used in PLD previously, notably by Eason's group at the University of Southampton [127]. This method of substrate heating has been adopted for the PLD system developed in this work as it allows the substrate heating to be maintained whilst simultaneously rotating the sample. For heating methods, such as resistive heating, where electrical contacts to the sample are required, sample rotation becomes a problem. One possible solution in this case can be the implementation of electrical rotary bush contacts but these solutions have been found to be less reliable [127]. The laser heating method is also a safer method for growth within high oxygen partial pressures. Ohashi *et al* [192] developed a PLD substrate Laser heating system, with a similar geometry to that used in this PLD, in which the laser is focussed onto the reverse side of the substrate from above. Their system uses an Nd:YAG laser optical fibre that is focussed through a viewport at the top of the vacuum chamber. Alternatively, the laser heating system developed by Eason *et al* [127] has a horizontal geometry. They utilise a 25 W CO<sub>2</sub> laser that can be focussed onto the back of the substrate using two different methods. One method they use to evenly heat the substrate is to raster scan the beam across the substrate. Another unique method they have developed is to spatially reformat the beam into a square profile, that covers the entire substrate by a ZnSe tetra-prism [193].

Using a CO<sub>2</sub> laser, operating at a wavelength of 10600 nm, is an efficient method for heating the oxide substrates used as they absorb strongly at this wavelength. Laser substrate heating was also chosen as it can be used to achieve the high substrate temperatures required, in excess of 1000°C

[127]. This method can be used to ramp the substrate temperature very rapidly, with ramping between room temperature and 800°C in a matter of seconds, enabling the flash heating of samples. Routinely, however, a controlled ramping of temperature is achieved by a gradual stepping of the laser power.

The laser used for the PLD substrate heating in this work is a 35 W 48-2 series SYNRAD carbon dioxide laser. This is a quasi-continuous wave laser, which means that the laser's pump source is only switched on for given time intervals, which are short enough to reduce thermal effects but still long enough to produce optically a state of continuous wave operation. The laser is powered by 30V DC, provided by a Farnell stabilised power supply. A 5 kHz, TTL pulsed signal is used to control the laser output, this signal is produced by a TG1010 function generator with an amplitude of 5 V. The laser power is controlled by modulation of the pulse width, so increasing the duty cycle of the signal increases the power of the laser. The signal generator allows the duty cycle to be adjusted in 0.1% steps enabling fine control of the output laser power. With the laser powered by the 30 V DC, a tickle pulse must first be applied. This is a pulse with a pulse length of 1  $\mu$ s (0.5% duty cycle) and acts to pre-ionise the laser gas to just below the lasing threshold so that any further increase in pulse width results in laser emission. Following this, the duty cycle can then be increased to produce the desired laser power.



Figure 4.2.20. Image of the 48-2 series SYNRAD CO<sub>2</sub> laser, mounted on the cooling base.

As is the case with all high power lasers, the laser must be cooled during operation to prevent overheating. To achieve this the laser is mounted on a base to which six cooling fans are attached, as shown in fig. 4.2.20. The CO<sub>2</sub> laser, and attached cooling fan base, is mounted on the top of the optical hutch, designed as the enclosure for the UV laser optics. The laser positioned on this



Figure 4.2.21. Image showing the PLD CO<sub>2</sub> laser substrate heating set up.

platform allows the emitted laser beam to be directed across the top of the PLD chamber, down through the ZnSe viewport and through the centre of the sample stage, onto the sample.

An image of the PLD substrate heating optics set up is shown in fig. 4.2.21. In order to mount the optics associated with the laser, a 300 mm wide platform is extended from the end of the optics hutch, as can be seen in the image. The platform has a grid of tapped holes, to replicate an optical bench for the mounting of optics. As shown in fig. 4.2.21, at the chamber end, the platform is supported from the top of the port 1 flange by two adjustable legs.

The CO<sub>2</sub> laser is designated as a class 4 laser and emits laser radiation that is invisible to the human eye. As such, it was imperative that the proper safety precautions were in place when using the laser. The same interlock is applied to the laboratory door, which is used for the UV laser, and appropriate eye protection is worn. Additionally, enclosure of the beam is achieved by the optical set up detailed in fig. 4.2.22.

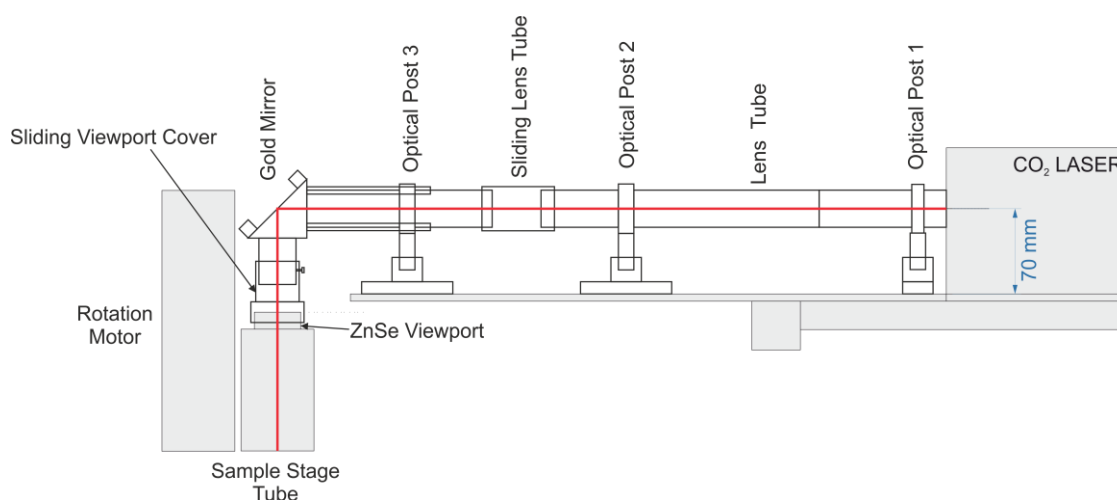


Figure 4.2.22. Schematic diagram of the CO<sub>2</sub> laser substrate heating optical set up.

The infrared beam exits the laser at a height of 70 mm above the height of the optics platform. To enclose the beam a series of 1-inch diameter lens tubes are used. These tubes are anodised in black to reduce any reflection of the laser beam and are supported by three optical posts, as shown in the schematic diagram. Between optical post 2 and 3, there is a 40 mm gap in the lens tube. This gap is designed so that lenses or other optical components may be inserted into the lens tube at this point, if required. To enclose the gap in the lens tube, a sliding lens tube piece was designed to slide over the existing tube. The third optical post is positioned close to the end of the optics platform with a 3-inch long lens tube extending to above the PLD chamber sample stage. On the end of the tube a 1-inch gold coated copper mirror is mounted in a right angled kinematic mirror mount. This mirror acts to reflect the laser beam down through the ZnSe viewport and through the sample stage onto the sample. The mirror mount has four tapped hole in which 6 mm cage rods are attached and support the mount. These rods can be extended to adjust the mirror mount position in the x direction, where the x direction is defined as the parallel to the initial direction of propagation of the laser. A final lens tube extends down from the mirror mount towards the ZnSe viewport, with a gap being left between the tube and the port, to allow for adjustment of the z-height of the sample stage. The gap also acts to aid the alignment of the laser, as the laser beam path can be checked in front of the viewport. To allow for flexibility in the height adjustment whilst enclosing the beam path after alignment, a sliding viewport cover tube was designed.

The laser is specified to have a near Gaussian beam profile and the beam waist diameter at the output of the CO<sub>2</sub> laser was measured to be 3.5 mm. The path length between laser and sample was also calculated to be  $(1250 \pm 45)$  mm and at this distance; the beam was measured to have diverged to a diameter of 4.5 mm. Given that, the substrates are 5 mm x 5 mm in size it was decided that no further manipulation of the beam size was required to heat the samples.

Once the laser had been aligned the PLD chamber was evacuated to a pressure of  $1 \times 10^{-7}$  mbar and a silicon substrate positioned in the sample holder. The sample heating system could then be tested on the Si substrate. It was observed that as the duty cycle, and hence power of the laser, was increased the substrate began to glow. The silicon initially glowed a faint red, before becoming brighter with increased laser power and eventually glowing a bright orange. An image of the glowing silicon substrate is shown in fig. 4.2.23(a), taken with an 80% laser duty cycle. Fig. 4.2.23(b) shows the incandescence of an  $\text{Al}_2\text{O}_3$  substrate heated with a laser duty cycle of 80%. By comparing the images in fig. 4.2.23, it can be seen that the  $\text{Al}_2\text{O}_3$  incandesces a much brighter white colour compared to the orange glow of the silicon, as expected due to the  $\text{Al}_2\text{O}_3$  having a larger emissivity than the silicon [194] [195].

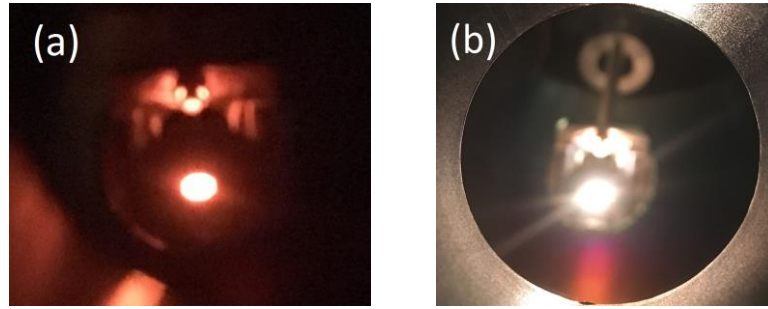


Figure 4.2.23. Images showing, (a) a silicon substrate, (b) an  $\text{Al}_2\text{O}_3$  substrate, heated by the  $\text{CO}_2$  laser with an 80% duty cycle.

The three different substrates used in the initial growths, using the PLD chamber, were Si, MgO and  $\text{Al}_2\text{O}_3$ . It was found that, while the Si withstood easily the substrate heating and temperature gradients involved, the MgO and  $\text{Al}_2\text{O}_3$  substrates were damaged in the process. Both the MgO and  $\text{Al}_2\text{O}_3$  appeared to crack and deform, when the laser power was greater than 20 W (60% duty cycle). By the form of the damage, it was suspected that this damage was caused by thermal expansion as the sample was heated. In order to overcome this problem, a Si substrate was used as an intermediate layer, as the Si is a better thermal conductor and will act to distribute the heat more evenly across the MgO or  $\text{Al}_2\text{O}_3$  substrate, via thermal conduction.

Before the growth of samples, the temperature of the substrates was calibrated as a function of laser power. To measure the temperature of the substrates during heating an infrared pyrometer was used. This measures the infrared radiation emitted by the substrate through incandescence to determine its temperature. Where the irradiance,  $j^*$ , is a function of the substrate temperature, given by the Stefan-Boltzmann law, equation 4.1 [196].

$$j^* = \xi \sigma_B T^4 \quad \text{Eqn. 4.1}$$

Where,  $\xi$  is the emissivity of the substrate and  $\sigma_B$  is the Stefan-Boltzmann constant. Hence, for a substrate with a given emissivity the temperature can be determined.

The pyrometer used is an Ircon MODLINE PLUS infrared thermometer and for was positioned pointing towards the surface of the sample, through port 13 of the PLD chamber. The controller of the pyrometer displays the temperature measured and this was recorded for the three different substrates, Si, MgO and  $\text{Al}_2\text{O}_3$ , as a function of  $\text{CO}_2$  laser duty cycle. It was found that as the temperature was increased the pyrometer became saturated, thus, neutral density (ND) filters were needed to reduce the light intensity at the pyrometer. These filters reduce the intensity of all wavelengths, numbered according to their transmittance (ND1 transmitting 50%, ND2 25% and ND3 12.5%). To measure between 450-600°C an ND1 filter was used, between 600-900°C an ND2 filter and above 900°C an ND3 filter.

At each duty cycle, the temperature was observed over a period of 5 minutes to ensure that the temperature had settled, before increasing the laser power. An emissivity of 0.3 [194] was used for

the silicon substrate, while for the MgO and Al<sub>2</sub>O<sub>3</sub> emissivity values of 0.35 [197] and 0.48 [195] were used, respectively. The graphs of the results, showing substrate temperature against laser duty cycle, are displayed in fig. 4.2.24. The relationship between duty cycle and substrate temperature follows a similar form for all three substrates and this relationship is non-linear. With increased duty cycle, the increase in temperature with each increment is reduced. The pyrometer does not measure below 250°C and it is seen that for all three substrates this temperature is exceeded with a laser duty cycle as low as 8%. In fig. 4.2.24(a), the silicon substrate reaches a temperature of over 900°C for an 80% duty cycle. For the MgO and Al<sub>2</sub>O<sub>3</sub>, in Fig. 4.2.24(b) and (c), these substrates follow a very similar temperature relationship at low duty cycles and as the duty cycles are increased they don't achieve as high a temperature as the silicon. Although the MgO still reaches 850°C at 80% duty cycle and the Al<sub>2</sub>O<sub>3</sub> reaches 880°C. These small reductions in temperature compared to Si are expected due to the presence of the extra silicon contact layer.

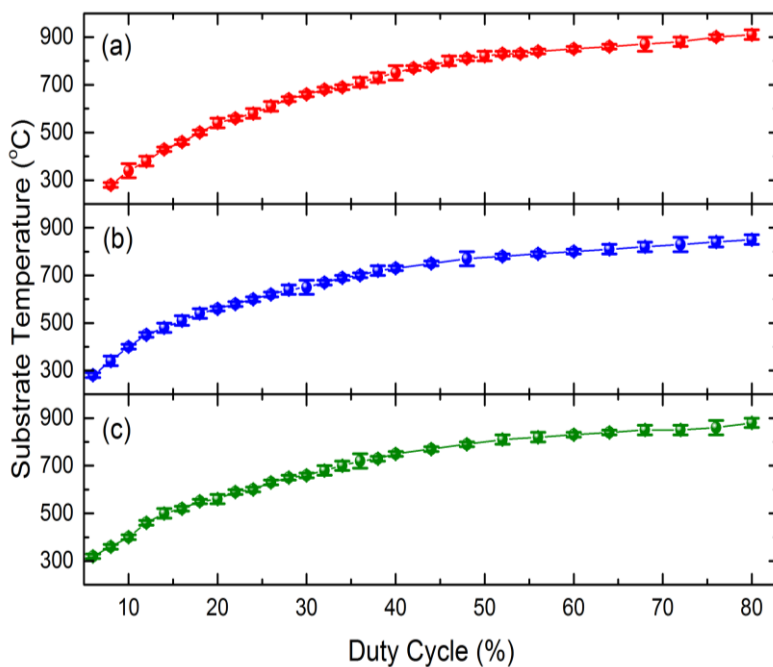


Figure 4.2.24. The substrate temperature as a function of CO<sub>2</sub> laser duty cycle for (a) a silicon substrate, (b) an MgO substrate and (c) Al<sub>2</sub>O<sub>3</sub> substrate, measured at a pressure of 1x10<sup>-7</sup>mbar.

The temperature could only be measured from the pyrometer scale reliably to the nearest 10°C, hence, this is the source of the error bars associated with the data in fig. 4.2.24. On occasions where the temperature fluctuated by more than this margin, this was accounted for in the error bars. These temperature variations were attributed to fluctuations in the CO<sub>2</sub> laser's power output. Additionally, there is some form of systematic error associated with the temperature, recorded by the pyrometer due to the values of emissivity used for each substrate. In reality, the emissivity of the substrates is a function of both temperature and wavelength thus varies depending on the exact relationship as temperature is changed. It is seen from the Stefan-Boltzmann law however, that the temperature has a far greater contribution to the irradiance measured for the substrate than the emissivity. As such, the effect of variations in emissivity on our temperature calibration is small. Given these considerations, the calibration graphs for the given substrate can be used as a guide for the duty cycle required to achieve a given substrate temperature.

The temperatures achieved cover the range desired for the growth of most oxide thin films [133] [198] [199] [200] [17]. To grow high quality Fe<sub>3</sub>O<sub>4</sub> thin films temperatures of the order of 500°C [200] are required and are readily achievable with this CO<sub>2</sub> laser heating, as are the temperatures previously used for the PLD growth of M-type hexaferrite thin films [133] [24] [20]. Hence, the laser

heating system works effectively and meets the demands required to grow high quality hexaferrite thin films.

#### 4.2.8 The constructed PLD growth system

The finished PLD growth system is shown in fig. 4.2.25. The rack to the right of the optical bench is used to house the controls for the turbo pumps, as well as the vacuum gauges and target manipulator controller.

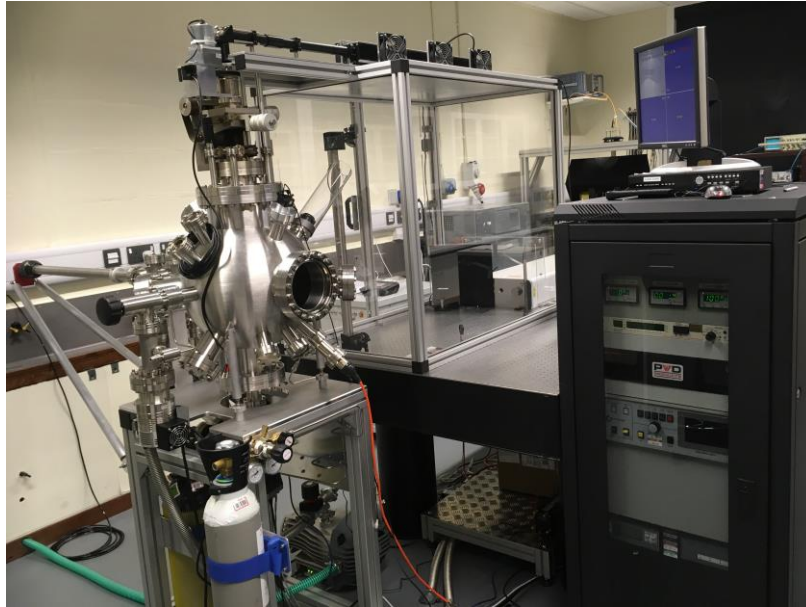


Figure 4.2.25. The PLD growth system with PLD chamber, load-lock, UV and CO<sub>2</sub> lasers.

### 4.3 Calibration of the PLD system by Fe<sub>3</sub>O<sub>4</sub> thin film growth

In this section, a series of thin films have been grown using the newly developed PLD, in order to test and calibrate the system. Magnetite thin films grown as a function of time, target-substrate distance and growth partial pressure have been characterised. Magnetite was chosen, as it is a ferrite with a much simpler structure than that of a hexaferrite, the growth of which is the ultimate aim for the PLD system. The series of films were grown from a Fe<sub>3</sub>O<sub>4</sub> target, all at a sample stage position of  $x = 11$  mm and  $y = 14$  mm, which corresponds to the substrate being positioned directly above the target.

These initial calibration films were grown at room temperature, as they were grown before the substrate heating system was in place. This still however enabled the calibration of the rest of the system. The films were grown on Si (001) substrates, which although having a poor lattice match to the desired magnetite phase [201], was chosen due to it being readily available and a heavily used semiconductor material in electronics and many technological uses of iron oxide thin films would require compatibility with a silicon like material [202]. The thin films characterised in this chapter were grown with the UV laser pulsed at 10 Hz and a pulse energy of 100 mJ. Due to the focussing of the laser beam, this results in the PLD target ablation with a laser fluence of approximately 3 Jcm<sup>-2</sup>.

#### 4.3.1 Deposition time calibration at an 8 cm target-sample distance

Initially Fe<sub>3</sub>O<sub>4</sub> films were grown, with a fixed target to sample distance of 8 cm, as a function of time. For each film, the conditions were kept constant only changing the deposition time. An oxygen partial pressure of  $1 \times 10^{-5}$  mbar was maintained during growth, as similar conditions had been found optimal for the growth of magnetite [203] [204] [200]. It is expected that if all the

growth conditions are reproducible then the thickness of the thin films should be directly proportional to the deposition time. Samples with deposition times of 2, 3, 4, 5, 6, 10, 15 and 20 minutes have been characterised both structurally and magnetically in this series.

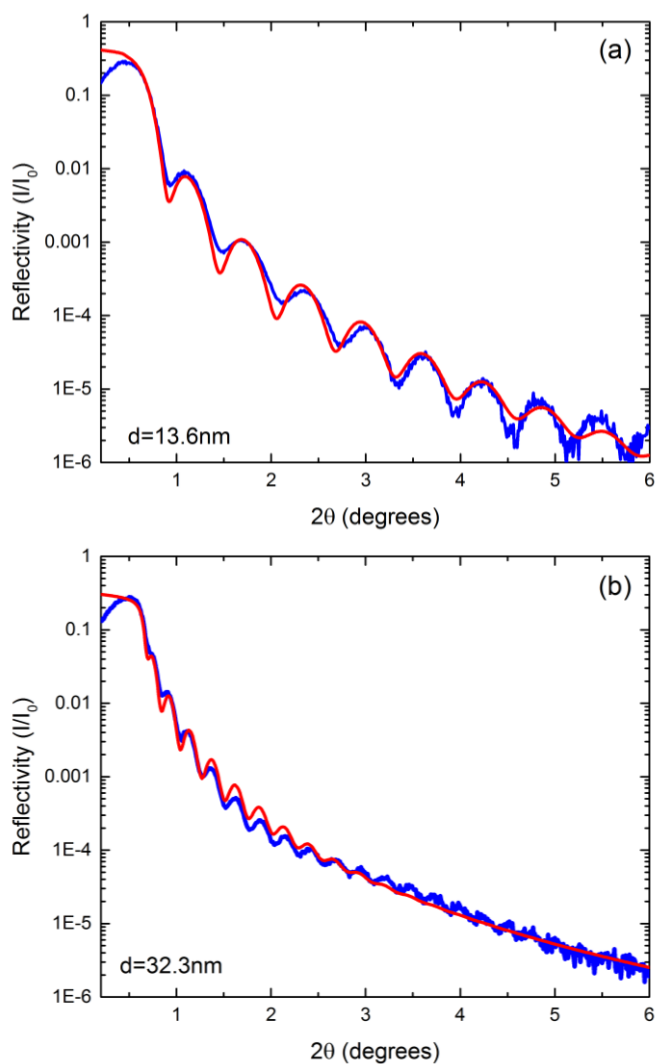


Figure 4.3.1. XRR measurement (blue) with fitted curve (red) for the  $\text{Fe}_3\text{O}_4$  on silicon thin films, (a) 3 minute deposition time, (b) 5 minute deposition time.

X-ray reflectivity measurements were performed on all of the samples in the series, primarily to determine the thicknesses of the films grown. The measurements were performed following the procedure outlined in section 3.2.2.3, and fitted using both the software packages Globalfit [147] and GenX [148]. XRR measurements for the films with deposition times of 3 and 5 minutes are shown in fig. 4.3.1. The measurements for these two samples are displayed as examples and corresponding measurements were obtained and fitted for all films in the series. The fitting procedure required the densities of both the substrate and film to be set. For the Si substrate a density of  $2.33 \text{ gcm}^{-3}$  [205] was used and a film density of  $5.18 \text{ gcm}^{-3}$  was set, in accordance with an  $\text{Fe}_3\text{O}_4$  composition [206]. Comparing the reflectivity measurements for both the 3 and 5-minute samples, it is evident that the Kiessig fringes have a longer period and are less damped for the film with the shorter deposition time. This suggests that the 3-minute film is thinner as expected. Indeed extraction of the fitting parameters reveals film thicknesses of  $(13.6 \pm 0.8) \text{ nm}$  and  $(32.3 \pm 0.9) \text{ nm}$ , for the 3-minute and 5-minute films, respectively.

The XRR for the films grown for 10, 15 and 20 minutes show no Kiessig fringes. As such, no definitive thickness values could be determined from their reflectivity. The absence of the Kiessig fringes for these films is due to their thicknesses being too large to be measured by XRR. This critical thickness limit is dependent on both the films density and surface roughness [140], with the surface

roughness also affecting how rapidly the XRR signal drops off with increased angle of incidence, damping the Kiessig fringes more rapidly [140]. The film thickness and surface roughness values extracted from fitting are all displayed in table 4.1.

Deposition time (minutes)	Thickness (nm)	rms Surface roughness (nm)	Resistance (k $\Omega$ )
2	11.7 $\pm$ 0.5	0.22 $\pm$ 0.06	500 $\pm$ 50
3	13.6 $\pm$ 0.8	0.24 $\pm$ 0.02	90 $\pm$ 20
4	21.7 $\pm$ 0.7	0.17 $\pm$ 0.04	50 $\pm$ 10
5	32.3 $\pm$ 0.9	0.22 $\pm$ 0.03	25 $\pm$ 5
6	36.6 $\pm$ 0.4	0.19 $\pm$ 0.04	20 $\pm$ 3
10	NA	NA	11 $\pm$ 1
15	NA	NA	8 $\pm$ 1
20	NA	NA	5.5 $\pm$ 0.3

Table 4.1. Table showing the XRR determined thicknesses and surface roughness of each sample as well as their measured resistances.

It is evident, from the values in table 4.1, that the thickness of the deposited films increases with deposition time. These values of thickness do not scale exactly, but approximately double as the deposition time is doubled. The error values associated with both the thickness and surface roughness are taken from the discrepancy between the fitting values calculated by the two different software.

The rms surface roughness values are all similar in magnitude, of the order of 0.2 nm, and no obvious correlation is seen between deposition time and film roughness. For epitaxial Fe<sub>3</sub>O<sub>4</sub> thin films grown on Si with a TiN seed layer Reisinger *et al* [207] measured roughness values between 0.3 and 0.7 nm. In many technological applications, a low surface roughness is essential and improves the films desired optical and electronic properties [208]. The roughness associated with the Si substrate surfaces was typically determined to be between 0.5 nm and 1 nm for all the films. These values are within the range reported in the literature for commercially produced and polished Si wafers [209]. Although the Si substrates were chemically cleaned before film growth, it is possible that the surface of the substrates oxidised, resulting in the formation of an ultrathin layer of silicon oxide at the substrate–film interface. However, no evidence of such a layer can be seen in the fringe pattern.

Film thickness has been plotted as a function of deposition time in fig. 4.3.2. Fitting of this relationship can then be used to determine the growth rate of thin films at the 8 cm target-sample distance and under the specific conditions used. A linear fit to the experimentally determined thicknesses is plotted in fig. 4.3.2. It is seen that the data points fit this trend relatively well, however several points lie away from the best fit line by a factors that are larger than their associated error bars. These variations in growth rate may be as a result of several experimental factors, such as laser power fluctuations during growth or variations in the chamber pressure. For the laser fluence, chamber pressure and target-sample distance of 8 cm used, the average growth rate can be determined by the gradient of the linear best-fit line. Thus, the growth rate was determined to be (5.9  $\pm$  0.3) nm/min. The average growth rate can be used to calculate values for the thicknesses of the 10, 15 and 20-minute films that are too thick to be determined by XRR. The thickness of the 10 minute film is found to be (59  $\pm$  3) nm and for the 15 and 20-minute films, (89  $\pm$  5) nm and (118  $\pm$  6) nm, respectively.

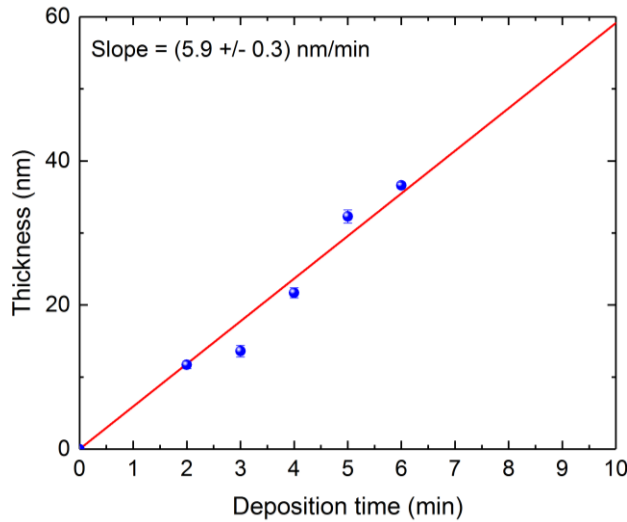


Figure 4.3.2. The relationship between deposition time and thickness for the films grown at a target-sample distance of 8cm. The red line represents a linear fit to the data points.

The resistances of the thin films grown are also displayed in table 4.1. The resistance of each film was measured by applying a current of 0.2 mA to the film and measuring the corresponding potential difference across the film. The current was applied by a Keithley 2601A SourceMeter and the voltage measured independently via an NI MyDAQ input interface. The thin films were contacted using a four-point probe technique [210]. The probe setup consists of four equally spaced (1 mm) metal tip contacts that are brought into contact with the thin film surface. A current is passed between the outer two contacts, with the voltage measured across the inner two. For a thin film, whose thickness ( $t$ ) is much smaller than the probe pin separation, as is the case for all the films grown in this work, the average film resistance ( $R_f$ ) is given by eqn. 4.2.

$$R_f = 4.17 \left( \frac{V}{I} \right) \quad \text{Eqn. 4.2}$$

Where the 4.17 is a geometrical factor that is dependent on the ratio of the sample width relative to the probe spacing and found from a table of standard ratios [210]. For each sample, the resistance was measured twice by applying the current in two different directions across the film, from left to right and top to bottom. The mean of these two values was taken and the range over which they varied used to determine the associated error value. It is evident from table 4.1 that the resistance of the films increases as the thickness increases. As theory states the relationship between resistance and film thickness is governed by eqn. 4.3 [211],

$$R_f = \frac{\rho_R}{t} \quad \text{Eqn. 4.3}$$

the resistance of the films should be inversely proportional to the film thickness. Hence, this relationship is investigated by plotting  $1/R_f$  against thickness, as shown in fig. 4.3.3. The film resistivity ( $\rho_R$ ) can also be found from the relation in eqn. 4.3.

Fig. 4.3.3 shows very clearly a linear relationship between film thickness and the inverse of the film resistance as anticipated. Interestingly the best-fit line intercepts the x-axis at a thickness value of 8nm, suggesting that the resistance of the film becomes much larger below this thickness. This perhaps indicates the presence of a dead layer, with the magnetic dead layer having a much higher resistivity than the rest of the film.

The slope of the linear relation in fig. 4.3.3, can be used, in accordance with eqn. 4.3, to calculate a value for the resistivity of the films grown.  $\rho_R$  is calculated to be  $(6.3 \pm 0.3) \times 10^{-4} \Omega \cdot \text{m}$ , which corresponds well to the range of resistivities reported in the literature for magnetite, with Morris and Williams reporting  $4 \times 10^{-4} \Omega \cdot \text{m}$  for polycrystalline samples [212] and Samura reporting  $4 \times 10^{-5} \Omega \cdot \text{m}$  for single crystal  $\text{Fe}_3\text{O}_4$  [213]. This provides a strong indication that the samples grown are

$\text{Fe}_3\text{O}_4$  and not a phase of  $\text{Fe}_2\text{O}_3$ , that is known to have much higher resistivity, of the order of  $200 \text{ } \Omega\cdot\text{m}$  [214]. The reason for this is that the  $\text{Fe}_2\text{O}_3$  does not possess the ability for hopping conduction that is possible in  $\text{Fe}_3\text{O}_4$ , due to the presence of both  $\text{Fe}^{2+}$  and  $\text{Fe}^{3+}$  at the octahedral sites.

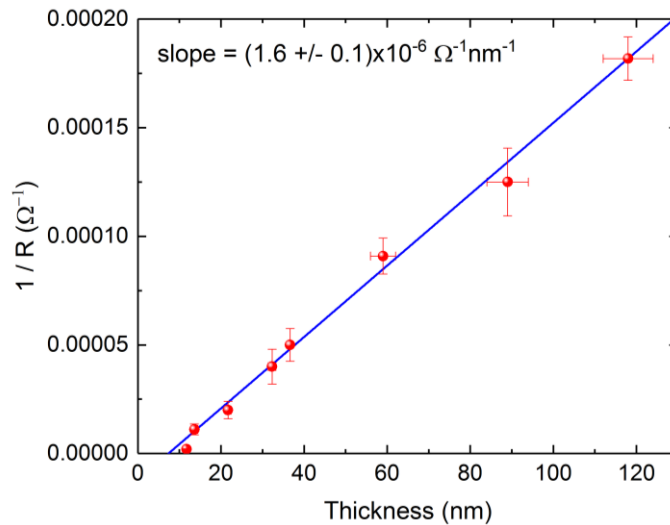


Figure 4.3.3. Graph showing the relationship between film thickness and  $1/R$  for the films grown at a target-sample distance of 8 cm. The blue line represents a linear fit to the data points.

XRD measurements performed on all eight films show the expected Si substrate peaks, however, no other diffraction peaks could be easily observed. Some samples show a weak broad peak at the angle associated with the magnetite (311) diffraction peak. This reflection is known to be the most intense for polycrystalline magnetite and can be used as a hallmark for the inverse cubic spinel structure [215]. These measurements then suggest that the samples are largely amorphous in nature, with some amount of polycrystalline ordering. This is not surprising given that the films were grown at RT and with a large lattice mismatch between the substrate and  $\text{Fe}_3\text{O}_4$  structure. Even with the presence of substrate heating, others have only grown polycrystalline  $\text{Fe}_3\text{O}_4$  thin films on Si (001) substrates [216] [217]. In order to grow epitaxial magnetite thin films one must grow on a substrate with a closer lattice match, such as MgO [200] [204].

Even for samples with readily indexed diffraction peaks, XRD cannot be used to easily distinguish between magnetite and maghemite due to their matching cubic crystal structure and very similar lattice constants [152]. As such, an alternative method is required to distinguish between the two phases, Raman spectroscopy, therefore, has been used. The Raman spectra of magnetite, maghemite and hematite are all distinctly different and thus can be used as a fingerprint to determine which phase or phases are present within the films [218] [219]. Magnetite is known to have 14 Raman active phonon modes. The most intense of which is the  $A_{1g}$  mode located at around  $672 \text{ cm}^{-1}$ . For Maghemite however this mode is still the most pronounced but is shifted to  $700 \text{ cm}^{-1}$ , with maghemite only having 5 Raman active modes. This shift then is often the easiest way to quickly distinguish between magnetite and maghemite using Raman spectroscopy [218]. Maghemite Raman spectra also display a broad peak at around  $1400 \text{ cm}^{-1}$ . There is no mode present for  $\text{Fe}_3\text{O}_4$  in this range of the spectrum, as such the presence of this peak can also be used to distinguish between the two phases. A relatively intense peak is also seen in this region for hematite, at  $1305 \text{ cm}^{-1}$  [220]. Hematite has a total of 7 Raman active modes, the most intense of which are typically at  $295 \text{ cm}^{-1}$  and  $229 \text{ cm}^{-1}$ , these being  $E_g$  and  $A_{1g}$  modes, respectively [218]. Raman spectra were acquired for the samples studied in this chapter, following the procedure outline in section 3.2.3. For direct comparison between samples the spectra were all normalised to the Si substrate peak at  $950 \text{ cm}^{-1}$ , and displayed in fig. 4.3.4.

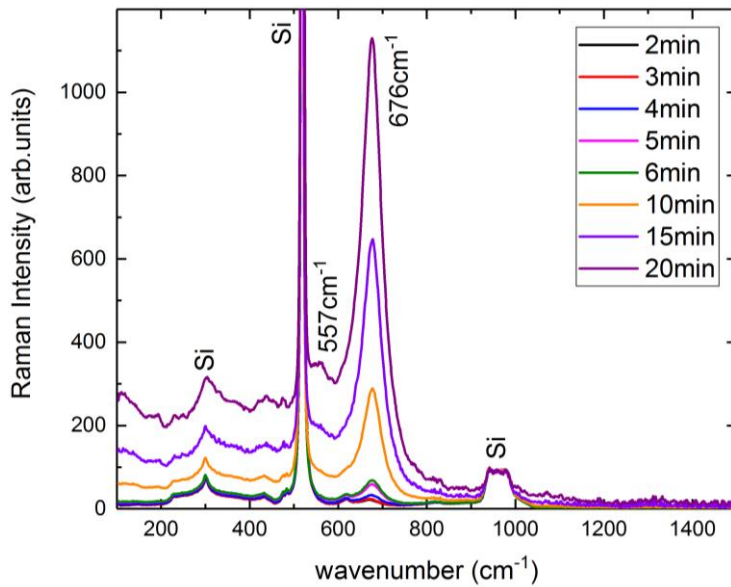


Figure 4.3.4. Graph showing the Raman spectra of the Fe<sub>3</sub>O<sub>4</sub> thin films, grown at a target-sample distance of 8 cm.

The Raman spectra, all have the prominent substrate peaks at 300 cm<sup>-1</sup>, 520 cm<sup>-1</sup> and 950 cm<sup>-1</sup>, with the 520 cm<sup>-1</sup> peak being by far the most intense. The spectra also show no sign of a peak in the range around 1300 – 1400 cm<sup>-1</sup>, this strongly indicates that the film has no maghemite or hematite phase. The strongest film peak in all spectra is located at 676 cm<sup>-1</sup>. This is within the narrow range of values reported in the literature for the A<sub>1g</sub> magnetite Raman mode [221]. Additionally with no peak present around 700 cm<sup>-1</sup>, which would represent the A<sub>1g</sub> mode in maghemite, this confirms that the films are single-phase magnetite in composition. To confirm this the magnetite T<sub>2g</sub> mode is seen at 557 cm<sup>-1</sup>. What is expected to be the third most intense magnetite mode, the E<sub>g</sub>, should be present at 310 cm<sup>-1</sup>, however, this peak cannot be easily distinguished as it lies under a more prominent substrate peak.

From observation of the 676 cm<sup>-1</sup> magnetite peak it is apparent that the Raman intensity of this mode increases significantly as the deposition time and hence the film thickness increases. It may be possible to correlate thickness to the Raman peak intensity and use this relation to indirectly determine the thickness of a magnetite thin film grown.

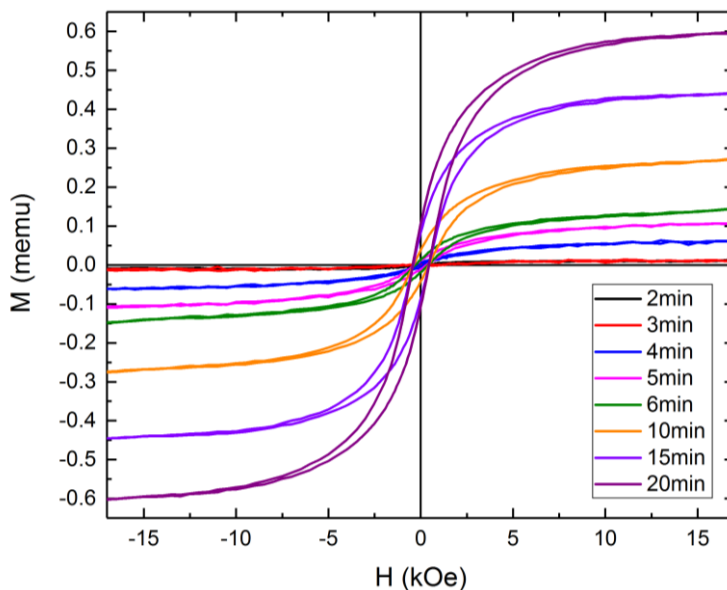


Figure 4.3.5. M(H) of the iron oxide thin films, grown at a target-sample distance of 8 cm.

VSM measurements performed on the samples are displayed in fig. 4.3.5. It is clear from the graph that  $M_s$  increases with increased sample deposition time as expected. The  $M_s$  values approximately scale linearly with sample thickness. By applying the sample thickness values previously determined, the saturation magnetisation per unit volume of each sample was calculated. The thickest of the samples have  $M_s$  values of 250 emu/cc. It may be expected that the  $M_s$  per unit volume would remain constant between samples, however it is seen that this reduces as the sample thickness is reduced. This effect may be indicative of a magnetically dead layer at the film-substrate interface. The  $M_s$  value of 250 emu/cc achieved is somewhat reduced compared to the theoretical bulk value for magnetite (480 emu/cc) [80], although this is anticipated given the films were grown at RT.

The coercivities of the films range between 100 to 450 Oe. These values are in the range of values reported in the literature for thin film magnetite samples [199] [222] [223] [203]. It is evident that  $H_c$  increases along with film thickness. A similar trend was also observed by Schemme *et al* [224], when studying  $Fe_3O_4$  films grown on MgO (001), who attributed this to strain affects caused by the substrate.

#### 4.3.2 Deposition time calibration at a 10 cm target-sample distance

Once the PLD growth system had been calibrated with a target-sample distance of 8 cm, the effect of changing target-sample distance was investigated. This was done by growing a series of samples with a larger target-sample distance of 10cm. Four samples were grown, under the same conditions as in section 4.3.1, with deposition times of 5, 10, 15 and 20 minutes. With a greater target-sample distance, it was anticipated that the growth rate of these films would be slower. Due to the increased distance, the ablated material reaches the substrate with a reduced kinetic energy. This may improve the films' properties and act to reduce the number of particulates.

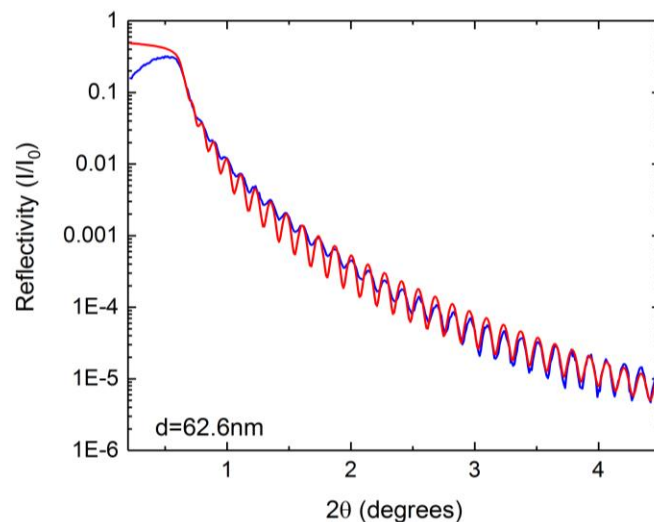


Figure 4.3.6. XRR measurement (blue) with fitted curve (red) for the 20-minute deposition time,  $Fe_3O_4$  on silicon thin film, grown at a 10cm target-sample distance.

XRR measurements performed on the four samples grown at this target-sample distance all display visible Kiessig fringes. The reflectivity data for the film grown with a 20-minute deposition time is shown in fig. 4.3.6. Good agreement is seen between the fit and experimental data for all four samples, allowing reliable film thickness values to be determined, as displayed in table. 4.2. In the table the roughness values, also determined by XRR, are stated, along with the measured resistances of the four films. Fitting to the 20-minute film XRR produces a thickness value of  $(62.6 \pm 0.6)$  nm, with clear Kiessig fringes visible at this thickness. For the samples grown at 8 cm this was not the case for samples of a comparable thickness, suggesting that the increased target-sample

distance acts to reduce the surface roughness of the films. Perhaps by the reduction in number and size of any particulates.

Deposition time (minutes)	Thickness (nm)	rms Surface roughness (nm)	Resistance (kΩ)
5	17.8 ± 0.3	0.16 ± 0.07	50 ± 5
10	27.3 ± 0.8	0.21 ± 0.05	40 ± 3
15	46.1 ± 0.4	0.09 ± 0.02	20 ± 1
20	62.6 ± 0.6	0.03 ± 0.01	16 ± 1

Table 4.2. Table showing the XRR determined thicknesses and surface roughness of each sample, grown at a 10 cm target-sample distance, as well as their measured resistances.

Through observation of the surface roughness values, table 4.2, it can be seen that indeed the roughness values are on average smaller than those measured for the films grown at an 8 cm distance. These results then suggest that the larger target-sample distance help reduce surface roughness. It is evident, again that the thickness of the samples increase as the deposition time is increased as expected.

Fig. 4.3.7, shows a linear relationship between deposition time and film thickness. At a 10 cm target-sample distance, this relationship gives a growth rate of (3.1 ± 0.1) nm/min, which is slower than the growth rate of the samples grown at 8cm for which a rate of (5.9 ± 0.3) nm/min was determined. These values indicate that the 2 cm increase in target-sample distance results in almost a 50% reduction in growth rate. Thus, as expected, the growth rate of the system is highly dependent on the target-sample distance.

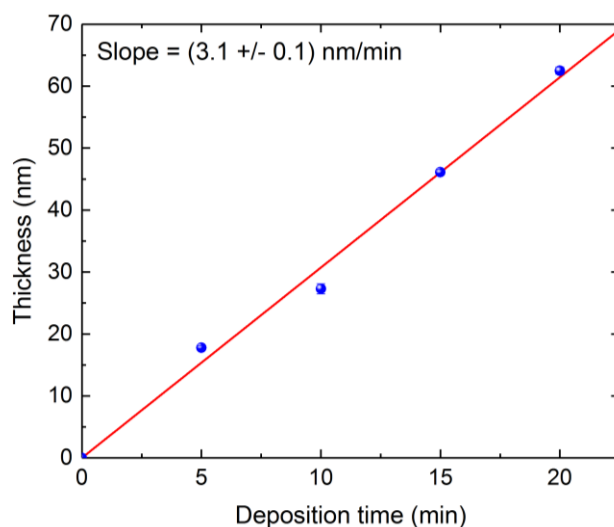


Figure 4.3.7. Graph showing the relationship between deposition time and thickness for the films grown at a target-sample distance of 10 cm. The red line represents a linear fit.

The resistance of these samples was also measured and are displayed in table 4.2. It is evident, as was the case for the samples grown at 8 cm, that the films’ resistance reduce with increased thickness. Again, by plotting the inverse of the resistance against film thickness, from the gradient of the linear fit a value for the resistivity of the films is calculated to be (1.0 ± 0.1)x10<sup>-3</sup> Ω·m., which is within the range of values reported in the literature for magnetite [212] [213].

To verify that the films were indeed single-phase magnetite Raman spectroscopy was performed. The Raman spectra obtained for the four films grown at a 10 cm target-sample distance are shown in fig. 4.3.8. It is apparent that the most prominent Fe<sub>3</sub>O<sub>4</sub> Raman mode is present for all four films at 676 cm<sup>-1</sup>, strongly indicating that the films are all single-phase magnetite. For the thicker films,

the shoulder of the  $T_{2g}$   $Fe_3O_4$  Raman active phonon mode can also be seen at  $557\text{ cm}^{-1}$ , further confirmation of the magnetite structure. As expected from the results for the films grown at  $8\text{ cm}$ , the  $A_{1g}$   $Fe_3O_4$  Raman peak height increases in intensity as deposition time and hence, film thickness is increased. It is apparent that this increase is non-linear, with the peak height increase becoming much larger for the thicker films. This relationship is investigated further in section 4.3.5.

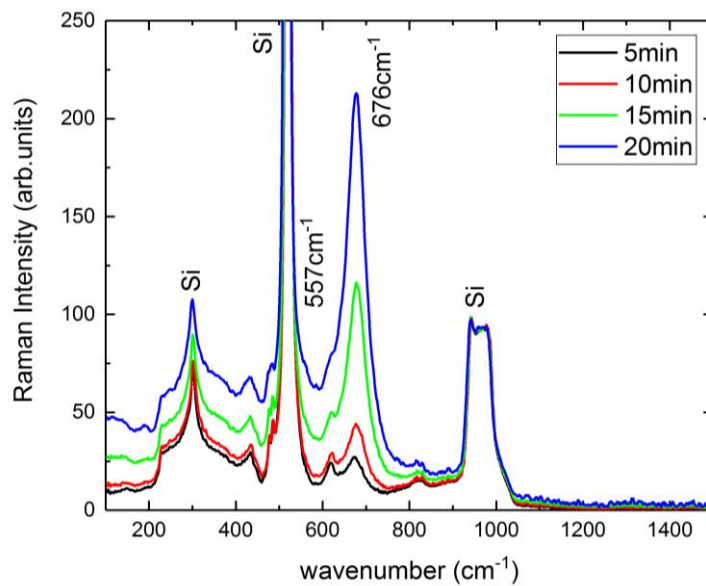


Figure 4.3.8. Raman spectra of the  $Fe_3O_4$  films, grown at a  $10\text{ cm}$  target-sample distance.

The magnetic properties of these samples were measured using VSM and the in-plane  $M(H)$  measurements, at RT, are shown in fig. 4.3.9. It is apparent, again, that  $M_s$  increases with film thickness and this increase is approximately linear in nature. Similar to the films grown at  $8\text{ cm}$ , the coercivities range between  $100$  and  $450\text{ Oe}$ , with  $H_c$  reducing for the thinner films.

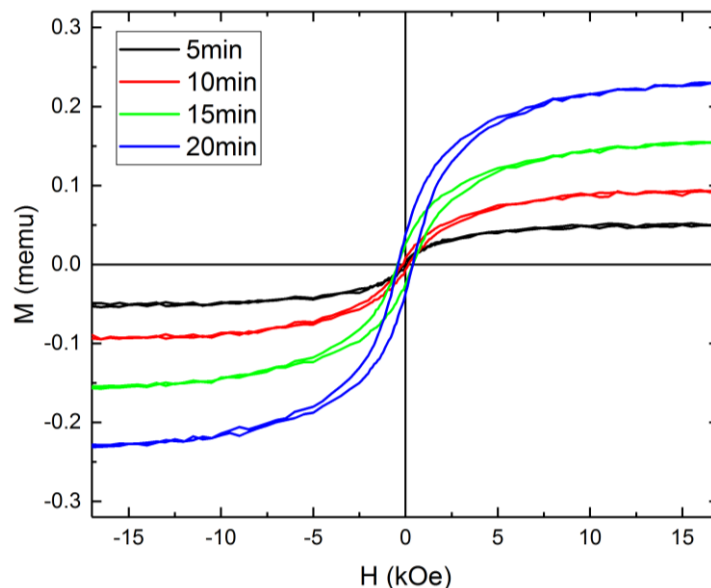


Figure 4.3.10. Graph showing the  $M(H)$  of the  $Fe_3O_4$  thin films, grown at a target-sample distance of  $10\text{ cm}$ .

Applying the film thickness values determined by XRR the saturation magnetisation per unit volume was calculated to be between  $130$  and  $200\text{ emu/cc}$ . These  $M_s$  values are comparable to those observed for the films of similar thickness in the series of films grown at  $8\text{ cm}$ . As the  $M_s$  per unit volume appears to reduce for the thinner films, this may again suggest the presence of a magnetically dead layer at the substrate-film interface.

In all, these results show little change in the films structural and magnetic properties, as a result of the increased target-substrate distance, other than the reduced growth rate. A reduction in surface roughness is observed, most likely due to the reduced incident energy of the plume of target material incident upon the sample surface.

### 4.3.3 Nitrogen growth pressure calibration

Once the system had been tested and calibrated as a function of deposition time and target-sample distance, the next logical step was to investigate the effect of growth pressure. As such, Fe<sub>3</sub>O<sub>4</sub> samples were grown as a function of an inert nitrogen partial pressure between 3x10<sup>-7</sup> mbar and 2x10<sup>-2</sup> mbar. Apart from the growth chamber partial pressure, all other growth parameters were kept constant, with a target-sample distance of 8 cm. Four samples were grown, each with a deposition time of 10 minutes, at partial pressures of 3x10<sup>-7</sup> mbar, 1x10<sup>-5</sup> mbar, 1x10<sup>-4</sup> mbar and 1x10<sup>-2</sup> mbar. It is anticipated that an increased pressure will reduce growth rate due to an increased number of collisions between the gas molecules and the species of the plume of target material. XRR measurements were performed to determine film thickness and surface roughness. These values are displayed in table 4.3. The films thicknesses decrease with increased growth pressure. We see a reduction in thickness of over 13 nm in the range of pressures used.

N <sub>2</sub> Growth pressure (mbar)	Thickness (nm)	rms Surface roughness (nm)	Resistance (kΩ)
3x10 <sup>-7</sup>	46.2 ± 0.8	0.15 ± 0.05	12 ± 1
1x10 <sup>-5</sup>	39.9 ± 0.5	0.26 ± 0.04	30 ± 2
1x10 <sup>-4</sup>	33.5 ± 0.6	0.12 ± 0.03	50 ± 5
1x10 <sup>-2</sup>	32.9 ± 0.8	0.28 ± 0.07	2500 ± 500

Table 4.3. Table showing the XRR determined thicknesses and surface roughness of each sample, grown as a function of nitrogen partial pressure, as well as their measured resistances.

The increase in nitrogen partial pressure does then affect the growth rate as anticipated, but the question to be now asked is what other effect the nitrogen partial pressure has on the properties of the films grown. The surface roughness values are comparable in magnitude to those measured for the films grown as a function of time. Additionally no obvious correlation can be found between surface roughness and the nitrogen growth pressure.

The resistances of the three films grown at 3x10<sup>-7</sup> mbar, 1x10<sup>-5</sup> mbar and 1x10<sup>-4</sup> mbar are very similar to the values measured for the films grown as a function of time, when taking into account their thickness. The resistivity of the film grown at the highest nitrogen pressure however, is much larger. The resistance measured for the film grown in the 1x10<sup>-5</sup> mbar oxygen partial pressure was 25 ± 5 kΩ, this is two orders of magnitude smaller than that of the 1x10<sup>-2</sup> mbar grown film, which has within error the same thickness. As such, the resistivity of this film must be of the order of a hundred times greater than the other films, implying that the higher nitrogen partial pressure has affected the structure of the thin film grown.

The Raman spectra, measured for the four films are shown in fig. 4.3.10. It is immediately apparent that the characteristic Fe<sub>3</sub>O<sub>4</sub> A<sub>1g</sub> peak is present for all films. There is also no clear evidence of the presence of any hematite or maghemite related Raman peaks. The Fe<sub>3</sub>O<sub>4</sub> A<sub>1g</sub> peak reduces in magnitude as the growth pressure is increased. This is, at least in part, due to the thickness of the films reducing with increased pressure. The sample with the much higher film resistance, grown at a pressure of 1x10<sup>-2</sup> mbar, however, has an A<sub>1g</sub> Fe<sub>3</sub>O<sub>4</sub> peak intensity that is smaller than expected when comparing to a film in the original series of comparable thickness. This further suggests that

this higher  $N_2$  partial pressure film has different structural properties to the others. Although the Raman shows that, the film is at least in part  $Fe_3O_4$  and does not contain any observable  $Fe_2O_3$  phase.

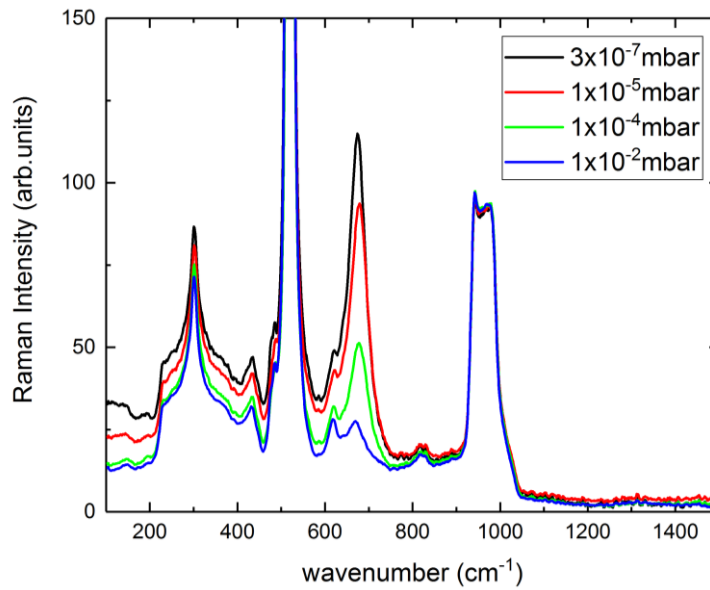


Figure 4.3.10. Raman spectra of the  $Fe_3O_4$  films, grown as a function of nitrogen partial pressure.

In fig. 4.3.11, the in-plane  $M(H)$  measurements performed at RT are shown. The magnetisation per unit volume is plotted for direct comparison between samples. If the four films all had the same composition and structure, one would expect the hysteresis loops to be identical. This is evidently not the case and in fact, we see that  $M_s$  reduces as the growth pressure is increased. The  $M_s$  of the sample grown at  $3 \times 10^{-7}$  mbar is of a similar order to that typically seen for the samples grown as a function of time, at 150 emu/cc, but as the growth pressure increases  $M_s$  is reduced and is as small as 30 emu/cc for the  $1 \times 10^{-2}$  mbar film. These results suggest that the presence of the inert nitrogen acts in some way to affect the magnetic structure of the film grown.

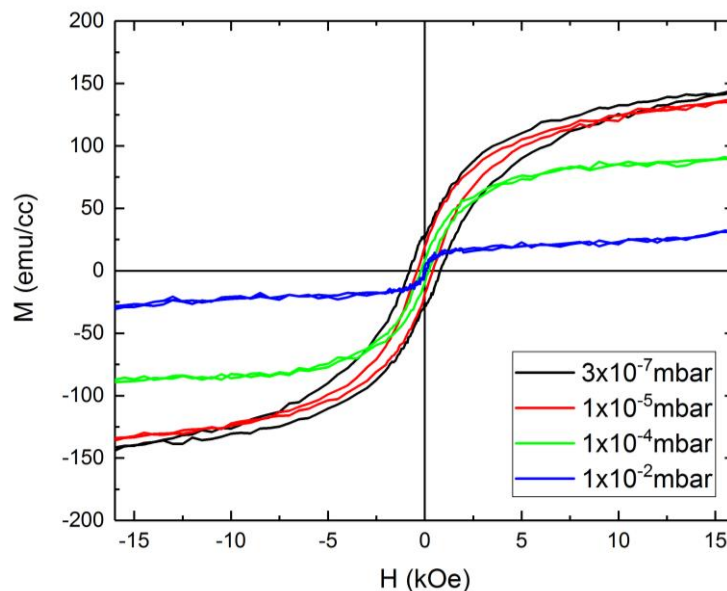


Figure 4.3.11.  $M(H)$  of the  $Fe_3O_4$  thin films, grown as a function of nitrogen partial pressure.

#### 4.3.4 Film properties as function of sample thickness

For the series of films grown in an oxygen partial pressure both at distances of 8 and 10 cm,  $M_s$  has been investigated as a function of film thickness and is plotted for both series of films in fig. 4.3.12.

It is evident that in the two cases the magnetisation increases linearly with film thickness. The relationship for the samples grown at a target-sample distance of 8cm is shown in fig. 4.3.12(a). Data points of all samples are within error of the linear fit line. It is clear from the figure that the best fit line does not pass through the origin. The line intercepts the x-axis at a thickness value of 10nm, suggesting that the films have a 10nm magnetically dead layer. The presence of a dead layer was also suggested by the differences in magnetisation per unit volume values, as well as the films resistance measurements shown in fig. 4.3.3. A dead layer formed at the interface between substrate and film may result from an intermediate structure forming in this region as the lattice transitions between the substrate and film. This layer may form due to strain, the presence of a silicon oxide layer on the substrate surface, pre-deposition or the ballistic collisions with the substrate surface by the high-energy plume material during deposition, creating a mixed layer.

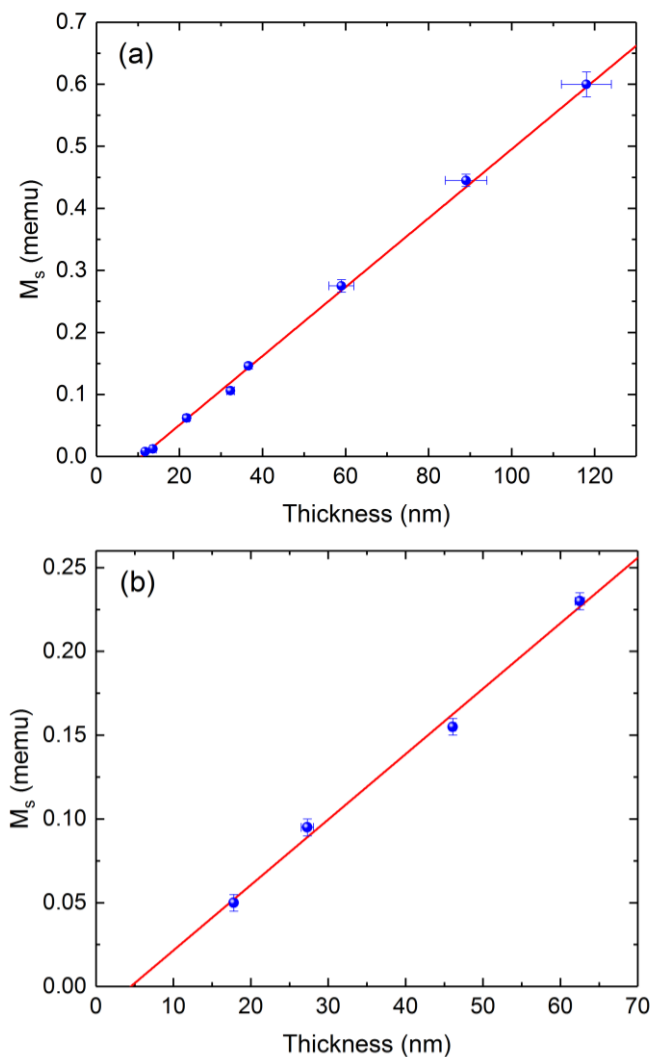


Figure 4.3.12. Graphs showing the relationship between deposition time and thickness for films grown at a target-sample distance of (a) 8 cm and (b) 10 cm.

Alternatively, Parkin *et al* [225] observed a 15 nm dead layer at the surface of magnetite thin films. They find no evidence that these surface layers are different structurally from the bulk of the film, however, they observe a higher number of defects in the surface region as a result of the oxidation process and attribute the dead layer formation to this. The exact effects of intrinsic defects on the magnetic properties of  $Fe_3O_4$  thin films is still an uncertain topic [226] and the magnetic properties of a surface or interface is thought to be strongly dependent on the surface reconstruction [226]. It is of course also possible that the total dead layer measured is a combination of both interface and surface dead layers. Further investigation using techniques such as cross-sectional

transmission electron microscopy are required to gain a more detailed understanding of the films structure and dead layer formation.

The  $M_s$  - thickness relationship for the samples grown at a 10 cm target-sample distance, shown in fig. 4.3.12(b), is again linear. The best-fit line fits closely to all the data points and it can be seen that the line intersects the x-axis at a thickness value of 4 nm. This suggests that for the samples, grown at an increased target-sample distance, the magnetic dead layer is smaller. It is possible that this reduction in the dead layer thickness is a consequence of the reduced plume energy upon incidence with the sample surface. As such, for the growth of future films the target-substrate distance will be an important consideration, with a balance between growth rate and dead layer reduction required. Naturally, for ultra-thin films the dead layer will have a greater effect on the films overall properties.

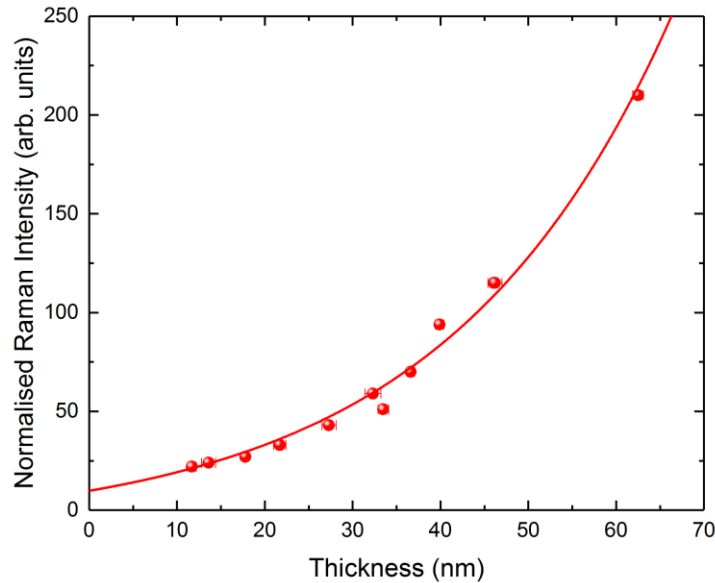


Figure 4.3.13. The normalised Raman intensity of the  $\text{Fe}_3\text{O}_4$   $A_{1g}$  phonon mode as a function of film thickness, for the  $\text{Fe}_3\text{O}_4$  films grown on silicon.

Previously, it was noticed that the intensity of the  $A_{1g}$   $\text{Fe}_3\text{O}_4$  Raman peak increased with film thickness and that this increase was non-linear. To investigate this further the Raman intensity of the  $A_{1g}$  peak was measured, after the spectra had been normalised, then plotted against film thickness, in fig. 4.3.13. This reveals that the increase in peak intensity with film thickness is exponential. The literature in fact suggests an exponential relationship should be observed via the Beer-Lambert law [227] [228]. The Raman response of thin films typically includes a contribution from the substrate due to the laser excitation penetrating through the film to the substrate. When this is the case, the attenuation effects of the film have been used to determine the films thickness. The film layer attenuates the intensity of the laser light passing through it according to the Beer-Lambert law [228].

$$I_{sub} \propto -e^{-\frac{4\pi k_1}{\lambda_{sub}}d} \quad \text{Eqn. 4.4}$$

which states that the intensity of the substrate peak  $I_{sub}$  is proportion to the exponential of the film thickness,  $d$ . Here  $\lambda_{sub}$  is the wavelength of the substrate scattered light and the  $k_1$  parameter is the imaginary part of the films complex refractive index.

In fig. 4.3.13, using an exponential function to fit the data points, it is seen that the points do indeed fit well to the exponential relationship and the Beer-Lambert law is upheld. As such, this relationship may be used for determining values of film thickness. Of course, this method of thickness determination is not as reliable as XRR but may be useful when the films are too thick to measure with XRR.

### 4.3.5 Fe<sub>3</sub>O<sub>4</sub> film grown with substrate heating

Once, the basic conditions and set up of the growth chamber had been tested, the substrate heating system was constructed and calibrated. As such, an attempt was made to grow an epitaxial Fe<sub>3</sub>O<sub>4</sub> thin film. In order to achieve this a substrate with a close lattice match to the magnetite structure was needed. MgO (001) was used as it is known to have a lattice constant that is almost exactly half that of Fe<sub>3</sub>O<sub>4</sub> [224]. The sample was grown at a target-substrate distance of 8cm and with a laser fluence of 3Jcm<sup>-2</sup>, in an oxygen partial pressure of 1x10<sup>-5</sup> mbar. The substrate was outgassed at a temperature of 250°C for 1 hour prior to growth and the film was grown at a temperature of 400°C for a deposition time of 8 minutes. This deposition time was chosen to ensure that the film was thin enough for its thickness to be measured by XRR and the other growth conditions were decided upon through observation of the growth conditions detailed in the literature [229] [203] [200].

The XRR measurement taken on the film grown is shown in fig. 4.3.14. For the fitting of the reflectivity curve, the density of the MgO substrate was taken to be 3.58 gcm<sup>-3</sup> [230]. The curve has clearly visible Kiessig fringes that when fitted reveal a film thickness of (33.6 ± 0.6) nm. The fitting procedure also suggests a film surface roughness of (0.20 ± 0.05) nm, which is well matched to the values found for the films grown on Si and very similar to those measured by Bertram *et al* [204] for Fe<sub>3</sub>O<sub>4</sub> thin films grown on MgO (001).

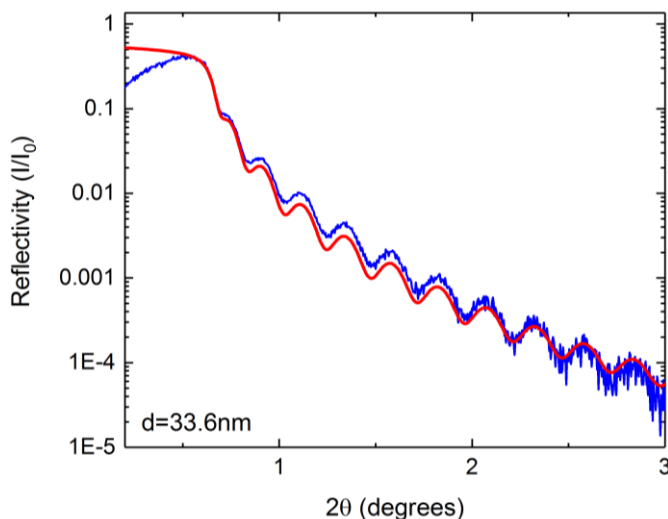


Figure 4.3.14. XRR (blue) with fitted curve (red) for the Fe<sub>3</sub>O<sub>4</sub> film grown on MgO (001).

XRD 2θ/ω measurements performed on the sample are displayed in fig. 4.3.15. These show that the film has an epitaxial crystal structure. The only peaks present are the MgO substrate (002) and (004), as well as two peaks that are higher in angle than the two substrate peaks, which correspond to the (004) and (008) magnetite diffraction peaks. As previously discussed, it is difficult to distinguish between magnetite and maghemite using XRD due to their crystal structures. Bertram *et al* [204] have seen very similar diffraction patterns to those measured here, for Fe<sub>3</sub>O<sub>4</sub> thin films grown on MgO (001). We see that the film peaks appear broader than the substrate peaks due to the films finite thickness. The positions of the film (004) and (008) peaks are 43.2° and 95.0°, respectively. These peak positions can then be used, by applying the method outlined in section 3.2.2.1, to determine the lattice constant of the film along the direction normal to the film plane. This is calculated to be (8.36 ± 0.02) Å, which is close to the Fe<sub>3</sub>O<sub>4</sub> bulk value of 8.396 Å [204] [206] and is within the range of values measured in the literature for magnetite thin films [203] [231] [204]. It was also expected that the lattice constant of the film would be lower than the bulk value, due to the strain from the substrate due to the 0.4% lattice mismatch.

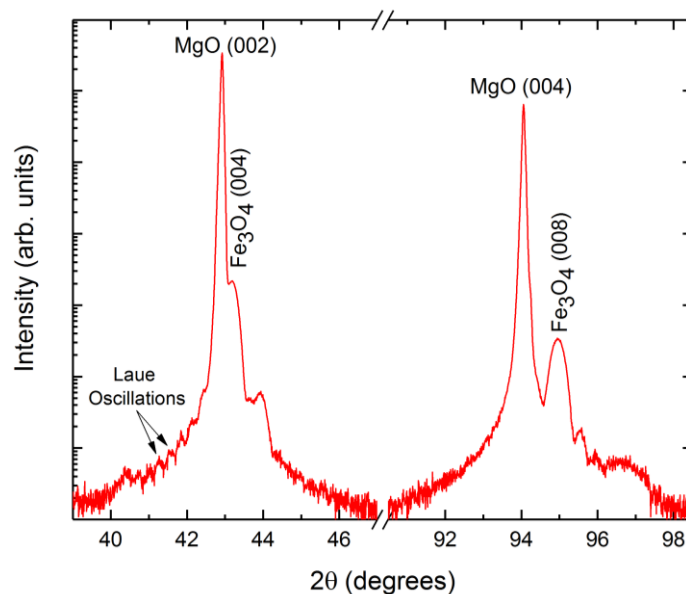


Figure 4.3.15. XRD measurement for the  $\text{Fe}_3\text{O}_4$  film grown on MgO (001).

Taking a closer look at the  $2\theta/\omega$  measurements, a fringe pattern can be seen about the Bragg peaks. These fringes are identified to be Pendellösung fringes, which are only present if the film is of high crystalline quality and suggest that the film has good homogeneity [204]. Pendellösung fringes are analogous to the Kiessig fringes observed via XRR, and appear as a result of interference phenomena, but in this case are specific to the crystalline phase [232].

A rocking curve measurement was performed about the film (008) diffraction peak. This is shown in fig. 4.3.16. The FWHM of the reflection was determined from the figure to be  $(0.10 \pm 0.01)^\circ$ . This small breadth of the film reflection indicates that the atomic plane spacing is relatively uniform throughout the film, with little relaxation towards the bulk. The low FWHM value ultimately suggests a high degree of orientation quality and is comparable to those reported in the literature for the high quality, epitaxial  $\text{Fe}_3\text{O}_4$  thin films that have been grown [233] [234].

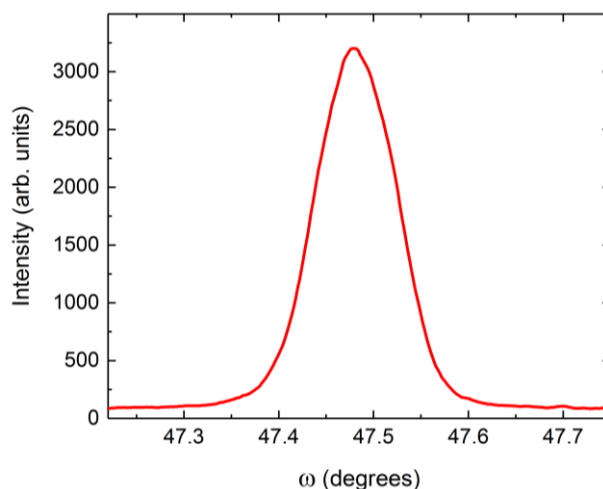


Figure 4.3.16. XRD rocking curve taken at the (008) diffraction peak, for the  $\text{Fe}_3\text{O}_4$  film grown on MgO (001).

The Raman spectrum of the sample, fig. 4.3.17, was measured, with the three most prominent  $\text{Fe}_3\text{O}_4$  Raman active phonon modes all clearly present. These three modes are the only three magnetite modes that could be observed by Jubb and Allen [218]. The intense  $A_{1g}$  peak is present at  $674\text{ cm}^{-1}$ , when combined with the previous XRD results confirms that the film is  $\text{Fe}_3\text{O}_4$  and the absence of any Raman peak that can be associated with either hematite or maghemite suggests that the film is single phase magnetite. Peaks are also seen in the spectra at both  $556\text{ cm}^{-1}$  and  $314\text{ cm}^{-1}$  which coincide with the positions reported in the literature for the  $T_{2g}$  and  $E_g$  modes,

respectively [221]. It is also worth noting that no peaks are present due to the MgO substrate, as MgO has a rock-salt structure and hence shows no first order Raman effect [235].

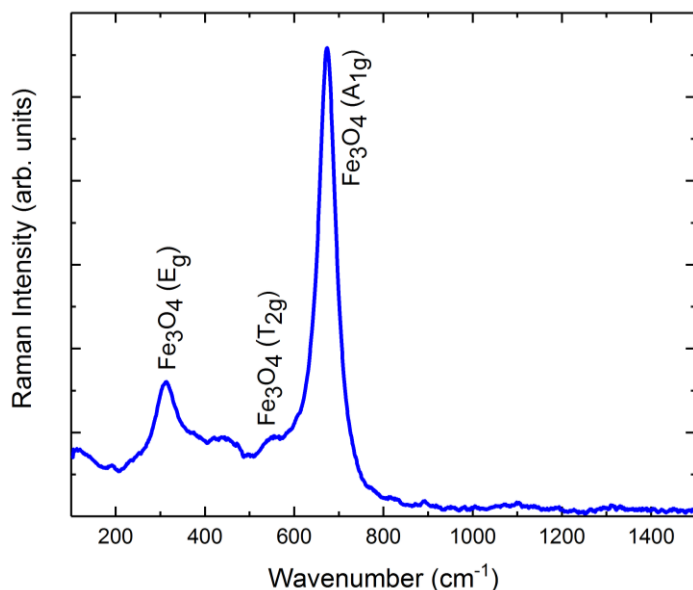


Figure 4.3.17. Raman spectrum measured for the Fe<sub>3</sub>O<sub>4</sub> film grown on MgO (001).

The magnetic properties of this Fe<sub>3</sub>O<sub>4</sub> film were investigated by VSM. The in-plane M(H) measurement is shown in fig. 4.3.18. This indicates an M<sub>s</sub> of (290 ± 30) emu/cc, which is smaller than the theoretical bulk value for magnetite (480 emu/cc) [80]. However, it is larger than the values obtained for the films grown on Si at RT. The M<sub>s</sub> for this film is actually comparable to values measured by Mauit *et al* [236] for Fe<sub>3</sub>O<sub>4</sub> on MgO. Matsuzaki *et al* [25] also observed a saturation magnetisation that was reduced from bulk, when measured as-grown, however an increase in M<sub>s</sub> was seen as a consequence of annealing the sample producing a bulk like stoichiometry.

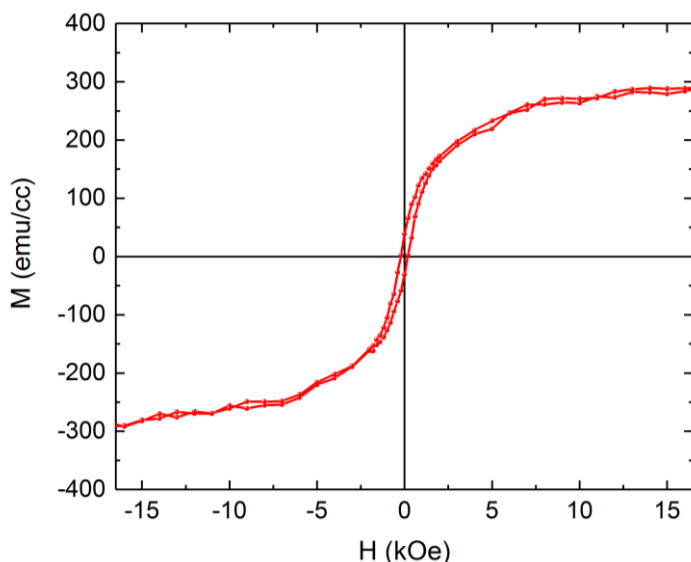


Figure 4.3.18. Graph showing the M(H) of the iron oxide thin film, grown on MgO (001).

It is noted that the magnetisation of the sample may not be completely saturated at the maximum field of 17 kOe displayed in fig. 4.3.18, as as-grown magnetite samples have been known to be difficult to saturate [25]. The reduced M<sub>s</sub> compared to bulk and high field required for saturation indicates that defects and anti-phase boundaries are likely present [25]. As was the case for the films grown on Si, it is possible that a dead layer may be present that would account for the reduced M<sub>s</sub>. The coercivity of the sample was measured to be (200 ± 20) Oe. This is within the range of

coercivities reported for magnetite thin films in the literature [199] [222] [223] [203] and is comparable to the values measured for films of a similar thickness grown on Si.

The resistance of the film was measured to be  $(27.6 \pm 0.4)$  k $\Omega$ , which results in a film resistivity of  $9.3 \times 10^{-4}$   $\Omega \cdot \text{m}$ , that corresponds well to the resistivities reported in the literature for magnetite, in the range of  $4 \times 10^{-4}$   $\Omega \cdot \text{m}$  for polycrystalline samples [212] [213], much lower than the resistivity of  $\text{Fe}_2\text{O}_3$  [214]. Using the four-point probe setup, the films magneto-transport properties were also investigated by the magnetoresistance (MR). The MR is found by measuring the resistance as a function of the applied magnetic field. For the measurements performed here, the field was applied normal to the film plane (out of plane). The MR is defined as  $[R(H)-R(0)]/R(0)$ , where  $R(H)$  and  $R(0)$  are the resistance with and without the applied magnetic field. MR measurements performed on magnetite have been shown in the literature to provide insight into the presence of structural effects within the sample measured [25] [237] [229]. The presence of a negative MR is widely accepted to be a result of the existence of antiphase domain boundaries (APBs) in the film, which are structural defects formed during growth [25]. A strong antiferromagnetic coupling across the APBs is considered to be the cause of both a negative MR and the high saturation magnetic fields seen for  $\text{Fe}_3\text{O}_4$  thin films [25]. As such, the form of the films MR relationship can provide insight into the presence and number of APBs within the sample.

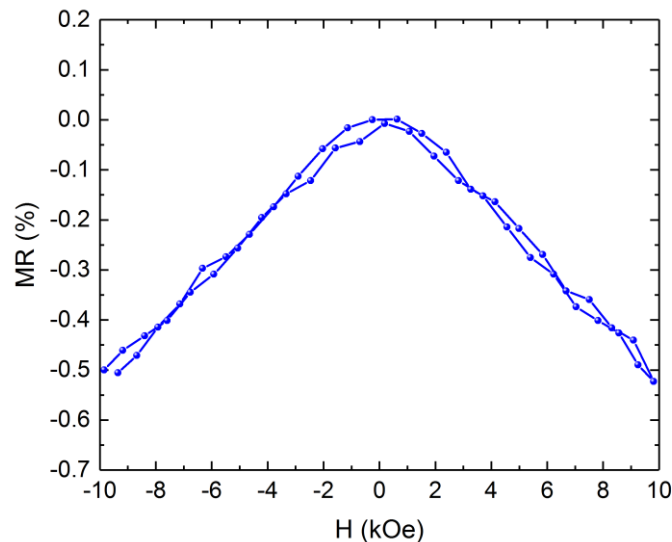


Figure 4.3.19. Graph showing the magnetoresistance, at 300 K, of the iron oxide thin film, grown on MgO (001).

The magnetoresistance measured for the epitaxial  $\text{Fe}_3\text{O}_4$  film is shown in fig. 4.3.19. Measurements of the resistance were taken between -10 and 10 kOe for numerous applied currents to ensure repeatability. It is apparent from the figure that we see a negative MR that increases with increased field strength. This relationship is consistent with that observed by others for the MR of magnetite thin films [236] [25] [237] [229]. In the bulk single crystal case, ideally zero magnetoresistance would be observed [237] [229], however the presence of APBs within a thin film result in the negative MR. As such, this result suggests the presence of antiphase boundaries within the film. This is not surprising, given that Matsuzaki *et al* [25] observed a similar effect, which was then reduced, or even removed, by post-annealing. For our film, at a field of 10 kOe an MR of 0.5% is measured, which is closely comparable to that observed by Matsuzaki *et al* [25] for their  $\text{Fe}_3\text{O}_4$  (111) films grown on YSZ. The MR measured here is in fact smaller than the 1.5% measured by Mauit *et al* [236] and 0.8% by Ziese and Blythe [229] for films grown on MgO. This indicates that although the film likely contains APB defects, as are common in most if not all as-grown  $\text{Fe}_3\text{O}_4$  films, their number is relatively low and can likely be reduced through post-annealing.

Collectively, the characterisation of this film shows that the PLD chamber developed meets the standards required and is capable of growing high quality epitaxial magnetite thin films with properties comparable to the  $\text{Fe}_3\text{O}_4$  thin films studied in the literature [226] [204] [218] [203] [25]. Annealing of the samples, under the right conditions, should also lead to a further enhancement in the films quality and further optimisation of the growth parameters should also enhance the films properties, but this is beyond the scope of this project.

#### 4.3.6 $\text{SrCo}_2\text{Ti}_2\text{Fe}_8\text{O}_{19}$ hexaferrite thin film growth

As a proof of concept, an M-type hexaferrite thin film has been grown by simulating growth conditions that have been reported in the literature to successfully produce high quality M-type hexaferrite thin films [133] [24] [17]. The film was again grown at a target-sample distance of 8 cm and with a laser fluence of  $3 \text{ Jcm}^{-2}$ . The target used had the chemical composition of  $\text{SrCo}_2\text{Ti}_2\text{Fe}_8\text{O}_{19}$ , chosen as it has been discovered to display strong ME coupling at room temperature [10] [24]. The film was grown on a  $\text{Al}_2\text{O}_3$  (0001) substrate as this has been commonly used in the literature, although the lattice mismatch between strontium ferrite (SrM) and  $\text{Al}_2\text{O}_3$  is large at 23% [122] [24]. An oxygen growth partial pressure of  $1 \times 10^{-4}$  mbar was used as oxygen pressures in this range have been shown to successfully produce M-type hexaferrite growth [24] [20] [238]. The film was grown with a substrate temperature of  $750^\circ\text{C}$  for a deposition time of 15 minutes.

XRR was used to determine the films thickness. Kiessig fringes were present in the reflectivity data and although weak could be used to determine a film thickness of  $(70 \pm 2)$  nm. At this point XRD measurements were performed, revealing that the film was a mixture of both M-type hexaferrite and cobalt ferrite phases. This is not surprising given that the complex hexaferrite structure is difficult to form and the mechanisms involved are not fully understood [6]. According to Pullar, M-type hexaferrite forms as the dominant phase between  $900^\circ\text{C}$  and  $1100^\circ\text{C}$  with  $\text{CoFe}_2\text{O}_4$  as a secondary phase. However, below  $800^\circ\text{C}$   $\text{CoFe}_2\text{O}_4$  becomes a dominant phase [6]. As such, to remove or reduce the cobalt ferrite phase, sources in the literature anneal the samples in the range between  $900^\circ\text{C}$  and  $1100^\circ\text{C}$  [24] [107]. Given this, the sample was post-annealed in a tube furnace at  $1050^\circ\text{C}$  for 1 hour, whilst an oxygen partial pressure of  $1 \times 10^{-2}$  mbar was controlled.

The XRD  $2\theta/\omega$  measurement is shown in fig. 4.3.20(a). This reveals the presence of numerous M-type hexaferrite (00n) diffraction peaks, with no other M-type peaks present this suggests that the film is epitaxial in nature. The intense sapphire (0006) substrate peak is also clearly identified. Four other diffraction peaks are also present and have been labelled with \*, these can be indexed to the cobalt ferrite (111), (222), (333) and (444) reflections. These are reduced in intensity compared to the M-type hexaferrite peaks, however, it is clear that a secondary phase of  $\text{CoFe}_2\text{O}_4$  is still present within the film but this is greatly reduced compared to the sample as-grown. Cobalt ferrite is a secondary phase that is commonly encountered when growing cobalt substituted hexaferrites and is also observed in some of the samples grown by collaborators in Boston, as well as by both Mohebbi *et al* [239] and Stibbe [240]. It is evident that further optimisation of the growth and post-annealing procedure is required in order to remove the cobalt ferrite secondary phase but the XRD shows that the PLD system is capable of growing epitaxial M-type hexaferrite films.

Given that the M-type hexaferrite film is epitaxial, the positions of the XRD peaks can be used as described in section 3.2.2.1, to determine its lattice constant normal to the film plane,  $c$ . To achieve this a plot of  $l^2$  against  $\sin^2 \theta$  for the M-type hexaferrite peak positions is used, as shown in fig. 4.3.21(b). It is seen that all the points fit well to a linear relationship, suggesting that the peaks are appropriately indexed. Analysis produces a lattice constant of  $(22.9 \pm 0.1) \text{ \AA}$ , which compares well to the literature with  $23.03 \text{ \AA}$  quoted by Pullar for SrM [6] and Wang *et al* [10] determining a value of  $23.102 \text{ \AA}$  for bulk  $\text{SrCo}_2\text{Ti}_2\text{Fe}_8\text{O}_{19}$ .

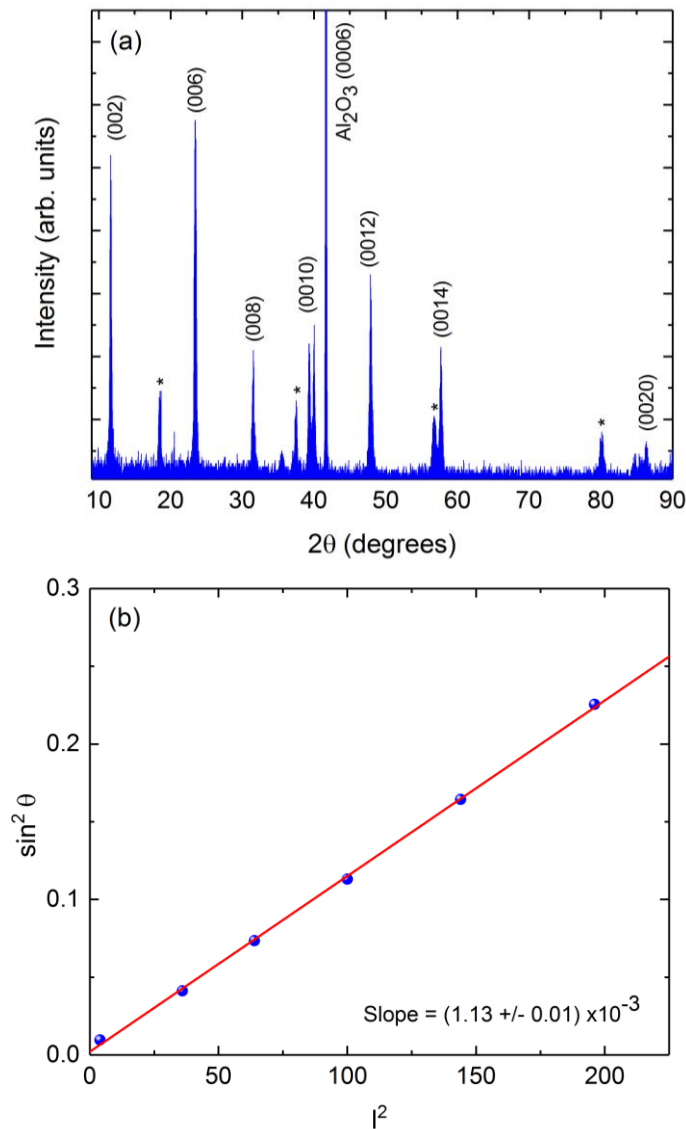


Figure 4.3.20. (a) XRD measurement for the  $\text{SrCo}_2\text{Ti}_2\text{Fe}_8\text{O}_{19}$  film grown on  $\text{Al}_2\text{O}_3$  (0001). (b) Plot of  $I^2$  against  $\sin^2 \theta$  for the M-type hexaferrite peak positions.

Fig. 4.3.21(a) shows the rocking curve measurement performed at the M-type hexaferrite (006) diffraction peak. A FWHM of  $(1.2 \pm 0.1)^\circ$  was determined for this reflection which is of the order observed by Dorsey *et al* for  $\text{BaFe}_{12}\text{O}_{19}$  grown on sapphire (0001) [20]. Suggesting that the film is of good crystalline quality and has a reasonably low orientation distribution.

A pole figure measurement was also performed on the M-type (006) diffraction peak to analyse the crystallographic texture of the film, as shown in fig. 4.3.21(b). At the centre of the pole figure a narrow intense point is seen, corresponding to the (006) reflection itself, suggesting a highly textured film. The pole figure measurement shows six further diffraction spots on a ring of  $30^\circ$  in the tilt angle ( $\chi$ ) and separated by  $60^\circ$  in the sample rotation angle ( $\varphi$ ) revealing a six-fold symmetry. This six-fold symmetry is due to the hexagonal structure of the hexaferrite, the presence of which confirms the epitaxial nature and high texture of the film [241]. The same symmetry is also seen for the (006) and (008)  $\text{BaFe}_{12}\text{O}_{19}$  diffraction peaks for high quality films grown on sapphire by Chen *et al* [242], with Geiler *et al* [122] obtaining the pole figure pattern for the (107) diffraction peak. No other peaks are visible in the measured range of tilt and rotation angles. This suggests that the film has a high degree of in-plane orientation.

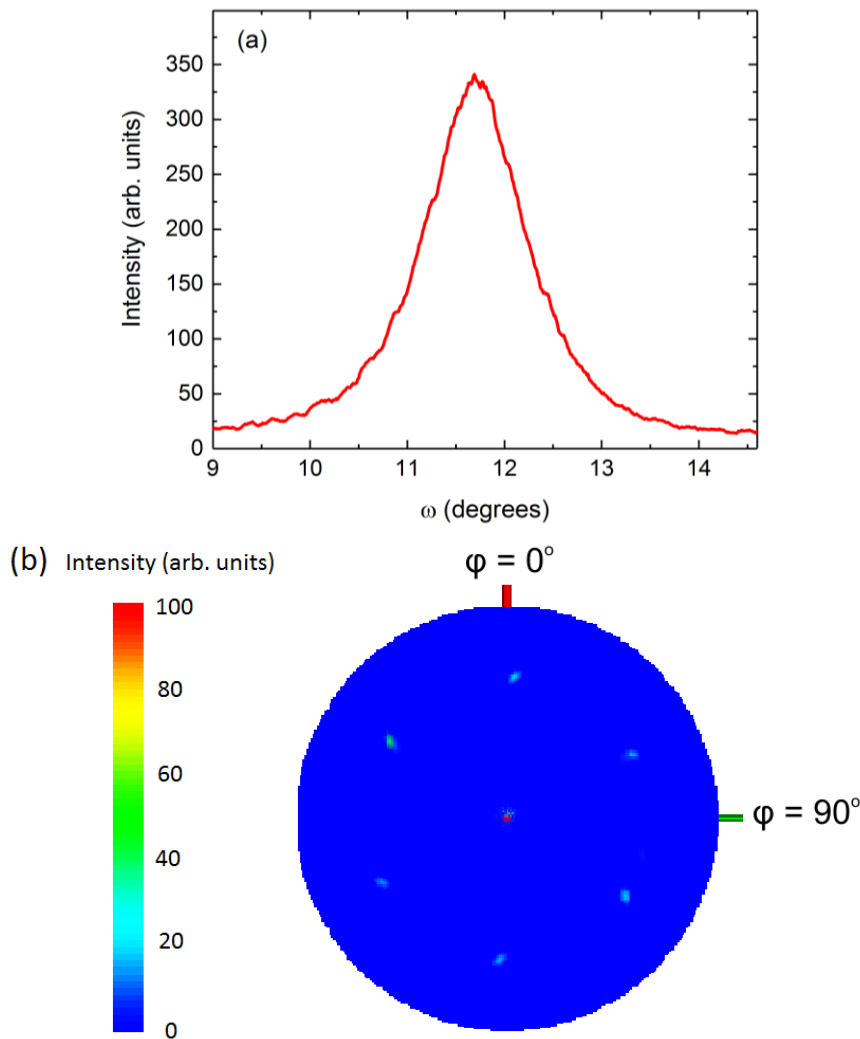


Figure 4.3.21. (a) XRD rocking curve measurement, (b) pole figure measurement performed at the (006) diffraction peak, for the  $\text{SrCo}_2\text{Ti}_2\text{Fe}_8\text{O}_{19}$  film grown on  $\text{Al}_2\text{O}_3$  (0001).

A film's texture can strongly influence its material and magnetic properties [151]. As such the samples  $M(H)$  characteristics have been studied and shown in fig. 4.3.22, for both in and out of plane geometries. The measurements show a saturation magnetisation at room temperature of  $(80 \pm 10)$  emu/cc. This value is smaller than that observed for bulk SrM samples at RT, with values of the order of 400 emu/cc [6] [243] [244]. Which may be expected due to the substitution of the non-magnetic Ti ions and the Co ions having a reduced magnetic moment compared to that of Fe. Both in and out of plane  $M(H)$  measurements display a coercivity of  $(760 \pm 20)$  Oe, which is smaller than the values measured in the literature for bulk SrM [6] [245] [243]. However, it has been shown that the Co and Ti substitutions have an important effect in reducing  $H_c$  [6] [246] [106]. It is expected that the substitution sites of the cobalt and titanium have a significant effect on the film's coercivity and for some  $\text{SrCo}_2\text{Ti}_2\text{Fe}_8\text{O}_{19}$  samples coercivities as small as 10 Oe have been observed [23] [24]. Although the value measured here is within the range expected. Additionally, it is apparent that the hysteresis loop measured with the magnetic field applied in plane is squarer than the out of plane. This indicates that the film has an easy axis of magnetisation that is closer to in plane than out of plane, which is a property also seen for samples studied in the literature [24] [106] [109].

Ultimately, these XRD and magnetometry measurements show that an epitaxial M-type hexaferrite thin film, with magnetic properties comparable to the literature, has been successfully grown by the PLD system. Proving that the system developed is capable of meeting the demands required for growing the complicated magnetic oxide structure.

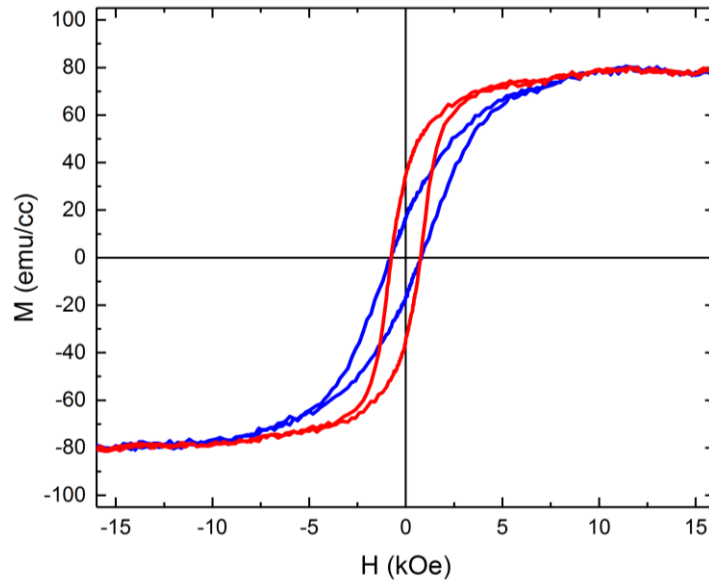


Figure 4.3.22. Graph showing the  $M(H)$  of the  $\text{SrCo}_2\text{Ti}_2\text{Fe}_8\text{O}_{19}$  thin film grown on  $\text{Al}_2\text{O}_3$  (0001).

#### 4.4 Summary and Conclusions

A bespoke PLD growth system has been designed and constructed, to specialise in the growth of magnetic oxide thin films. The system has been developed to allow for the growth of multi-block or layered systems, such as the R, S and T-blocks of hexaferrites, by utilising an alternating target approach. The substrate heating system has been fully tested for several commonly used substrates, including silicon and MgO.

Through the growth of a series of  $\text{Fe}_3\text{O}_4$  thin films, on silicon, the system deposition rate has been calibrated in terms of deposition time, chamber pressure and target-sample distance. Subsequently, the growth of an epitaxial magnetite thin film was achieved with properties comparable to those reported in the literature for a high quality as-grown film [25]. An epitaxial M-type hexaferrite has also been successfully grown again with material properties that compare well to the literature [23] [10] [24]. The hexaferrite film includes a cobalt ferrite impurity phase that should be reduced and removed with further optimisation of the growth and annealing conditions. The system, through the growth of these films, has ultimately been proven capable of producing high quality magnetic oxides. Additionally, epitaxial yttrium iron garnet thin films have been grown, that are not presented in this work, with close to bulk like magnetic properties.

## Chapter 5: Soft X-ray Spectroscopy Study of SrCo<sub>2</sub>Ti<sub>2</sub>Fe<sub>8</sub>O<sub>19</sub> Hexaferrite thin films

### 5.1. Introduction

In this chapter the study of two M-type hexaferrite thin films will be presented. The films were grown by PLD using a single target of composition SrCo<sub>2</sub>Ti<sub>2</sub>Fe<sub>8</sub>O<sub>19</sub>. As detailed in chapter 2, Co-Ti doped strontium ferrites have been shown to display strong magnetoelectric effects at room temperature [10] [24]. However, the magnetoelectric coupling mechanisms present within such materials are not yet well understood, nor are the specific roles of the Co and Ti substitutions. To investigate the valence and occupation of the cations present within the films element specific soft x-ray spectroscopy has been performed and the magnetic contributions of both the iron and cobalt have been studied via X-ray Magnetic Circular Dichroism (XMCD) analysis.

The two films studied in this chapter were both grown under the same conditions and following the same growth procedure. One film was grown with a thickness of 0.9 μm similar to that of the SrCo<sub>2</sub>Ti<sub>2</sub>Fe<sub>8</sub>O<sub>19</sub> films studied by Mohebbi *et al* [24], the first reported displaying ME coupling. The second film was grown to be much thinner, at only 50 nm. Film thicknesses were measured using a profilometer. The films were grown by PLD on 5 mm x 5 mm single crystal sapphire (0001) substrates at 600°C under a (200 ± 5) mTorr partial pressure of oxygen. The SrCo<sub>2</sub>Ti<sub>2</sub>Fe<sub>8</sub>O<sub>19</sub> target was prepared by conventional ceramic techniques and its chemical composition verified by both x-ray diffraction and energy dispersive x-ray analysis. A KrF excimer laser was used to ablate the target with a wavelength of 248 nm and an energy of 400 mJ per pulse. The laser was pulsed at 10Hz and the film was grown with the substrate positioned at a distance of 4.8 cm from the target. After deposition, the films were annealed in an oxygen atmosphere at 1050°C for 40 minutes and a 2 nm Au capping layer deposited.

As is well established, M-type hexaferrites have a general composition MFe<sub>12</sub>O<sub>19</sub>, where M represents a Ba, Sr or Pb atom, and are built from a stacking sequence of R and S blocks, RSR\*S\*, where \* indicates an 180° rotation about the c-axis [79]. There are three different cation coordinations within the M-type structure, octahedral, tetrahedral and trigonal bipyramidal. The aim of this study has been to investigate the cation sites occupied by the substituted Co and Ti ions. As previously discussed there are contradictions in the literature as to which lattice sites are preferentially occupied [10] [15] [88] [86]. The coordination and valence of the elements present within the SrCo<sub>2</sub>Ti<sub>2</sub>Fe<sub>8</sub>O<sub>19</sub> samples have been determined using X-ray spectroscopy techniques. The magnetic properties of the samples have also been probed in an attempt to gain understanding into how the Co and Ti substitutions affect the magnetic structure of SrM.

The measurements have shown that the 0.9 μm film displays magnetic properties characteristic of the magnetoelectric SrCo<sub>2</sub>Ti<sub>2</sub>Fe<sub>8</sub>O<sub>19</sub> samples reported in the literature. The thinner 50 nm film on the other hand exhibits significant differences in its magnetic properties and the x-ray spectroscopy results reveal a difference in the magnetic contributions from both the iron and cobalt ions. The causes for this change in magnetic structure with film thickness are discussed with the effects of strain and grain size both being considered.

### 5.2. 0.9 μm SrCo<sub>2</sub>Ti<sub>2</sub>Fe<sub>8</sub>O<sub>19</sub> single target thin film

#### 5.2.1. EDX Analysis

An EDX measurement representative of the film as a whole is displayed in fig. 5.2.1. It can be seen from the figure that peaks are present at energies that indicate the presence of all the expected film constituent elements, Fe, Co, Ti and O. In addition to these elements aluminium, carbon and gold have been indexed, the Al being present in the sapphire substrate, along with a proportion of

the oxygen. Additionally, the Au is present as the films capping layer and the carbon may be explained by its presence in the atmosphere of the SEM chamber or contamination from the carbon tabs used to secure the samples position. All samples measured by this system indicate the presence of C in the system.

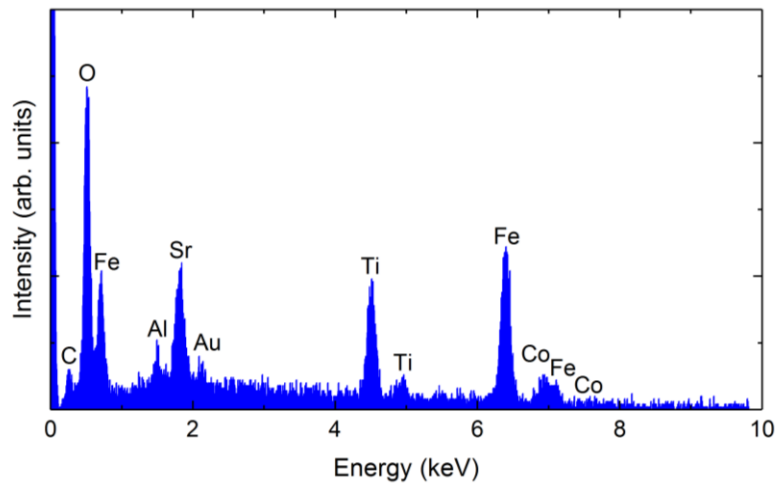


Figure. 5.2.1. EDX spectrum obtained for the 0.9  $\mu\text{m}$   $\text{SrCo}_2\text{Ti}_2\text{Fe}_8\text{O}_{19}$  thin film.

The atomic weights of the elements present in fig. 5.2.1, have been used as detailed in section 3.2.1, to determine the relative abundance of each film element, except oxygen as it is present in both film and substrate. As such the relative abundance of the other film elements were compared, assuming the expected oxygen contribution. This analysis indicates a film composition of  $\text{Sr}_{1.1}\text{Co}_{1.8}\text{Ti}_{2.2}\text{Fe}_{7.9}\text{O}_{19}$ , which compares closely to the  $\text{SrCo}_2\text{Ti}_2\text{Fe}_8\text{O}_{19}$  growth target composition and that intended for the film. The analysis indicates that the area of the film studied here has a small Co deficiency, compensated for by an over-abundance of Ti. Such a small variation in Co and Ti doping levels is not expected to drastically effect the films properties however, as the work of Izadkhah *et al* [107] showed only small changes in ME coupling as the ratio of Co and Ti was varied over this range.

### 5.2.2. X-ray Diffraction Measurements

X-ray diffraction measurements have been performed to gain insight into the crystalline quality of the film. The  $2\theta/\omega$  measurement, shown in fig. 5.2.2(a), was carried out with a step size of  $0.01^\circ$  and an integration time of 1 second. The (0006) sapphire substrate peak is present at an angle of  $41.68^\circ$ . The additional substrate peaks seen around this peak are due to the (0006) substrate  $\text{L}\alpha_2$ ,  $\text{L}\alpha_1$  and  $\text{K}\beta$  reflections and the (0009) substrate peak is also visible at  $64.58^\circ$ . The other Bragg peaks present are indexed to the hexagonal P63/mmc M-type hexaferrite structure and the data reveals that the sample is polycrystalline in nature. The presence of the (006) and (008) reflections indicate some preference for the (00n) direction, although any such ordering is weak. Several of the other diffraction peaks present, such as the (107), are commonly observed in M-type films [24] [109].

The positions of the XRD peaks can be used, as described in section 3.2.2.1, to calculate the films lattice constants,  $a$  and  $c$ . To determine  $c$ , a plot of  $l^2$  against  $\sin^2\theta$  for the M-type hexaferrite (00n) peak positions was used, as shown in fig. 5.2.2(b). The (000) point is included to allow enough points for the fitting of a gradient. Analysis produces a lattice constant of  $c = (23.0 \pm 0.1) \text{ \AA}$ . This value compares closely to literature with  $23.03 \text{ \AA}$  quoted by Pullar for SrM [6] and Wang *et al* determining a value of  $23.102 \text{ \AA}$  for bulk  $\text{SrCo}_2\text{Ti}_2\text{Fe}_8\text{O}_{19}$  [10]. The peak positions of the other M-type reflections were then used to calculate the in plane lattice constant, producing  $a = (5.88 \pm 0.03) \text{ \AA}$ , which is again in good agreement with literature values [10] [6].

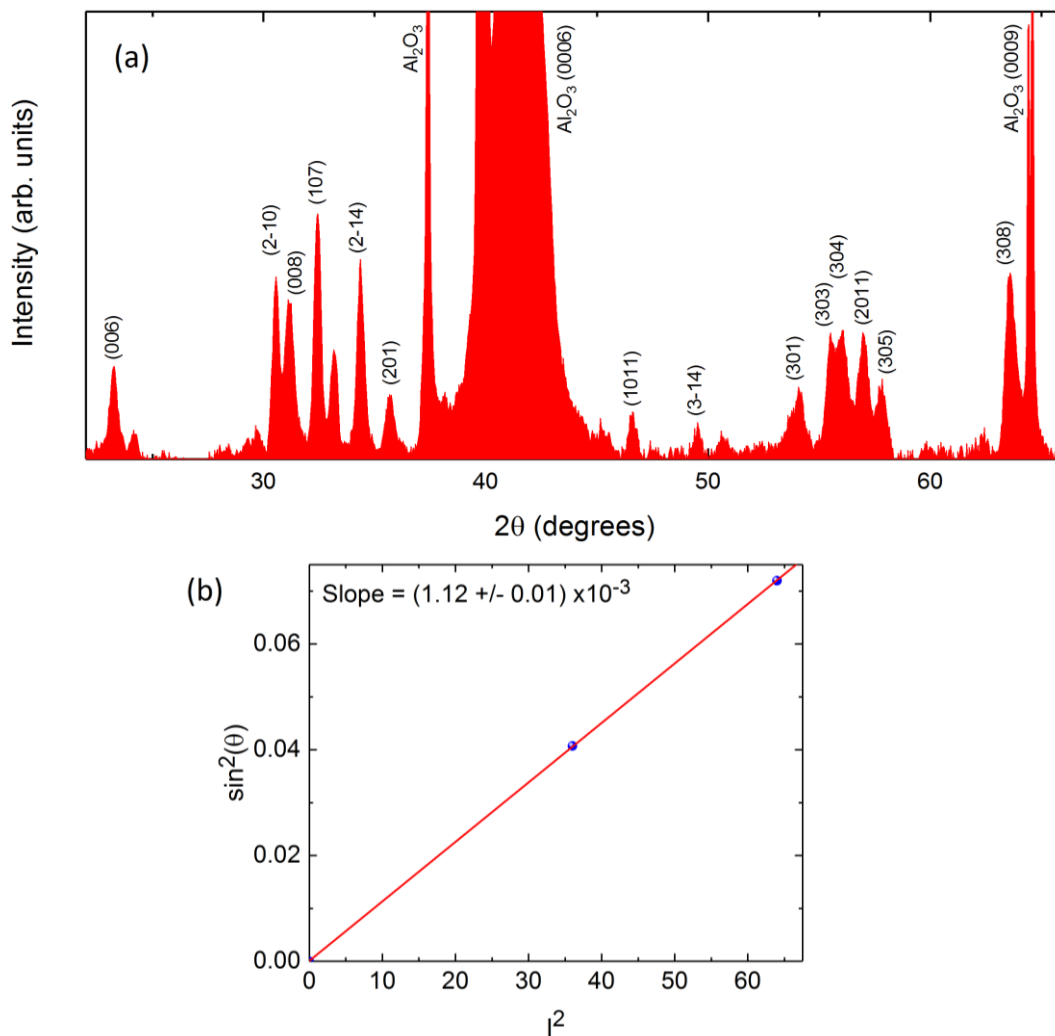


Figure 5.2.2. (a) X-ray diffraction  $2\theta/\omega$  measurement. (b) Plot of  $l^2$  against  $\sin^2\theta$  for the M-type hexaferrite peak positions of the  $0.9 \mu\text{m}$   $\text{SrCo}_2\text{Ti}_2\text{Fe}_8\text{O}_{19}$  film.

Fig. 5.2.3(a) shows the rocking curve measurement performed at the M-type hexaferrite (008) diffraction peak. A FWHM of  $(2.4 \pm 0.1)^\circ$  was determined for this reflection which is larger than many values reported in the literature for an M-type hexaferrite thin film, however, the literature values reported tend to be for thinner epitaxial films. For example, Geiler *et al* [21] report a FWHM of  $0.3^\circ$  for an epitaxial  $\text{BaFe}_{12}\text{O}_{19}$  film grown by PLD. It is not surprising we see a larger rocking curve FWHM due to the polycrystalline nature of the film resulting in a greater angular distribution of film planes. Dorsey *et al* [20] reported FWHM values ranging between  $0.4^\circ$  and  $1.5^\circ$  for  $\text{BaFe}_{12}\text{O}_{19}$  grown on sapphire (0001) via PLD and demonstrated that the FWHM increased as a function of film thickness.

A pole figure measurement performed on the films (008) Bragg reflection is shown in fig. 5.2.3(b). An intense peak is observed at the centre of the pole figure as expected; however, a distribution in intensity is also seen across the tilt angle,  $\chi$ . This is representative of a polycrystalline film, with little or no degree of texture, as suggested by the  $2\theta/\omega$  measurement.

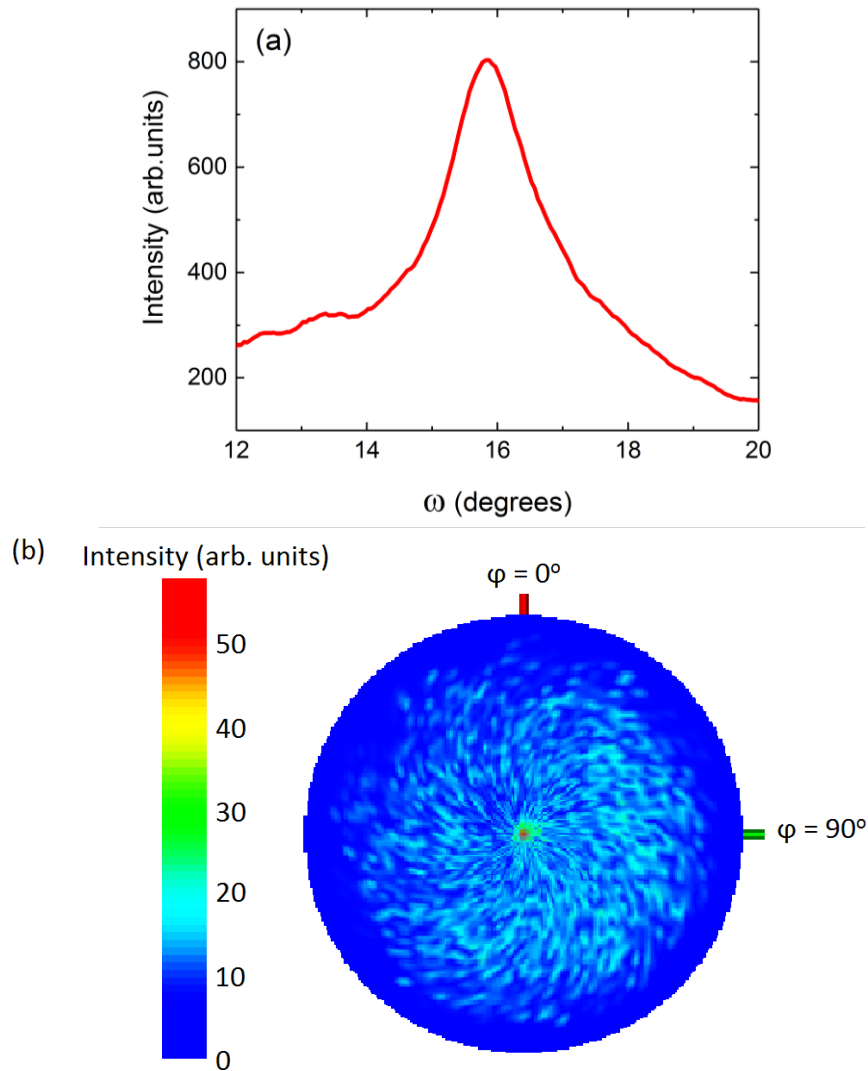


Figure 5.2.3. (a) XRD rocking curve measurement, (b) pole figure measurement performed at the (008) diffraction peak, for the  $0.9 \mu\text{m}$   $\text{SrCo}_2\text{Ti}_2\text{Fe}_8\text{O}_{19}$  film grown on  $\text{Al}_2\text{O}_3$  (0001).

### 5.2.3. Temperature dependent Magnetometry

Fig. 5.2.4 displays the in plane and out of plane hysteresis loops measured at 300 K. It is apparent that the hysteresis loop measured with the magnetic field applied in plane is squarer than the out of plane. This indicates that the film has an easy axis of magnetisation that is closer to in plane than out of plane, as expected from the literature [24] [106] [109]. This was also observed for the sample grown to test the newly developed PLD system in chapter 4. The measurements show a saturation magnetisation at room temperature of  $(170 \pm 20)$  emu/cc, which is smaller than that observed for bulk SrM samples at RT (400 emu/cc) [6] [243] [244]. This is as expected due to the substitution of the non-magnetic titanium ions and the cobalt ions having a reduced magnetic moment compared to that of iron. It is clear, when considering the magnetic structure of SrM [37], that the substitution sites of the Co and Ti will heavily affect  $M_s$ . The room temperature  $M_s$  measured for this film is larger than that measured by Mohebbi *et al* [24] who determined an  $M_s$  of 120 emu/cc for their  $\text{SrCo}_2\text{Ti}_2\text{Fe}_8\text{O}_{19}$  film, grown and annealed under the same conditions.

In and out of plane  $M(H)$  measurements display coercivities of  $(20 \pm 5)$  Oe and  $(30 \pm 5)$  Oe, respectively, which are considerably smaller than the values measured in the literature for bulk strontium ferrite [6] [245] [243]. This is as expected, given it has been shown that the Co and Ti substitutions have an important effect in reducing  $H_c$  [6] [246] [106]. In fact for some  $\text{SrCo}_2\text{Ti}_2\text{Fe}_8\text{O}_{19}$  samples coercivities as small as 10 Oe have been observed [23] [24]. The  $H_c$  of this film is within

the range of values seen in the literature for  $\text{SrCo}_2\text{Ti}_2\text{Fe}_8\text{O}_{19}$  samples that have been found to display ME coupling, with Wang *et al* observing a coercivity of 100 Oe for bulk polycrystalline  $\text{SrCo}_2\text{Ti}_2\text{Fe}_8\text{O}_{19}$  [10] and Zentkova *et al* reporting 10 Oe for a  $\text{SrCo}_2\text{Ti}_2\text{Fe}_8\text{O}_{19}$  single crystal [23]. For the film grown under the same conditions, Mohebbi *et al* determined a value of 20 Oe [24].

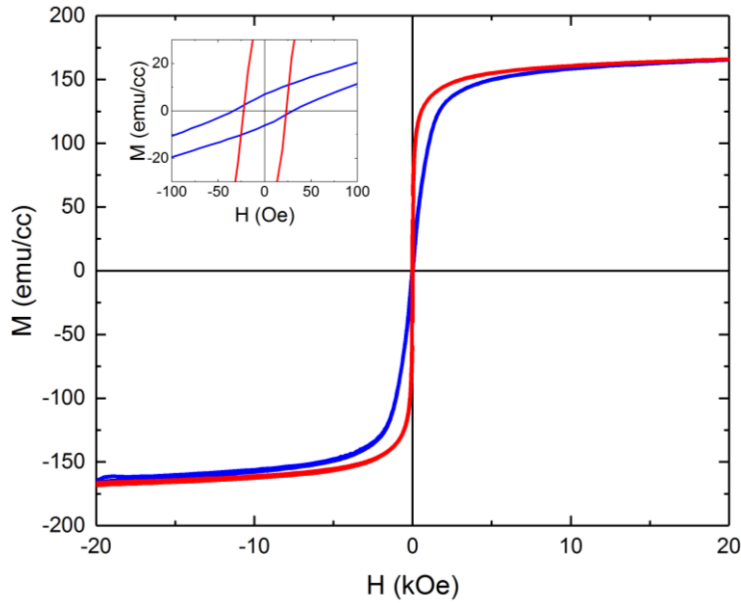


Figure 5.2.4. Graph showing the in plane (red) and out of plane (blue)  $M(H)$  at 300 K for the  $0.9\mu\text{m}$   $\text{SrCo}_2\text{Ti}_2\text{Fe}_8\text{O}_{19}$  thin film.

In plane  $M(H)$  measurements performed at a range of temperatures between 10 K and 500 K are shown in fig. 5.2.5. It is immediately apparent that both  $M_s$  and  $H_c$  are reduced with increasing temperature. Between 300 K and 235 K, the coercivity remains unchanged at  $(20 \pm 5)$  Oe, however below this temperature  $H_c$  is increased significantly, becoming as large as 1 kOe by 10 K. It is evident that at 10 K, 30 kOe is not a large enough field to magnetically saturate the sample, however at this field a magnetisation of  $(280 \pm 30)$  emu/cc is measured, which is 170% of that measured at 300 K. In fact, it is apparent  $M_s$  reduces more significantly with increased temperature. This relationship is similar in form to that observed for SrM [247], however, the  $H_c$  relationship is different to SrM for which  $H_c$  increases with temperature [247]. Kubo *et al* observed a similar temperature dependence of coercivity to that observed here however, for Co-Ti doped BaM [248]. Kreisel *et al*

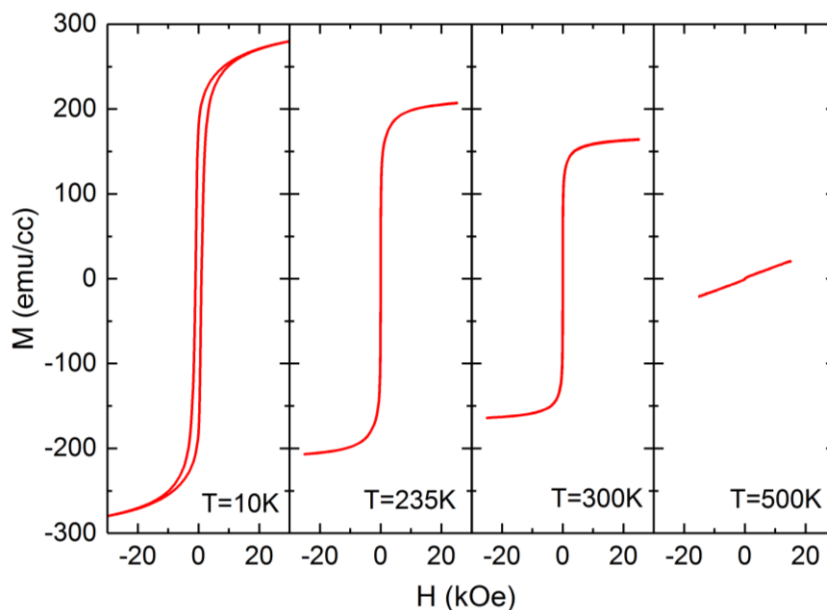


Figure 5.2.5.  $M(H)$  measurements performed at different  $T$  for the  $0.9\mu\text{m}$   $\text{SrCo}_2\text{Ti}_2\text{Fe}_8\text{O}_{19}$  thin film.

[15] showed the magnetic properties of Co-Ti doped M-type hexaferrites to be temperature sensitive as seen here. They suggested this is as a consequence of the  $Ti^{4+}$  cation substitutions interrupting the magnetic interactions between the RS and R\*S\* blocks resulting in conical magnetic structures becoming more pronounced at lower temperatures and contributing to the anisotropy [15].

By 500 K the hysteresis in  $M(H)$  has drastically reduced but is still present. This suggests that the samples Curie temperature is above 500 K, which is consistent with the work of Wang *et al* [10], who determined a Curie temperature of 740 K for  $SrCo_2Ti_2Fe_8O_{19}$ . To investigate this and the temperature dependent magnetic properties of the sample further field cooled (FC) and zero field cooled (ZFC)  $M(T)$  measurements have been performed. The measurements were taken with a 300 Oe magnetic field applied in the plane of the film, between 5 and 500 K. For the FC measurement, a 30 kOe field was applied during cooling.

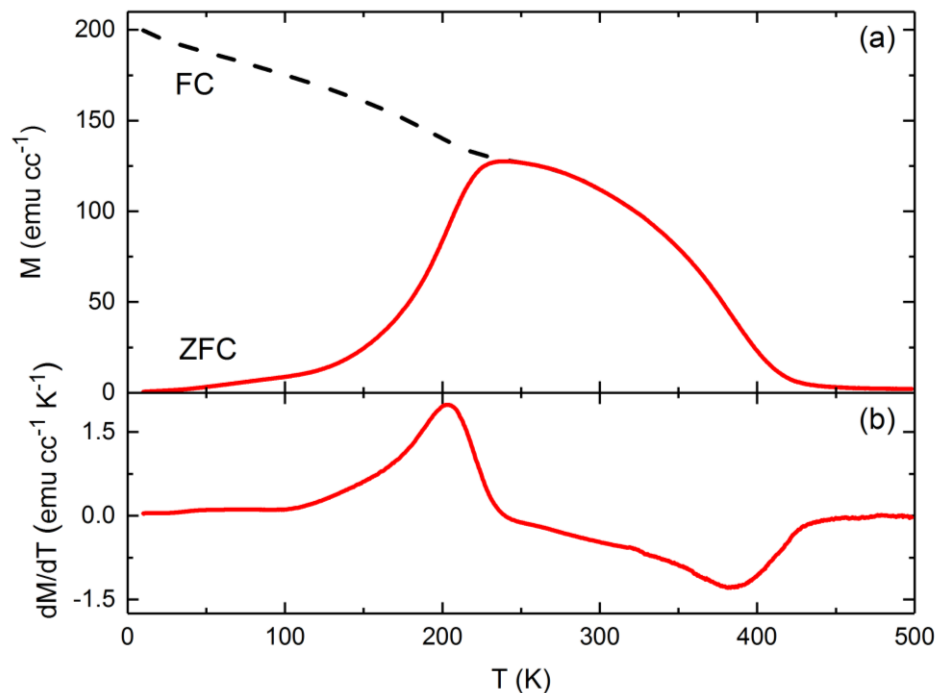


Figure 5.2.6. (a)  $M(T)$  obtained via VSM, measured at 300 Oe for FC and ZFC conditions, (b) The derivative of the ZFC  $M(T)$  obtained for the  $0.9 \mu m$   $SrCo_2Ti_2Fe_8O_{19}$  thin film.

In fig. 5.2.6(a), for the field cooled case increasing the temperature from 10 K causes the magnetisation to steadily decrease as is typical of a simple ferro/ferrimagnet material. However around 230 K the slope of the FC  $M(T)$  flattens before falling again. It is at approximately this temperature that both the FC and ZFC measurements come together and at higher temperatures are identical. Below 230 K, the magnetisation of the ZFC curve decreases sharply and is as small as just 1 emu/cc at 10 K.

The peak in the ZFC  $M(T)$  data at 230 K for this sample, has been seen in other hexaferrites and has often been interpreted as a change in magnetic order [247] [249] even though the microscopic origin of  $M(T)$  is extremely complicated in multi-sublattice magnetic oxides. For a simple 2-sublattice system the discontinuities in  $M(T)$  can be attributed to a number of effects such as a change between a collinear ferromagnetic order to an order with canted spins or due to a magnetic compensation point as has been discussed in detail by Smit and Wijn [250]. In systems with more than two sublattices, such as the hexaferrites, it is not possible to infer the magnetic order directly from  $M(T)$  without complementary information such as that provided by neutron diffraction [251]. However, in the M-type hexaferrites an easy cone of magnetization [6] develops when doping with Co-Ti above a critical level ( $x = 1.1$ ) as a result of non-collinearity [6] [250]. This has also been shown to have the effect of dramatically reducing  $H_c$  as supported by the  $M(H)$  measurements.

The general shape of the  $M(T)$  curve has also been observed by others for  $\text{SrCo}_2\text{Ti}_2\text{Fe}_8\text{O}_{19}$  samples [10] [106] [23]. At around 400 K, it can be seen that the magnetisation drops significantly and reaches a small but non-zero magnetisation by 500 K, the limit to which we were able to measure. Both Wang *et al* [10] and Zentkova *et al* [23] report that the magnetisation remains small up to values of 740K and 768K, respectively, at which it suddenly drops to zero, they determine this to be the Curie temperature in their samples. Both values are close to the 743 K Curie temperature of the parent compound SrM [6].

To gain further insight into the  $M(T)$  relationship, the ZFC measurement has been differentiated, as shown in fig. 5.2.6(b). This displays the gradient of the ZFC  $M(T)$  curve and how it changes with temperature, it can be used to determine turning points in the  $M(T)$  relationship. The differentiated curve shows a positive peak at 205 K ( $T_1$ ) and a negative peak at 380 K ( $T_2$ ). Both Wang *et al* [10] and Zentkova *et al* [23] have also observed these two turning points for  $\text{SrCo}_2\text{Ti}_2\text{Fe}_8\text{O}_{19}$  samples. Based on the results of neutron diffraction, Wang *et al* postulate that the  $T_2$ , at 380 K corresponds to a transition between a conical magnetic phase to a collinear ferrimagnetic phase [10]. This suggests that a non-collinear magnetic structure, previously thought to be a prerequisite for ME coupling in hexaferrites, is present within the sample up to above RT. It is possible that the turning point at 205K ( $T_1$ ) is the result of a transition between one non-collinear structure to another. It is also noted that the dramatic reduction in  $H_c$  with temperature, observed in fig. 5.2.5, also coincides with the transition in the  $M(T)$  at around 200 K. It is observed, however, that this turning point coincides with the separation of the FC and ZFC curves, which, in ferrimagnetic oxides, is often attributed to blocking behaviour [160]. Therefore, further measurements, such as neutron diffraction, are required to investigate this for the  $\text{SrCo}_2\text{Ti}_2\text{Fe}_8\text{O}_{19}$  structure, complicated for this sample given its polycrystalline thin film nature.

#### 5.2.4. Ferromagnetic Resonance Measurements

The FMR signal has been measured by monitoring the microwave losses in the hexaferrite films at a fixed RF frequency as a function of an external dc magnetic field. The measurements were performed using a lock-in amplifier technique described in section 3.3.2.

The differentiated FMR response for the 0.9  $\mu\text{m}$  film, taken at 10 GHz, is displayed in fig. 5.2.7(a). The measurement was performed in 5 mT steps between 0.4 and 0.0 T. FMR is an important characterisation tool for hexaferrites as they are already an important material for microwave applications [6] [82]. If the ME coupling present in hexaferrites could be correlated to ferromagnetic resonance, this could open the door to numerous microwave applications, such as resonators, filters and phase shifters that are both magnetically and electrically controllable [252]. The resonance field ( $H_r$ ) and linewidth ( $\Delta H$ ) have been extracted by fitting the data with eqn. 3.14 [161], in accordance with the procedure detailed in section.3.3.2. In fig. 5.2.7(a) the experimental data is shown in blue and the fit equation in red. It is clear that the experimental data fits well to the theoretical relation. This then produces a resonance field value of  $(1380 \pm 20)$  Oe and a linewidth of  $(600 \pm 30)$  Oe, assuming the  $M_s$  value obtain from VSM.

The resonance field value measured at 10 GHz is in the range of  $H_r$  values measured in the literature for hexaferrite samples [24] [253]. Ebnabbasi [253] for a single crystal  $\text{Sr}_3\text{Co}_2\text{Fe}_{24}\text{O}_{41}$  sample determined a resonance field of 1200 Oe and a linewidth of 750 Oe, both of which are closely comparable to the values measured here. For the first  $\text{SrCo}_2\text{Ti}_2\text{Fe}_8\text{O}_{19}$  magnetoelectric thin film reported, Mohebbi *et al* [24] observed a resonance with an  $H_r$  of 2 kOe and  $\Delta H$  of 1000 Oe. A narrower linewidth indicates a lower total damping, an effect that could be explained by an improvement in crystalline quality. However, relatively broad linewidths are typical for cobalt-substituted ferrites [107] and the resonance will also be broadened due to the inhomogeneous magnetic distribution as a result of the polycrystalline nature of the sample [24].

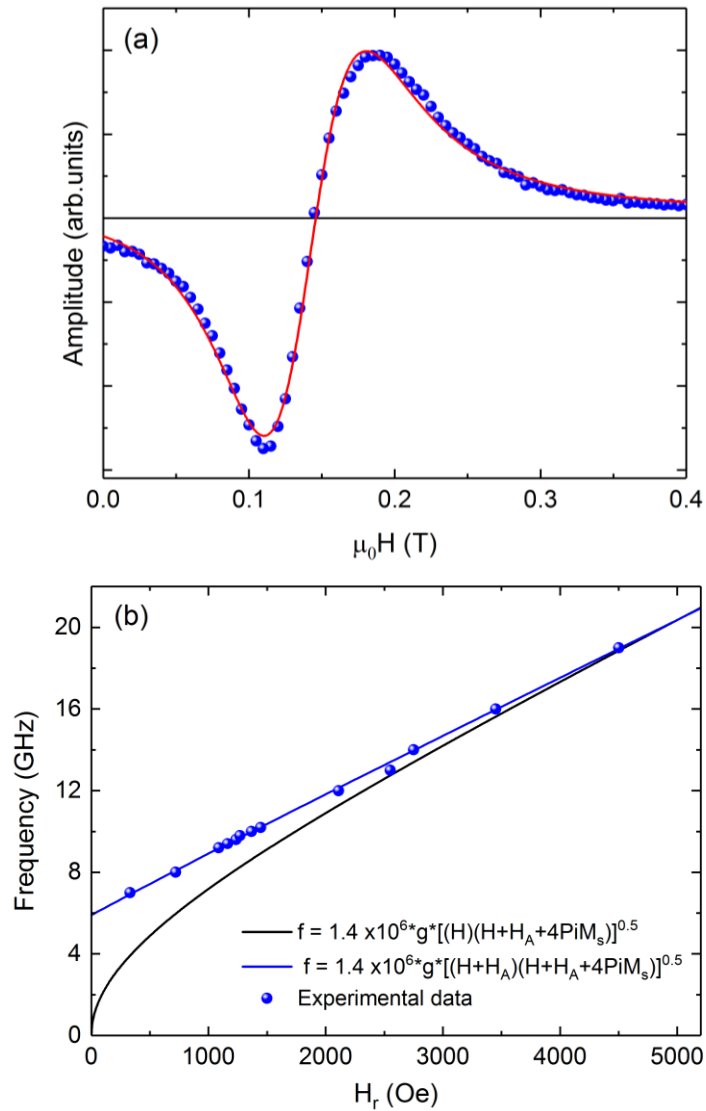


Figure. 5.2.7. (a) In-plane FMR at 10GHz and (b) frequency as a function of resonance field for the 0.9  $\mu\text{m}$   $\text{SrCo}_2\text{Ti}_2\text{Fe}_8\text{O}_{19}$  thin film.

The FMR was measured over a range of frequencies between 7 and 18 GHz and for each frequency  $H_r$  was extracted. Frequency could then be plotted against resonance field, as displayed in fig. 5.2.7(b). Based on the work of Kittel [164], the frequency dependence can be used to deduce  $g$ -factor values and anisotropy field ( $H_A$ ) values, assuming the  $M_s$  values obtained from VSM. Additionally, the relationship between  $H_r$  and frequency is dependent on whether the uniaxial anisotropy is normal to the film plane and whether it is a hard or easy axis [165]. If the sample has a uniaxial anisotropy with an axis that lies out of the film plane, as is the case for BaM / SrM with large  $c$ -axis anisotropy, then the frequency,  $H_r$  relationship will be governed by eqn. 3.18, as depicted by the black line in fig. 5.2.7(b). Alternatively, if the sample has an in plane uniaxial anisotropy axis, then the relationship described by eqn. 3.17 would hold, plotted in blue in fig. 5.2.7(b). Through fitting of the experimental data with both relationships, it is apparent that eqn. 3.17 is a far better fit; this confirms that the sample does not possess a simple ferrimagnetic arrangement along the  $c$ -axis, as is the case for un-doped SrM. It can be seen that for the out of plane anisotropy relation the frequency falls to zero with the resonance field, however, this is not the case for an in plane anisotropy, or indeed for an anisotropy axis at an angle of less than  $90^\circ$  to the film plane. In plane angular measurements reveal an isotropic relationship in this plane, as such this suggests that the axis lies at an unknown angle between in and out of plane as could be explained by the presence of a conical magnetic structure.

The fitting of experimental data in fig. 5.2.7(b) produces a g-factor of 2.0. This appears typical for a ferrite structure with values around 2 often seen for ferrite, hexaferrite and spinel structures [24] [60] [107]. It has also been observed that cobalt substitutions typically reduce the g-factor due to orbital contributions [107], resulting in a g value the same as that of the free electron.

### 5.2.5. Element Specific Soft X-ray Magnetic Spectroscopy

To gain a more detailed understanding of the role of Co-Ti substitutions within the sample, XAS at the Ti L<sub>2,3</sub> absorption edge and XAS/XMCD measurements at the Co and Fe L<sub>2,3</sub> absorption edges have been performed. This has allowed the valency, co-ordination and the magnetic response of the individual elements to be determined. The procedure and experimental set up for obtaining the XAS and XMCD measurements are detailed in section 3.4.

The Ti XAS measured at the L<sub>2,3</sub> edges for the 0.9 μm single target film is shown in fig. 5.2.8. Spectra were acquired for both RCP and LCP x-rays with no difference observed between the two. Four distinct peaks are visible in the XAS, which suggests an octahedral symmetry. In this case, the crystal field splits the degenerate 3d orbitals into an e<sub>g</sub> and a t<sub>2g</sub> configuration where the t<sub>2g</sub> consists of the d<sub>xy</sub>, d<sub>xz</sub>, and d<sub>yz</sub> orbitals and the e<sub>g</sub> configuration, the higher energy d<sub>z<sup>2</sup></sub> and d<sub>x<sup>2</sup>-y<sup>2</sup></sub> orbitals. Thus, two peaks are expected for each spin orbit split initial state (2p<sup>3/2</sup>, 2p<sup>1/2</sup>). The deeper penetrating FY data also showed the same four-peak form, confirming that the surface sensitive TEY spectra are representative of the film as a whole.

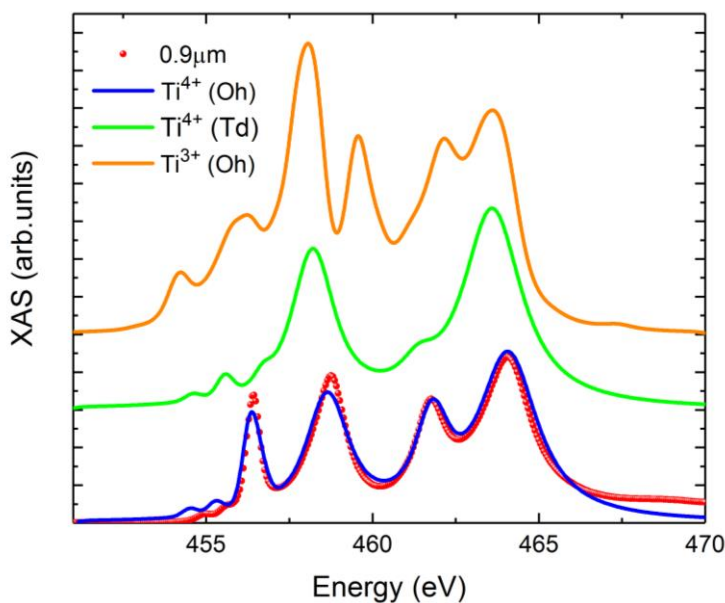


Figure. 5.2.8. Ti L<sub>2,3</sub> XAS measured for the 0.9 μm SrCo<sub>2</sub>Ti<sub>2</sub>Fe<sub>8</sub>O<sub>19</sub> thin film at 300K in TEY (red data points). The blue solid line is the simulated spectra from an atomic XAS multiplet calculation of Ti<sup>4+</sup> in an octahedral co-ordination with 10D<sub>q</sub> = 1.9 eV. Equivalent calculations for octahedral Ti<sup>3+</sup> (orange line) and Ti<sup>4+</sup> in a tetrahedral co-ordination with 10D<sub>q</sub> = -0.9 eV (green line) are also plotted.

In fig. 5.2.8, the spectrum has been compared to those generated by atomic multiplet calculations. For the octahedral case, the multiplet calculations were simulated with a 10D<sub>q</sub> of 1.9 eV and for the tetrahedral simulation a 10D<sub>q</sub> of -0.9 eV was used. These values are consistent with crystal field theory, with the tetrahedral crystal field parameter being negative 4/9 of the octahedral [176]. The Slater parameters were reduced to 80% of the Hartree-Fock values and the Lorentzian broadening values for each of the four peaks in the simulated octahedral Ti<sup>4+</sup> spectrum were 0.1 eV, 0.6 eV, 0.5 eV and 1.0 eV respectively, in order to best fit the experimental data.

The simulated spectrum for Ti<sup>4+</sup> in an octahedral co-ordination, in fig. 5.2.8, agrees well with the experimental data. The calculated spectra for Ti<sup>4+</sup> in a tetrahedral co-ordination shows only two

significant peaks unlike the four peaks seen for the octahedral simulation and the experimental spectrum. The calculated spectrum for the  $\text{Ti}^{3+}$  octahedral case looks different again, with the peak separations different to the experimental data. Hence, it is clear that the Ti ions in the sample have a 4+ valency and octahedral co-ordination.

Three different octahedral lattice sites are present within the M-type structure; these are the 2a in the S-block, the  $4f_2$  in the R-block and the 12k at the boundary between R and S-blocks. Although the XAS data cannot be used independently to determine which exact octahedral lattice positions are occupied by the Ti, it is expected they preferentially occupy the 12k sites, as suggested in the literature [6] [83]. Occupation of the 12k sites would magnetically de-couple the R- and S-blocks, thought to be a pre-requisite for the formation of the non-collinear magnetic structure reported in  $\text{SrCo}_2\text{Ti}_2\text{Fe}_8\text{O}_{19}$  [6]. In order to confirm the occupation of the 12k sites however, an alternative approach is required, such as Extended X-ray Absorption Fine Structure (EXAFS) measurements.

As it has been shown that the  $\text{Ti}^{4+}$  ions preferentially occupy the octahedral lattice sites, the occupation and valence of the magnetic Co and Fe ions are now investigated. The Co XAS and XMCD at the  $L_{2,3}$  edges are displayed in Fig. 5.2.9(a). Unusually, four peaks can be seen in the spectral range measured for the Co XAS. The peaks at 778 and 793 eV are associated with the Co  $L_3$  and  $L_2$  edges, respectively, as anticipated, however, two additional lower intensity peaks are observed, unexpectedly, at 783 and 798 eV. These peaks have been identified as belonging to the Ba  $M_5$  and  $M_4$  edges, which suggests the presence of barium ions within the film or on the sample holder. Ba was not intended by the growers to be a constituent of the film and it is possible that it may be due to a contamination of the sample holder during measurement or film surface contamination. It is worth noting that the EDX measurements showed no presence of Ba within the film, and these peaks have also been seen when measuring the Co edge in other samples. This suggests that these Ba peaks are from the sample holder rather than the film itself.

Both Co and Fe XMCD spectra have been fitted with atomic multiplet calculations. These fits are shown in black in fig. 5.2.9. For both the Fe and Co spectra the octahedral simulation uses a 10Dq of 1.1 eV and the tetrahedral a 10Dq of -0.5 eV with Slater parameters reduced to 72% of the Hatree-Fock values. To simulate the trigonal bipyramidal site the  $S_6$  symmetry was used with 10Dq = 0.8 eV,  $D\tau = 0.08$  eV and  $D\sigma = 0.01$  eV. It is noted that for these values of the crystal field parameters, used for the trigonal bipyramidal, the five d-orbitals break up into two doublets  ${}^2E''(d_{zx}, d_{yz})$  and  ${}^2E'(d_{x^2-y^2}, d_{xy})$  plus a singlet  ${}^2A'_1(d_{z^2})$  with  ${}^2A'_1 > {}^2E' > {}^2E''$  as expected for this symmetry. The Co XAS lineshape can be fitted by a superposition of  $\text{Co}^{2+}$  spectra in octahedral, tetrahedral and trigonal bipyramidal environments, suggesting that the Co ions occupy all three different cation sites in the M-type structure. It also indicates that the Co has a 2+ valence, which is as expected from the literature [15] [6] to compensate for the 4+ valence of the titanium. The XMCD in fig. 5.2.9(a) is zero at the energies corresponding to the Ba peaks, as anticipated. Responses are seen at both the Co  $L_3$  and  $L_2$  edges. The most prominent peak at the  $L_3$  edge is positive whilst the  $L_2$  is predominantly negative. The XMCD lineshape provides information on the uncompensated moments in the ferrimagnetic structure. Fits to the XMCD using atomic multiplet calculations confirm that the cobalt has a 2+ valence and is a combination of octahedral, tetrahedral and trigonal contributions. The simulated spectrum shown in fig. 5.2.9(a) consists of 69% octahedral, 13% tetrahedral and 18% trigonal bipyramidal, where variations in the site ratios of the order of 5% produce large changes to the spectra.

It has been previously reported [6] [10] [247] that the  $\text{Co}^{2+}$  prefer to initially occupy the tetrahedral  $4f_1$  and the octahedral 2a sites, although there is significant contradiction in the literature as to which of the two is preferred over the other [10] [15] [254]. The preference for  $\text{Co}^{2+}$  in the tetrahedral ( $4f_1$ ) sites has been reported to be due to the large  $\text{Co}^{2+}$  cation radius ( $r_{\text{Co}(2+)} = 0.58$  Å) which stabilizes the S-block compared to the smaller  $\text{Fe}^{3+}$  cation ( $r_{\text{Fe}(3+)} = 0.49$  Å) [15] [10]. However,

the presence of  $\text{Fe}^{2+}$ , which has a larger ionic radius ( $r_{\text{Fe}^{2+}} = 0.63 \text{ \AA}$ ) than  $\text{Co}^{2+}$ , may modify this picture and force more of the  $\text{Co}^{2+}$  into the 2a or other octahedral sites. It is seen from the fitting that Co ions occupy both tetrahedral and octahedral lattice sites. However, a greater amount substitute to the  $\text{O}_h$  sites suggesting that they are preferred in this case. Additionally, around a fifth of the Co ions occupy the 2b trigonal bipyramidal sites, this is in line with the work of Cabanas *et al* [86], who stated that above a critical doping concentration the Co begin to occupy the 2b sites. The Co trigonal bipyramidal magnetic contribution is anti-parallel to the octahedral. It is also anti-parallel to the Fe octahedral component shown in fig. 5.2.9(b), thus the majority of octahedral Fe cations within the M-type structure, which is in agreement with the finding of Williams *et al* for Co-Ti doped BaM [254].

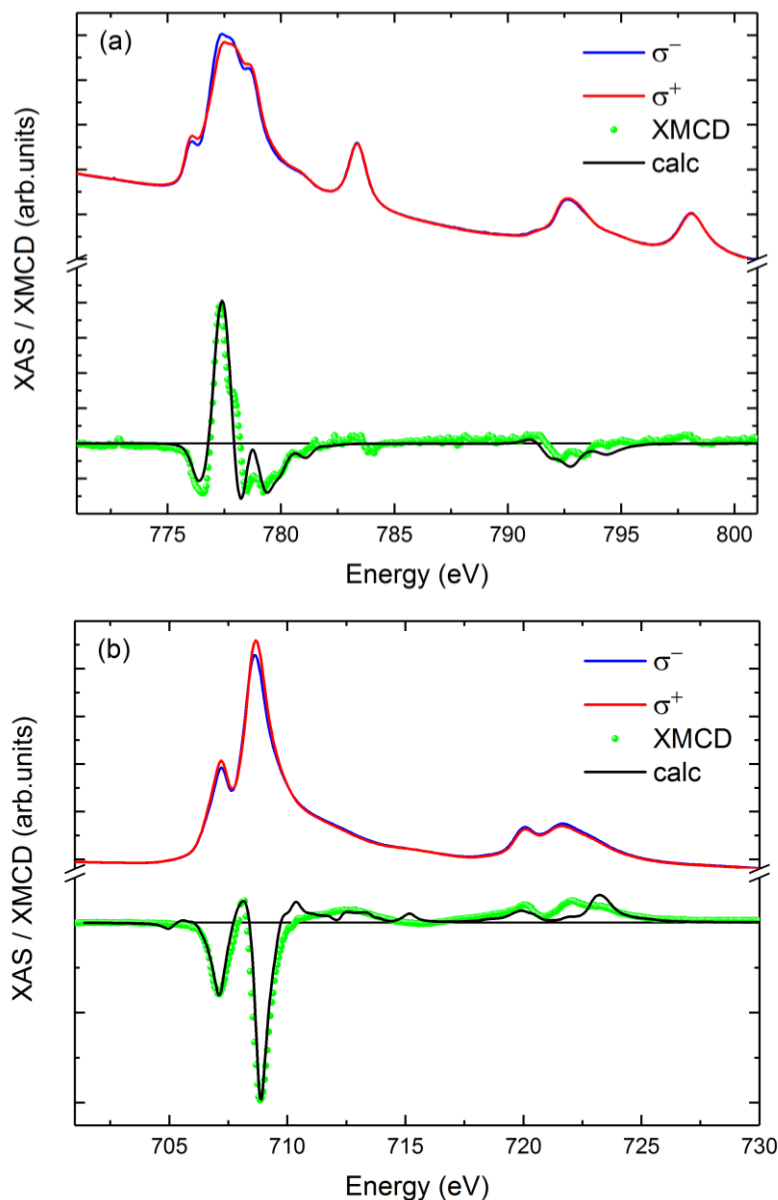


Figure. 5.2.9. XAS at the (a) Co and (b) Fe  $L_{2,3}$  edges for  $\sigma^-$  (blue) and  $\sigma^+$  (red) x-rays, measured for the 0.9  $\mu\text{m}$   $\text{SrCo}_2\text{Ti}_2\text{Fe}_8\text{O}_{19}$  thin film at 300 K in TEY. The corresponding XMCD is plotted (green) with the fit using atomic multiplet calculations (black).

The Co occupation of 2b trigonal bipyramidal sites is believed to play a significant role in the formation of non-collinear magnetic structures within Co-Ti doped hexaferrites [6], hence may be important for the ME coupling present in such materials. The large reduction in  $H_c$  seen for this sample compared to SrM, is also likely to be due to Co substitution into the 2b site, which is known to be responsible for the large anisotropy in SrM [6]. Given this, it may be possible to tentatively

use  $H_c$  as an indicator for 2b Co occupation in  $\text{SrCo}_2\text{Ti}_2\text{Fe}_8\text{O}_{19}$ , although, to prove this connection further investigation into the magnetic structure using a method such as neutron diffraction would be required on a range of samples.

Fig. 5.2.9(b) shows the LCP and RCP XAS and corresponding XMCD measured at the Fe  $L_{2,3}$  edges at  $T = 300\text{K}$ . The form of the XAS spectra are typical for an iron oxide, with a splitting in the peaks at both edges. In the XMCD lineshape, three peaks are seen at the  $L_3$  edge, two negative and one positive. The same three-peak shape is also seen for the XMCD of  $\text{Fe}_3\text{O}_4$  samples [255]. The three peaks correspond to contributions from octahedrally co-ordinated  $\text{Fe}^{2+}$ , octahedral  $\text{Fe}^{3+}$  and tetrahedral  $\text{Fe}^{3+}$ . For the M-type hexaferrite structure, spins located at the Fe  $T_d$  sites are aligned anti-parallel to the majority of spins at the Fe  $O_h$  sites [6]. Hence, the positive peak in the XMCD is due to tetrahedrally co-ordinated  $\text{Fe}^{3+}$  and the two negative contributions are due to the octahedrally co-ordinated  $\text{Fe}^{2+}$  and  $\text{Fe}^{3+}$ .

The Fe XMCD spectrum has also been fitted using atomic multiplet calculations. The calculations agree with the experimental data excellently at the  $L_3$  edge for a fit that is 80% octahedral and 20% tetrahedral. It is noted that this does not represent the relative Fe occupancy of the sites as for example, in the typical M-type unit cell the spins of the Fe at the octahedral  $4f_2$  sites are aligned anti-parallel to the other  $O_h$  sites and therefore would reduce the magnetic octahedral contribution

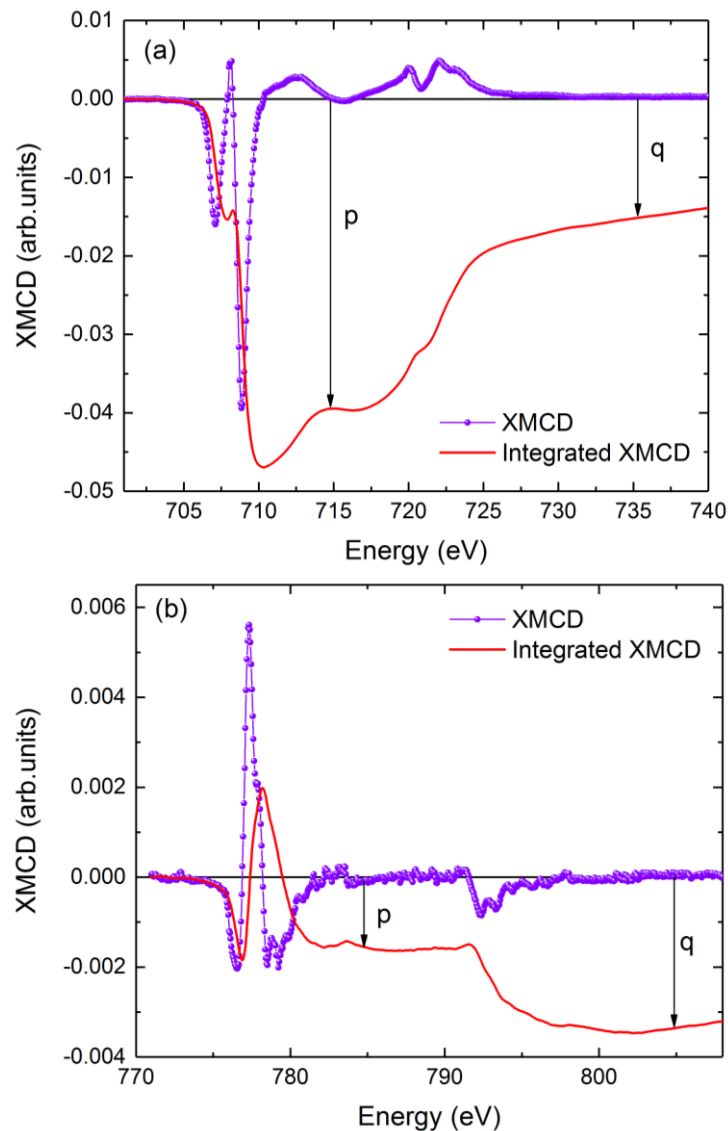


Figure. 5.2.10. (a) Fe and (b) Co  $L_{2,3}$  edge XMCD (purple) and integrated XMCD (red), measured for the  $0.9\ \mu\text{m}$   $\text{SrCo}_2\text{Ti}_2\text{Fe}_8\text{O}_{19}$  thin film at 300 K in TEY. The quantities p and q are illustrated.

to the XMCD signal. It does however show that the total magnetic contribution of the  $O_h$  sites is four times that of the  $T_d$  and their projections are in opposite directions.

It is also observed that the  $O_h$  contribution consists of Fe with both a 2+ and 3+ valence, 27% of the overall fit being octahedrally co-ordinated  $Fe^{2+}$ . This is unexpected as the hexaferrite structure is usually considered to only contain  $Fe^{3+}$ . The occurrence of  $Fe^{2+}$  is most likely due to incomplete oxidation during growth, and the occurrence of which requires further investigation into and optimisation of the growth parameters. The presence of  $Fe^{2+}$  within the material is detrimental to magnetoelectric materials as it provides a conductive pathway, due to polaronic hopping, between the  $Fe^{2+} / Fe^{3+}$  ions located at octahedral sites, suppressing electric polarisation. Thus, if the  $Fe^{2+}$  could be removed or reduced this could result in an enhancement of any ME coupling present.

For both Co and Fe measurements the FY and TEY spectra were of the same relative form, suggesting that the surface sensitive TEY could be considered representative of the film as a whole. Although, in the Fe FY spectra, significant self-absorption effects were observed at the  $L_3$  edge the rest of the data closely resembled the TEY signal.

In fig. 5.2.10, the integrated Fe and Co L-edge XMCD are plotted. In order to perform sum rules analysis, the quantities  $p$  and  $q$  are determined and illustrated in the figure. The branching ratios,  $p/q$ , at both Fe and Co edges have been used, as detailed in section 3.4.6, to calculate the orbital to spin magnetic moment ratio. The integrated Fe spectrum in fig. 5.2.10(a), shows a non-zero  $q$  value that is smaller than  $p$ , suggesting a partially quenched orbital moment. The Fe spectrum produces  $m_L / m_{S_{eff}} = 0.13$ , with the form of the integrated curve appearing similar to those reported for  $Fe_3O_4$  [256] [257] as expected due to the co-ordinations involved, however, the  $m_L / m_{S_{eff}}$  ratio is larger [256] [257].

In fig. 5.2.10(b) the integrated Co spectrum has a considerably different form to that of the Fe spectrum, with  $q$  larger than  $p$ , suggesting a branching ratio less than one. This produces a large negative orbital to spin moment ratio,  $m_L / m_{S_{eff}} = -1.133$ . This result would appear to be unusual if we considered the Co contribution to come from a single site. However, the form of the Co integrated curve can be explained if we consider the contributions from  $O_h$ ,  $T_d$  and Trig sites, collectively.

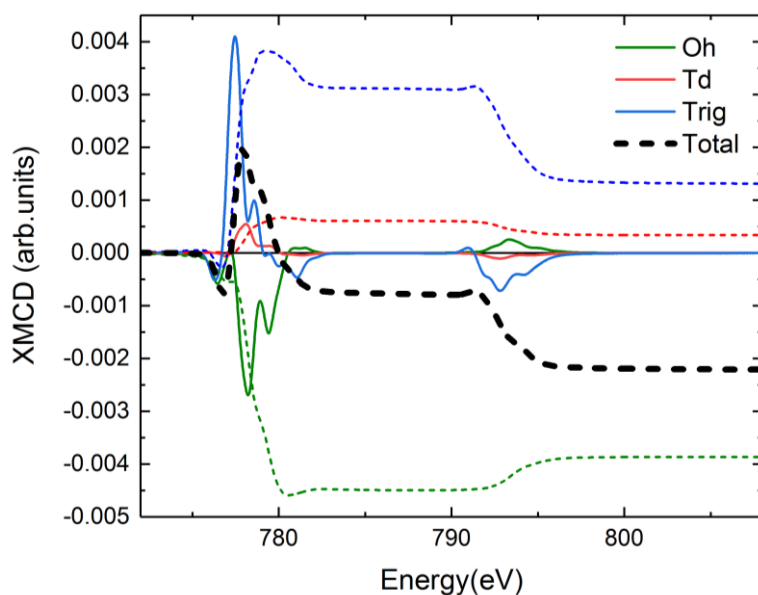


Figure. 5.2.11. Co  $L_{2,3}$  edge XMCD spectra obtained via multiplet calculations for  $O_h$  (green),  $T_d$  (red) and Trig (blue) in the ratios used to fit the  $0.9 \mu m$   $SrCo_2Ti_2Fe_8O_{19}$  spectrum, and the corresponding integrated XMCD (dashed lines). The sum of the three integrated spectra is shown in black.

Fig. 5.2.11 displays the integrated spectra for the three different co-ordinations, produced by atomic multiplet calculations. The ratios of the three different spectra presented are those determined from the fitting of the Co XMCD in fig. 5.2.9(a) and the sum of the three integrated spectra is shown in black, it is clear that this resembles closely the experimentally obtained integrated curve. The unusual shape can be seen to be a consequence of each of the co-ordination contributions having a different orbital moment quenching. It is seen from the figure that the octahedral co-ordination only produces a small amount of orbital quenching, as indicated by the small step in the integrated curve at the  $L_2$  edge. The trigonal bipyramidal co-ordination on the other hand has a much larger quenching of the orbital moment, which is expected due to the lower symmetry.

Element specific hysteresis measurements were also performed at the Co and Fe L-edges. The measurements were performed by recording the XMCD at a fixed energy on the edge, relative to a pre-edge position, as a function of the magnetic field applied. For the Co, measurements were taken at the  $L_3$  edge, with an on edge energy of 777.8 eV, this corresponds to the positive peak in the XMCD lineshape, and an off-edge energy of 772 eV was used. The  $L_3$  edge could not be used for the Fe due to self-absorption effects in the FY signal. As such, the Fe  $L_2$  edge was used with an on energy of 722.5 eV and an off-edge energy of 732 eV. As the  $L_2$  edge has an opposite sign to the  $L_3$ , the sign of the Fe XMCD hysteresis was inverted in order to aid comparison between the Co and Fe measurements.

The element specific  $M(H)$  measurements were acquired at 1.6 K, 230 K and 300 K, in order to investigate the temperature dependence of the individual Co and Fe contributions to the samples overall magnetisation. The hysteresis loops obtained at 230 K for Co and Fe are shown in fig. 5.2.12(a) and (b), respectively. The Co and Fe measurements have the opposite sign, a positive moment is observed for a negative field in Co and a positive moment is seen for a positive field in Fe. This is consistent with the XMCD results as the projections of the Co and Fe  $L_3$  edges are in the opposite direction, as can be seen in fig. 5.2.9. This suggests that the dominant magnetic contribution to the Co  $L_3$  edge has a moment aligned anti-parallel to the net direction of the Fe octahedral moments.

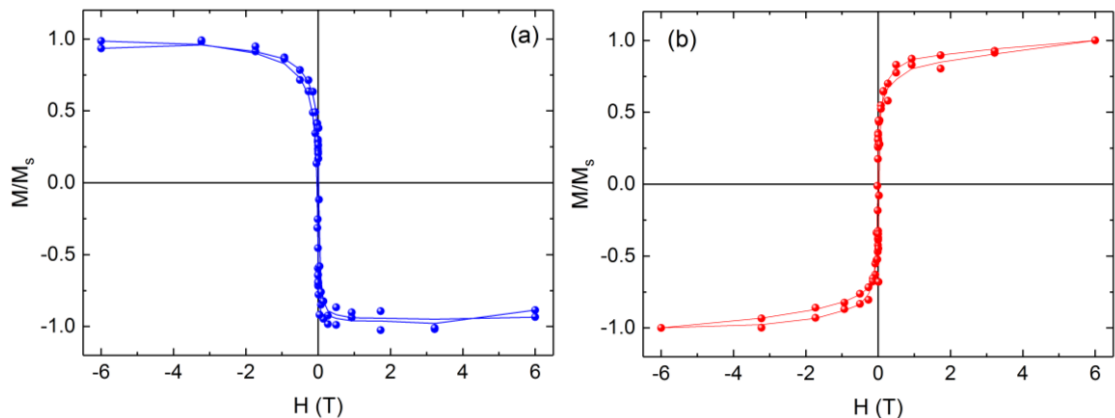


Figure 5.2.12. (a) Co and (b) Fe element specific hysteresis measurements obtained at 230 K for the  $0.9 \mu\text{m}$   $\text{SrCo}_2\text{Ti}_2\text{Fe}_8\text{O}_{19}$  thin film in FY.

Both the Co and Fe hysteresis measurements at 230 K have small coercivities of less than the 100 Oe resolution of the magnet, the same is also observed at 300 K. This is consistent with the VSM measurements that showed no change in sample coercivity between 230 and 300 K. An increase in coercivity is measured at 1.6 K, with both Co and Fe measurements producing a value of 500 Oe, such an increase is again consistent with VSM measurements.

### 5.3. 50 nm SrCo<sub>2</sub>Ti<sub>2</sub>Fe<sub>8</sub>O<sub>19</sub> single target thin film

As an investigation into the effects of film thickness, a SrCo<sub>2</sub>Ti<sub>2</sub>Fe<sub>8</sub>O<sub>19</sub> film at a much thinner thickness of 50 nm has been studied. This film was again grown via PLD from a single SrCo<sub>2</sub>Ti<sub>2</sub>Fe<sub>8</sub>O<sub>19</sub> target under identical conditions to the 0.9 μm film, except the deposition time was reduced. Like the 0.9 μm sample, the film was then annealed in an oxygen atmosphere at 1050°C for 40 minutes.

#### 5.3.1. EDX analysis

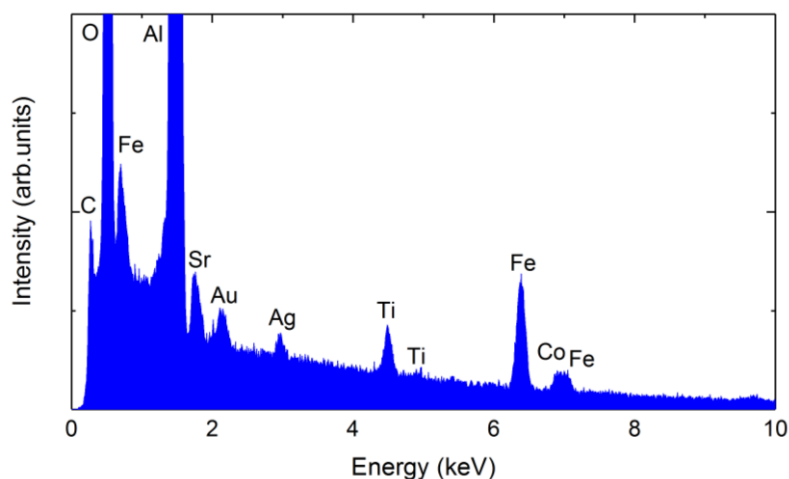


Figure 5.3.1. EDX spectrum obtained for the 50 nm SrCo<sub>2</sub>Ti<sub>2</sub>Fe<sub>8</sub>O<sub>19</sub> thin film.

EDX spectroscopy measurements were also performed for the 50 nm film. A spectrum typical of that seen for the sample is shown in fig. 5.3.1. The spectrum shows clear peaks for all the elements anticipated to be present in both the film and substrate. A much more intense Al peak is observed from the substrate, in comparison to the 0.9 μm film, which is as expected due to the much thinner nature of the film. The presence of gold is also indicated due to the film's Au capping layer. A carbon peak was also seen, as was the case for all other samples studied, in addition to a peak corresponding to Ag, the presence of which is thought to have arisen due to the use of silver conducting paint when contacting the film during x-ray spectroscopy measurements. Quantitative analysis of the EDX spectra suggests a film composition of Sr<sub>0.9</sub>Co<sub>1.9</sub>Ti<sub>2.1</sub>Fe<sub>8.1</sub>O<sub>19</sub>, which is within the error range of the target composition.

#### 5.3.2. X-ray Diffraction Measurements

X-ray diffraction measurements have been performed on the 50 nm sample. The 2θ/ω measurement can be seen in fig. 5.3.2(a). All peaks present can be indexed to either the substrate or the M-type hexaferrite P6<sub>3</sub>/mmc structure, showing that the film is single phase M-type hexaferrite. Many of the hexaferrite Bragg peaks observed are indexed to (00n) reflections. These also appear as the most intense film peaks. The only other film peaks present are the (107), (3-18) and (3-19) reflections, suggesting that the film has a high degree of orientation towards the (00n) growth direction, without being perfectly epitaxial.

It is postulated that the higher degree of (00n) ordering is due to the thickness of the film. The (0001) sapphire substrate has a 23% conventional lattice mismatch with the M-type hexaferrite structure. This may cause the hexaferrite to grow epitaxially, initially, under a strained state, however as the thickness of the film is increased the effect of the strain on the upper layers is reduced and the film relaxes into polycrystalline growth. This may be an oversimplified picture however, as it is possible that a better lattice match can be made with the oxygen sublattice in the Al<sub>2</sub>O<sub>3</sub> substrate. Alternatively, Liu *et al* [115] reported the formation of an Fe<sub>2</sub>O<sub>3</sub> (0001)

intermediate layer for the growth of BaM on Al<sub>2</sub>O<sub>3</sub> (0001), which assists in accommodating the lattice mismatch between the M-type hexaferrite and Al<sub>2</sub>O<sub>3</sub>, although no Fe<sub>2</sub>O<sub>3</sub> phase is observed in the XRD measurements. To further investigate this effect a series of films would need to be grown and studied as a function of film thickness, although this is beyond the scope of this work.

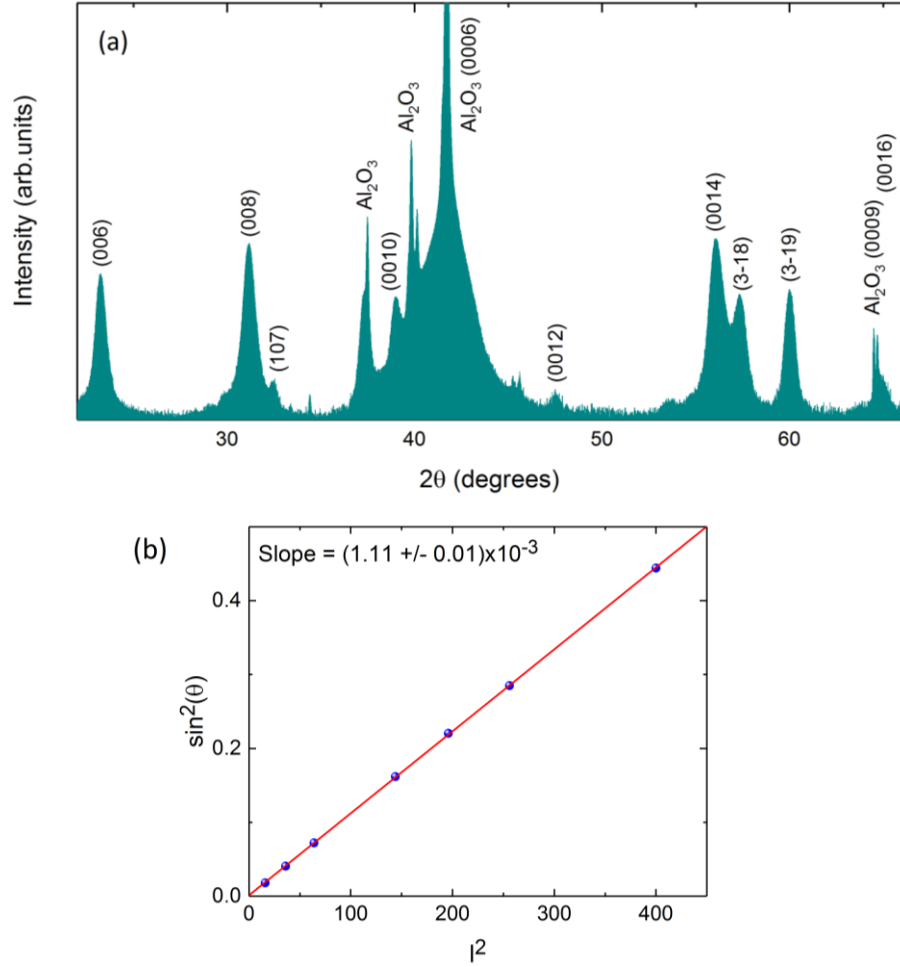


Figure 5.3.2. (a) X-ray diffraction 2θ/ω measurement (b) Plot of I<sup>2</sup> against sin<sup>2</sup> θ for the M-type hexaferrite peak positions of the 50 nm SrCo<sub>2</sub>Ti<sub>2</sub>Fe<sub>8</sub>O<sub>19</sub> film.

The positions of the XRD peaks have been used to determine the films lattice constants  $a$  and  $c$ . A plot of  $I^2$  against  $\sin^2 \theta$  for the M-type hexaferrite (00n) peak positions is used, as shown in fig. 5.3.2(b), is used to determine the  $c$ -axis lattice constant. It is seen that all points fit closely to a linear best-fit line, indicating that the peaks are all indexed correctly. Analysis using the slope of the linear fit produces a lattice constant of  $c = (23.1 \pm 0.1) \text{ \AA}$ . This value is larger but to within error of that determined for the 0.9 μm film and again compares well to literature [10]. The peak positions of the (107), (3-18) and (3-19) reflections were then used to calculate the in-plane lattice constant, producing  $a = (5.87 \pm 0.05) \text{ \AA}$ . A small reduction in the in-plane lattice constant with respect to the literature values for polycrystalline samples is found with  $a = 5.89 \text{ \AA}$  [10]. This indicates a compressive strain on the film due to the smaller lattice constant of the substrate. Through comparison of the 2θ/ω measurements performed for the two films, it is evident that the film peaks are broader for the 50 nm film. According to the Scherrer equation (eqn. 5.1), the broadening of the diffraction peak,  $\beta_L$ , is inversely proportional to the mean crystallite size,  $\tau$  [258].

$$\tau = \frac{\kappa\lambda}{\beta_L \cos \theta} \quad \text{Eqn. 5.1.}$$

Here  $\lambda$  is the x-ray wavelength,  $\theta$  is the Bragg angle and  $\kappa$  is a shape factor, typically around 0.9. Using the FWHM of the Bragg peaks for the 50 nm film, according to the Scherrer equation,

produces a mean crystallite size of the order of 20 nm, assuming a shape factor of 0.9. This value does not account for any broadening due to inhomogeneous strain in the film, such as that due to defects, thus it is expected that the true mean crystallite size is larger than this value. For larger grain sizes, effects such as instrumental broadening limit the sharpness of the Bragg peaks. As a consequence of this, Scherrer analysis cannot be quantitatively applied to the 0.9  $\mu\text{m}$  film, however, this indicates that the 0.9  $\mu\text{m}$  has a larger grain size.

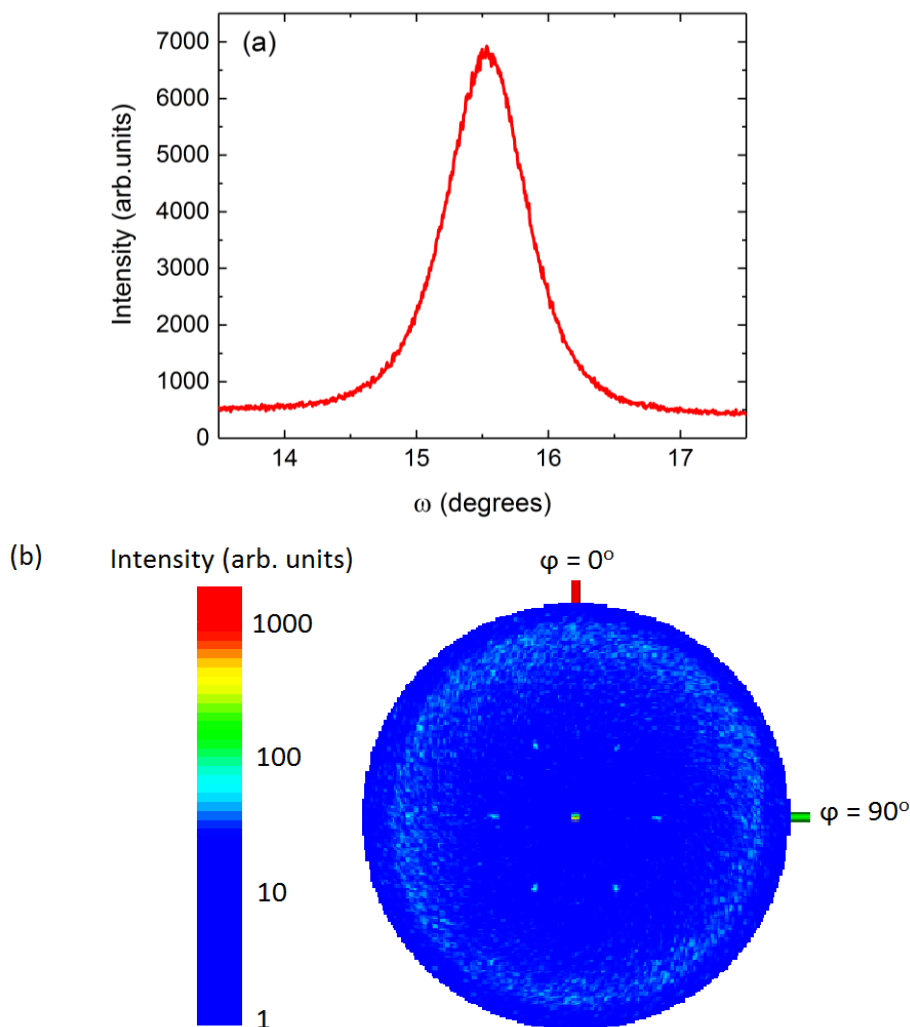


Figure 5.3.3. (a) XRD rocking curve measurement, (b) pole figure measurement performed at the (008) diffraction peak, for the 50 nm  $\text{SrCo}_2\text{Ti}_2\text{Fe}_8\text{O}_{19}$  film grown on  $\text{Al}_2\text{O}_3$  (0001).

Fig. 5.3.3(a) shows the rocking curve measurement performed at the M-type hexaferrite (008) diffraction peak. For this reflection a FWHM of  $(0.7 \pm 0.1)^\circ$  was determined, which is narrower than the value obtained for the 0.9  $\mu\text{m}$  film again suggesting an improvement in crystalline quality. This also supports the work of Dorsey *et al* [20] who showed the FWHM values for BaM Films increased as a function of film thickness. A FWHM of  $0.7^\circ$  compares well with other epitaxial M-type hexaferrite films grown on sapphire, with  $1.2^\circ$  measured for the film grown in chapter 4 and Geiler *et al* [21] reporting a FWHM of  $0.3^\circ$  for an epitaxial  $\text{BaFe}_{12}\text{O}_{19}$  film grown by PLD.

A pole figure measurement was also performed at the (008) diffraction peak to analyse the crystallographic texture of the film, as shown in fig. 5.3.3(b). At the centre of the pole figure a narrow intense point is seen, corresponding to the (008) reflection itself, which suggests a highly textured film. The pole figure measurement also shows six diffraction spots on a ring of  $30^\circ$  in the tilt angle ( $\chi$ ) and separated by  $60^\circ$  in the sample rotation angle ( $\phi$ ) revealing a six-fold symmetry. This is the same as that observed for the epitaxial film grown in chapter 4, as well as in the literature [242] [122], and is due to the hexagonal structure of the hexaferrite. This symmetry confirms the

highly oriented nature and texture of the film [241]. A distribution in intensity can also be seen on a ring at high angles, between 10 and 30° in  $\chi$ . This then indicates that the film is not perfectly oriented, in agreement with the observations of peaks outside the (00n) family in the  $2\theta/\omega$  data, and improvements can still be made to its texture.

### 5.3.3. Temperature dependent Magnetometry

For the 50 nm sample, like the 0.9  $\mu\text{m}$ , in plane temperature dependent magnetic measurements have been performed using a VSM-SQUID. Measurements performed at 10 K, 200 K, 300 K and 500 K are all shown in fig. 5.3.4.

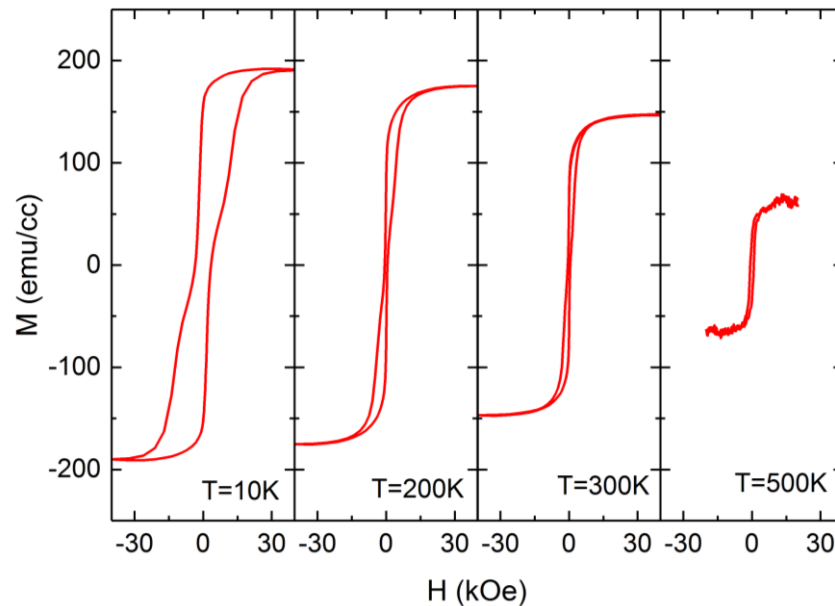


Figure 5.3.4.  $M(H)$  measurements performed at different temperatures for the 50 nm  $\text{SrCo}_2\text{Ti}_2\text{Fe}_8\text{O}_{19}$  thin film.

At 300 K an  $M_s$  of  $(150 \pm 20)$   $\text{emu/cc}$  was measured, this compares closely to the  $(170 \pm 20)$   $\text{emu/cc}$  determined at the same temperature for the 0.9  $\mu\text{m}$  film, as well as thin film literature values [24]. However, the coercivity measured at 300 K is larger than that of the 0.9  $\mu\text{m}$  sample, at  $(550 \pm 20)$  Oe, this is also larger than many  $\text{SrCo}_2\text{Ti}_2\text{Fe}_8\text{O}_{19}$  samples in the literature with Wang *et al* observing a coercivity of 100 Oe for bulk polycrystalline  $\text{SrCo}_2\text{Ti}_2\text{Fe}_8\text{O}_{19}$  [10] and for a 1  $\mu\text{m}$  film, Mohebbi *et al* [24] determined a value of 20 Oe. The value measured for this 50 nm film is still much less than that typically observed for undoped SrM, showing that the Co and Ti substitutions still act to reduce coercivity but in this case to a lesser extent. One explanation for this may be due to the smaller film thickness and strain effects or alternatively the Co and Ti may have been forced into different sites compared to the 0.9  $\mu\text{m}$  film reducing the cobalt's effect on  $H_c$ .

The significant difference in  $M(H)$  at all temperatures between the 50 nm and the 0.9  $\mu\text{m}$  films is that the 50 nm hysteresis displays a wasp-waisted effect. It is seen that the hysteresis loop narrows as the field approaches zero and then opens up again. A pre-requisite for wasp-waisted hysteresis is the existence of two or more magnetic components within the material, that have contrasting coercivities [259]. The effect can be seen in composite samples containing two magnetic phases, each with a different coercive field; however, the XRD measurements show the presence of only one crystalline phase within this film suggesting that the existence of two phases within the film is not the explanation for the effect observed. The wasp-waisted hysteresis effect can also be caused by a distribution in grain sizes, in which the coercivity is size dependent [259]. Alternatively, it may also be conceivable, that for the Co-Ti doped hexaferrite structure, the substitutions occur at different sites within the lattice for different grains, producing different coercivities within the film. If this was proven to be the case, one could then postulate that the differences in substitution sites

could be caused by the effects of strain from the substrate changing which sites are energetically favourable for substitution. However, the presence of the effect ultimately suggests that the magnetic structure of the 50 nm film is different to the 0.9  $\mu\text{m}$  and further measurements such as the  $M(T)$  and XMCD analysis may help provide an explanation.

The temperature dependent  $M(H)$  measurements show that the coercivity of the sample increases at low temperature, much like the 0.9  $\mu\text{m}$  film. Between 300 and 200 K the coercivity only increases by a relatively small amount to  $(600 \pm 20)$  Oe and a much larger increase is seen between 200 and 10 K, with a value of  $(3500 \pm 100)$  Oe being observed. As was also the case for the 0.9  $\mu\text{m}$  sample,  $M_s$  reduces with increasing temperature, with a maximum magnetisation of  $(190 \pm 20)$  emu/cc observed at 10 K. This value is significantly smaller than the 280 emu/cc measured for the 0.9  $\mu\text{m}$  sample, suggesting that the  $M(T)$  relationships may differ. It is also apparent that  $M_s$  is reduced less rapidly than for the 0.9  $\mu\text{m}$  sample above 300 K and a significant hysteresis loop is still observed, fig. 5.3.4, at 500 K with an  $M_s$  of  $(70 \pm 10)$  emu/cc.

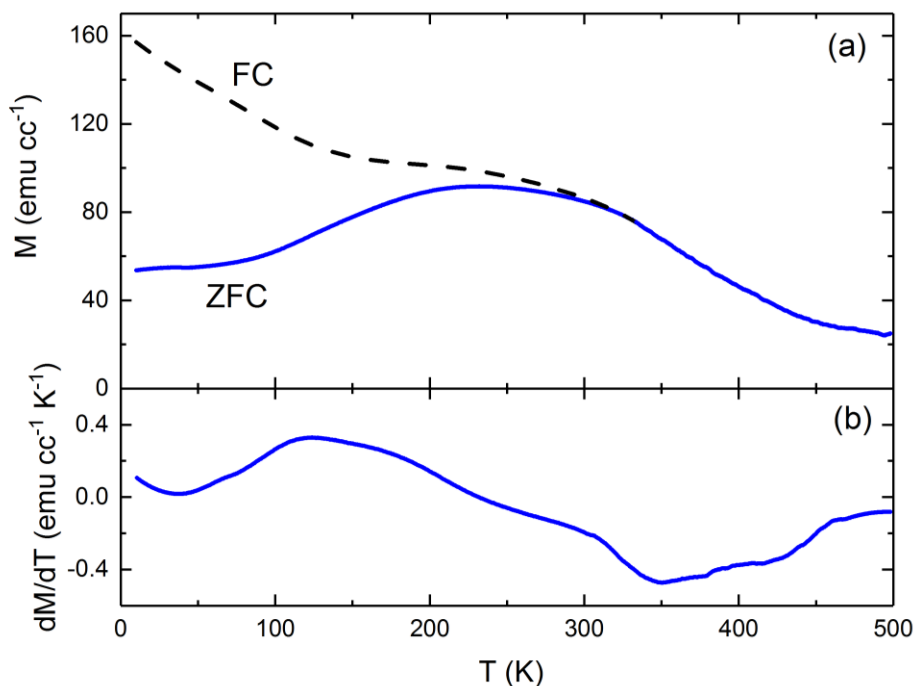


Figure 5.3.5. (a)  $M(T)$  obtained via VSM, measured at 300 Oe for FC and ZFC conditions, (b) The derivative of the ZFC  $M(T)$  obtained for the 50 nm  $\text{SrCo}_2\text{Ti}_2\text{Fe}_8\text{O}_{19}$  thin film.

The temperature dependent magnetic properties have been investigated further, by performing field cooled and zero field cooled  $M(T)$  measurements. The measurements were taken under the same conditions as the 0.9  $\mu\text{m}$  sample, with a 300 Oe in plane magnetic field, between 5 and 500 K. In fig. 5.3.5(a), the FC and ZFC curves follow a similar form to the 0.9  $\mu\text{m}$  case. It is apparent, however, that at low temperature the measured moment for the ZFC levels off at 50 emu/cc compared to  $\sim 0$  emu/cc for the 0.9  $\mu\text{m}$  film. Likewise the FC curve only reaches a magnetisation of 160 emu/cc at  $T = 10$  K, compared to 200 emu/cc for the 0.9  $\mu\text{m}$  film. For  $T > 300$  K  $M$  drops off more gradually for the 50 nm film and is still as large as 25 emu/cc at 500 K, an effect that is also evident from the  $M(H)$  measurements. The general shape of the  $M(T)$  curve is still of the same general shape to those observed by others for  $\text{SrCo}_2\text{Ti}_2\text{Fe}_8\text{O}_{19}$  samples [10] [106] [23].

The differentiated ZFC  $M(T)$  shown in fig. 5.3.5(b), displays both a positive and negative peak, much like the 0.9  $\mu\text{m}$  measurement, at two temperatures defined as  $T_1$  and  $T_2$ . It is seen that both  $T_1$  and  $T_2$  occur at lower temperatures for the 50 nm film, 125 K and 350 K, respectively. Thus, it is apparent from these measurements that the general trend in temperature dependence of magnetic properties is the same between the 50 nm sample and the thicker films reported, both here and in the literature. There are however, significant differences in the transition temperatures and the

coercivities, indicating changes to the magnetic structure. The dynamic magnetic properties of this sample could not be investigated as FMR measurements were not possible due to the thickness of the film resulting in a weak FMR response.

### 5.3.4. Element Specific Soft X-ray Magnetic Spectroscopy

The Ti XAS measured for the 50 nm film at 300 K, is shown in fig. 5.3.6. The spectrum displays four distinct peaks and is almost identical to that observed for the 0.9  $\mu\text{m}$  film, suggesting octahedrally co-ordinated Ti. Comparison to spectra generated from atomic multiplet calculations confirm that the Ti within the film have a 4+ valence and are octahedrally co-ordinated. This is consistent with that expected from the literature [6] [83], which suggests the Ti ions preferentially occupy the 12k sites acting to magnetically de-couple the R- and S-blocks [6].

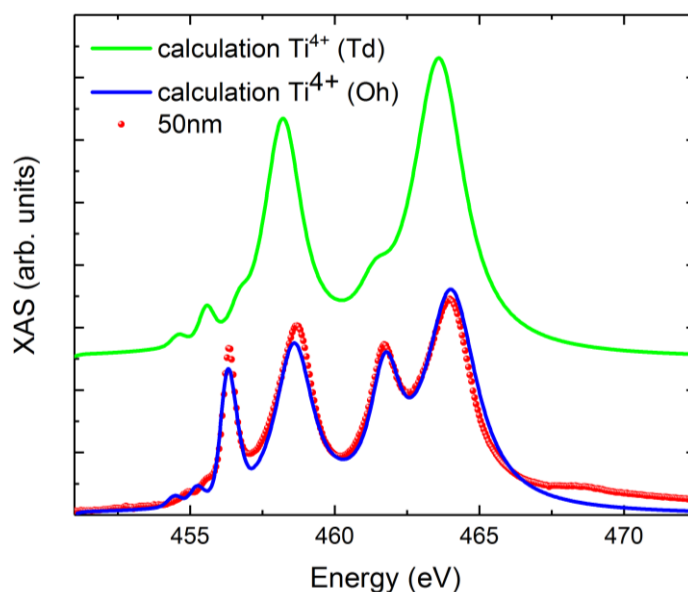


Figure. 5.3.6. Ti  $L_{2,3}$  XAS measured for the 50 nm  $\text{SrCo}_2\text{Ti}_2\text{Fe}_8\text{O}_{19}$  thin film at 300 K in TEY (red data points). The blue solid line is the simulated spectra from an atomic XAS multiplet calculation of  $\text{Ti}^{4+}$  in an octahedral co-ordination with  $10Dq = 1.9$  eV. An equivalent calculation for  $\text{Ti}^{4+}$  in a tetrahedral co-ordination with  $10Dq = -0.9$  eV is given by the green line.

The XAS and XMCD measurements performed at the Co  $L_{2,3}$  edges are shown in fig. 5.3.7(a). The lineshape of the Co XAS shows only minor differences compared to the 0.9  $\mu\text{m}$  measurement and comparison to multiplet calculations indicates that it is a superposition of octahedral, tetrahedral and trigonal bipyramidal  $\text{Co}^{2+}$  spectra. As was the case for the 0.9  $\mu\text{m}$  film, two additional peaks are also seen in the range measured for the Co XAS spectra. These peaks indicate the presence of barium, as discussed in section 5.2.6, likely due to the sample holder.

The Co XMCD in contrast shows significant differences to that of the 0.9  $\mu\text{m}$  sample. It is now seen that the relative amplitude of the positive contribution at the  $L_3$  edge is diminished with the negatively defined contribution increasing in amplitude. Good fits to the XMCD spectra are again obtained through atomic multiplet calculations, using the same parameters as described for the 0.9  $\mu\text{m}$  fitting, shown in black in fig. 5.3.7(a). The fitting for this sample reveals a  $\text{Co}^{2+}$  occupation consisting of 85% octahedral, 9% tetrahedral and 6% trigonal bipyramidal. Hence, we see a reduction in magnetic contribution from the tetrahedral and trigonal bipyramidal sites, compared to the 0.9  $\mu\text{m}$  film, which is accompanied by an increase in the octahedral contribution. This measurement then indicates that the sites occupied by the Co ions are different for the thinner film and provides an explanation for the differing magnetic properties.

In fig. 5.3.7(b), the Fe XAS lineshape is consistent with that observed for the thicker  $\text{SrCo}_2\text{Ti}_2\text{Fe}_8\text{O}_{19}$  film. The corresponding Fe XMCD again displays three distinct peaks at the  $L_3$  edge, with multiplet

fitting attributing these to  $O_h$   $Fe^{2+}$ ,  $T_d/Trig$   $Fe^{3+}$  and  $O_h$   $Fe^{3+}$ , respectively. Comparing Fe XMCD spectra between the 0.9  $\mu m$  and 50 nm sample it is clear that the ratio of the three peak heights is different, with the  $T_d/Trig$  contribution more prominent for the 50 nm case. Atomic multiplet fitting produces a ratio that is 70% octahedral and 30% tetrahedral / trigonal bipyramidal. This suggests that the octahedral Fe contribution is reduced with respect to the 0.9  $\mu m$  case, which is consistent with the Co XMCD results that indicate a greater octahedral Co contribution.

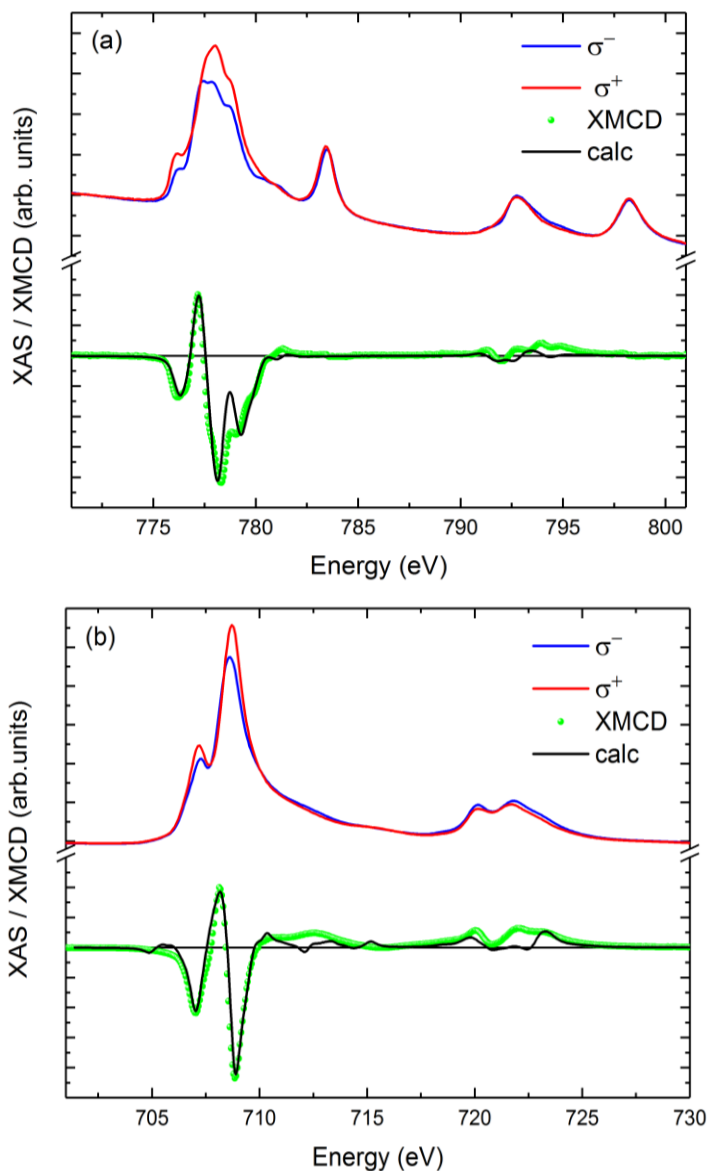


Figure. 5.3.7. XAS at the (a) Co and (b) Fe  $L_{2,3}$  edges for  $\sigma^-$  (blue) and  $\sigma^+$  (red) x-rays, measured for the 50 nm  $SrCo_2Ti_2Fe_8O_{19}$  thin film at 300 K in TEY. The corresponding XMCD is plotted (green) with the fit using atomic multiplet calculations (black).

The integrated XMCD spectra for Fe and Co are displayed in fig. 5.3.8(a) and (b), respectively. The integrated Fe spectrum has the same general form as that seen for the 0.9  $\mu m$  film; however, it is apparent that the orbital moment is quenched to a greater extent for the 50 nm film producing a smaller  $m_L / m_{S_{eff}}$  of 0.016. This corresponds to a g-factor of 2.03, which is typical for a ferrite structure with values around 2 often seen for Fe in ferrite structures [24] [60] [107].

At the Co edge, the integrated spectrum looks significantly different to the 0.9  $\mu m$  film; q is now smaller than p but only by a small amount suggesting only a weak partial quenching of the orbital moment. Analysis produces a large  $m_L / m_{S_{eff}}$  of 0.411, this value and the form of the integrated Co XMCD, closely resembles that of the simulated octahedral spectrum displayed in fig. 5.2.12. This is as expected with the multiplet fitting indicating an 85%  $O_h$  contribution.

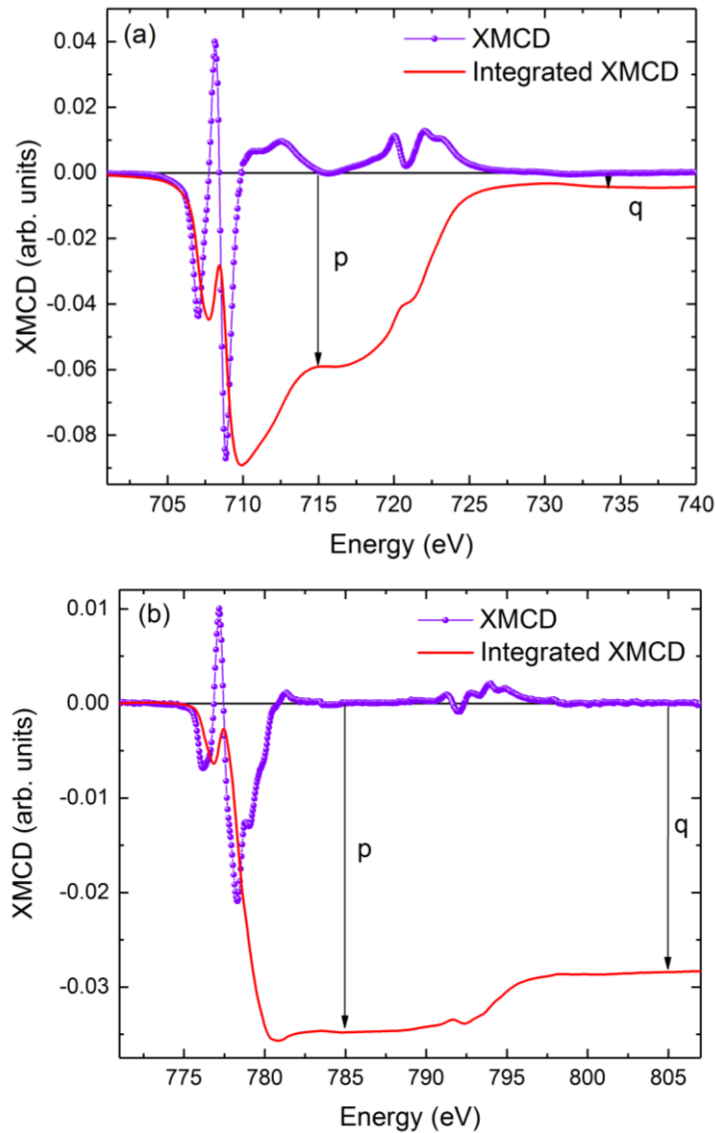


Figure. 5.3.8. (a) Fe and (b) Co  $L_{2,3}$  edge XMCD (purple) and the corresponding integrated XMCD (red), measured for the 50 nm  $\text{SrCo}_2\text{Ti}_2\text{Fe}_8\text{O}_{19}$  thin film at 300 K in TEY.

Element specific XMCD hysteresis measurements have again been performed at both the Co and Fe L-edges. Loops were obtained at temperatures of 1.6 K, 230 K and 300 K, using the same energies as described for the 0.9  $\mu\text{m}$  film. Comparing the Co and Fe measurements, in fig. 5.3.9(a) and (b), respectively, it is evident that the signs of the Co and Fe curves are the same, with a negative field producing a negatively defined net magnetic moment. This is different to the 0.9  $\mu\text{m}$  case, suggesting that the Co moment, at the measuring energy, is opposite in the 50 nm film, as seen in the XMCD measurements due to a larger octahedral contribution.

It is apparent that the coercivities, of both the Co and Fe loops, are larger than those measured for the 0.9  $\mu\text{m}$  sample, supporting the coercivities seen in the VSM measurements. At 300 K, the Co has a coercivity of 2 kOe, increasing to 3 kOe by 230 K and becoming as large as 8.5 kOe by 1.6 K. For both Co and Fe, we see that  $H_c$  reduces with increased temperature, an effect that was again seen by VSM. The Fe  $H_c$  at 300 K is less than 100 Oe but at 230 K has increased, more significantly than for the 0.9  $\mu\text{m}$  film, to 1 kOe, reaching 3 kOe by 1.6 K. The Fe specific hysteresis measurements in fig. 5.3.9(a), all show a wasp-waisted effect. This shows that the wasp-waisted effects, seen in the VSM measurements, are due solely to the Fe contribution.

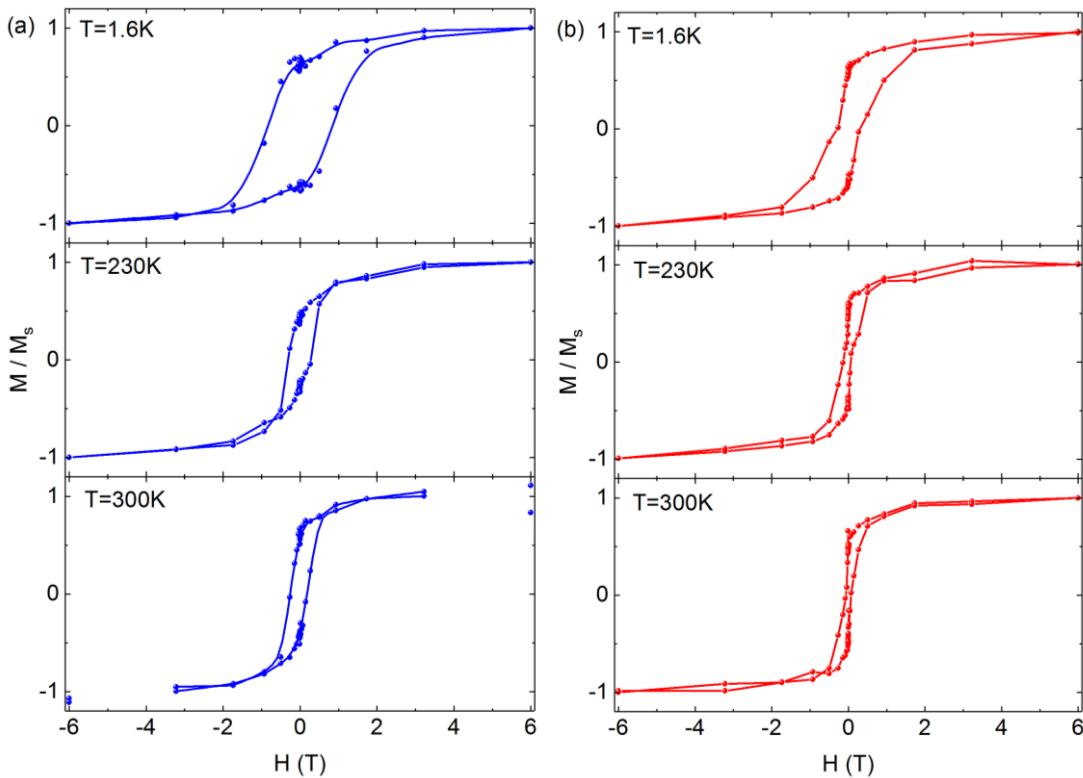


Figure 5.3.9. (a) Co and (b) Fe element specific hysteresis measurements obtained at 1.6 K, 230 K and 300 K for the 50 nm  $\text{SrCo}_2\text{Ti}_2\text{Fe}_8\text{O}_{19}$  thin film in FY.

#### 5.4. Summary and Conclusions

In the 0.9  $\mu\text{m}$  thin film, a  $\text{SrCo}_2\text{Ti}_2\text{Fe}_8\text{O}_{19}$  film, grown using a single target PLD technique, has been characterised both structurally and magnetically. At 300 K a low coercivity of  $(20 \pm 5)$  Oe is measured, supporting claims in the literature that the Co substitution into the M-type structure drastically reduces  $H_c$  [6] [246] [106]. The temperature dependent magnetic properties of the film also appear characteristic of those seen in the literature [24] [10] [23].

XAS and XMCD measurements were performed at the Fe, Co and Ti L-edges, and fitted with atomic multiplet calculations to determine the co-ordination and valences of each element, as well as investigate their contribution to the samples overall magnetic structure. The Fe XMCD reveals a percentage of the octahedrally co-ordinated Fe has a 2+ valence, the presence of which is detrimental to magnetoelectric materials as it provides a conductive pathway, due to polaronic hopping, suppressing electric polarisation. Thus, if the  $\text{Fe}^{2+}$  could be removed this could result in the enhancement of the ME coupling present in such materials [24]. Ti XAS measurements confirm that the Ti have a 4+ valence as well as a strong preference for the occupation of octahedral sites, which supports the literature that suggests they preferentially occupy the 12k octahedral sites [6] [83]. An effect, which is thought to magnetically de-couple the R- and S-blocks, a pre-requisite for the formation of the non-collinear magnetic structure reported [6]. Additionally, XMCD at the Co edge indicates that the Co have a 2+ valence and are substituted to all three different co-ordinations. Around a fifth of the Co ions occupy the 2b trigonal bipyramidal sites, which is consistent with Cabanas *et al* [86], who stated that the Co occupy the 2b sites above a critical doping concentration. This is also believed to play a significant role in the formation of non-collinear magnetic structures within Co-Ti doped hexaferrites [6].

In addition to the 0.9  $\mu\text{m}$  thin film, a much thinner film of 50 nm, grown by the same growth procedure, has been characterised using x-ray spectroscopy techniques. Structural characterisation indicates that this thinner film has a smaller grain size and a close to epitaxial crystalline ordering.

Dorsey *et al* [20] showed that the crystalline structure of M-type hexaferrite films grown on sapphire (0001) is dependent upon film thickness. They showed that the crystalline quality is reduced with film thickness and above a critical thickness; epitaxial growth is no longer possible. This effect is seen here between the 50 nm and 0.9  $\mu\text{m}$  films. We postulate that the lattice mismatch between film and substrate causes the hexaferrite to grow epitaxially, initially, under a strained state, however as the thickness of the film is increased the effect of the strain on the upper layers is reduced and the film relaxes into polycrystalline growth.

The 50 nm film displays magnetic properties that differ from the 0.9  $\mu\text{m}$  film and literature. A significantly larger coercivity is observed at RT and the M(T) measurements show significant changes in the phase transition temperatures. The XMCD results present a significant difference in the magnetic contribution of the Co, with a greater proportion of octahedrally co-ordinated cobalt and a reduction in both tetrahedral and trigonal bipyramidal contributions. This differently co-ordinated Co then provides an explanation for the differing magnetic properties of the thinner film. To summarise, the 0.9  $\mu\text{m}$   $\text{SrCo}_2\text{Ti}_2\text{Fe}_8\text{O}_{19}$  film displays magnetic properties characteristic of the  $\text{SrCo}_2\text{Ti}_2\text{Fe}_8\text{O}_{19}$  samples in the literature and it has been shown that the Ti ions preferentially occupy octahedral lattice sites whilst the Co ions occupy  $\text{O}_h$ ,  $\text{T}_d$  and Trig sites, with the greatest contribution coming from the octahedral. Alternatively, the thinner 50 nm film displays a different magnetic structure; with the  $\text{Co}^{2+}$  ions occupy a different ratio of lattice sites. We postulate that this effect may be caused by the strain of the substrate on the thinner film, resulting in a change to the preferential occupation sites of the Co ions. In order to substantiate this claim however, further investigations are required on numerous films, grown as a function of film thickness, to eliminate other possible causes of this effect, such as unintended variations in growth conditions etc.

## Chapter 6: Enhanced MagnetoElectric Effect in M-type Hexaferrites by Co substitution into Trigonal Bipyramidal Sites

### 6.1 Introduction

M-type hexaferrite thin films are again studied in this chapter with a composition  $\text{SrCo}_2\text{Ti}_2\text{Fe}_8\text{O}_{19}$ . However, rather than being grown by single target PLD these samples have been grown from multiple targets, via an Alternating Target Laser Ablation Deposition (ATLAD) technique, in an attempt to force the  $\text{Co}^{2+}$  and  $\text{Ti}^{4+}$  substitutions into different sites. These thin films have been characterised, both structurally and magnetically, in order to observe the effects the substitution sites have on the films properties. X-ray spectroscopy techniques have been used to determine the occupation sites of the Co and Ti dopants, allowing for the observation of an enhanced ME coupling as a consequence of the Co occupation of trigonal bipyramidal lattice sites.

As explained previously, M-type hexaferrites can be described as a sequence of  $\text{RSR}^*\text{S}^*$  (\* indicates an  $180^\circ$  rotation around the c axis) layers [6]. The unit cell of an M-type hexaferrite is shown in Fig.6.1.  $\text{Fe}^{3+}$  cations occupy both octahedral and tetrahedral co-ordinated sites in the S block (Wyckoff positions 2a and 4f<sub>1</sub>) and octahedral sites (12k and 4f<sub>2</sub>) in the R block. The Sr ion located at 2d strongly distorts the site located at the 2b positions giving rise to a bi-pyramidal 5 fold co-ordination [250].

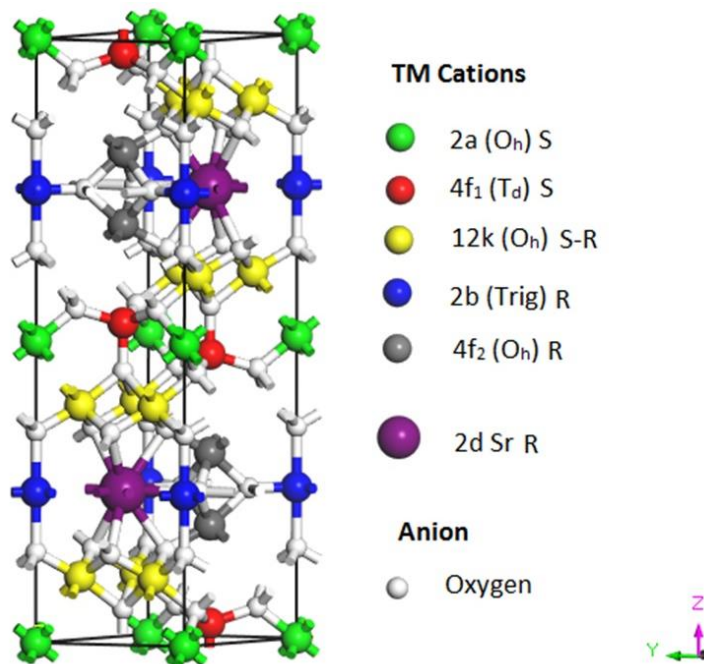


Figure. 6.1. Perspective view of the M-type structure showing Wyckoff positions, co-ordination and block of the cations.

It is known that a result of the Co and Ti substitutions is to stabilize a non-collinear longitudinal conical magnetic structure [6] [83]. For ME multiferroics the spiral magnetic state is of high interest as magnetically induced ferroelectrics are typically found when a complex magnetic order (spiral) exists [260].  $\text{Co}^{2+}$  substitutions in ferrite structures are also a well-known source of magnetoelastic coupling due to the large orbital moment of  $\text{Co}^{2+}$  compared to  $\text{Fe}^{3+}$  [37]. As the linear ME coupling is directly proportional to the magnetoelastic coupling, or magnetostriction,  $\lambda_m$ , this implies that an increase in  $\lambda_m$  increases  $\alpha$  [57]. However, this picture is oversimplified in that the material also requires a mechanism, such as the piezoelectric effect or electrostriction, for coupling the applied electric field into strain.

Several mechanisms for magnetically induced ferroelectricity have been proposed previously. Jia *et al* [51] classifying the origin of magnetically induced ferroelectric polarization into three main

mechanisms: the exchange-striction mechanism, spin-current mechanism, and the d-p hybridization mechanism. However, recently a unique magnetic-ion-induced displacive electric polarization was reported in (Ba,Sr)Fe<sub>12</sub>O<sub>19</sub> [14] providing a further route for multiferroicity in hexaferrites. The authors demonstrated that the competition between long range Coulomb interactions and short range Pauli repulsion in the (TM)O<sub>5</sub> bi-pyramidal unit, unique to the hexaferrite structure, favours an off centre displacement of the TM ion inducing a local electric dipole. The role of the bi-pyramidal trigonal site to ME effects in these materials has not received significant attention as yet but it seems that it may be important in several of the mechanisms, i.e. due to the displacement of the magnetoelastic ion resulting in a non-centrosymmetric local environment and its role in the non-collinearity of the spins in the structure.

In this chapter it is shown that the ME coefficient,  $\alpha$ , can be significantly enhanced by doping Co<sup>2+</sup> into the R-block of the hexaferrite structure which contains the 5-fold trigonal bi-pyramidal site. The samples studied were grown on single crystal sapphire (0001) substrates at 600°C under a (200 ± 5) mTorr partial pressure of oxygen, at NorthEastern University, Boston. The ATLAD technique was used to deposit Co and Ti ions in the S or R block of the ME hexaferrite material, allowing for different site occupancies compared to deposition from a single target [122]. During film growth, the R block was grown by depositing from a target of SrFe<sub>(4- $\delta$ )</sub>Ti<sub>0.5 $\delta$</sub> Co<sub>0.5 $\delta$</sub> O<sub>7</sub> whilst the S block was grown by depositing from a target of Fe<sub>(1+0.25 $\delta$ )</sub>Ti<sub>0.5(1-0.25 $\delta$ )</sub>Co<sub>0.5(1-0.25 $\delta$ )</sub>O<sub>3</sub>. Three samples were grown with  $\delta = 0.0, 0.2$  and  $0.4$ . It is noted that irrespective of the value of  $\delta$  the chemical formula was held constant, SrFe<sub>8</sub>Ti<sub>2</sub>Co<sub>2</sub>O<sub>19</sub>, but for  $\delta = 0$  the aim was to try and force Ti and Co ions to reside only in the S block. Deposited films were post-annealed in oxygen at 1050 °C for 40 minutes in order to increase the resistivity of the sample [5], and then capped with 2 nm of Au. The substrates had a lateral size of 5 mm x 5 mm and the deposited film thicknesses were estimated using a profilometer to measure the thickness of another film that was placed alongside the samples during growth. This produced film thicknesses of 10, 1, and 1  $\mu\text{m}$  for  $\delta = 0.0, 0.2$ , and  $0.4$ , respectively. From these measurements, the volumes of the hexaferrite films were calculated.

Given that for the  $\delta = 0.0$  sample all of the Co and Ti are substituted to only the S block, it would be expected that these cations would occupy only the 2a, 12k and 4f<sub>1</sub> sites. This means that the Co and Ti could only have octahedral or tetrahedral occupation. However, given Ti has a strong preference for octahedral sites [254] [86], octahedrally co-ordinated Ti was expected. With increasing  $\delta$  the Co and Ti substitutions are directed less towards the S block and more of the cobalt and titanium dopants are forced into the R-block. This opens up the possibility of the Co occupying the 2b trigonal bipyramidal sites. Hence, through the investigation of these samples insight has been gained into the role that cobalt occupation of the trigonal bipyramidal site has on the magnetoelectric coupling mechanism present.

## 6.2 EDX Chemical Composition analysis

EDX analysis has been performed for all three samples in order to investigate their chemical composition. Spectra representative of each film are displayed in fig. 6.2. In the figure, it is evident that peaks are present, for all three films, at energies that indicate the presence of all the expected film constituents, Fe, Co, Ti and O. In addition to these elements, carbon and gold peaks are seen, the C being present in the chamber atmosphere and the Au measured due to its presence in the films capping layer. In the  $\delta = 0.2$  and  $\delta = 0.4$  measurements Al peaks are seen due to the substrate, along with a proportion of the O. Such substrate contributions are not seen for the  $\delta = 0.0$  measurement, however, due to this film being thicker than the other two.

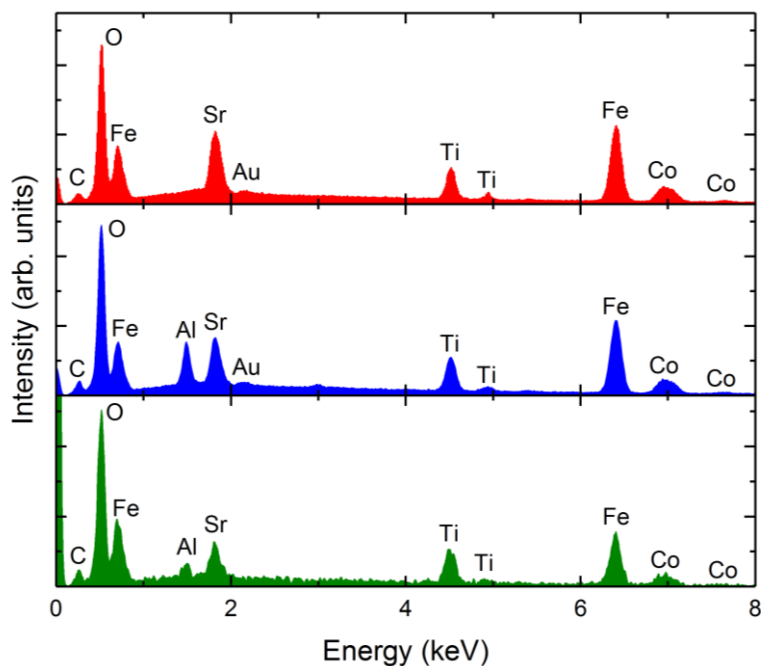


Figure. 6.2. EDX spectra obtained for  $\delta = 0.0$  (red),  $\delta = 0.2$  (blue) and  $\delta = 0.4$  (green).

These EDX measurements were used, as detailed in section 3.2.1, to determine the relative abundance of each film element. This analysis indicates that all three films have a composition that closely resembles the intended  $\text{SrCo}_2\text{Ti}_2\text{Fe}_8\text{O}_{19}$  formula. Film compositions of  $\text{Sr}_{1.2}\text{Co}_{1.9}\text{Ti}_{1.8}\text{Fe}_{8.1}\text{O}_{19}$ ,  $\text{Sr}_{1.1}\text{Co}_{1.9}\text{Ti}_{2.0}\text{Fe}_{8.2}\text{O}_{19}$  and  $\text{Sr}_{0.8}\text{Co}_{1.9}\text{Ti}_{2.2}\text{Fe}_{8.1}\text{O}_{19}$  were calculated for  $\delta = 0.0$ ,  $\delta = 0.2$  and  $\delta = 0.4$ , respectively. These results confirm that all expected film constituents are present in each film with Co-Ti doping consistent with that expected from the growth procedure.

### 6.3 X-ray Diffraction Measurements.

XRD  $2\theta/\omega$  measurements for all three samples are shown in fig. 6.3. The (0006) sapphire substrate peak is present in all three films at an angle of  $41.68^\circ$ . The additional substrate peaks seen around this peak for the in figure 6.3(a) and (b) are due to the (0006) substrate  $\text{La}_2$ ,  $\text{La}_1$  and  $\text{K}\beta$  reflections. The substrate peak in figure 6.3(c), for the  $\delta = 0.4$  sample, is reduced in intensity with respect to the other films. As the diffractometer was aligned to the film peaks, this suggests that there is a greater offset between film and substrate planes for this sample. The  $\delta = 0.0$  and  $\delta = 0.2$  measurements also show the (0009) substrate peak.

The Bragg peaks, for each film, are indexed to the M-type hexaferrite structure and the data reveals that all the samples are polycrystalline in nature. Several diffraction peaks observed are present for all 3 films, such as the (107), (201), (203) and (301) reflections. The  $\delta = 0.4$  sample although being polycrystalline shows a stronger preference for orientated growth along the (00n), with the (006), (008), (0010) and (0014) reflections all being prominent. Also for the  $\delta = 0.4$  sample we see the presence of a peak that can only be indexed to cobalt ferrite,  $\text{CoFe}_2\text{O}_4$ . This peak is solitary and has an intensity that is  $10^2$  x smaller than the most intense hexaferrite peak. Suggesting that the  $\text{CoFe}_2\text{O}_4$  secondary phase is minimal and should not have significant effects on the films properties. XRD patterns reveal the hexagonal P63/mmc structure for all three films. The analysis produces lattice spacing's of  $a = 5.87(2) \text{ \AA}$ ,  $c = 23.05(4) \text{ \AA}$  for  $\delta = 0.0$ ,  $a = 5.84(2) \text{ \AA}$ ,  $c = 23.05(4) \text{ \AA}$  for  $\delta = 0.2$  and  $a = 5.87(3) \text{ \AA}$ ,  $c = 22.93(4) \text{ \AA}$  for  $\delta = 0.4$ , which are in good agreement to the range of values found in the literature [6]. These lattice constants were calculated from the relative peak positions and spacing's of the M-type hexaferrite peaks by applying the method outlined in chapter 3.2.2.1.

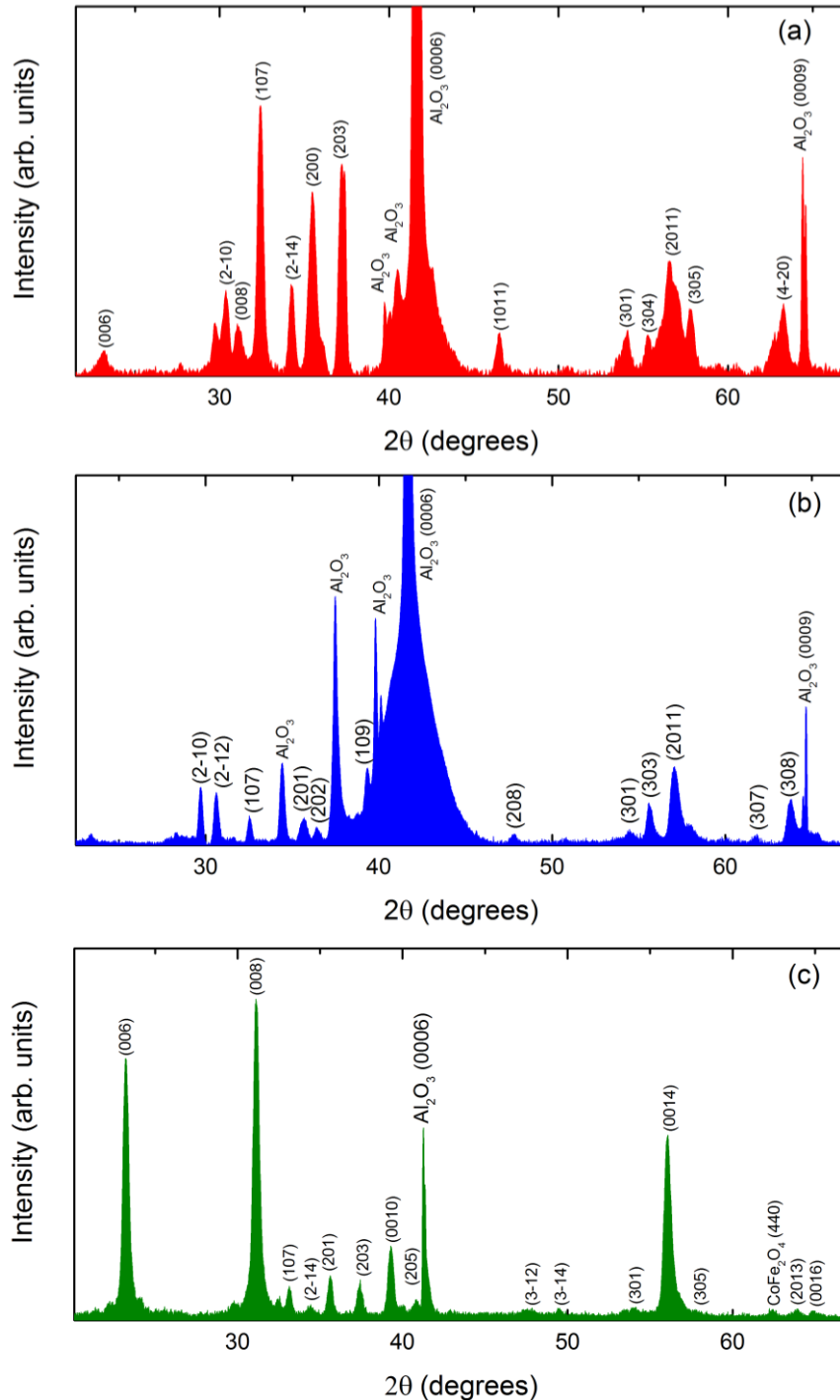


Figure 6.3. X-ray diffraction measurements for (a)  $\delta = 0.0$ , (b)  $\delta = 0.2$  and (c)  $\delta = 0.4$ .

To summarise, XRD measurements confirm that all three films are polycrystalline M-type hexaferrite with lattice constants in good agreement with literature values [6].

#### 6.4 Temperature dependent Magnetometry

The samples magnetic properties were investigated using a VSM-SQUID. The magnetometry measurements were performed between 10 K and 500 K, with  $M(H)$  loops measured over a range of fixed temperatures between 10 K and 320 K.

Fig. 6.4(a)(b)(c) show the in and out of plane  $M(H)$  measurements for the  $\delta = 0.0$ ,  $\delta = 0.2$  and  $\delta = 0.4$  samples at 300 K, respectively. For the  $\delta = 0.0$  sample the  $M_s$ , of  $(120 \pm 10)$  emu/cc, is reduced compared to that observed for bulk SrM at RT, with values of the order of 400 emu/cc [6] [243] [244]. This is as expected due to the substitution of the non-magnetic Ti ions and the Co ions having

a reduced magnetic moment compared to that of iron. According to Gorter's two-sublattice model, the theoretical  $M_s$  at 0K is determined by the difference in magnetic moment between two antiferromagnetically orientated sublattices within the M-type structure. For SrM, sublattice A consists of 8  $Fe^{3+}$  ions, including the 12k, 2a and 2b positions, whilst sublattice B has 4  $Fe^{3+}$  ions, the 4f<sub>1</sub> and 4f<sub>2</sub>. Each  $Fe^{3+}$  has an associated magnetic moment of 5.92  $\mu_B$  [37]. Thus, according to Gorter's model SrM has a theoretical  $M_s$  of  $(8-4) \times 5.92 = 23.68 \mu_B$ . This theoretical value has been confirmed by experiment at low temperatures [37]. Based on this model the substitution of Co and Ti into the structure will affect the saturation magnetisation in a way that depends heavily on the substitution sites.

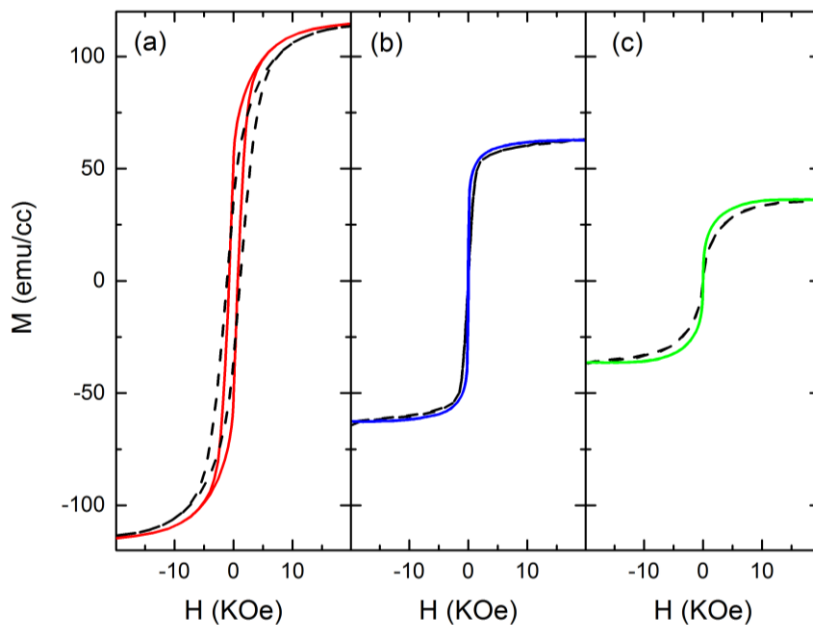


Figure 6.4. VSM for (a)  $\delta = 0.0$ , (b)  $\delta = 0.2$  and (c)  $\delta = 0.4$  measured at 300 K. The coloured lines are the in-plane measurements and the dashed lines out of plane.

The  $\delta = 0.0$  sample also has an in plane coercivity of  $(720 \pm 20)$  Oe, which again is smaller than the values observed for bulk SrM values [6] [245] [243]. Coercivities of the order of 3000 Oe and larger have been determined for SrM [6], however it has been shown that the Co and Ti substitutions have an important effect in reducing coercivity [6] [246] [106]. The in plane measurement has a  $M_r/M_s$  ratio of 0.46 which suggests a similar squareness to that typically seen for SrM [245]. For the out of plane measurement, we see a reduced remanence with respect to in plane and a  $M_r/M_s$  of 0.31. This suggests that the film has an easy axis of magnetisation that is closer to in plane than out of plane. A similar trend is also observed for the other two sample as seen in figs. 6.4(b) and (c). The  $\delta = 0.2$  sample has an  $M_s$  of  $(60 \pm 10)$  emu/cc and an  $H_c$  of  $(60 \pm 5)$  Oe in plane. A  $M_r/M_s$  ratio of 0.25 is observed, which is smaller than the  $\delta = 0.0$  sample. The  $\delta = 0.4$  sample has a further reduced  $M_r/M_s$  ratio of 0.07 with an  $M_s$  of  $(40 \pm 10)$  emu/cc and coercivity of  $(30 \pm 5)$  Oe. There is also an obvious trend of a reducing  $M_r/M_s$  for increasing  $\delta$ . This may be as a consequence of a change in the magnetic structure, if the spin spiral magnetic structure is present as expected for  $SrCo_2Ti_2Fe_8O_{19}$  samples [10] [24], then this may be attributed to changes in the magnetisation cone angle throughout the structure, or the type of chiral spin structure formed.

It is apparent from fig. 6.4, that all three samples have an  $M_s$  smaller than that expected for SrM. If we assume Gorter's model this implies that the Co and Ti substitutions must be to sites that reduce the overall magnetic moment [37].  $M_s$  also appears to reduce with increased  $\delta$ , which suggests that this reduction in  $M_s$  is a consequence of the Co and Ti being able to enter the R-block of the hexaferrite structure, however further investigation is required to identify the specific sites responsible for this effect.

The  $H_c$  values measured for the  $\delta = 0.2$  and  $0.4$  samples are similar to the  $0.9 \mu\text{m}$  single target film studied in chapter 5 and those measured in the literature for  $\text{SrCo}_2\text{Ti}_2\text{Fe}_8\text{O}_{19}$  [10] [23] [24]. Wang *et al* observing a coercivity of 100 Oe [10], Zentkova *et al* 10 Oe [23] and Mohebbi *et al* 20 Oe [24]. It is postulated that, the drastic reduction in  $H_c$  seen at 300K for  $\delta = 0.2$  and  $0.4$ , compared to  $\delta = 0.0$ , is due to the Co occupation of the trigonal bipyramidal sites, which is of course not possible for the  $\delta = 0.0$  sample due to the substitutions only taking place in the S-block. Previous work by Ataie *et al* [261] on SrM has shown that  $H_c$  is affected by the samples grain size. Although grain size will have an effect, the low coercivities of less than 100 Oe are primarily due to the Co and Ti substitutions with all literature values for SrM being much higher [6]. The large reduction in  $H_c$  compared to SrM, is thought to be, as a result of the reduction in anisotropy field with the substitution of  $\text{Co}^{2+}$  and  $\text{Ti}^{4+}$  for  $\text{Fe}^{3+}$  [10]. It has also been shown previously that for the related BaM, doping with Co and Ti results in the reduction of coercivity, with the formation of a cone of magnetisation, as a result of non-collinearly coupled spins, contributing to this reduction [262] [6].

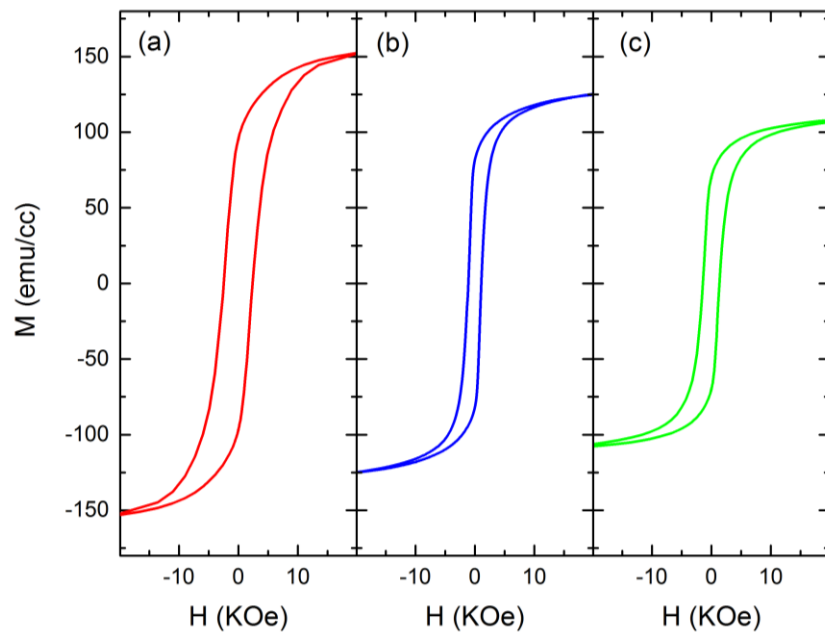


Figure 6.5. VSM for (a)  $\delta = 0.0$ , (b)  $\delta = 0.2$  and (c)  $\delta = 0.4$  measured at 10 K.

VSM hysteresis loops taken at 10 K for all three samples are shown in fig. 6.5. A similar relationship to that seen at room temperature is seen between the samples with the  $\delta = 0.0$  sample having a larger  $M_s$  and  $H_c$  than the non-zero  $\delta$  samples.  $M_s$  has increased for all three samples compared to the measurements taken at 300 K. At 10K the  $\delta = 0.0$  sample has a coercivity of  $(2350 \pm 50)$  Oe, this is more than twice that seen at 300 K. The  $\delta = 0.2$  and  $\delta = 0.4$  samples Coercivities have also significantly increased compared to RT with values of  $(1080 \pm 50)$  Oe and  $(1400 \pm 50)$  Oe, respectively, these trends are consistent with those observed for the  $0.9 \mu\text{m}$  film in chapter 5.

Studies by Kreisel *et al* [15] have shown the magnetic properties of Co-Ti doped M-type hexaferrites to be temperature sensitive, particularly for the levels of doping studied here. They suggested this is as a consequence of the  $\text{Ti}^{4+}$  substitutions interrupting the magnetic interactions in such a way that the RS and R\*S\* blocks become magnetically de-coupled, which results in conical magnetic structures becoming more pronounced at lower temperatures and contributing to the anisotropy. For the  $M(H)$  measured at different temperatures,  $M_s$ ,  $M_r$  and  $H_c$  have been extracted and plotted as a function of temperature, as displayed in fig. 6.6. Fig. 6.6(a) shows that for all samples  $M_s$  reduces with increased temperature. It is evident that all three samples follow the same approximate relationship between  $M_s$  and temperature. The rate of reduction in  $M_s$  appears greater as the temperature approaches 300K for the  $\delta = 0.2$  and  $0.4$  samples than for the  $\delta = 0.0$  sample. The  $M_s(T)$  relationship is similar in form to that observed for SrM [247]. However, the  $H_c(T)$

relationship, fig. 6.6(c), is different to SrM for which  $H_c$  increases with temperature [247]. Again  $H_c(T)$  for both the  $\delta = 0.2$  and  $0.4$  samples follow a similar relationship to each other. With increasing temperature from 10 K a sharp reduction in  $H_c$  on approaching a critical temperature ( $T_{crit} \approx 180$  K) is observed for  $\delta = 0.2$  and  $0.4$  whilst a more gradual decrease occurs for  $\delta = 0.0$  which shows a levelling off in the coercivity values at around 300 K. These differences in magnetic behaviour again indicate that the  $\delta = 0.0$  sample has a different magnetic structure compared to the non-zero  $\delta$  samples.

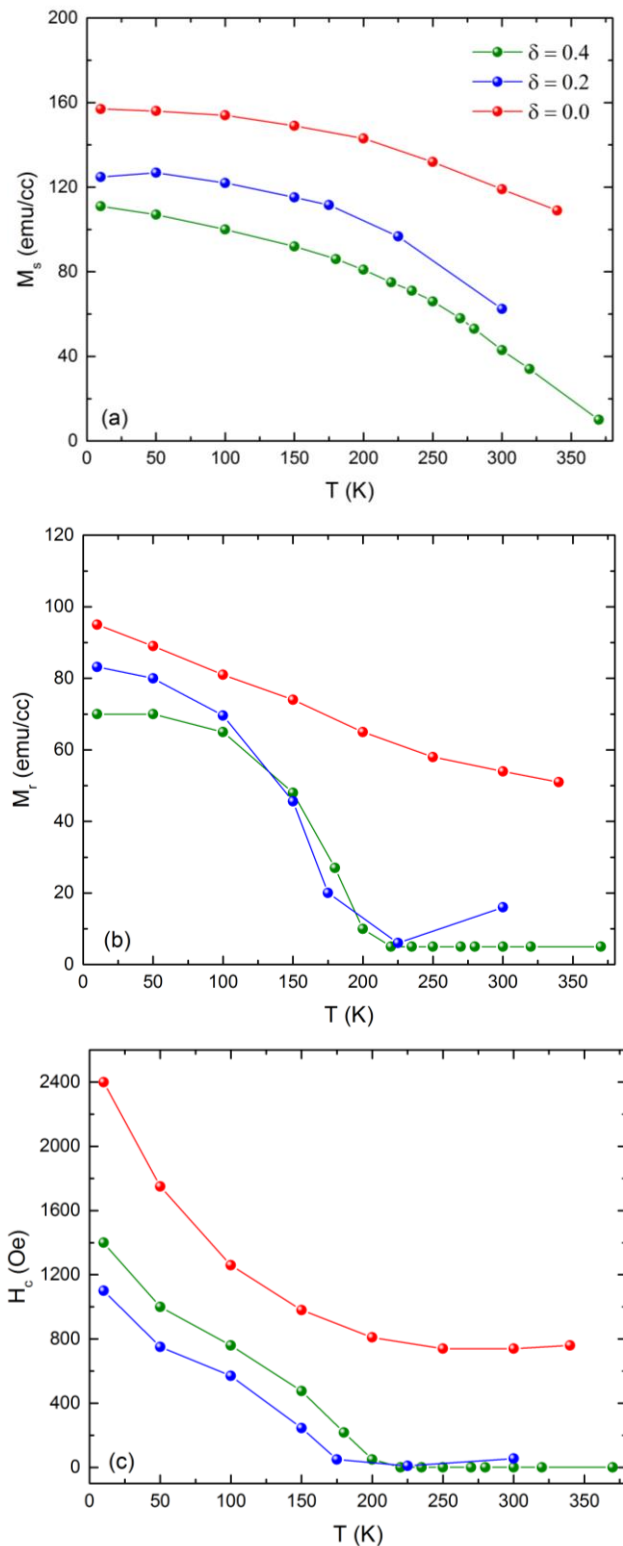


Figure. 6.6. VSM as a function of temperature for  $\delta = 0.0$  (red),  $\delta = 0.2$  (blue) and  $\delta = 0.4$  (green), showing (a)  $M_s$  vs T. (b)  $M_r$  vs T. (c)  $H_c$  vs T.

In fig. 6.6(b)  $M_r$  is plotted as a function of temperature. The graph shows that  $M_r$  reduces with increased  $T$  before levelling off at around 180K for the  $\delta = 0.2$  and 0.4 samples.  $M_r$  for the  $\delta = 0.0$  sample also reduces with increased temperature but follows a more linear relationship up to RT. The  $\delta = 0.2$  and 0.4 relationships are similar in form to the FC  $M(T)$  relationships seen in the literature for  $\text{SrCo}_2\text{Ti}_2\text{Fe}_8\text{O}_{19}$  samples measured at a low magnetic field [106] [10]. These measurements indicate a change in magnetic structure between  $\delta = 0.0$  and  $\delta = 0.2, 0.4$  samples. The derivative of the  $M_r(T)$  relationship is shown in fig. 6.7. This has been plotted to gain insight into the magnetic compensation points of each sample. It is again apparent that the form of the relationship seen for the  $\delta = 0.0$  sample is different to that seen for the other two samples. The turning point in the  $\delta = 0.2$  relationship is seen at  $(150 \pm 20)$  K and for the  $\delta = 0.4$  sample this is slightly higher at a temperature of  $(180 \pm 10)$  K.

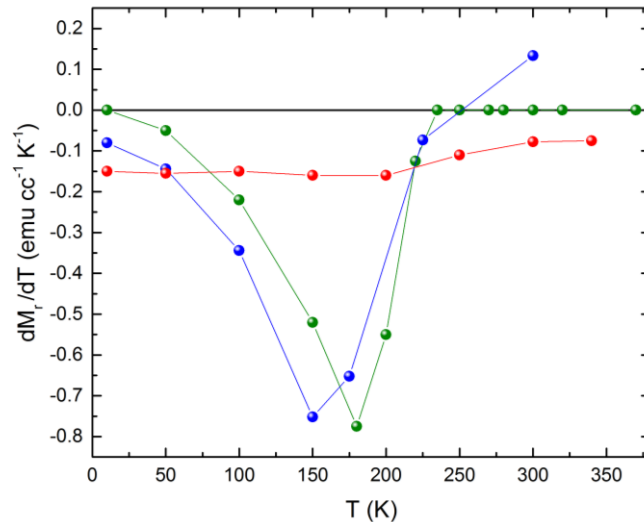


Figure 6.7. The derivative of  $M_r$  with respect to temperature for  $\delta = 0.0$  (red),  $\delta = 0.2$  (blue) and  $\delta = 0.4$  (green).

To further investigate the magnetic relationships of the samples,  $M(T)$  measurements were performed with the applied field parallel to the surface as a function of temperature between 5 K and 500 K. Fig. 6.8(a,b,c) show  $M(T)$  measured in an applied field of 300 Oe after zero field cooling and field cooling at 30 kOe.

For the  $\delta = 0.2$  FC case, Fig. 6.8(b), increasing the temperature from 10 K causes the magnetization to steadily decrease as one would expect for a simple ferro / ferrimagnet material. However around 200 K the slope of  $M(T)$  flattens before falling again. A similar effect is seen for  $\delta = 0.4$  and for both samples the flattening of the slope in  $M(T)$  occurs at the same temperature as a peak seen in the ZFC data. This behaviour is not evident for  $\delta = 0.0$ , Fig. 6.8(a), which shows a shallower and nearly linear decrease in  $M$  over the same temperature range for the FC data. However a peak, albeit less pronounced, is also seen in the ZFC  $M(T)$ . The peak in the ZFC  $M(T)$  data for hexaferrites is often interpreted as a change in magnetic order [247] [249] even though it is not possible to infer the magnetic order directly from  $M(T)$  without complementary information such as that provided by neutron diffraction [251].

In M-type hexaferrites an easy cone of magnetization [6] develops when doping with Co-Ti above a critical level ( $x = 1.1$ ) as a result of non-collinearity [6] [250] which also has the effect of dramatically reducing  $H_c$ . This is supported by the  $M(H)$  measurements in figs 6.4, 6.5 and 6.6, which show that all three samples have a reduced coercivity compared to un-doped SrM. However, it is also seen that the  $\delta = 0.2$  and 0.4 samples have much smaller coercivities than the  $\delta = 0.0$  sample, as well displaying a different temperature dependence. This suggests that the role of the Co and Ti substitutions is different between the  $\delta = 0.0$  and non-zero  $\delta$  samples, which has a consequence in

terms of their magnetic properties. It is apparent that substitutions of the Co and Ti to the R-block sites results in a change in magnetic behaviour.

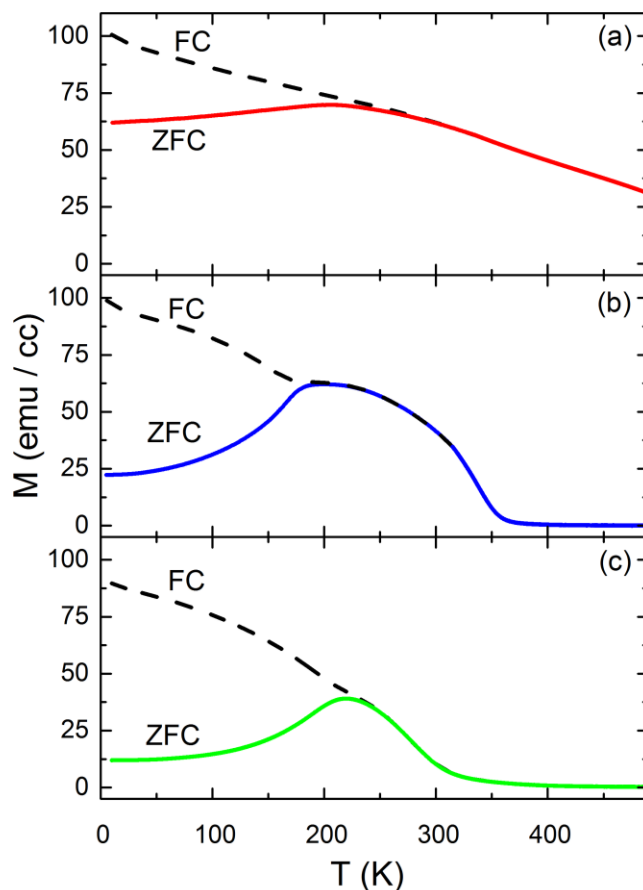


Figure 6.8.  $M(T)$  obtained via VSM for (a)  $\delta = 0.0$ , (b)  $\delta = 0.2$  and (c)  $\delta = 0.4$  measured at 300 Oe for FC and ZFC conditions.

The general shape of the  $M(T)$  curve, for the  $\delta = 0.2$  and  $0.4$  samples, is very similar in form to that of the  $0.9 \mu\text{m}$  single target sample and has also been observed by others for  $\text{SrCo}_2\text{Ti}_2\text{Fe}_8\text{O}_{19}$  samples [10] [106] [23]. Wang *et al* [10] postulate, based on the results of neutron diffraction, that the point at which the  $M(T)$  flattens, at around 370 K, corresponds to the transition from a conical magnetic structure phase to a collinear ferrimagnetic phase. Measuring to a higher temperature, they also observe the point where the magnetisation drops suddenly to zero indicating a Curie temperature of 740 K, which is comparable to the Curie temperature of SrM [10]. For single crystal  $\text{SrCo}_2\text{Ti}_2\text{Fe}_8\text{O}_{19}$ , Zentkova *et al* [23] observe a slightly higher  $T_c$  of 768 K. In this work, they also observe a transition close to 370 K and again attribute this to a transition in magnetic structure from non-collinear to collinear ordering [23].

Comparing the  $M(T)$  measurements to the  $H_c(T)$  data in fig. 6.6(b), it is interesting that the drastic drop off in coercivity (180 K) corresponds closely to the peak observed in the ZFC  $M(T)$  data. Indicating that the two are linked, further supporting the existence of a magnetic phase transition. The ZFC  $M(T)$  measurements have been differentiated and are displayed in fig. 6.9 and can be used to determine turning points in the  $M(T)$  relationship. The differentiated curves all display a positive peak in the region 160 – 190 K and display a negative peak at higher temperature which suggests two significant turning points in the  $M(T)$  relationship as seen for the  $0.9 \mu\text{m}$  single target film studied in chapter 5. The turning points are much less pronounced for the  $\delta = 0.0$  sample and this curve appears noisier due to the much shallower gradients seen in the  $M(T)$ .

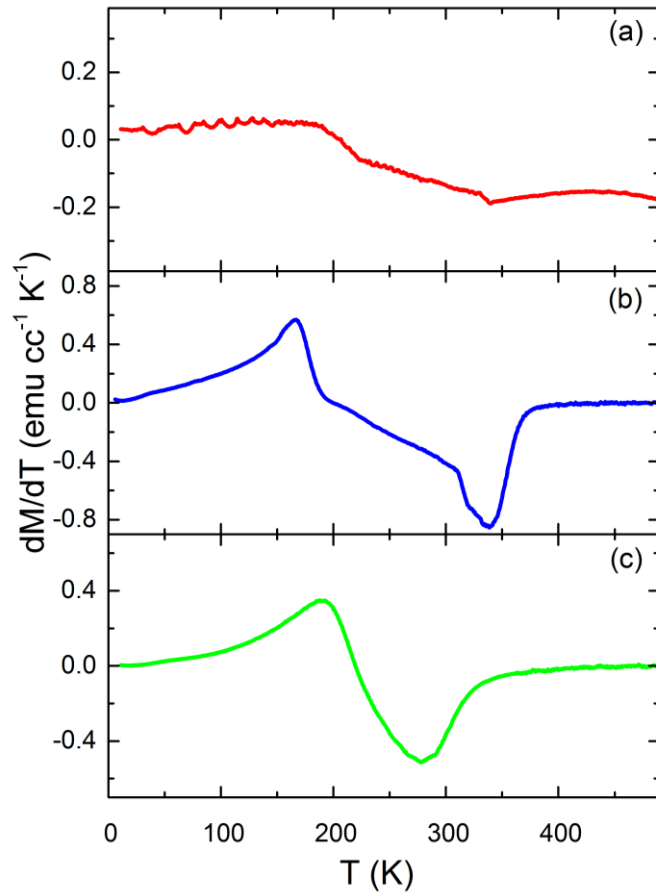


Figure 6.9. The derivative of the ZFC  $M(T)$  for (a)  $\delta = 0.0$ , (b)  $\delta = 0.2$  and (c)  $\delta = 0.4$  at 300 Oe.

The initial turning point ( $T_1$ ) for the  $\delta = 0.2$  sample is at 165 K, whereas for the  $\delta = 0.4$  sample  $T_1$  is at a higher temperature of 185 K. The second turning point ( $T_2$ ) occurs at 334 K for  $\delta = 0.2$  and 280 K  $\delta = 0.4$ . This indicates that any transition from a spiral spin to a collinear ferrimagnetic one happens at a higher temperature for the  $\delta = 0.2$  sample as is also suggested by fig. 6.8. Additionally, for the  $\delta = 0.4$  sample, the  $T_2$  transition, thought to be the transition to ferrimagnetic order, occurs below RT indicating that a non-collinear magnetic structure is not stable at RT for this sample. Hence, any ME coupling observed at 300 K may not be due to the reported spin spiral mechanism [13]. For the other samples even if a conical spin structure is present, this may not have the cycloidal component required for improper ferroelectricity under the inverse Dzyaloshinskii-Moriya mechanism [12]. Most sources have reported doped M-type hexaferrites to have either a ferrimagnetic, screw or longitudinal conical spin structure, in the absence of an applied transverse magnetic field [105] [15] [6]. As such, it may be possible that the spontaneous polarisation, and resulting ME coupling, is induced via an alternative mechanism and not by the presence of a transverse conical spin structure. One possible mechanism is discussed in chapter 7 of this work, as a displacive electric polarisation induced by the presence of a magnetoelastic  $\text{Co}^{2+}$  ion at the trigonal bipyramidal site of the M-type hexaferrite structure.

### 6.5 Ferromagnetic Resonance Measurements

Figure 6.10 displays the differentiated FMR response for the three samples  $\delta = 0.0, 0.2$  and  $0.4$  taken at 10 GHz with the magnetic field swept in 50 Oe steps from high field to low. The measurements were performed using a lock-in amplifier technique described in section 3.3.2. The resonance field ( $H_r$ ) and linewidth ( $\Delta H$ ) have been extracted by fitting the data with eqn. 3.14 [161].

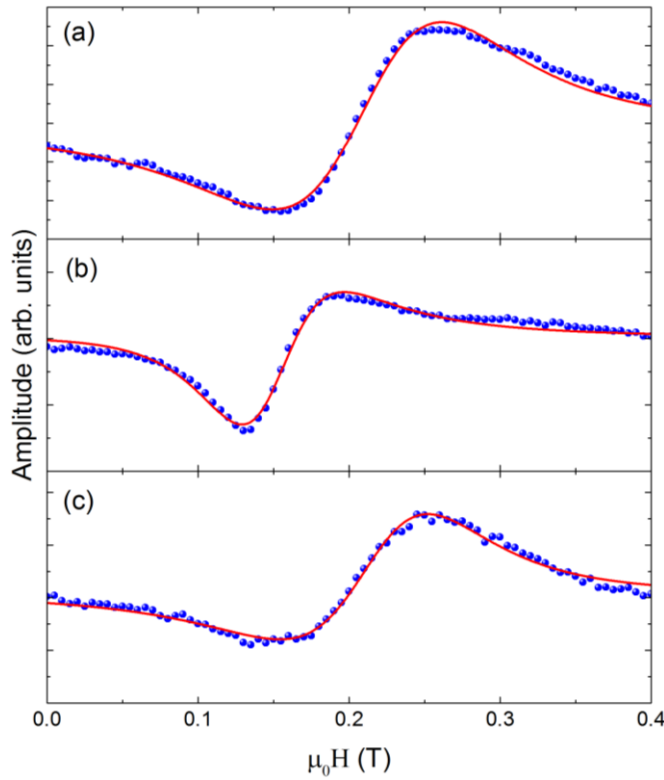


Figure. 6.10. In-plane FMR at 10 GHz for the (a)  $\delta = 0.0$ , (b)  $\delta = 0.2$  and (c)  $\delta = 0.4$  samples.

The fit to the  $\delta = 0.0$  resonance gives a resonance field of  $(2140 \pm 20)$  Oe. Fitting also produces a very similar value for the  $\delta = 0.4$  sample of  $(2190 \pm 30)$  Oe and for the  $\delta = 0.2$  it was measured to be lower with a value of  $(1490 \pm 20)$  Oe. All these values are within the range seen in the literature at 10 GHz for Co and Ti doped SrM [24] [107]. The FMR linewidths measured for hexaferrites range between  $<100$  to  $2000$  Oe [263] and can depend on several things such as sample composition and structure [264]. Linewidths of  $(970 \pm 20)$  Oe,  $(560 \pm 30)$  Oe and  $(830 \pm 40)$  Oe are measured for the  $\delta = 0.0$ ,  $0.2$  and  $0.4$  samples, respectively, which compare well to the  $(600 \pm 30)$  Oe linewidth measured for the  $0.9 \mu\text{m}$  single target film.

The FMR measurements have been performed for all three samples over a range of frequencies between 3 GHz and 18 GHz. Each individual measurement has then been fitted, the resonance field extracted and frequency ( $f$ ) plotted against  $H_r$ . These measurements are displayed in fig. 6.11. As discussed in chapter 3.3.2, the relationship between  $H_r$  and frequency will be different depending on whether the uniaxial is normal to the film plane and whether it is a hard axis [165]. If the sample has an in plane uniaxial anisotropy, then the following relationship would hold [165]

$$f = 1.4 \times 10^6 g \sqrt{((H_r + H_A)(H_r + H_A + 4\pi M_s))} \quad \text{Eqn. 3.17.}$$

In eqn. 3.17,  $g$  is the  $g$ -factor and  $H_A$  is defined as the anisotropy field. Alternatively, if the uniaxial anisotropy axis lies out of plane, as is the case for BaM with large  $c$ -axis anisotropy, then the frequency,  $H_r$  relationship will be different and governed by eqn. 3.18. [165]

$$f = 1.4 \times 10^6 g \sqrt{(H_r(H_r - H_A + 4\pi M_s))} \quad \text{Eqn. 3.18.}$$

Hence, the relationship between frequency and  $H_r$  may be used to gain insight into which relationship is followed by these  $\text{SrCo}_2\text{Ti}_2\text{Fe}_8\text{O}_{19}$  samples giving an indication of the magnetic order present.

As can be seen in fig. 6.11(a,b), the  $\delta = 0.0$  and  $0.2$  samples clearly follow the relationship described by eqn. 3.17, suggesting that the anisotropy axis does not lie out of plane for these samples. The axis therefore must lie at an angle of less than  $90^\circ$  to the film plane, as would be the case for a non-collinear magnetic structure. The  $\delta = 0.4$  frequency relationship, fig. 6.11(c), has a smaller

resonance field at low frequency values, meaning that there is a diminished difference between the two fits at low frequency values. However, this can be explained by a larger  $g$  value with the data points still fitting closer to the in plane anisotropy relationship.

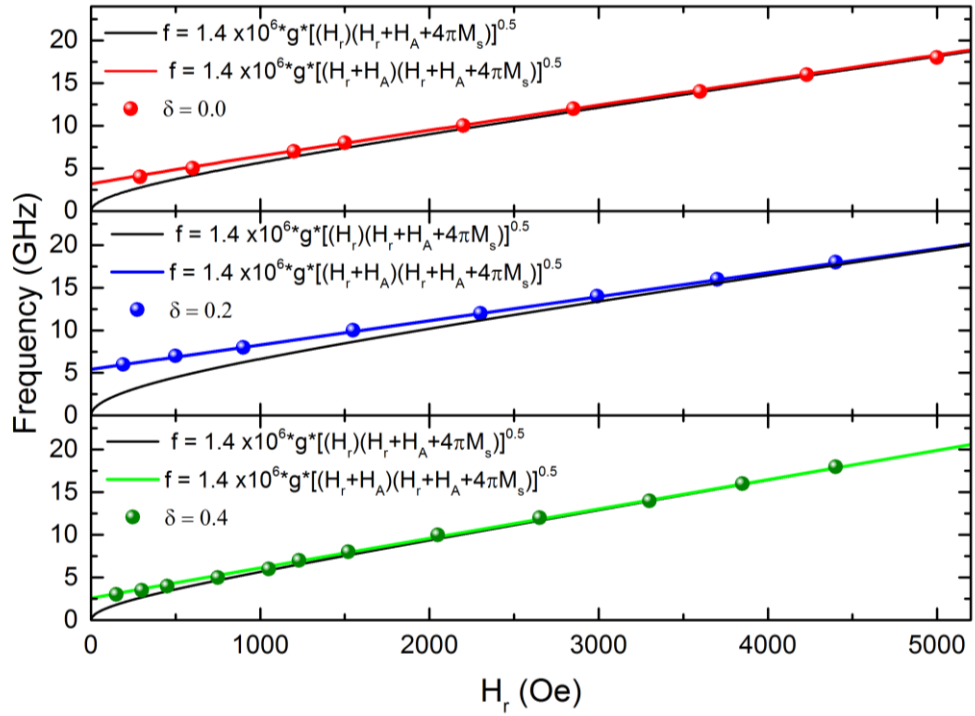


Figure. 6.11. Frequency as a function of resonance field measured by in-plane FMR for (a)  $\delta = 0.0$ , (b)  $\delta = 0.2$  and (c)  $\delta = 0.4$ .

Fitting with eqn. 3.17, in fig. 6.11, assumes an in-plane anisotropy axis; however, the presence of a non-collinear magnetic structure would result in an anisotropy axis at some unknown angle between in and out of plane. This would then result in a frequency dependence governed by the more general case of eqn. 3.16, which for an anisotropy axis angle of less than  $90^\circ$  can also produce good agreement with the experimental data. Given that  $M_s$  can be taken from the VSM measurements, fitting the experimental data with the in-plane frequency relation can allow values of  $g$  to be determined. For  $\delta = 0.0$ , fitting indicates a  $g$  value of 2.07, which is again consistent with the  $g$ -factor measured for the  $0.9 \mu\text{m}$  single target film. A  $g$ -factor of around 2 has typically been seen for ferrite, hexaferrite and spinel structures [24] [60] [107] and it has also been observed that cobalt substitutions typically act to reduce the  $g$ -factor due to orbital contributions [107]. The  $\delta = 0.2$  data suggests a  $g$ -factor of 2.0 which is similar to that seen for  $\delta = 0.0$  and for the  $\delta = 0.4$  sample we see a  $g$ -factor of 2.45 which is larger but still within the range measured for hexaferrites [24] [107] [60].

The ratios of orbital ( $m_l$ ) and spin ( $m_s$ ) magnetic moments can also be determined from the Lande  $g$ -factor values. This ratio is related to the  $g$ -factor such that  $m_l/m_s = (g-2)/2$  [265]. Using this relationship  $m_l/m_s = 0.035$  for the  $\delta = 0.0$  sample,  $m_l/m_s = 0.0$  for  $\delta = 0.2$  and  $m_l/m_s = 0.225$  for  $\delta = 0.4$ . In the case of 3d transition metals, the orbital magnetic moment is almost completely quenched by the surrounding crystal fields [265]. Thus, this explains why  $g$  is expected to be close to the free electron value of 2. We see this in the cases of the  $\delta = 0.0$  and  $\delta = 0.2$  samples and a slightly larger orbital to spin magnetic moment ratio for the  $\delta = 0.4$  sample, indicating that the orbital moment in this sample is larger.

## 6.6 Magnetoelectric Coupling Measurements

An important part of the investigation into these samples is to correlate their magnetoelectric properties to the variation in cobalt and titanium substitution to the R-block. This will allow insight into role that the Co and Ti substituted to different sites play in the ME coupling mechanism. It may even be possible to enhance the ME effect by directing the substitutions into specific sites within the hexaferrite structure.

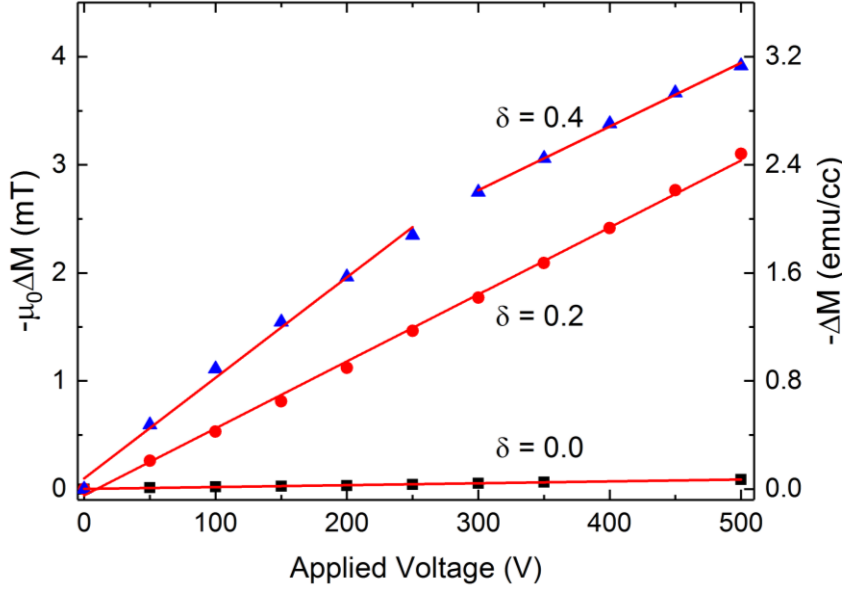


Figure 6.12. Change in M as a function of applied voltage, for  $\delta = 0.0$  (black),  $\delta = 0.2$  (red) and  $\delta = 0.4$  (blue). Measurements were taken with an applied bias field of 400 Oe and E parallel to M.

For the ME coupling measurements, a voltage (V) was applied across the film thickness and substrate with changes to the magnetization, as measured by VSM, recorded as a function of V. See section 3.5 for further details. The ME coupling is shown in Fig. 6.12 as the change in magnetisation ( $\Delta M$ ) as a function of applied voltage for  $\delta = 0.0$ ,  $\delta = 0.2$  and  $\delta = 0.4$ . The measurements were taken in an applied magnetic field of 400 Oe.

The converse magneto-electric coefficient ( $\alpha$ ) is defined as [55]

$$\alpha = \mu_0 \frac{\partial M}{\partial E} \quad \text{Eqn. 3.44.}$$

where  $E = \frac{V}{d_s} \left( \frac{\epsilon_s}{\epsilon_f} \right)$  is the electric field across the film, as defined in section 3.5. The relative permittivity  $\epsilon_s = 10$  for sapphire whilst for M-type hexaferrites  $\epsilon_f$  can range between  $\approx 20$  and 5000 [107] [266] but is highly dependent on the conductivity of the film and therefore the amount of  $\text{Fe}^{2+}$  in the sample. Given we do not know the exact d.c value of  $\epsilon_f$  for the films, but assume they are approximately equal for all three samples due to similar amounts of  $\text{Fe}^{2+}$ , we calculate the ratio of the magnetoelectric coefficients for the two films to give

$$\Lambda_1 = \frac{\alpha(0.2)}{\alpha(0.0)} = 36$$

$$\Lambda_2(1) = \frac{\alpha(0.4)}{\alpha(0.0)} = 53 \quad \Lambda_2(2) = \frac{\alpha(0.4)}{\alpha(0.0)} = 34$$

For  $\delta = 0.2$ ,  $\alpha$  has increased by over an order of magnitude compared to  $\delta = 0.0$ . For  $\delta = 0.4$  there are two linear regions where the gradient and therefore strength of the ME coupling change with voltage. Two ratios are therefore given,  $\Lambda_2(1)$  and  $\Lambda_2(2)$ , for these two regions. The  $\delta = 0.4$  measurement shows a similar large enhancement of  $\alpha$  compared to the  $\delta = 0.0$  film.

Fig. 6.12 shows a linear magnetoelectric effect. Previous works, often showing non-linear behaviour, measured  $\alpha$  at remanence or close to it [102] [24] and therefore may have suffered from non-linearities due to domain motion, or in the case of bulk samples, non-linear effects due to changes in electrical conductivity with the applied voltage. When a current can flow, second order ME effects may also contribute [267]. These measurements were performed with in an applied magnetic field of 400 Oe, after saturating the sample, to remove domain motion effects and the voltage was applied across substrate and film in series, with the substrate dominating the conductivity. In addition, an average of 50 measurements at each applied E-field was taken, each 1 second apart. The quantity plotted in fig. 6.12, is an average of those 50 measurements and has a small standard deviation meaning that the change in M is due to the E-field and not a heating effect that would increase with time.

To conclusively rule out the possibility of an extrinsic heating affect, let us consider that the maximum power dissipation in the film due to the applied voltage. The contacts to measure the ME effect are on the backside of the substrate and the Au capping layer of the hexaferrite film. Sapphire has a resistivity of  $10^{16} \Omega \cdot \text{cm}$  at 300 K [268]. For the sample dimensions, this gives a resistance of approximately  $10^{15} \Omega$ . At the highest voltage applied (500V) the maximum possible power to the sample from Joule heating is then  $2.5 \times 10^{-10} \text{ W}$ . In addition, hexaferrites have a specific heat capacity of the order  $2.5 \text{ J/gK}$  [250]. Assuming all the power heats only the hexaferrite film, rather than both film and substrate, then given the film mass is of the order  $1 \times 10^{-4} \text{ g}$  (density of BaM =  $5.28 \text{ g/cc}$  [6]), a maximum temperature rise of  $1 \times 10^{-6} \text{ K/s}$  is expected, which is far below the temperature stability of any VSM over the measurement timescale. However, if this temperature rise was significantly higher, the slope of  $M(T)$  at 300 K for each  $\delta$ , fig. 6.8, would allow  $\Delta M$  to be calculated for a given  $\Delta T$ . At 300 K the sample with the largest  $dM/dT$  is  $\delta = 0.2$ . To note  $dM/dT = -0.14, -0.44$  and  $-0.36$  (emu/ccK) for  $\delta = 0.0, 0.2$  and  $0.4$  respectively. If the change in M with the applied voltage was a heating effect then the change should be largest for  $\delta = 0.2$ , which concludes that the changes in magnetisation measured must be as a consequence of a first order ME coupling. From fig. 6.12 the data points for the  $\delta = 0.4$  sample appear to deviate from a linear relationship for voltages greater than 300 V, with the gradient reducing. This change in relationship is indicative of piezoelectric strain - voltage characteristics, which may indicate an additional ME coupling mechanism, which can be described by the  $\Delta\alpha_{ij}$  term, discussed in section 2.5.1, known to be a function of the piezoelectric constant.

If we assume a hexaferrite film permittivity of 20, which would be the smallest expected, for all three samples [266], then tentative values of the magnetoelectric coupling constants can be determined. With the substrate thickness measured to be 0.3 mm, the magnetoelectric coupling coefficient of the  $\delta = 0.4$  sample is determined to be  $4.6 \times 10^{-9} \text{ s m}^{-1}$ .  $\alpha = 3.8 \times 10^{-9} \text{ s m}^{-1}$  for  $\delta = 0.2$  and  $\alpha = 1.0 \times 10^{-10} \text{ s m}^{-1}$  for  $\delta = 0.0$ . These values for the  $\delta = 0.2$  and  $0.4$  samples, of the order of  $10^{-9} \text{ s m}^{-1}$ , are comparable to those reported in the literature, with Ebnabassi *et al* reporting a converse ME coupling of  $7.6 \times 10^{-10} \text{ s m}^{-1}$  in bulk polycrystalline Z-type hexaferrite [102]. The same paper also reports an  $\alpha$  of  $2.4 \times 10^{-10} \text{ s m}^{-1}$  for bulk polycrystalline  $\text{SrCo}_2\text{Fe}_8\text{O}_{19}$  [102].  $\text{SrCo}_2\text{Ti}_2\text{Fe}_8\text{O}_{19}$  films have been reported in the literature with  $\alpha$  values of  $6.07 \times 10^{-9} \text{ s m}^{-1}$  [24] and  $1.01 \times 10^{-8} \text{ s m}^{-1}$  [107], both of which are of the order of the values measured here. It is important to remember that the permittivity value assumed contains some approximation, as such definitive  $\alpha$  values can not be deduced. However, it is evident that the ME coupling values measured for the samples here are comparable to the values reported in the literature and are large relative to the effects reported in other materials, with  $\alpha = 4 \times 10^{-12} \text{ s m}^{-1}$  in  $\text{Cr}_2\text{O}_3$  for example [269].

The enhancement of  $\alpha$  for the  $\delta = 0.2, 0.4$  films with respect to the  $\delta = 0.0$  film, strongly indicates that Co and Ti doping to the R-block drastically increases the ME coupling coefficient. This being the case, it is probable that the occupation of a certain R-block site by either Co or Ti is responsible

for an enhanced ME effect. It is also possible that there is a secondary ME coupling mechanism, not controlled by a conical magnetic structure, induced due to these substitutions, as also suggested by the M(T) measurements. As such, determination of which sites are occupied by the Co and Ti is crucial to understanding this enhancement of the magnetoelectric coupling.

### 6.7 Element Specific Soft X-ray Magnetic Spectroscopy

To gain a more detailed understanding of the role of Co-Ti substitutions, we performed XAS at the Ti  $L_{2,3}$  absorption edge and XAS/XMCD measurements at the Co and Fe  $L_{2,3}$  absorption edges in order to determine valency, co-ordination and the magnetic response of the individual elements. The XMCD gives a direct and element-specific measurement of the projection of the 3d magnetic moment along the x-ray polarization vector [177], as described in section 3.4. Figure 6.13 shows the Ti XAS measured at the  $L_{2,3}$  edges for  $\delta = 0.0, 0.2$  and  $0.4$ . The spectra obtained for the three samples are all nearly identical, with four distinct peaks present. The differences seen in the spectra at energies above the fourth peak are due solely to differences in background.

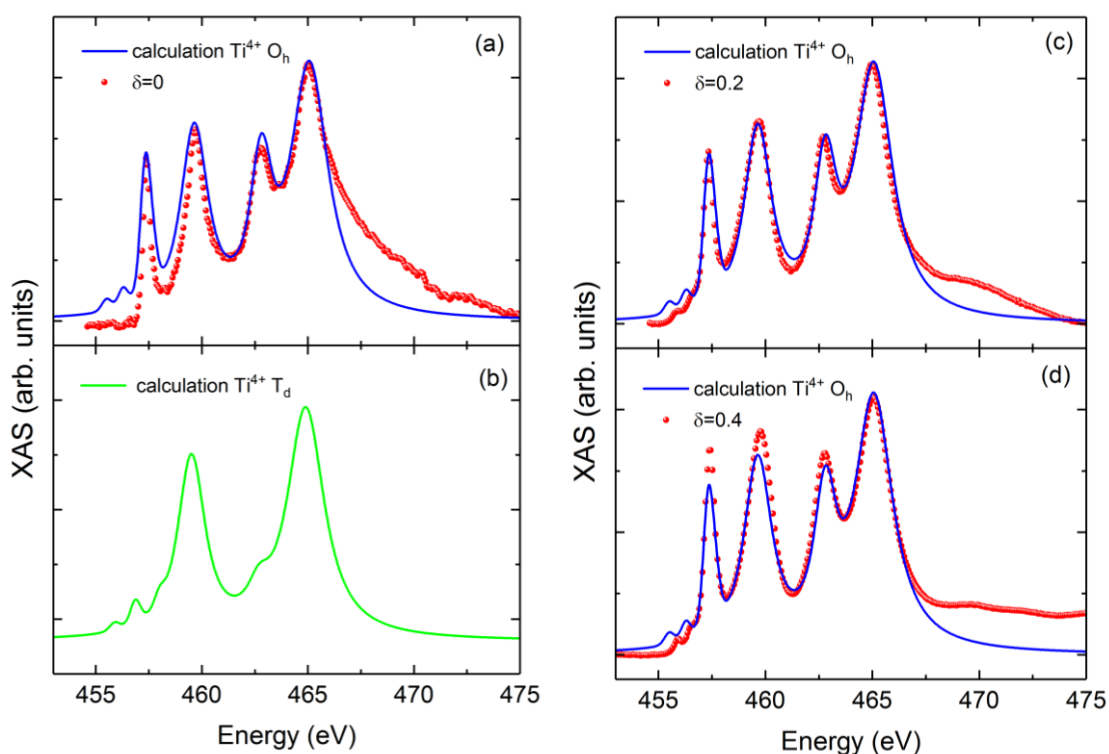


Figure 6.13. (a) Ti  $L_{2,3}$  XAS measured for  $\delta = 0.0$  at 300 K in TEY (red). The blue solid line is the simulated spectra from an atomic multiplet calculation of  $Ti^{4+}$  in an octahedral co-ordination with  $10Dq = 1.9$  eV. (b) An equivalent calculation for of  $Ti^{4+}$  in a tetrahedral co-ordination with  $10Dq = -0.9$  eV. (c) Ti  $L_{2,3}$  XAS measured for  $\delta = 0.2$ . (d) Ti  $L_{2,3}$  XAS measured for  $\delta = 0.4$ .

Excellent agreement between the experimental data and atomic multiplet calculations, shown as the solid line in Fig. 6.13(a,c,d) is found for  $Ti^{4+}$  in an octahedral co-ordination. Fig. 6.13(b) also shows the calculated spectra for tetrahedral  $Ti^{4+}$ , this shows only two significant peaks unlike the four peaks seen for the octahedral simulation and the experimental spectra. Hence, it is clear that the spectra are very similar to those seen for the single target films, with the Ti ions in the samples having a  $4^+$  valency and occupy octahedral sites.

Given that, the M-type structure contains three different  $O_h$  lattice sites, the 2a in the S-block, the  $4f_2$  in the R-block and the 12k at the block boundary; it cannot be said from these measurements which octahedral Wyckoff positions are occupied by the Ti. It is expected from the literature [6] [83] that the majority will occupy the 12k sites, and act to magnetically de-couple the R- and S-

blocks, although, complementary measurements are needed in the form of EXAFS in order to support this.

Figure 6.14 shows XAS and XMCD data for (a,d)  $\delta = 0$ , (b,e)  $\delta = 0.2$  and (c,f)  $\delta = 0.2$  at the Fe and Co  $L_{2,3}$  edges respectively. The XMCD spectra have been fitted using atomic multiplet calculations. The crystal field parameters used for these calculations are the same as those detailed in chapter 5 for the single target films. However, the % weighting of the valences and three possible co-ordinations were adjusted to best fit the experimental data.

The XAS at the Fe  $L_{2,3}$  edges for all samples show multiplet structure typical of an iron oxide. Three peaks (two negative and one positive) are present in the Fe XMCD spectra, similar to that found for  $Fe_3O_4$  [255]. These peaks correspond to contributions from  $O_h Fe^{3+}$ ,  $T_d Fe^{3+}$  and  $O_h Fe^{2+}$ . For the M-type hexaferrite structure, spins located at the Fe  $T_d$  sites are aligned anti-parallel to the majority of spins at the Fe  $O_h$  sites [6]. Hence, the positive peak in the XMCD is due to tetrahedrally co-ordinated  $Fe^{3+}$ . Fits to the Fe XMCD data show that the  $\delta = 0.0$  spectra is best represented by ~70% octahedral co-ordinated and ~30% tetrahedral or trigonal co-ordinated Fe. It is again noted that this should not be taken as the relative Fe occupancy of the sites but their overall magnetic contribution. The occurrence of  $Fe^{2+}$ , probably due to incomplete oxidation during growth, was also seen for the single target films and is detrimental to magnetoelectric materials as it provides a conductive pathway, suppressing electric polarisation.

Figures 6.14(b) & 6.14(c) show the Fe XAS and XMCD for  $\delta = 0.2$  and  $\delta = 0.4$  respectively. The XAS lineshape is similar to that for  $\delta = 0.0$ , however, atomic multiplet fits to the XMCD data reveal a smaller  $T_d / O_h$  ratio, (24:76) for  $\delta = 0.2$  and (22:78) for  $\delta = 0.4$ , compared to  $\delta = 0.0$ . It is also noted that the amount of  $Fe^{2+}$  is the same for all samples, to within error.

The  $\delta = 0.0$  XAS / XMCD data at the Co  $L_{2,3}$  edges is shown in Fig. 6.14(d). The XAS lineshape is a superposition of  $Co^{2+}$  spectra in  $O_h$  and  $T_d$  environments. However, the XMCD lineshape, which provides information on the uncompensated moments in the ferrimagnetic structure, is predominantly from  $O_h Co^{2+}$ . Fits to the Co XMCD data using atomic multiplet calculations, show that the majority of the XMCD is due to  $O_h Co$  (~70%) with a 30%  $T_d$  contribution for the  $\delta = 0.0$  sample. No trigonal component is present, as expected due to its position in the R-block. As can be seen from the figure, the sign of the XMCD peak is negative, parallel to the majority of the Fe peaks indicating the net Co magnetic contribution is aligned parallel to the majority of the Fe spins. Thus for  $\delta = 0.0$  the Co seems to have been substituted into both  $O_h$  and  $T_d$  sites whilst Ti has entered into only the  $O_h$  sites.

XAS and XMCD at the Co  $L_{2,3}$  edges for  $\delta = 0.2$  and 0.4, Fig.6.14(e, f), show differences in the XAS and XMCD lineshape compared to  $\delta = 0.0$ . Analysis of the XAS and XMCD data with atomic multiplet calculations shows that the magnetic contribution from Co has now significantly changed with respect to the  $\delta = 0.0$  film, to a situation where  $Co^{2+}$  ions in trigonal sites becomes more important as  $\delta$  increases ( $O_h:T_d:S_6 = 55:23:22, 59:17:24$  for  $\delta = 0.2$  and 0.4 respectively). As  $\delta$  increases, less Co is doped into the S-block so we expect the amount of  $T_d Co$  to decrease, as found experimentally. As can be seen from the Fig. 6.14(e, f) the spins of the tetrahedral / trigonal co-ordinated  $Co^{2+}$  align anti-parallel with the octahedral Fe.

For  $\delta = 0.0$  the XAS lineshape can be modelled by a superposition of  $O_h$  and  $T_d Co^{2+}$  spectra. For  $\delta = 0.0$  the Ti-Co substitution is intended to occur only in the S-block i.e. the 2a,  $4f_1$  and 12k sites. It has been shown [10] [6] [247] [55] that Ti has a strong preference for the 12k sites whilst  $Co^{2+}$  prefers the  $4f_1$  and the 2a sites, although there is significant contradiction in the literature [10] [15] [254]. The  $\delta = 0.0$  cobalt XMCD spectrum clearly shows that the total magnetic contribution from the Co sites in the structure is parallel to the Fe  $O_h$  sites and predominantly from  $O_h$  co-ordinated  $Co^{2+}$ .

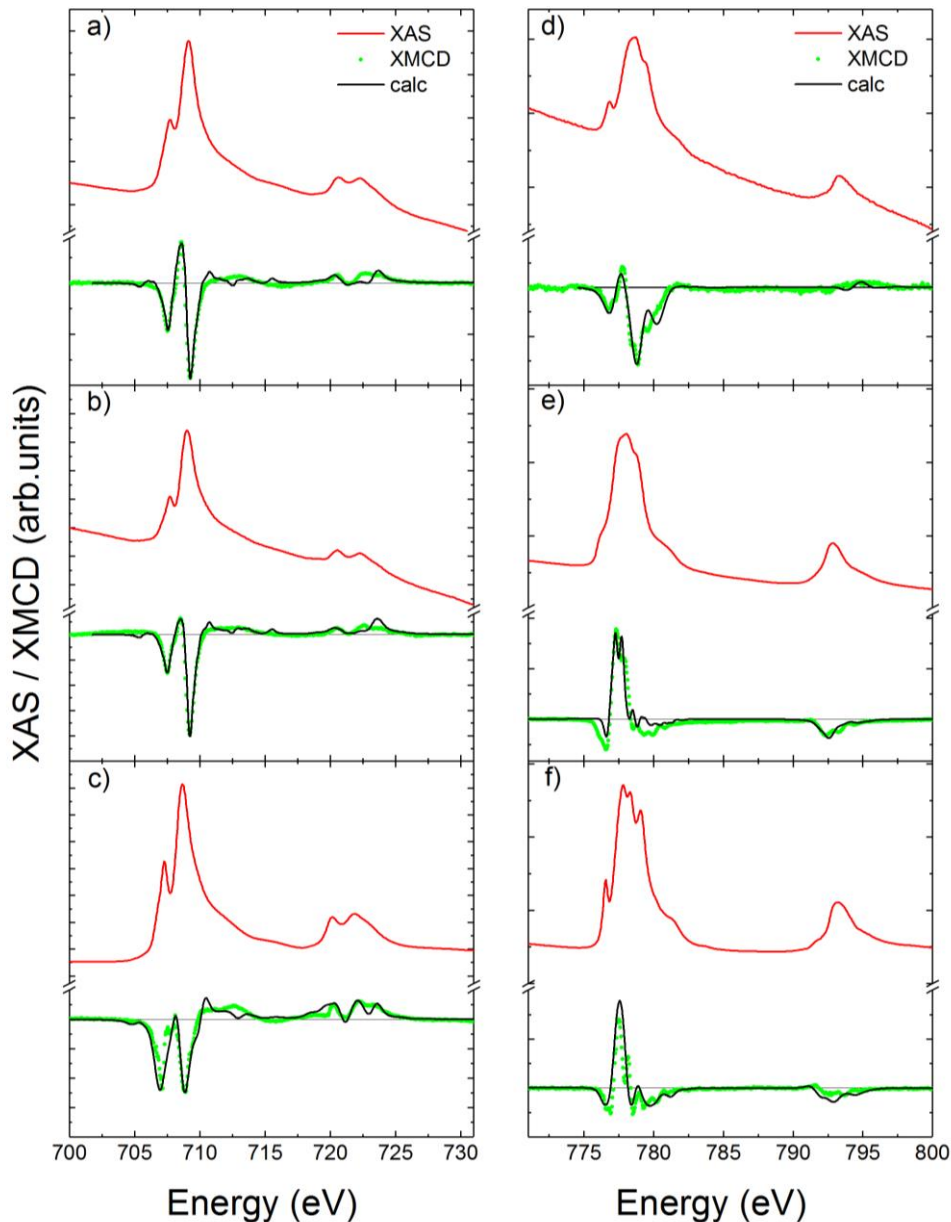


Figure 6.14. Experimental XAS (red) and XMCD (green) spectra for (a)  $\delta = 0.0$ , (b)  $\delta = 0.2$  and (c)  $\delta = 0.4$  at the Fe  $L_{2,3}$  edges. Experimental XAS (red) and XMCD (green) spectra for (d)  $\delta = 0.0$ , (e)  $\delta = 0.2$  and (f)  $\delta = 0.4$  at the Co  $L_{2,3}$  edges. Atomic multiplet simulations of the XMCD are shown in black. Spectra were measured at  $T = 230$  K,  $\mu_0 H = 6$  T and with the X-ray propagation vector parallel to H and at 60 degrees with respect to the surface normal.

For  $\delta = 0.2$  the Co XAS spectra is a superposition of octahedral, trigonal and tetrahedral  $\text{Co}^{2+}$  spectra. As doping now takes place in both the R and S block, all sites may be occupied. A large change in the coercivity, Fig. 6.4 (b), is seen for this sample that is likely to be due to substitution into the trigonal 2b site which is known to be responsible for the large anisotropy in the parent compound [6]. The magnetic contribution from the Co has a component anti-parallel to the Fe  $\text{O}_h$  sites and a good fit to the XMCD spectra is based on a ratio of  $\text{O}_h:\text{T}_d:\text{S}_6 \sim 55:23:22$ . The Co moment, or at least a component of the moment, on the 2b trigonal site is anti-parallel to the majority of octahedral Fe cations, which is in agreement with the finding of Williams *et al* for  $\text{BaTiCoFeO}$  [254].

For  $\delta = 0.4$  the XAS and XMCD at the Co  $L_{2,3}$  edges show an intriguing effect. Although the XAS spectra is dominated by  $\text{O}_h \text{Co}^{2+}$ , the XMCD shows that the magnetic response is almost identical to that for  $\delta = 0.2$  film. The small increase in the octahedral and trigonal components is as expected from the increase in  $\delta$ . Although in the hexaferrite structure there are more sites of octahedral

symmetry compared to tetrahedral and trigonal, the magnetic contributions are close to a 60:40 ratio for octahedral to tetrahedral/trigonal. This can be explained by the fact that there is an approximately equal amount of octahedral Co with opposite spins, which contribute additively to the XAS but cancel each other out in the XMCD.

It is apparent from these results that the  $\text{Ti}^{4+}$  cations strongly prefer the occupation of octahedral sites as supported by the literature [6] [10] and the  $\text{Co}^{2+}$  occupation of the 2b trigonal bipyramidal sites is responsible for a significant enhancement in the ME coupling. Magnetometry measurements also suggest a drastic reduction in coercivity for samples with trigonal bipyramidal like cobalt magnetic contributions. These results show promise for multiferroic device applications as if the amount of  $\text{Fe}^{2+}$  could be reduced a further enhancement of the ME coupling should be possible.

## 6.8 Summary and Conclusions

$\text{SrCo}_2\text{Ti}_2\text{Fe}_8\text{O}_{19}$  Samples have been studied that were grown via an ATLAD technique. In the deposition the R block was simulated by depositing from a target of  $\text{SrFe}_{(4-\delta)}\text{Ti}_{0.5\delta}\text{Co}_{0.5\delta}\text{O}_7$  and the S block was simulated by depositing from a target of  $\text{Fe}_{(1+0.25\delta)}\text{Ti}_{0.5(1-0.25\delta)}\text{Co}_{0.5(1-0.25\delta)}\text{O}_3$ , with  $\delta = 0.0, 0.2$  and  $0.4$ . EDX and XRD analysis confirm that all three samples are polycrystalline M-type hexaferrite,  $\text{SrCo}_2\text{Ti}_2\text{Fe}_8\text{O}_{19}$ . VSM magnetometry measurements indicate a drastic reduction in coercivity at 300K for  $\delta = 0.2$  and  $0.4$  samples compared to  $\delta = 0.0$ . It is postulated that this is due to the cobalt occupation of the trigonal bipyramidal sites. The  $M(T)$  relationships for the  $\delta = 0.2$  and  $0.4$  samples are also characteristic of those measured for other hexaferrites which display transitions from spin spiral to ferrimagnetic order [10] [23].

Ultimately, a combination of VSM magnetometry and XAS / XMCD at the Fe and Co  $L_{2,3}$  edges have been used to study the effect of Co substitution on the magnetoelectric coefficient in Co-Ti doped SrM hexaferrites. Multiplet features in the Co XMCD suggest that Co entering the trigonal 2b sites play an important role in the magnetoelectric effect in these materials. Naively one may have expected  $\alpha$  to increase with the amount of Co in the octahedral sites due to the increased magnetoelasticity. However, the situation is more complex and it is apparent that both magnetoelasticity and a mechanism associated with the Co occupation of the 2b trigonal bipyramidal site are important for enhancing  $\alpha$ . If this observed enhancement of the ME coupling, due to the Co occupation of trigonal bipyramidal sites, can be understood and optimised, this may lead to a huge step towards practical ME driven device applications.

## Chapter 7: Co enhancement of the magnetic-ion-induced polarisation at the hexaferrite trigonal bipyramidal sites

### 7.1 Introduction

The results of chapter 6 indicated that the sites to which the Co and Ti substitute within the M-type hexaferrite,  $\text{SrCo}_2\text{Ti}_2\text{Fe}_8\text{O}_{19}$ , have a significant effect on the ME coupling. It is apparent that the occupation of the 2b trigonal bipyramidal sites by cobalt ions enhances the magnetoelectric effect. Thus, the aim of this chapter is to investigate the mechanism through which this enhancement occurs. This has been achieved by studying the effect of the substitutions on the energy potential of the trigonal bipyramidal site.

Inspiration for this method of investigation came from Shen *et al* [14] who reported the presence of a magnetic ion induced displacive electric polarisation within the trigonal bipyramidal sites of both  $\text{BaFe}_{12}\text{O}_{19}$  and  $\text{SrFe}_{12}\text{O}_{19}$ . Such a displacive electric polarisation mechanism appears to be rarely found with magnetic ions, due to their partially filled d-orbitals. If the mechanism can be enhanced, by the presence of cobalt ions at the site, may explain the increased ME effects observed. In conventional ferroelectrics, such as the perovskite barium titanate, the local electric dipole often requires the displacement of a non-magnetic transition metal ion with an empty 3d shell due to the hybridization between the empty d orbital and filled oxygen 2p orbitals [270]. This has restricted the materials found with simultaneous dielectric and magnetic orders, and as previously discussed, certain magnetic hexaferrites have been found to display ferroelectricity via improper mechanisms. Shen *et al* [14] measured the dielectric properties of both  $\text{BaFe}_{12}\text{O}_{19}$  and  $\text{SrFe}_{12}\text{O}_{19}$ , showing a permittivity along the c-axis that increases steadily with decreasing temperature before saturating below  $\sim 5.5\text{K}$ . This behaviour is characteristic of quantum paraelectric materials such as  $\text{SrTiO}_3$  [271] and only occurs along the c-axis, suggesting that the electric dipoles in the M-type hexaferrite are along the c axis. As such, Shen *et al* [14] advocates that the origin of the local electric dipoles must be related to the magnetic  $\text{Fe}^{3+}$  ions within the BaM/SrM structure.

Other experiments have suggested the presence of off-equatorial displacements at the trigonal bipyramidal 2b sites [272] [273]. If displaced ions in these sites have a lower energy in the displaced position, then a local electric dipole,  $P$ , along the c-axis would be induced. Shen *et al* [14] calculated the local energy potential of the trigonal bipyramidal sites and showed the presence of a double well potential, characteristically seen for a ferroelectric. This infers that the competition between the long-range Coulomb interaction and short-range Pauli repulsion in the  $\text{FeO}_5$  bipyramidal unit of  $(\text{Ba,Sr})\text{Fe}_{12}\text{O}_{19}$  favours an off-centre displacement of the  $\text{Fe}^{3+}$  ion. The method employed for their calculations has been discussed in section 2.6.2.5, and has been suggested as a possible mechanism for magnetoelectric coupling.

In this chapter, the M-type hexaferrite crystal structure was modelled and the effects of both Co and Ti substitutions on the local potential of the 2b trigonal bipyramidal site have been studied. The structures were modelled using Materials Studio [274] and the geometries optimised using the CASTEP 8.0 density functional theory (DFT) code [275]. Initially, calculations were performed for  $\text{SrFe}_{12}\text{O}_{19}$  and compared to the results of Shen *et al* [14] to ensure consistency. Following this, both structures with Co and Ti doped into different sites independently were investigated with the results showing an increase in the energy barrier of the double well potential at the 2b site as a result of 2b substituted Co and 12k substituted Ti. However, the largest enhancement of the double well potential was observed for a  $\text{SrCo}_2\text{Ti}_2\text{Fe}_8\text{O}_{19}$  structure, with 2b Co and 12k Ti, indicating that the combined substitutions of both the Co and Ti to these sites acts to stabilise a mechanism for ferroelectricity along the c-axis. This provides a possible explanation for the enhanced ME effect observed due to Co trigonal site doping in chapter 6.

## 7.2 Simulation the M-type Hexaferrite structure

The M-type hexaferrite structure was simulated using the Materials Studio [274] software, by creating an hexagonal unit cell of the P63/mmc space group and initial lattice constants,  $a = 5.89 \text{ \AA}$  and  $c = 23.17 \text{ \AA}$ . Initially a  $\text{Sr}^{2+}$  was placed at the 2d cation site, all other cations were set as  $\text{Fe}^{3+}$ , and all anions allocated as  $\text{O}^{2-}$ . This structure then represented a  $\text{SrFe}_{12}\text{O}_{19}$  unit cell. In order to investigate a substituted structure, such as  $\text{SrCo}_2\text{Ti}_2\text{Fe}_8\text{O}_{19}$ , this unit cell was replicated and the appropriate substitutions made by changing a percentage of the particular lattice site to the substituting element. The SrM structure produced by Materials Studio is shown in fig. 7.1.

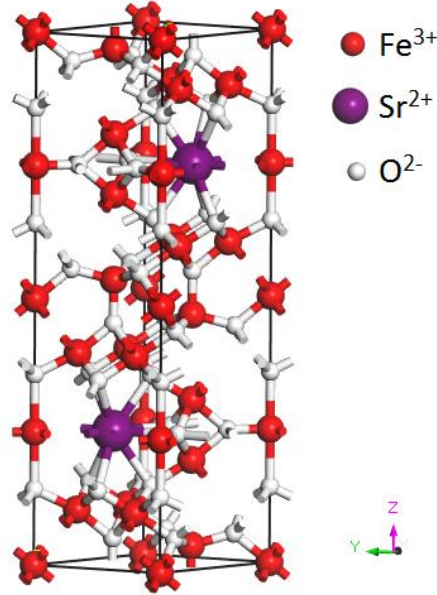


Figure 7.1. Perspective view of the SrM structure as simulated using Materials Studio [274].

To perform the trigonal bipyramidal site potential energy calculations, accurate values of the bond lengths surrounding the site are required. In order to find these bond lengths from the simulated structures their geometry must first be optimised. The geometry optimisation was performed using the CASTEP 8.0 density functional theory (DFT) code [275], and the bond lengths could then be taken from the resulting energy minimised structure.

The CASTEP programme is a first principles quantum mechanical code widely used for performing electronic structure calculations. It can be used to calculate a wide range of properties of materials that can be modelled as an assembly of electrons and nuclei. CASTEP is based on density functional theory. DFT is an alternative approach to quantum mechanics that utilises the electronic charge density to bypass the particles wavefunction. While it is not possible to solve the N-electron Schrodinger equation directly, DFT provides a method to determine the ground state electronic structure of a system [276].

The one particle Schrödinger equation is given by eqn. 7.1. [276]

$$\left(-\frac{\hbar^2}{2m}\nabla^2 + \hat{V}\right)\Psi(\mathbf{r}, t) = i\hbar\frac{\partial\Psi(\mathbf{r}, t)}{\partial t} \quad \text{Eqn. 7.1.}$$

However, to solve this for a real material the equation is complicated by the inclusion of M nuclei and N electrons. A simplification can be made in the Born-Oppenheimer approximation, which makes use of the fact that the nuclei are considered localised with respect to the electrons [276]. Additionally the Kohn-Sham equations convert the many body Schrodinger equation for N electrons into N equations each with one quasi-particle, as represented by eqns. 7.2 and 7.3. [276]

$$\left(-\frac{\hbar^2}{2m}\nabla^2 + V[\rho](\mathbf{r}) + V_{xc}[\rho](\mathbf{r})\right)\varphi_b(\mathbf{r}) = \epsilon_b\varphi_b(\mathbf{r}) \quad \text{Eqn. 7.2.}$$

$$\rho(\mathbf{r}) = \sum_{j=1}^N |\varphi_j(\mathbf{r})|^2 \quad \text{Eqn. 7.3.}$$

where  $V[\rho]$  and  $V_{xc}[\rho]$  are density functionals. Additionally, the code uses pseudopotentials to simplify the calculations, replacing the nuclei and inner electrons with pseudo-ions.

In a crystal lattice, where the nuclei are arranged in a reciprocal repeating pattern, further simplifications can be made by modelling the potential acting on the electrons as periodic. For a system with lattice vector,  $L$ , Bloch's theorem states that in a periodic potential, the density has the same periodicity and the possible wavefunctions are all quasi-periodic:

$$\varphi_k(\mathbf{r}) = e^{i\mathbf{k}\cdot\mathbf{r}} U_k(\mathbf{r}) \quad \text{Eqn. 7.4.}$$

where  $U_k(\mathbf{r}+\mathbf{L}) = U_k(\mathbf{r})$  and  $e^{i\mathbf{k}\cdot\mathbf{r}}$  is an arbitrary phase factor. Since  $U_k(\mathbf{r})$  is periodic, it can be expressed as a 3D Fourier series:

$$U_k(\mathbf{r}) = \sum_{\mathbf{G}} c_{\mathbf{G}k} e^{i\mathbf{G}\cdot\mathbf{r}} \quad \text{Eqn. 7.5.}$$

Here  $c_{\mathbf{G}k}$  are coefficients and  $\mathbf{G}$  are the reciprocal lattice vectors. Each  $e^{i\mathbf{G}\cdot\mathbf{r}}$  represent a plane-wave travelling perpendicular to the vector  $\mathbf{G}$  [276].

The number of plane waves used in a CASTEP calculation is controlled by a parameter known as the cut off energy ( $E_{cut}$ ), such that only planes waves with energies less than  $E_{cut}$  are used in the calculation. Eqn. 7.6 is used to define  $E_{cut}$ . [276]

$$E_{cut} = \frac{\hbar^2}{2m} |\mathbf{G}^2| \quad \text{Eqn. 7.6.}$$

The cut off energy is a key convergence parameter, larger values correspond to better results, however, take a larger amount of computational power, as such, before the geometry optimisation calculations are performed an  $E_{cut}$  value that provides a reliable groundstate energy must be found. The groundstate energy is found by solving the system's Schrödinger equation to find the eigenenergies and eigenfunctions, which are represented in terms of the coefficients  $c_{\mathbf{G}k}$ . To perform this calculation, CASTEP takes an initial guess at the wavefunctions and computes the density; from this, the Schrödinger equation is solved. If the energy has changed then this process is repeated, with a modified approximation of the wavefunction, until the energy change is smaller than the set energy tolerance [276]. To determine a suitable  $E_{cut}$  for the SrM structure, the groundstate energy ( $E_{GS}$ ) of the system was calculated for different values of the cut off energy. The results of these calculations are displayed in fig. 7.2.

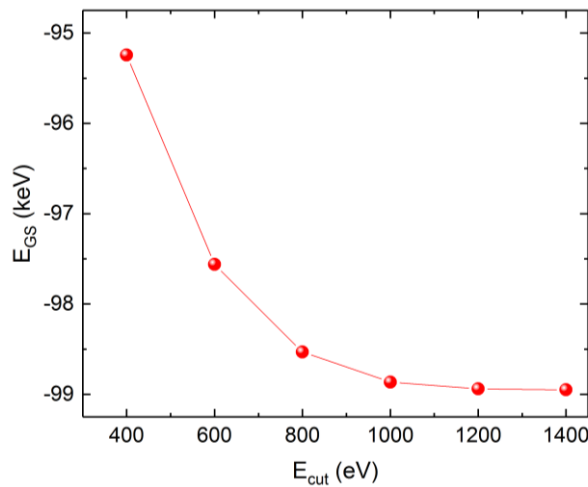


Figure 7.2. The groundstate energy of the simulated SrM system as a function of cut off energy, calculated using CASTEP 8.0 [275].

Each energy calculation was performed with a convergence parameter of  $5 \times 10^{-5}$  eV, using the General Gradient Approximation (GGA) of DFT and with a Perdew-Burke-Ernzerhof (PBE) parameterisation. The exchange correlation potential,  $V_{xc}$ , used in the definition of the Schrödinger

equation, in eqn. 7.2, is not known and GGA is one of the commonly used, and most reliable, approaches for approximating the exchange correlation [277]. Furthermore, PBE is a form of the GGA functional, developed by Perdew, Burke and Ernzerhof, that does not use experimentally fitted parameters in its approximation of the functional, which provides accurate results for a wide range of systems [277]. It is seen from fig. 7.2 that the calculated value of the groundstate energy converges as the cut off energy is increased. Between 1200 and 1400 eV very little energy change is seen, which suggests an  $E_{\text{cut}}$  of 1200 eV is suitable when performing calculations on this structure. Hence, for all the geometry optimisation calculations performed in this work a cut off energy of 1200 eV has been used.

Geometry optimisation could then be performed on each of the simulated hexaferrite structures, each with different site substitutions. The aim of a geometry optimisation calculation is to generate the optimal (lowest energy) structure of the material. A geometry optimization typically proceeds as a set of single point energy calculations, where the groundstate energy of the structure is calculated. This then allows the calculation of the forces experienced by the structures atomic nuclei. The force experienced by a nucleus,  $I$ , at position,  $R_I$ , is given by eqn. 7.7.

$$F_I = - \left\langle \frac{\partial E}{\partial R_I} \right\rangle \quad \text{Eqn. 7.7.}$$

The minimisation of the forces experienced by the nuclei can then be used to find the groundstate positions of the atoms. Thus, the structure corresponding to the local minima in energy is found with respect to the lattice constants and the atomic positions within the lattice.

The geometry optimisation was run until the residual force on each ion within the structure was less than 0.01 eV/Å and with a stress component of less than 0.02 GPa. Additionally, it was ensured that the maximum displacement of any ion, in the optimised structure, from the previous iteration was less than  $2 \times 10^{-3}$  Å, to ensure a minima in the structural energy was achieved. For each iteration of the optimisation, the energy was calculated with a convergence tolerance of  $1 \times 10^{-6}$  eV. A PBE exchange functional was again used, a method that produced reliable geometry optimisation results for Feng *et al* [87] in their exchange integral study of  $\text{SrCo}_2\text{Ti}_2\text{Fe}_8\text{O}_{19}$ .

The bond lengths associated with the trigonal bipyramidal site can then be determined from the geometry optimised structures and will be used to calculate the potential energy profile associated with the ions situated at the site.

### 7.3 Trigonal Bipyramidal site Potential Energy Calculation

To investigate the mechanism for electrical polarisation induced at the trigonal bipyramidal sites in  $\text{Ba}(\text{Sr})\text{Fe}_{12}\text{O}_{19}$ , as described in section 2.6.2.5, Shen *et al* [14] calculated the local potential energy profile along the c-axis,  $U_{\text{total}}(z)$ , for the trigonal bypramidal site, using the phenomenological local potential energy, defined by eqn. 7.8.

$$U_{\text{total}}(z) = U_{\text{Coulomb}}(z) + U_{\text{repulsion}}(z) \quad \text{eqn. 7.8.}$$

The total potential energy is the sum of the Coulomb potential,  $U_{\text{Coulomb}}(z)$ , between the  $\text{Fe}^{3+}$  and  $\text{O}^{2-}$  and the short-range Pauli repulsion potential,  $U_{\text{repulsion}}(z)$ , which are defined by eqns. 7.9 and 7.10, respectively.

$$U_{\text{Coulomb}}(z) = - \frac{18e^2}{4\pi\epsilon\sqrt{r_0^2+z^2}} - \frac{6e^2}{4\pi\epsilon(r_1+z)} - \frac{6e^2}{4\pi\epsilon(r_1-z)} \quad \text{eqn. 7.9}$$

$$U_{\text{repulsion}}(z) = 3\beta c_{\pm} \exp \left[ \frac{\left( r_+ + r_- - \sqrt{r_0^2 + z^2} \right)}{\rho_f} \right] + \beta c_{\pm} \exp \left[ \frac{r_+ + r_- - (r_1 + z)}{\rho_f} \right] + \beta c_{+-} \exp \left[ \frac{r_+ + r_- - (r_1 - z)}{\rho_f} \right] \quad \text{eqn. 7.10}$$

where  $\beta$  is a constant (taken to be  $1.35 \times 10^{-19}$  J),  $c_{+} = 1$  is Pauling's valence factor, and  $\rho_f$  is an arbitrary parameter assumed constant for a given material ( $\rho_f = 0.314 \text{ \AA}$ ) [26].  $r_{+}$  is the ionic radius of the cation at the trigonal bipyramidal site ( $0.58 \text{ \AA}$  for  $\text{Fe}^{3+}$  with a co-ordination number of 5) and  $r_{-} = 1.4 \text{ \AA}$  is the ionic radius of  $\text{O}^{2-}$  [110]. The permittivity,  $\epsilon$ , of the hexaferrite was calculated assuming a dielectric constant of 100, to ensure consistency with the work of Shen *et al* [14]. For the case in which  $\text{Co}^{2+}$  ions are located at the 2b trigonal bipyramidal sites, the cation ionic radius,  $r_{+}$ , in the calculation is changed accordingly to  $0.67 \text{ \AA}$  [110]. Additionally,  $r_0$  and  $r_1$  are the in-plane and out-of-plane bond lengths in the bi-pyramid for the 2b sites, as defined by fig. 7.3.

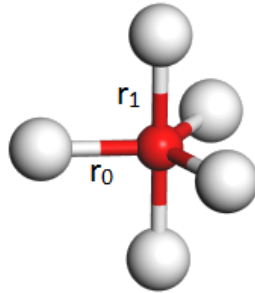


Figure 7.3. The interatomic distances  $r_0$  and  $r_1$  at the trigonal bipyramidal site.

In the work of Shen *et al* [14] these bond lengths were obtained for the  $\text{BaFe}_{12}\text{O}_{19}$  and  $\text{SrFe}_{12}\text{O}_{19}$  structures experimentally from the neutron diffraction studies of Aleshko-Ozhevskii *et al* [278]. However, in this work the bond lengths,  $r_0$  and  $r_1$ , have been determined using the geometry optimised simulations for the different substituted structures. Initially the calculation of the bipyramidal site potential, performed by Shen *et al* [14], for the  $\text{SrFe}_{12}\text{O}_{19}$  structure will be repeated to ensure consistency with their work. Following this, the potential is calculated for structures with Ti and Co doping and the effect of the doping on the potential experienced by the cations at the 2b site is investigated.

#### 7.4 Energy Potential Calculation for $\text{SrFe}_{12}\text{O}_{19}$

The  $\text{SrFe}_{12}\text{O}_{19}$  simulated structure produced bond lengths at the trigonal bipyramidal site of  $r_0 = 1.842 \text{ \AA}$  and  $r_1 = 2.382 \text{ \AA}$ . These values differ from the experimental values used by Shen *et al* [14] and scale by multiplication factors of 1.01 and 0.97, respectively, to coincide with experiment. Additionally, the bond lengths calculated for  $\text{BaFe}_{12}\text{O}_{19}$ , also differ from experiment by the same proportions. As such, all bond lengths calculated by CASTEP will be scaled by these two factors. This produces in bond lengths of  $r_0 = 1.86 \text{ \AA}$  and  $r_1 = 2.31 \text{ \AA}$  for the  $\text{SrFe}_{12}\text{O}_{19}$  structure. The bond lengths were used to calculate the Coulomb and repulsion potential terms, at the 2b trigonal bipyramidal site, as described in section 7.3, and are plotted in fig.7.4.

Both the Coulomb and repulsion potentials match those presented by Shen *et al* [14], supporting their results. The  $U_{\text{Coulomb}}$  term shows a single well potential about  $z = 0$ , while the  $U_{\text{repulsion}}$  term displays a double well feature, characteristic of electrical polarisation. These calculations indicate that for SrM, the short-range Pauli repulsions, and not the Coulomb forces, favour an off equatorial arrangement of the  $\text{Fe}^{3+}$  ions at the trigonal bipyramidal sites.

The repulsion potential in fig. 7.4(b) has minima in energy for an off-equatorial cation displacement of  $\pm 0.15 \text{ \AA}$ , as determined by Shen *et al* [14]. For SrM an energy barrier, according to the  $U_{\text{repulsion}}$  term, ( $\Delta E$ ) of 2 meV is observed. The summation of the Coulomb and repulsion potentials results in a potential,  $U_{\text{total}}$ , which still contains the double well feature indicating the existence of local electric dipoles. At room temperature, the thermal energy ( $k_B T$ ) is 25.7 meV. As such, the energy barrier is easily overcome by thermal agitation, resulting in an "average" equatorial potential, providing no net polarisation via this mechanism.

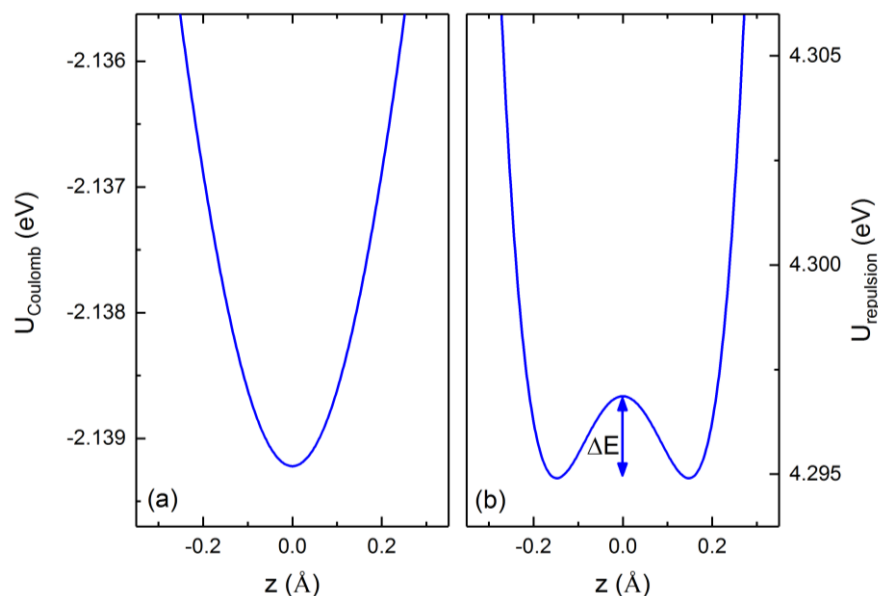


Figure 7.4. The calculated energy potentials (a)  $U_{\text{Coulomb}}$  and (b)  $U_{\text{repulsion}}$  as a function of off-equatorial 2b cation displacement in  $\text{SrFe}_{12}\text{O}_{19}$ .

The potential calculations carried out for  $\text{SrFe}_{12}\text{O}_{19}$  are consistent with those produced by Shen *et al* [14] and hence provide a basis from which to reproduce the calculations for the M-type structures with Co and Ti substitutions.

### 7.5 Calculations for Co substitutions

The effect of cobalt substitutions into the SrM structure, on the potential energy at the trigonal bipyramidal sites, has been investigated through the study of structures with Co ions substituted to different Wyckoff positions. X-ray spectroscopy measurements performed in chapters 5 and 6 indicated that within the M-type structure Co ions occupy a combination of octahedral, tetrahedral and trigonal bipyramidal sites. As such, three different strontium ferrite structures have been simulated with Co substitutions to a different site in each. The sites substituted are the  $4f_1$  tetrahedral, the 2a octahedral and finally the 2b trigonal bipyramidal. All three structures were optimised in the same way as the  $\text{SrFe}_{12}\text{O}_{19}$  case and the bond lengths  $r_0$  and  $r_1$  extracted. These values for the three different structures are displayed in table 7.1.

Co substitution site	$r_0$ (Å)	$r_1$ (Å)
$4f_1$ (tetrahedral)	1.8597	2.3098
2b (trigonal bipyramidal)	1.9065	2.3872
2a (octahedral)	1.8589	2.3149

Table 7.1. Table showing the  $r_0$  and  $r_1$  trigonal bipyramidal site inter-atomic distances for strontium ferrite with Co substituted to different lattice sites.

It is evident that substitution of the Co ions to the  $4f_1$  and 2a lattice sites have little effect on the trigonal site bond lengths, with both structures producing values closely comparable to that of  $\text{SrFe}_{12}\text{O}_{19}$ . Neither the 2a or  $4f_1$  sites are directly connected to the 2b, within the M-type structure, as such little effect is expected on  $r_0$  and  $r_1$  for these substitutions, however, with  $\text{Co}^{2+}$  ions placed at the trigonal sites, we seen an increase in both  $r_0$  and  $r_1$ . From these bond lengths both  $U_{\text{Coulomb}}$  and  $U_{\text{repulsion}}$  were calculated. For the case in which  $\text{Co}^{2+}$  occupied the trigonal site, the radius of the positive ion  $r_+$  was set to 0.67 Å and the  $6e^2$  term in the Coulomb potential becomes  $4e^2$ . The  $U_{\text{Coulomb}}$

plots for all three structures display the same single well form and again the  $U_{\text{repulsion}}$  potentials show a double well characteristic, as plotted in fig. 7.5.

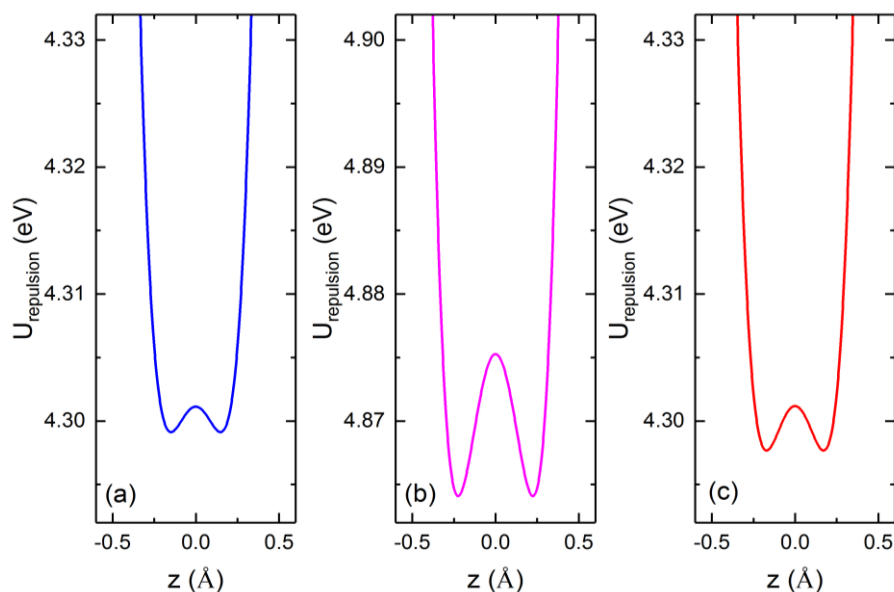


Figure 7.5. The calculated Pauli repulsion energy potentials,  $U_{\text{repulsion}}$ , as a function of off-equatorial 2b cation displacement in  $\text{SrCo}_2\text{Fe}_{10}\text{O}_{19}$ , with the Co ions substituted to (a)  $4f_1$  tetrahedral, (b) 2b trigonal bipyramidal and (c) 2a octahedral sites.

The structure with tetrahedral Co, has a trigonal site potential closely comparable to that of  $\text{SrFe}_{12}\text{O}_{19}$ , displaying an energy barrier of 2 meV and minima in  $z$  at  $\pm 0.15 \text{ \AA}$ . Comparing this to the potential of the 2a octahedrally substituted structure, fig. 7.5(c), we see a small increase in both the energy barrier and cation displacement minima, to 3.5 meV and  $\pm 0.17 \text{ \AA}$ , respectively. For substitution to the trigonal site, however, we observe a significant increase in the energy barrier to 9.5 meV, an effect which in isolation is not enough to overcome thermal effects at RT, but indicates that the Co occupation of the trigonal bipyramidal sites acts to increase the potential of the induction of a ferroelectric polarisation at the site. If stabilised this could provide an alternative mechanism for magnetoelectric coupling within the structure, explaining the enhancement in ME coupling observed in chapter 6 for increased trigonal site Co occupation.

It is also observed in fig. 7.5(b), that the 2b Co occupation increases the off-equatorial separation of the two minima in the double well potential, resulting in a displacement of  $0.23 \text{ \AA}$ . This suggests that if an electric dipole can be stabilised, the resultant polarisation will be greater due to Co occupation of the trigonal sites.

## 7.6 Calculations for Ti substitutions

In the magnetoelectric M-type hexaferrites studied, both Co and Ti are substituted into the strontium ferrite structure. Having studied the effect of Co substitutions in the previous section, we will now look at the effects of Ti substitutions to different sites within the lattice. X-ray spectroscopy results indicated that the  $\text{Ti}^{4+}$  strongly prefer occupation of octahedral sites, as such Ti substitutions to two different octahedral sites, the 2a and 12k, have been investigated as well as the  $4f_1$  tetrahedral. The substitutions were made to the structure such that an overall composition of  $\text{SrTi}_2\text{Fe}_{10}\text{O}_{19}$  was maintained. After geometry optimisation, the bond lengths were measured and are displayed in table 7.2.

Comparing the inter-atomic distances to those of SrM, for all three different structures, the in-plane Fe-O distances show little variation. However, for the  $4f_1$  and 2a substituted cases the out of plane distances,  $r_1$ , are reduced significantly compared to SrM and conversely the 12k substitution

results in an elongation of the  $r_1$  distance. When we consider the M-type structure, it is apparent that the 12k sites are bonded to the same oxygen atom as that forming the  $r_1$  bond in the 2b site. As such, it is to be expected that placing the Ti ions at the 12k sites would distort the trigonal bipyramidal site in such a way.

Ti substitution site	$r_0$ (Å)	$r_1$ (Å)
4f <sub>1</sub> (tetrahedral)	1.8718	2.1740
12k (octahedral)	1.8722	2.4174
2a (octahedral)	1.8585	2.2776

Table 7.2. Table showing the  $r_0$  and  $r_1$  trigonal bipyramidal site inter-atomic distances for strontium ferrite with Ti substituted to different lattice sites.

For the Ti substituted structures the Coulomb potentials all take the same form, with a single well about  $z = 0$ . However, when we consider the  $U_{\text{repulsion}}$  term significant differences are observed. In figs. 7.6(a) and (c) the  $U_{\text{repulsion}}$  potentials for the 4f<sub>1</sub> and 2a substitutions now show a single well potential, due to the reduction in  $r_1$  distances. This indicates that Ti occupation of these sites acts to suppress the induction of any dipole formation at the trigonal bipyramidal sites. On the other hand, the structure with 12k Ti substitutions, fig. 7.6(b), shows a double well potential with an energy barrier that is greatly increased compared to SrM. In fact in this structure we observe  $\Delta E = 62$  meV, which is more than two times the room temperature thermal energy. In addition, the minima in the potential occur at a larger off-equatorial displacement of  $\pm 0.37$  Å, an effect similar to that of the 2b Co substitutions.

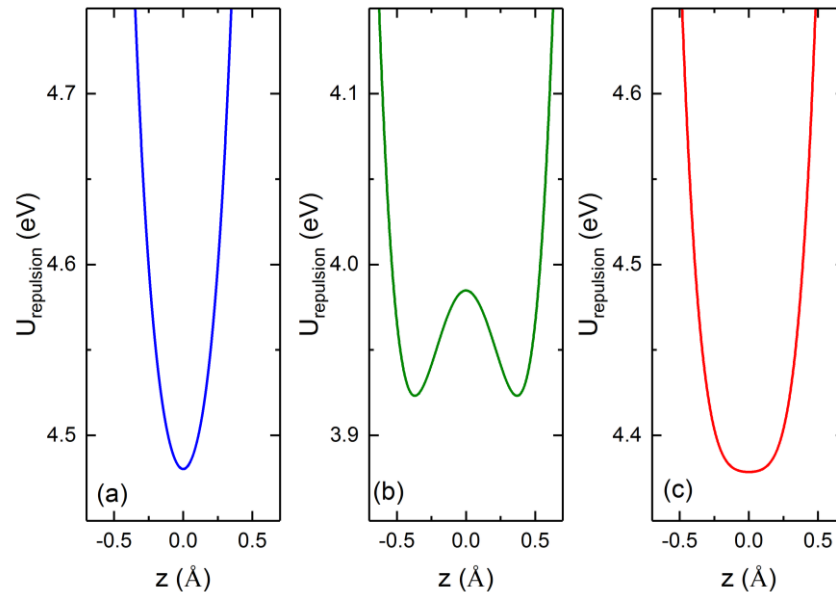


Figure 7.6. The calculated Pauli repulsion energy potentials,  $U_{\text{repulsion}}$ , as a function of off-equatorial 2b cation displacement in  $\text{SrTi}_2\text{Fe}_{10}\text{O}_{19}$ , with the Ti ions substituted to (a) 4f<sub>1</sub> tetrahedral, (b) 12k and (c) 2a octahedral sites.

These results suggest that along with the Co occupation of 2b sites, the 12k Ti substitutions are important for the induction of electrical polarisation, proposed at the trigonal bipyramidal sites.

### 7.7 Calculations for combined Co and Ti substitution

The previous calculations have suggested that the occupation of the 2b and 12k sites by Co and Ti, respectively, act independently to increase the energy barrier of the double well potential at the

2b sites. As such, a structure has been simulated with a composition of  $\text{SrCo}_2\text{Ti}_2\text{Fe}_8\text{O}_{19}$  and all the Ti and Co substituted to the 12k sites and 2b sites, respectively.

With the structure optimised using the method previously discussed, this produced inter-atomic distances at the trigonal bipyramidal site of  $r_0 = 1.9106 \text{ \AA}$  and  $r_1 = 2.4791 \text{ \AA}$ , both of which are significantly increased with respect to the un-doped structure. The increase in  $r_1$  is greater than that in  $r_0$  and through comparison with the previous simulations; it is evident that the  $r_0$  increase is due largely to the Co, whilst the change in  $r_1$  is a summation of the effects of the two substitutions. The Coulomb potential for this structure shows very little difference with respect to the other structures, with again a single well potential about  $z = 0$ . The  $U_{\text{repulsion}}$  potential is shown for this structure, alongside that of  $\text{SrFe}_{12}\text{O}_{19}$ , in fig. 7.7.

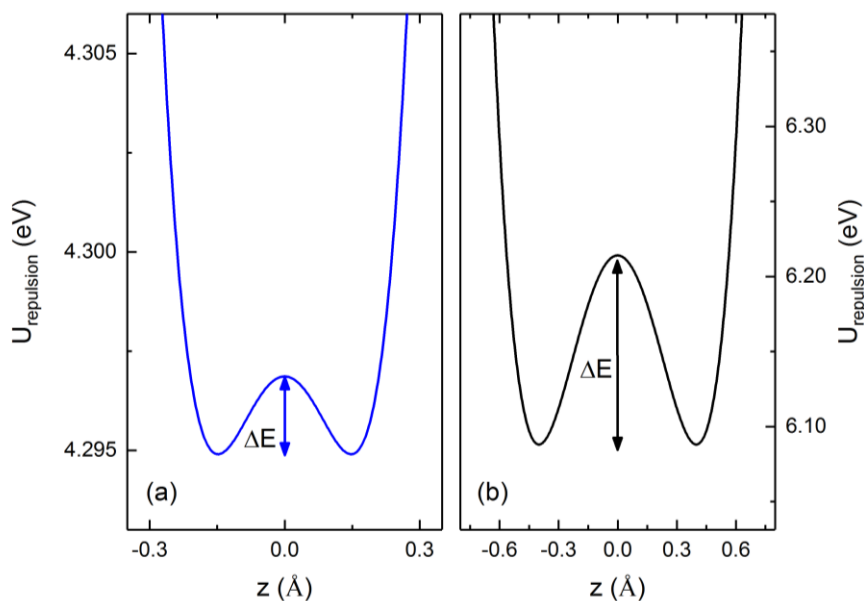


Figure 7.7. The calculated Pauli repulsion energy potentials,  $U_{\text{repulsion}}$ , as a function of off-equatorial 2b cation displacement,  $z$ , for (a)  $\text{Fe}^{3+}$  and (b)  $\text{Co}^{2+}$  in the trigonal bipyramidal site and  $\text{Ti}^{4+}$  in the octahedral 12k site.

The  $U_{\text{repulsion}}$  term again displays the double well form for the  $\text{SrCo}_2\text{Ti}_2\text{Fe}_8\text{O}_{19}$  structure, with 2b and 12k, Co and Ti. Comparing the two potentials it is evident that the energy barrier is increased significantly by the doping from 2 to 120 meV. This energy barrier is also significantly larger than for the structures with Co and Ti doping in isolation, hence, the combined effects of both Co and Ti doping to the 2b and 12k sites, respectively, produces the largest enhancement in stabilisation of the electric dipole at the 2b sites. In addition, it is observed that the off-equatorial displacement of the well minima is increased in comparison to the other structures, to a displacement of  $0.4 \text{ \AA}$ .

It can be concluded from these simulations that both the Co occupation of 2b sites as well as the Ti substitution to the 12k, act to enhance and stabilise a mechanism for ferroelectricity based on the induction of electric dipole moments at the trigonal bipyramidal sites. In addition, the  $\text{Co}^{2+}$  substituted to the 2b site is known to be magnetoelastic [37]. As such, local distortions introduced by the 12k Ti and 2b Co ions affect the piezoelectric strain coefficient as well as the magnetoelastic coupling. The combination of the two provides a route to increase the magnetoelastic coupling coefficient as was first shown theoretically in [57] where an additional term can be added to  $\alpha$  which is proportional to the product of the magnetoelastic and piezoelectric tensors of the material, as discussed in section 2.5.1.

To gain further insight into the lattice requirements for local electric dipoles at the trigonal bipyramidal site, Shen *et al* [14] produced a phase diagram for the existence of a double well potential, a graph that has been reproduced in fig. 7.8. Investigating the extreme conditions for

each potential,  $U_{\text{Coulomb}}$  and  $U_{\text{repulsion}}$ , at  $z = 0$ , it is seen that in order for the Coulomb term to favour an off-equatorial displacement of the cation eqn. 7.11 must be satisfied.

$$\frac{\partial^2 U_{\text{Coulomb}}}{\partial z^2} \Big|_{z=0} < 0 \quad \text{eqn. 7.11}$$

This produces the structural condition that  $r_1/r_0 > (4/3)^{1/3}$ , which is plotted as the green line in fig. 7.8. Alternatively, for the repulsion term to produce a double well potential, the criteria of eqn. 7.12 must in this case be satisfied.

$$\frac{\partial^2 U_{\text{repulsion}}}{\partial z^2} \Big|_{z=0} < 0 \quad \text{eqn. 7.12}$$

Analysis of this condition then results in the lattice requirements,  $e^{r_1/\rho_f} > 2/3((r_0/\rho_f)e^{r_0/\rho_f})$ , as represented by the blue line in fig. 7.8. It is evident from the figure that the formation of a double well potential depends upon the relative magnitudes of  $r_1/\rho_f$  and  $r_0/\rho_f$ . In the central yellow shaded region, the existence of a double well potential is forbidden and in the green region it must occur in both the Coulomb and repulsion terms.

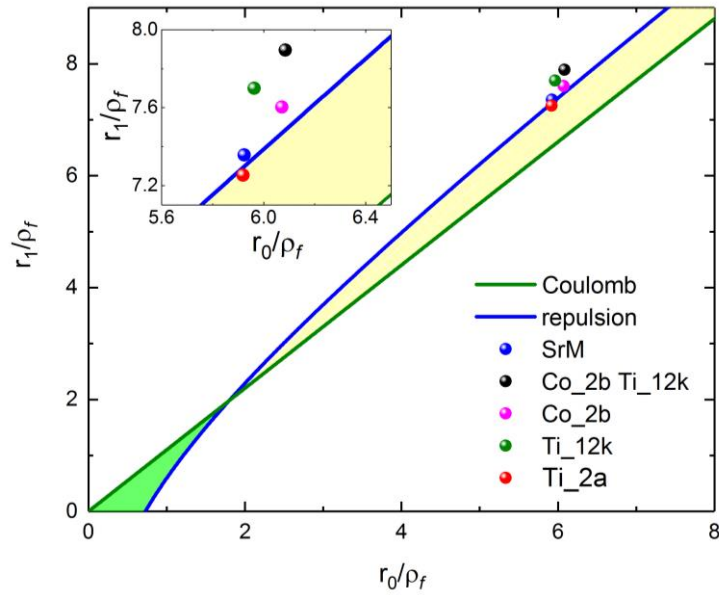


Figure 7.8. Phase diagram plot of  $r_1/\rho_f$  against  $r_0/\rho_f$ . In the central yellow region, the double well potential is forbidden. In the lower green region it must occur and outside these regions it is possible due to the competing interactions [14].

In fig. 7.8, points on the phase diagram represent the positions of the simulated structures studied. It is seen that all the structures lie above the Coulomb double well limit, thus, as observed display a single well Coulomb potential. The inset of the figure shows that the un-doped strontium ferrite structure is situated just within the  $U_{\text{repulsion}}$  limit explaining the presence of a small double well potential. The structure with Ti doped to the 2a sites is located in the region within which the double well is forbidden in both potentials, which is consistent with the single well potentials observed for this structure. The diagram shows that with Co substitution to the 2b sites and Ti substitution of the 12k sites independently, move the structure further away from the repulsion limit, hence we see enhancements in the double well potential. The combination of both substitutions produces a further shift from the repulsion limit, an effect that is also seen in the increased double well potential for the  $\text{SrCo}_2\text{Ti}_2\text{Fe}_8\text{O}_{19}$  structure.

## 7.8 Summary and Conclusions

In this chapter, M-type hexaferrite structures have been simulated using Materials Studio [274] and their geometries optimised using the CASTEP 8.0 DFT code [275]. This allowed the inter-atomic

distances associated with the 2b trigonal bipyramidal sites to be extracted and used to calculate the local potential of the 2b trigonal bipyramidal site.

The  $\text{SrFe}_{12}\text{O}_{19}$  structure was simulated and the local energy potential calculated along the c-axis showed consistency with the work of Shen *et al* [14], displaying a double well potential, a characteristic indicative of ferroelectric polarisation. However, the energy barrier for the SrM case was shown to be smaller than thermal energy at RT, resulting in an 'average' equatorial position, providing no net polarisation.

Subsequently, structures with Co doping to different lattice sites were investigated. The results showed that Co substitutions to the trigonal bipyramidal sites increased the energy barrier of the double well potential as well increase the displacement of minima from the equatorial position. Investigating the effects of Ti substitutions it was seen that doping to the 12k octahedral sites had a similar effect on the trigonal bipyramidal site potential, whereas doping to the 2a and  $4f_1$  sites had the adverse effect and prohibited the double well feature entirely. In light of these results, an  $\text{SrCo}_2\text{Ti}_2\text{Fe}_8\text{O}_{19}$  structure, with 2b Co and 12k Ti, displayed the maximum observed double well energy barrier as well as the largest off-equatorial displacement of minima, 0.4 Å. The energy barrier in this case is significantly larger than RT thermal energy, suggesting that the Co and Ti substitutions to these sites act to stabilise a local electric polarisation along the c-axis.

The presence of such a lattice-induced dipole at the bipyramidal site has also been investigated by Tang *et al* [279] in Sc doped barium ferrite. Their work indicates the presence of two possible mechanisms for ferroelectricity, one due to an improper ferroelectric mechanism, governed by the inverse Dzyaloshinskii-Moriya mechanism and the other due to the trigonal bipyramidal site instability. They show that for  $\text{BaSc}_{1.8}\text{Fe}_{10.2}\text{O}_{19}$ , at temperatures too high to support a conical magnetic structure, hence improper ferroelectricity, electric dipoles are still present. Thus, in addition to enhancing the ferroelectric polarisation at RT, the presence of a lattice-induced dipole at the 2b sites in the  $\text{SrCo}_2\text{Ti}_2\text{Fe}_{12}\text{O}_9$  structure may enable ferroelectricity in the material to temperatures higher than previously anticipated.

Additionally, Wang and Xiang [280] have investigated the structural instability of the trigonal bipyramidal site for the M-type hexaferrite and demonstrated that for  $\text{BaFe}_{12}\text{O}_{19}$  the ferroelectric state is energetically favourable in an external electric field. Our results suggest that the substitution of Co and Ti in to the 2b and 12k may act to stabilise the ferroelectric polarisation even in the absence of an applied field. Although in Co-Ti doped hexaferrites not all the cations in the 2b sites will be substituted by Co, an increase in Co into these sites, as evidenced by the XAS/XMCD data in chapter 6, enhances the ability for the structure to polarize as well as providing a magnetoelastic ion, in the form of  $\text{Co}^{2+}$ . As such, local distortions, introduced by the Co and Ti ions in the 2b and 12k sites, affect the piezoelectric strain coefficient as well as the magnetoelastic coupling. The combination of the two provides a route to increase the magnetoelectric coupling coefficient as was first shown theoretically by Vittoria *et al* [57], where an additional term can be added to  $\alpha$  which is proportional to the product of the magnetoelastic and piezoelectric tensors of the material. Therefore, it seems that both Co substitution into the 2b trigonal sites and Ti substitution into the 12k octahedral sites provide a mechanism for enhancing the magnetoelectric effect in this material.

## Chapter 8: Conclusions and Future Work

### 8.1 Summary of Works

The work of this thesis was undertaken with two main objectives. The first has been to design and develop a PLD growth system to enable the growth of high quality transition metal oxide thin films, such as hexaferrites. The second objective was to characterise the structural, magnetic and magnetoelectric properties of  $\text{SrCo}_2\text{Ti}_2\text{Fe}_8\text{O}_{19}$  hexaferrite thin films grown by PLD and ATLAD, in order to gain insight into the mechanisms governing their ME properties. With respect to this study, soft x-ray magnetic spectroscopy has provided a unique method for investigating the element specific magnetic contributions from each film co-ordination.

#### 8.1.1 Summary of PLD Development

PLD was chosen as the most suitable technique for the growth of magnetic oxide thin films as it allows for stoichiometric growth of complex unit cells, a variation of which, ATLAD, has previously been demonstrated as a technique to produce high quality hexaferrite films allowing for cation substitution on the atomic scale due to non-equilibrium growth [133] [21] [24]. As such, in this work, a bespoke PLD growth system has been successfully designed and developed.

The system is catered towards the growth of complex oxides whilst remaining versatile, enabling the growth of a wide range of thin film materials. The PLD system incorporates a specifically designed target manipulator, allowing for up to 6 targets, which all rotate individually and can be indexed rapidly. This design allows for the growth of hexaferrite thin films with the R and S-block layers grown from separate targets. Using this ATLAD method, the composition of the targets could be controlled in such a way that dopant ions can be positioned in just one of the R or S blocks, as demonstrated by Geiler *et al* [21]. Target ablation is achieved with a frequency quadrupled Nd:YAG laser, pulsed at 10 Hz, and the sample can be heated during growth using a unique 35 W  $\text{CO}_2$  laser setup. The PLD also incorporates a load-lock system allowing for quick sample transfer, without breaking vacuum. Finally, the system design enables samples to be grown and annealed safely in an oxygen partial pressure, which is important for the growth of oxide films in order to control the stoichiometry and ensure that any oxygen lost during the ablation of the target is replaced [19].

Following the growth system's successful construction, it was tested and calibrated through the growth of a series of  $\text{Fe}_3\text{O}_4$  thin films. The growth of these films allowed the system deposition rate to be calibrated in terms of deposition time, chamber pressure and target-sample distance. The substrate heating system has also been calibrated for several commonly used substrates, including  $\text{Al}_2\text{O}_3$ , Si and MgO. Substrate temperatures in excess of  $900^\circ\text{C}$  have been realised, showing that the substrate heating mechanism is capable of achieving the conditions required for the formation of M-type hexaferrite films [21] [24] [6]. Subsequently, as an initial test of the system, the growth of an epitaxial magnetite thin film was achieved with properties comparable to those reported in the literature for a high quality as-grown film [25]. This demonstrates that the PLD system developed is effective for the growth of high quality oxide thin films.

The system's ability to grow complex hexaferrite thin films has been tested and the successful growth of an epitaxial M-type hexaferrite, with material properties that compare well to the literature [23] [10] [24], has been realised. The hexaferrite film does, however, include a cobalt ferrite impurity phase that should be reduced and removed with further optimisation of the growth and annealing conditions. The system, through the growth of these films, has ultimately been proven capable of producing high quality magnetic oxide thin films.

### 8.1.2 Summary of Soft X-ray Magnetic Spectroscopy Hexaferrite thin film Study

A soft x-ray spectroscopy study of  $\text{SrCo}_2\text{Ti}_2\text{Fe}_8\text{O}_{19}$  thin films has been performed in this work. M-type hexaferrites of this composition had been previously shown to display a strong magnetoelectric coupling at room temperature [10] [24]. The aim of this study was to investigate the roles of the Co and Ti dopants on the hexaferrites magnetic structure, as well as correlating this to the magnetoelectric coupling mechanism.

Initially a  $\text{SrCo}_2\text{Ti}_2\text{Fe}_8\text{O}_{19}$  film was studied, that had been grown by PLD from a single target of the same composition to a thickness of 0.9  $\mu\text{m}$ . The film had been grown, and annealed, under the same conditions as those detailed by Mohebbi *et al* [24], for the first reported  $\text{SrCo}_2\text{Ti}_2\text{Fe}_8\text{O}_{19}$  film displaying ME coupling. Structural characterisation of the film reveals a polycrystalline nature and magnetic characterisation produces a low coercivity of  $(20 \pm 5)$  Oe at 300 K, supporting claims in the literature that the Co substitution into the M-type structure drastically reduces  $H_c$  [6] [246] [106]. The temperature dependent magnetic properties of the film also appear characteristic of those seen in the literature for  $\text{SrCo}_2\text{Ti}_2\text{Fe}_8\text{O}_{19}$  [24] [23] [10].

XAS and XMCD measurements were performed at the Fe, Co and Ti L-edges, and fitted with atomic multiplet calculations to determine the relative contributions of different co-ordinations and valences for each element, as well as investigate their contribution to the samples overall magnetic structure. The Ti XAS measurements confirm that the Ti ions have a 4+ valence as well as a strong preference for the occupation of octahedral sites, which supports the literature that suggests they preferentially occupy the 12k octahedral sites [6] [83]. An effect, which is thought to magnetically de-couple the R- and S-blocks, a pre-requisite for the formation of the non-collinear magnetic structure reported in  $\text{SrCo}_2\text{Ti}_2\text{Fe}_8\text{O}_{19}$  [6]. Additionally, XMCD at the Co edge indicates that the Co have a 2+ valence and are substituted to all three different co-ordinations, octahedral, tetrahedral and trigonal bipyramidal. It is observed that around a fifth of the Co ions occupy the 2b trigonal bipyramidal sites, which is consistent with Cabanas *et al* [86], who stated that the Co occupy the 2b sites above a critical doping concentration. It is also believed that the doping of Co to these sites play a significant role in the reduction of coercivity observed within Co-Ti doped hexaferrites [6]. Interestingly, it is also seen from the Fe XMCD that a percentage of the octahedrally co-ordinated Fe has a 2+ valence, the presence of which will be detrimental to magnetoelectric coupling as it provides a conductive pathway, due to polaronic hopping between  $\text{Fe}^{2+}$  and  $\text{Fe}^{3+}$  ions, ultimately suppressing electric polarisation.

To conclude, this film displays magnetic properties that strongly resemble those reported in the literature for  $\text{SrCo}_2\text{Ti}_2\text{Fe}_8\text{O}_{19}$  bulk and thin film samples [106] [23] [10] [24] [107]. Given this, the x-ray spectroscopy results obtained for this film can be used as representative of a conventionally grown PLD film for comparison to the ATLAD grown films, later studied.

As well as the 0.9  $\mu\text{m}$  thin film, a much thinner film of 50 nm, grown by the same single target PLD growth procedure, has been studied. Structural characterisation shows that this thinner film has a close to epitaxial crystalline ordering. The 50nm film displays magnetic properties that differ from the 0.9  $\mu\text{m}$  film and literature, with a significantly larger coercivity observed at RT and significant changes in the M(T) phase transition temperatures. The XMCD results for this film present a significant difference in the magnetic contribution of the Co, with a greater proportion of octahedrally co-ordinated Co and a reduction in both tetrahedral and trigonal bipyramidal contributions. This differently co-ordinated Co then provides an explanation for the differing magnetic properties of the thinner film. It is postulated that this effect may be caused by the strain of the substrate on the thinner film, resulting in a change to the preferential occupation sites of the Co ions. In order to substantiate this claim however, further investigations are required, to eliminate other possible causes of this effect.

In addition to the single target films, three SrCo<sub>2</sub>Ti<sub>2</sub>Fe<sub>8</sub>O<sub>19</sub> films have been studied that were grown via an ATLAD technique. In the deposition the R block was simulated by depositing from a target of SrFe<sub>(4-δ)</sub>Ti<sub>0.5δ</sub>Co<sub>0.5δ</sub>O<sub>7</sub> and the S block was simulated by depositing from a target of Fe<sub>(1+0.25δ)</sub>Ti<sub>0.5(1-0.25δ)</sub>Co<sub>0.5(1-0.25δ)</sub>O<sub>3</sub>, with  $\delta = 0.0, 0.2$  and  $0.4$ . The aim of this study was to investigate the effect of forcing the Co and Ti substitutions into different sites, by controlling the block into which they are substituted. For  $\delta = 0.0$ , all dopants were forced to reside solely in the S-block, containing the octahedral 2a and 12k sites as well as the 4f<sub>1</sub> tetrahedral, whereas for the  $\delta = 0.2$  and  $0.4$  films an increasing proportion of substitutions are directed towards the R-block, opening up the possibility of trigonal bipyramidal site occupation.

These thin films have been characterised, both structurally and magnetically, in order to observe the effects the substitution sites have on the films properties. X-ray diffraction confirms that all three films are polycrystalline M-type hexaferrite. Magnetometry measurements, however, indicate a drastic reduction in H<sub>c</sub> at 300 K for  $\delta = 0.2$  and  $0.4$  samples compared to  $\delta = 0.0$ . The M(T) relationships for the  $\delta = 0.2$  and  $0.4$  samples are also characteristic of those measured for other hexaferrites which display transitions from spin spiral to ferrimagnetic order [10] [23], a behaviour which is not prominent for the  $\delta = 0.0$  film. In addition to these changes in magnetic properties, over an order of magnitude increase in the converse ME coupling is observed as Co and Ti doping to the R-block is increased.

Given these observations, to gain a more detailed understanding of the role of Co-Ti substitutions in SrM, we performed XAS at the Ti L<sub>2,3</sub> absorption edge and XAS/XMCD measurements at the Co and Fe L<sub>2,3</sub> absorption edges in order to determine the valency, co-ordination, and magnetic response of the individual elements. For all three samples, the Ti XAS spectra strongly indicate Ti<sup>4+</sup> with an octahedral co-ordination. This is as anticipated from the literature [6] [83] and in accordance with the study of the single target films. Co L<sub>2,3</sub> edge XMCD measurements performed for the  $\delta = 0.0$  film indicate uncompensated Co moments to be due to octahedral Co (~70%) with a 30% tetrahedral contribution. However, XAS and XMCD at the Co L<sub>2,3</sub> edges for  $\delta = 0.2$  and  $0.4$ , show differences in the XAS and XMCD lineshape compared to the  $\delta = 0.0$  film. Atomic multiplet fitting shows that the magnetic contribution from Co significantly changes to a situation where Co<sup>2+</sup> ions in trigonal sites become more important as  $\delta$  increases. Hence, the observed enhancement of ME coupling can be correlated to the introduction of Co<sup>2+</sup> ions into the 2b trigonal bipyramidal sites. This work has shown that the Co occupation of trigonal bipyramidal sites plays a key role in the magnetoelectric coupling observed within such M-type hexaferrites

The importance of Co<sup>2+</sup> at the trigonal bipyramidal sites to the macroscopic magnetic properties and magnetoelectric coupling is intriguing. To investigate the mechanism through which the ME coupling enhancement occurs, the effect of the Co-Ti substitutions on the energy potential of the trigonal bipyramidal site has been studied. Inspiration for this method of investigation came from Shen *et al* [14] who reported the presence of a magnetic ion induced displacive electric polarisation within the trigonal bipyramidal sites of SrFe<sub>12</sub>O<sub>19</sub>. If the mechanism reported can be enhanced, by the presence of cobalt ions at the site, this may explain the increased ME effects observed.

In this study, M-type hexaferrite structures, with Co and Ti substitutions performed to specific lattice sites, were simulated using the CASTEP 8.0 DFT code [275]. These structures were then used to calculate the local potential of the 2b trigonal bipyramidal site. The results showed that Co substitutions to the trigonal bipyramidal sites increased the energy barrier of the double well potential, indicative of ferroelectric polarisation, as well increase the displacement of minima from the z-axis equatorial position. Investigating the effects of Ti substitutions it was seen that doping to the 12k octahedral sites had a similar effect on the trigonal bipyramidal site potential to that of the trigonal Co, whereas doping to the 2a and 4f<sub>1</sub> sites had the adverse effect and prohibited the double well feature entirely. The enhancement due to the 12k Ti occurs as a result of the 12k

octahedral cage sharing an oxygen ion with the trigonal bipyramidal. In light of this, a  $\text{SrCo}_2\text{Ti}_2\text{Fe}_8\text{O}_{19}$  structure, with 2b Co and 12k Ti substitutions, was simulated. This structure displayed the maximum observed double well energy barrier as well as the largest off-equatorial displacement of minima, 0.4 Å. The energy barrier in this case is significantly larger than RT thermal energy, suggesting that the Co and Ti substitutions to these sites act to stabilise a local electric polarisation along the c-axis.

Although in Co-Ti doped hexaferrites not all the Co ions will be substituted to the trigonal bipyramidal sites, an increase in trigonal bipyramidal Co enhances the ability for the structure to polarize as well as providing a magnetoelastic ion, in the form of  $\text{Co}^{2+}$ . As such, local distortions, introduced by the Co and Ti ions in the 2b and 12k sites, affect the piezoelectric strain coefficient as well as the magnetoelastic coupling. The combination of the two provides a route to increase the magnetoelectric coupling coefficient as was first shown theoretically by Vittoria *et al* [57], where an additional term can be added to  $\alpha$  which is proportional to the product of the magnetoelastic and piezoelectric tensors of the material. Therefore, this work has shown that both Co substitution into the 2b trigonal sites and Ti substitution into the 12k octahedral sites provide a mechanism for enhancing the magnetoelectric effect in this material.

## 8.2 Future Work

Having summarised the findings and progress achieved in this body of work, this section will discuss the direction of further development of the PLD growth system, as well as future investigations into magnetoelectric hexaferrites. Emphasis is placed on enhancing the ME coupling further, with an increased understanding of the magnetoelectric mechanisms, and ultimately the tailoring of the structures properties towards technological applications.

### 8.2.1 Future PLD Growth and Development

With respect to the PLD growth system, several further developments can still be made in order to improve the systems versatility. Provision has been made to allow for the incorporation of E-beam evaporators into the growth chamber. The addition of these to the system would allow metal capping layers to be deposited on a films surface in-situ. For this to be made possible, the system would need to be baked in order to achieve lower pressures, meaning that following PLD film growth the chamber could be pumped down to base pressure and a capping layer grown. Furthermore, the system has been designed to allow for the addition of a RHEED gun and screen in the future, enabling the in-situ characterisation of the film or substrates surface structure. Finally, the system could also benefit from the incorporation of a crystal thickness monitor, which if placed next to the sample during growth can be used to indicate film thickness.

In terms of future film growth with the PLD system, more films should to be grown in order to optimise several growth parameters such as substrate growth temperature and chamber partial pressure. Of course, these parameters are all dependent on the type of film being grown, thus as different films are studied, and these should be optimised on an individual basis. The effect of varying laser fluence on film properties should also be studied.

With respect to M-type hexaferrite growth, work is required in order to optimise growth conditions, such optimisation should remove the secondary cobalt ferrite phase observed. It is thought that the introduction of this secondary phase is due to either the oxygen chamber pressure or the substrate temperature; as such, these two parameters should be investigated first. Once hexaferrite growth conditions have been optimised for deposition from a single target, attempts should be made to grow the hexaferrite block by block from two targets, to simulate the R and S-blocks, in accordance with the ATLAD growth method. This will require a carefully timed sequence of target movement, in order to produce the layered structure. If achieved, however, it will enable

the substitution of cations to specific blocks, as achieved in chapter 6 by a collaborator's well-established growth system. Such a development would open up the possibility of investigating the effects of further manipulating the substitution sites within the M-type hexaferrite structure with the aim of further enhancing magnetoelectric coupling.

### 8.2.2 Future Hexaferrite thin film Development

One avenue of investigation, in the study of ME hexaferrites, would be into the effects of film thickness on the films properties. The results of chapter 5 suggested that thin films on  $\text{Al}_2\text{O}_3$  (0001) grow epitaxially initially before relaxing towards polycrystalline growth above a critical thickness, with such effects also observed by Dorsey *et al* [20] for  $\text{BaFe}_{12}\text{O}_{19}$ . In addition to this, the thinner film displays magnetic properties that differ from the thicker film, both here and in the literature [24] [107], with XMCD measurements at the Co  $L_{2,3}$  edges indicating a change in the Co occupation sites. In order to investigate the effect further and substantiate this result, further studies are required. This may include the growth of a series of films, as a function of thickness. Where magnetic and x-ray spectroscopy studies of these films should indicate whether the results obtained for the 50nm film in chapter 5 are a consequence of thickness and eliminate other possible causes of this effect, such as unintended variations in growth conditions etc. Maintaining the characteristic bulk magnetic properties, such as low coercivity, and magnetoelectric properties in thin film form will be crucial for future device applications of  $\text{SrCo}_2\text{Ti}_2\text{Fe}_8\text{O}_{19}$ . For example, electrically controlled magnetic data storage devices would require thicknesses typically of the order of several nanometres to maintain a high storage density [281], whilst maintaining a strong ME coupling; as such, it would be important to maintain the trigonal bipyramidal site Co doping. Ultimately, if the epitaxial nature of the thinner films could be combined with a larger amount of Co trigonal bipyramidal substitutions, the combined effect should result in an even greater ME coupling than previously observed, due to a larger net polarisation.

As a complementary method to the L-edge soft x-ray spectroscopy, x-ray spectroscopy measurements performed at the K-edge would allow for the extraction of Extended X-ray Absorption Fine Structure (EXAFS). Analysis of such element specific EXAFS measurements could provide the exact lattice sites of the Co and Ti substitutions, information which could result in a more detailed understanding of which lattice sites are preferentially occupied by the dopants within the M-type structure. Additionally, EXAFS analysis can provide experimental values of the interatomic distances. These values at the trigonal bipyramidal sites could then be used to verify the simulations performed in chapter 7, showing that the Co and Ti substitutions to the 2b and 12k sites adjust the structure in such a way as to increase the stability of a lattice induced electric polarisation. This work has shown that Co substitutions to the trigonal bipyramidal sites act to enhance the magnetoelectric coupling via this mechanism, however, it is seen by experiment that only a proportion of the Co are substituted to the 2b sites. One would intuitively expect that the ME coupling would be maximised if all the Co could be substituted to these sites. A worthwhile pursuit would then be to investigate ways of increasing the proportion of trigonal bipyramidal Co within the M-type hexaferrite structure. It may be possible to achieve this using the ATLAD thin film growth technique, with target compositions tailored to force all of the Co into the R-block, in which the 2b trigonal bipyramidal site resides.

The mechanism for improper ferroelectricity in these M-type hexaferrites is not yet fully understood. In light of this, further studies should be performed with the aid of neutron diffraction measurements, to determine the magnetic structures within  $\text{SrCo}_2\text{Ti}_2\text{Fe}_8\text{O}_{19}$  samples. These measurements would provide information on the forms of conical magnetic structure present, with temperature dependent measurements revealing the magnetic transitions and their critical temperatures. This technique could correlate the turning points seen in the  $M(T)$  measurements to

magnetic phase transitions, a step crucial for understanding the improper ferroelectricity driven magnetoelectric coupling mechanism. It is still unclear whether this mechanism is present within the M-type structure as most studies have suggested conical structures without a cycloidal component [105] [6]. An alternative ME coupling mechanism, in the form of a lattice induced polarisation at the Co doped 2b sites, has been reported in this work, however, it is possible that both mechanisms exist simultaneously, if the magnetic structure includes a transverse conical component. An additional step may also be to investigate the effect of different Co and Ti doping sites on the magnetic structure, via this method. Neutron diffraction measurements were not possible, for the thin films studied here in, due to their polycrystalline nature, however, the growth of single crystal  $\text{SrCo}_2\text{Ti}_2\text{Fe}_8\text{O}_{19}$  samples are planned specifically for neutron diffraction studies.

Lastly, as a further way to optimise the ME coupling within  $\text{SrCo}_2\text{Ti}_2\text{Fe}_8\text{O}_{19}$  films, the  $\text{Fe}^{2+}$  content should be reduced. It was observed via XMCD that all the films studied had a proportion of octahedral  $\text{Fe}^{2+}$ , and it is expected that this can be reduced or removed through optimisation of the films growth and post-annealing conditions. The presence of the  $\text{Fe}^{2+}$  suggests that the films are under-oxidised; as such, it may be that the key parameter for its removal is the oxygen partial pressure, be it in growth or annealing. The  $\text{Fe}^{2+}$  is detrimental to the magnetoelectric effect as it provides a conductive pathway, due to polaronic hopping, suppressing electric polarisation, thus the removal of such would result in a larger ME coupling.

The key to achieving practical magnetoelectric device applications lies in the stabilisation of a large ME coupling at room temperature. The RT stability has already been achieved in  $\text{SrCo}_2\text{Ti}_2\text{Fe}_8\text{O}_{19}$ , however, increases in the ME coupling strength are still required before device applications are realised. One method for the enhancement of ME coupling has been demonstrated in this work, with Co trigonal site doping. Further optimisation of this coupling; be it due to epitaxial growth or the reduction of  $\text{Fe}^{2+}$  could open up the possibility of numerous practical applications. Such potential applications include; as spintronic tunnel junctions [3], multiferroic hard drives [2], RF filters and antennas [1]. Controlling magnetism by an applied electric field is a crucial prerequisite for creating ultra-low power, high density, MRAM. In this regard M-type hexaferrites are already widely used as data storage media [6], this combined with the discovered magnetoelectric properties in Co-Ti doped SrM, promotes them as a leading candidate for such applications.

## List of Abbreviations

MRAM	Magneto-resistive Random Access Memory
ME	Magnetoelectric
PLD	Pulsed Laser Deposition
ATLAD	Alternating Target Laser Ablation Deposition
UHV	Ultra-High Vacuum
XAS	X-ray Absorption Spectroscopy
XMCD	X-ray Magnetic Circular Dichroism
DFT	Density Functional Theory
GKA	Goodenough-Kanamori-Anderson
DM	Dzyaloshinskii-Moriya
PZT	Lead Zirconate Titanate
BTO	Barium Titanate
RT	Room Temperature
PMN-PT	Lead Magnesium Niobate – Lead Titanate
SrM	Strontium Ferrite
BaM	Barium Ferrite
O <sub>h</sub>	Octahedral
T <sub>d</sub>	Tetrahedral
FMR	Ferromagnetic Resonance
EXAFS	Extended X-ray Absorption Fine Structure
SEM	Scanning Electron Microscopy
EDX	Energy Dispersive X-ray
XRD	X-ray Diffraction
FWHM	Full Width at Half Maximum
XRR	X-ray Reflectivity
VSM	Vibrating Sample Magnetometer
SQUID	Superconducting Quantum Interference Device
ZFC	Zero Field Cooled
FC	Field Cooled
RF	Radio Frequency
CPW	Co-planar Waveguide
RCP	Right hand Circular Polarised
LCP	Left hand Circular Polarised
FY	Fluorescence Yield
TEY	Total electron Yield
Nd:YAG	Neodymium-doped: Yttrium Aluminium Garnet
UV	Ultra-Violet
RHEED	Reflection High Energy Electron Diffraction
MFC	Mass Flow Controller
GGA	General Gradient Approximation
PBE	Perdew-Burke-Ernserhof

## References

- [1] C. A. F. Vaz, "Electric field control of magnetism in multiferroic hetrostructures," *J.Phys.Condens.Matt.*, vol. 24, 333201, 2012.
- [2] M. Opel, "Spintronic Oxides Grown by Laser MBE," *J.Phys.D*, vol. 45, pp 1-57. 2012.
- [3] L. Bocher *et al*, "Atomic and Electronic Structure of the BaTiO<sub>3</sub>/Fe Interface in Multiferroic Tunnel Junctions," *Nano. Lett.*, vol. 12, pp. 376-382, 2012.
- [4] T. A. Ostler *et al*, "Strain Induced Vortex Core Switching in Planar Magnetostrictive Nanostructures," *Phys. Rev. Lett.*, vol. 115, 067202, 2015.
- [5] Y. Kitagawa *et al*, "Low-field magnetoelectric effect at room temperature," *Nature Materials*, vol. 9, pp. 797-802, 2010.
- [6] R. C. Pullar, "Hexagonal Ferrites: A Review of the Synthesis, Properties and Applications of Hexaferrite Ceramics," *Progress in Materials Science*, vol. 57, no. 7, pp. 1191-1334, 2012.
- [7] T. Kimura *et al*, "Electric Polarization Rotation in a Hexaferrite with Long-Wavelength Magnetic Structures," *Phys. Rev. Lett.*, vol. 94, 137201, 2005.
- [8] T. Kimura *et al*, "Magnetic and magnetoelectric properties of Ba<sub>2-x</sub>Sr<sub>x</sub>Ni<sub>2</sub>Fe<sub>12</sub>O<sub>22</sub>Ba<sub>2-x</sub>Sr<sub>x</sub>Ni<sub>2</sub>Fe<sub>12</sub>O<sub>22</sub> single crystals with Y-type hexaferrite structure," *J. Appl. Phys*, vol. 110, no. 3, 033920, 2011.
- [9] T. Kimura *et al*, "Magnetism and magnetoelectricity of a U-type hexaferrite Sr<sub>4</sub>Co<sub>2</sub>Fe<sub>36</sub>O<sub>60</sub>," *Appl. Phys. Lett.*, vol. 98, no. 21, 212504, 2011.
- [10] L. Wang *et al*, "Electric control of magnetism at room temperature," *Sci. Rep.*, vol. 2, no. 223, 10.1038, 2012.
- [11] P. W. Anderson, "New Approach to the Theory of Superexchange Interactions," *Phys. Rev.*, vol. 115, no. 2, pp. 2-13, 1959.
- [12] T. Kimura, "Magnetoelectric Hexaferrites," *Annu. Rev. Condens. Matter Phys.*, vol. 3, pp. 93-110, 2011.
- [13] K. Ebnabbasi and C. Vittoria, "Converse magnetoelectric experiments on a room-temperature spirally ordered hexaferrite," *Phys. Rev. B*, vol. 86, 024430, 2012.
- [14] S. P. Shen, Y. S. Chai, J. Z. Cong, P. J. Sun, J. Lu, L. Q. Yan, S. G. Wang and Y. Sun, "Magnetic-ion-induced displacive electric polrization in FeO<sub>5</sub> bipyramidal units of (Ba, Sr)Fe<sub>12</sub>O<sub>19</sub> hexaferrites," *Phys. Rev. B*, vol. 90, 180404, 2014.
- [15] J. Kreisel *et al*, "An investigation of the magnetic anisotropy change in BaFe<sub>12-2x</sub>Ti<sub>x</sub>Co<sub>x</sub>O<sub>19</sub> single crystals," *J. Magn. Magn. Matter*, vol. 224, pp. 17-29, 2001.
- [16] D. Blank, M. Dekkers and G. Rijnders, "Pulsed laser deposition in Twente: from research tool towards industrial deposition," *J. Phys. D: Appl. Phys.*, vol. 47, 034006, 2014.
- [17] P. Dorsey, S. E. Bushnell, R. G. Seed and C. Vittoria, "Magnetic and Structural Characteristics of Pulsed Laser Deposited Epitaxial Y<sub>3</sub>Fe<sub>5</sub>O<sub>12</sub> Films," *IEEE Transactions on Magnetics*, vol. 29, no. 6, pp. 3069-3071, 1993.
- [18] G. Eres and H. Christen, "Recent Advances in Pulsed Laser Deposition of Complex Oxides," *J.Phys.Cond.Matt*, vol. 20, 264005, 2008.
- [19] P. Willmott and J. Huber, "Pulsed Laser Vapourisation and Deposition," *Rev. Mod. Phys.*, vol. 72, pp. 315-328, 2000.
- [20] P. C. Dorsey *et al*, "Oriented Barium Hexaferrite Thick Films Grown on C-plane and M-plane Sapphire Substrates," *IEEE Transactions on Magnetics*, vol. 30, no. 6, pp. 4512-4517, 1994.
- [21] A. L. Geiler *et al*, "BaFe<sub>12</sub>O<sub>19</sub> thin films grown at the atomic scale from BaFe<sub>2</sub>O<sub>4</sub> and alpha-Fe<sub>2</sub>O<sub>3</sub> targets," *Appl. Phys. Lett.*, vol. 91, 1062510, 2007.
- [22] R. Eason, Pulsed Laser Deposition of Thin Films, John Wiley & Sons, Inc., 2007.

- [23] M. Zentkova *et al*, "Preparation and physical properties of M-type hexaferrite  $\text{SrCo}_2\text{Ti}_2\text{Fe}_8\text{O}_{19}$ ," *Ferroelectrics*, vol. 499, pp. 1-8, 2016.
- [24] M. Mohebbi, K. Ebnabbassi and C. Vittoria, "First observation of magnetoelectric effect in M-type hexaferrite thin films," *J. Appl. Phys.*, vol. 113, 17C710, 2013.
- [25] K. Matsuzaki *et al*, " $\text{Fe}_3\text{O}_4(111)$  thin films with bulk-like properties: growth and atomic characterization," *J. Phys. D: Appl. Phys.*, vol. 46, 022001, 2013.
- [26] S. P. Marshall and J. B. Sokoloff, "Phonon Spectrum for Barium Ferrite," *Phys. Rev. B*, vol. 44, no. 2, pp. 619-627, 1991.
- [27] C. Ederer and N. Spaldin, "Weak ferromagnetism and magnetoelectric coupling in bismuth ferrite," *Phys. Rev. B*, vol. 71, 060401, 2005.
- [28] T. Kimura *et al*, "Magnetic control of ferroelectric polarization," *Nature*, vol. 426, pp. 55-58, 2003.
- [29] N. A. Spaldin and M. Fiebig, "The renaissance of Magnetoelectric Multiferroics," *Science*, vol. 309, pp. 391-392, 2005.
- [30] D. Jiles, Introduction to magnetism and magnetic materials (Third Edition), London: CRC Press, 2015.
- [31] A. Rae, Quantum mechanics, Taylor & Francis, 2008.
- [32] K. M. Krishnan, Fundamentals and Applications of Magnetic Materials, Oxford: Oxford University Press, 2016.
- [33] S. Blundell, Magnetism in Condensed Matter, Oxford: Oxford University Press, 2001.
- [34] K. D. Sattler, Handbook of nanophysics: principles and methods, Boca Raton: CRC Press, 2010.
- [35] V. Z. Paes and D. H. Mosca, "Effective elastic and magnetoelastic anisotropies for thin films with hexagonal and cubic crystal structures," *Journal of Magnetism and Magnetic Materials*, vol. 330, pp. 81-87, 2013.
- [36] R. kajimoto *et al*, "C-type antiferromagnetic ordering in the single-layered manganite  $\text{Nd}_{0.22}\text{Sr}_{1.78}\text{MnO}_4$ ," *Physica B: Condensed Matter*, vol. 312, pp. 760-762, 2002.
- [37] G. F. Dionne, Magnetic Oxides, Springer, 2009.
- [38] M. S. I. S. Suzuki, "Lecture note on solid state physics," *Department of Physics, State University of New York at Binghamton*, may 2009.
- [39] S. V. Streltsov and D. I. Khomskii, "Orbital physics in transition metal compounds: new trends," *Physics-Uspexhi*, vol. 60, no. 11, pp. 1121-1146, 27.
- [40] L. I. Koroleva and L. P. Mitina, "The Antisymmetric Spin-Coupling in Hexagonal Ferrites," *phys. stat. sol.*, vol. 5, pp. 55-60, 1971.
- [41] T. Moriya, "Anisotropic Superexchange Interaction and Weak Ferromagnetism," *Phys. Rev.*, vol. 120, pp. 91-98, 1960.
- [42] M. Lines and A. Glass, Principles and Applications of Ferroelectrics and Related Materials, Oxford University Press, 1977.
- [43] C. Kittel, Introduction to Solid State physics (7th Edition), New York: Wiley & sons, 1996.
- [44] R. W. Whatmore, "Piezoelectric and Pyroelectric Materials and Their Applications," in *Electronic Materials*, Boston MA, Springer, pp. 283-290, 1991.
- [45] L. Martin, Y.-H. Chu and R. Ramesh, "Advances in the growth and characterisation of magnetic, ferroelectric and multiferroic oxide thin films," *Matl. Sci. Eng. R*, vol. 68, pp. 89-133, 2010.
- [46] E. Zolotoyabko, Basic concepts of crystallography, Wiley-VCH, 2011.

- [47] V. Sundar and R. E. Newnham, "Electrostriction and Polarisation," *Ferroelectrics*, vol. 135, pp. 443-446, 1992.
- [48] J. Li *et al*, "Molecular ferroelectrics: where electronics meet biology," *Phys. Chem. Chem. Phys.*, vol. 15, pp. 20786-20796, 2013.
- [49] A. J. Moulson and J. M. Herbert, "Piezoelectric Ceramics," in *Electroceramics: Materials, Properties, Applications*, London, Chapman and Hall, pp. 265-317, 1990.
- [50] T. Kimura and Y. Tokura, "Magnetoelectric phase control in a magnetic system showing cycloidal/conical spin order," *J. Phys.: Condens. Matter*, vol. 20, 434204, 2008.
- [51] C. Jia *et al*, "Bond electronic polarization induced by spin," *Phys. rev. B*, vol. 74, 224444, 2006.
- [52] C. Jia *et al*, "Microscopic theory of spin-polarization coupling in multiferroic transition metal oxides," *Phys. Rev. B*, vol. 76, 144424, 2007.
- [53] H. Katsura, N. Nagaosa and V. Balatsky, "Spin Current and Magnetoelectric Effect in Noncollinear Magnets," *Phys. Rev. Lett.*, vol. 95, 057205, 2005.
- [54] Y. Wang, J. Hu, Y. Lin and C.-W. Nan, "Multiferroic and magnetoelectric composite nanostructures," *NPG Asia Mater.*, vol. 2, no. 2, pp. 61-68, 2010.
- [55] W. Eerenstein, "Multiferroic and magnetoelectric materials," *Nature*, vol. 442, pp. 759-765, 2006.
- [56] L. W. Martin *et al*, "Multiferroics and magnetoelectrics: thin films and nanostructures," *J. Phys.: Condens. Matter*, vol. 20, 434220, 2008.
- [57] C. Vittoria, S. Somu and A. Widom, "Tensor properties of the magnetoelectric coupling in hexaferrites," *Phys. Rev. B*, vol. 89, no. 13, 134413, 2014.
- [58] W. F. Brown, R. M. Hornreich and S. Shtrikman, "Upper Bound on the Magnetoelectric Susceptibility," *Phys. Rev.*, vol. 168, no. 2, pp. 574-577, 1968.
- [59] J. Lou *et al*, "Equivalence of direct and converse magnetoelectric coefficients in strain-coupled two-phase systems," *Appl. Phys. Lett.*, vol. 100, 102907, 2012.
- [60] K. Ebnabbasi, M. Mohebbi and C. Vittoria, "Strong magnetoelectric coupling in hexaferrites at room temperature," *J. Appl. Phys.*, vol. 113, 17C707, 2013.
- [61] J. J. Yang *et al*, "Electric field manipulation of magnetization at room temperature in multiferroic  $\text{CoFe}_2\text{O}_4$  /  $\text{Pb}(\text{Mg}_{1/3}\text{Nb}_{2/3})_{0.7}\text{Ti}_{0.3}\text{O}_3\text{CoFe}_2\text{O}_4$  /  $\text{Pb}(\text{Mg}_{1/3}\text{Nb}_{2/3})_{0.7}\text{Ti}_{0.3}\text{O}_3$  heterostructures," *Appl. Phys. Lett.*, vol. 94, 212504, 2009.
- [62] C. W. Nan *et al*, "Multiferroic magnetoelectric composites: Historical perspective, status and future directions," *J. Appl. Phys.*, vol. 103, 031101, 2008.
- [63] M. Bichurin, V. Petrov and G. Srinivasan, "Theory of low-frequency magnetoelectric coupling in magnetorstrictive-piezoelectric bilayers," *Phys. Rev. B.*, vol. 68, 054402, 2003.
- [64] H. Zheng, J. Wang, L. Mohaddes-Ardabili, M. Wuttig and L. Salamanca-Riba, "Three-dimensional heteroepitaxy in self-assembled  $\text{BaTiO}_3$  -  $\text{CoFe}_2\text{O}_4$ ," *Appl. Phys. Lett.*, vol. 85, pp. 2035-2037, 2004.
- [65] J. M. Rondinelli *et al*, "Carrier-mediated magnetoelectricity in complex oxide heterostructures," *Nature Nanotechnology*, vol. 3, pp. 46-50, 2008.
- [66] W. Eerenstein, M. Wiora, J. L. Prieto, J. F. Scott and N. D. Mathuri, "Giant sharp and persistent converse magnetoelectric effects in multiferroic epitaxial heterostructures," *Nature Materials*, vol. 6, pp. 348-351, 2007.
- [67] E. A. Castel, "Magnetic field dependence of the effective permittivity in  $\text{BaTiO}_3$  /Ni," *Appl Phys Lett*, vol. 92, 233110, 2008.
- [68] S. Geprags *et al*, "Electric field controlled manipulation of the magnetization in Ni/ $\text{BaTiO}_3$ /Ni/ $\text{BaTiO}_3$  hybrid structures," *Appl. Phys. Lett.*, vol. 96, 142509, 2010.

- [69] E. A. Parkes, "Voltage controlled modification of flux closure domains in planar magnetic," *Appl Phys Lett*, vol. 105, 062405, 2014.
- [70] J. Ryu *et al*, "Magnetoelectric properties in piezoelectric and magnetostrictive laminate composites," *Jpn. J. Appl. Phys.*, vol. 40, pp. 4948-4951, 2001.
- [71] T. R. Paudel *et al*, "Intrinsic defects in Multiferroic BiFeO<sub>3</sub> and their effect on Magnetism," *Phys. Rev. B*, vol. 85, pp. 1-8, 2012.
- [72] J. Wang *et al*, "Epitaxial BiFeO<sub>3</sub> multiferroic thin film heterostructures," *Science*, vol. 299, pp. 1719-1722, 2003.
- [73] M. Angst *et al*, "Charge ordering in LuFe<sub>2</sub>O<sub>4</sub>: Antiferroelectric ground state and coupling to Magnetism," *Phys. Rev. Lett*, vol. 101, 227601, 2008.
- [74] A. Stucky *et al*, "Shinning light on CuO for exploring high T<sub>c</sub> multiferroics," *J. Phys. Conf. Ser.*, vol. 556, 012012, 2014.
- [75] Z. Wang *et al*, "Magnetoelectric effect and phase transitions in CuO in external magnetic fields," *Nature Communications*, vol. 7, 10295, 2016.
- [76] D. M. Evans *et al*, "Magnetic switching of ferroelectric domains at room temperature in multiferroic PZTFT," *Nat. Commun.*, vol. 4, p. 1534, 2013.
- [77] G. K. Thompson and S. J. Evans, "The structure-property relationships in M-type hexaferrites: Hyperfine interactions and bulk magnetic properties," *J. Appl. Phys.*, vol. 73, pp. 6295-6297, 1993.
- [78] L. P. Koroleva and L. I. Mitina, "The Antisymmetric Spin-Coupling in Hexagonal Ferrites," *phys. stat. sol.*, Vols. (a) 5, pp. 55-60, 1971.
- [79] M. Mohebbi, K. Ebnabbi and C. Vittoria, "In-situ deposition of c-axis oriented Barium Ferrite films for Microwave applications," *IEEE Transactions on Magnetics*, vol. 49, no. 7, pp. 4207-4209, 2013.
- [80] J. Smit and H. P. Wijn, Ferrites, Eindhoven: Philips Technical Library, 1959.
- [81] J. J. Went *et al*, "Ferroxdure, A Class of New Permanent Magnet Materials," *Philips Technical Review*, vol. 13, p. 194, 1952.
- [82] A. T. Wise *et al*, "M-type barium hexaferrite synthesis and characterisation for phase shifter applications," *J. Appl. Phys.*, vol. 109, 07E535, 2011.
- [83] M. Soda *et al*, "Magnetic Ordering in Relation to the Room-Temperature Magnetoelectric Effect of Sr<sub>3</sub>Co<sub>2</sub>Fe<sub>24</sub>O<sub>41</sub>," *Phys. Rev. Lett.*, vol. 106, no. 8, 087201, 2011.
- [84] O. Kubo *et al*, "Properties of Ba ferrite particles for perpendicular magnetic recording media," *IEEE Trans. Magn. Magn.*, vol. 18, no. 6, pp. 1122-1124, 1982.
- [85] H. Kojima, "Chapter 5 Fundamental properties of hexagonal ferrites with magnetoplumbite structure," in *Handbook of Ferromagnetic Materials: vol 3*, Amsterdam, North-Holland Physics Publishing, pp. 305-391, 1982.
- [86] M. V. Cabanas *et al*, "The Solid Solution BaFe<sub>12-x</sub>Co<sub>x</sub>Ti<sub>x</sub>O<sub>19</sub> (0<x<6): Cationic Distribution by Neutron Diffraction," *Journal of solid State Chemistry*, vol. 111, pp. 229-237, 1994.
- [87] M. Feng *et al*, "Exchange Integrals in Magnetoelectric Hexaferrite (SrCo<sub>2</sub>Ti<sub>2</sub>Fe<sub>8</sub>O<sub>19</sub>): A density functional study," *J. Appl. Phys.*, vol. 115, 17D908, 2014.
- [88] G. B. Teh *et al*, "A study of magnetoplumbite-type (M-type) cobalt-titanium substituted barium ferrite BaCo<sub>x</sub>Ti<sub>x</sub>Fe<sub>12-2x</sub>O<sub>19</sub> (x=1-6)," *Materials Chemistry and Physics*, vol. 105, pp. 253-259, 2007.
- [89] X. Battle *et al*, "Cation distribution and intrinsic magnetic properties of Co-Ti doped M-type barium ferrite," *J. Appl. phys.*, vol. 70, no. 3, pp. 1614-1623, 1991.
- [90] M. V. Rane *et al*, "Characterization of BaFe<sub>12-2x</sub>Co<sub>x</sub>Zr<sub>x</sub>O<sub>19</sub> (0 ≤ x ≤ 0.5) synthesised by citrate gel precursor route," *J. Magn. Magn. Mater.*, vol. 153, pp. 1-4, 1996.

- [91] C. S. Wang *et al*, "Structure and magnetic properties of Zn–Ti-substituted Ba-ferrite particles for magnetic recording," *Journal of Magnetism and Magnetic Materials*, vol. 183, no. 1, pp. 241-246, 1998.
- [92] X. Z. Zhou *et al*, "Co-Sn substituted barium ferrite particles," *J. Appl. Phys.*, vol. 75, p. 5556, 1994.
- [93] V. G. Harris *et al*, "Large-scale chemical synthesis of shape and size controlled  $\text{BaFe}_{12-x}\text{Sc}_x\text{O}_{19}$  platelets for in-plane oriented thick screen printed films," *J. Appl. Phys*, vol. 103, 07E515, 2008.
- [94] C. Vittoria *et al*, "Magnetic and microwave properties of basal-plane oriented  $\text{BaFe}_{11}\text{In}_1\text{O}_{19}$  ferrite thick films processed by screen printing," *J. Appl. Phys*, vol. 103, 07F710, 2008.
- [95] S. H. Chun *et al*, "Realisation of giant magnetoelectricity in helimagnets," *Phys. Rev. Lett.*, vol. 104, 037204, 2010.
- [96] Y. S. Chai, "Electrical control of large magnetisation reversal in a helimagnet," *Nature Communications*, vol. 5, p. 4208, 2014.
- [97] K. Taniguchi *et al*, "Ferroelectric Polarization Reversal by a Magnetic Field in Multiferroic Y-type Hexaferrite  $\text{Ba}_2\text{Mg}_2\text{Fe}_{12}\text{O}_{22}$ ," *Appl. Phys. Express*, vol. 1, 031301, 2008.
- [98] S. P. Shen *et al*, "Nonvolatile electric field control of magnetization in a Y-type hexaferrite," *Sci. Rep.*, vol. 5, p. 8254, 2015.
- [99] R. C. Pullar and A. K. Bhattacharya, "The synthesis and characterization of the hexagonal Z ferrite,  $\text{Sr}_3\text{Co}_2\text{Fe}_{24}\text{O}_{41}$ , from a sol-gel precursor," *Mater. Res. Bull.*, vol. 36, pp. 1531-1538, 2001.
- [100] K. Ebnabbasi *et al*, "Magneotelectric effects on Sr Z-type hexaferrite at room temperature," *J. Appl. Phys.*, vol. 111, 07C719, 2012.
- [101] K. Ebnabbasi *et al*, "Magnetoelectric effects at microwave frequencies on Z-type hexaferrite," *Appl. Phys. Lett.*, vol. 101, 062406, 2012.
- [102] K. Ebnabbasi, M. Mohebbi and C. Vittoria, "Room Temperature magnetoelectric effects in bulk poly-crystalline materials of M- and Z-type hexaferrites," *J. Appl. Phys*, vol. 113, 17C703, 2012.
- [103] X. Wang *et al*, "Giant magnetoresistance due to magnetoelectric currents in  $\text{Sr}_3\text{Co}_2\text{Fe}_{24}\text{O}_{41}$  hexaferrites," *Appl. Phys. Lett.*, vol. 105, 112408, 2014.
- [104] K. Okumura *et al*, "Magnetism and magnetoelectricity of a U-type hexaferrite  $\text{Sr}_4\text{Co}_2\text{Fe}_{36}\text{O}_{60}$ ," *Appl. Phys. Lett.*, vol. 98, 212504, 2011.
- [105] Y. E. A. Tokunaga, "Multiferroic M-Type Hexaferrites with a Room-Temperature Conical State and Magnetically Controllable Spin Helicity," *Phys. Rev. Lett*, vol. 105, 257201, 2010.
- [106] M. Mihalik *et al*, "The magnetic Properties of Single Crystal  $\text{SrCo}_2\text{Ti}_2\text{Fe}_8\text{O}_{19}$  Compound," *20th International conference on Magnetism*, vol. 75, pp. 259-265, 2015.
- [107] H. Izadkhah *et al*, "Effects of cobalt substitutions on the magnetoelectric coupling of M-type hexaferrite films," *Appl. Phys. Lett*, vol. 106, 142905, 2015.
- [108] S. Zare, H. Izadkhah and C. Vittoria, "Deposition of magnetoelectric hexaferrite thin films on substrates of silicon," *Journal of Magnetism and Magnetic Materials*, vol. 420, pp. 245-248, 2016.
- [109] S. Zare *et al*, "Magnetoelectric hexaferrite thin film growth on oxide conductive layer for applications at low voltages," *Journal of Magnetism and Magnetic Materials*, vol. 412, pp. 255-258, 2016.
- [110] R. D. Shannon, "Revised effective ionic radii and systematic studies of interatomic distances in halides and chalcogenides," *Acta Crystallogr. A*, vol. 32, pp. 751-767, 1976.

- [111] K. K. Mallick, P. Shepherd and R. J. Green, "Magnetic properties of cobalt substituted M-type barium hexaferrite prepared by co-precipitation," *Journal of Magnetism and Magnetic Materials*, vol. 312, pp. 418-429, 2007.
- [112] M. Cernea *et al*, "Magnetic properties of  $\text{Ba}_x\text{Sr}_{1-x}\text{Fe}_{12}\text{O}_{19}$  ferrites prepared by different methods," *Journal of Alloys and Compounds*, vol. 561, pp. 121-128, 2013.
- [113] P. A. Marino-Castellanos *et al*, "Structural and magnetic study of the  $\text{Ti}^{4+}$  doped barium hexaferrite ceramic samples: theoretical and experimental results," *Physica B*, vol. 406, pp. 3130-3136, 2011.
- [114] X. Sui *et al*, "Microstructural origin of the perpendicular anisotropy in M-type barium hexaferrite thin films deposited by RF magnetron sputtering," *IEEE Transactions on Magnetics*, vol. 29, no. 6, pp. 3751-3753, 1993.
- [115] H. Liu *et al*, "Epitaxial relationship of MBE grown barium hexaferrite (0001) films on sapphire (0001)," *Journal of Crystal Growth*, vol. 312, pp. 671-675, 2010.
- [116] Y. S. Kim *et al*, "Sr flux stability against oxidation in oxide-MBE environment: flux, geometry, and pressure dependence," *J. Vac. Sci. Technol. A*, vol. 28, no. 2, p. 271, 2010.
- [117] X. Zhiyong *et al*, "Properties of Ba-hexaferrite thin films with different thicknesses," *Applied Surface Science*, vol. 271, pp. 362-368, 2013.
- [118] T. L. Hylton, M. A. Parker and K. R. Coffey, "Properties of epitaxial Ba-hexaferrite thin films on A-, R-, and C-plane oriented sapphire substrates," *J. Appl. Phys*, vol. 73, no. 10, pp. 6257-6259, 1993.
- [119] F. Huang *et al*, "Oxygen Pressure Dependence of Laser Deposited Barium Ferrite Films on  $\text{LiCoO}_2(111)$ ," *IEEE Transactions on Magnetics*, vol. 31, no. 6, pp. 3826-3828, 1995.
- [120] Z. Y. Guo, W. L. Zhang, H. Ji *et al*, "Influence of substrate temperature on the texture of barium ferrite film by magnetron sputtering," *Appl. Surf. Sci*, vol. 255, no. 8, pp. 4443-4445, 2009.
- [121] S. Capraro, J. P. Chatelon, H. Joisten *et al*, "Magnetic properties of sputtered barium ferrite thick films," *J. Appl. Phys*, vol. 93, no. 12, pp. 9898-9901, 2003.
- [122] A. L. Geiler *et al*, "Atomic Scale Design and Control of Cation Distribution in Hexagonal Ferrites," *Phys. Rev. Lett*, vol. 101, 067201, 2008.
- [123] G. Hubler and D. Christey, *Pulsed Laser Deposition of Thin Films*, Wiley, 1994.
- [124] H. Christen *et al*, "Pulsed Electron Deposition of Fluorine based precursors for  $\text{YBa}_2\text{Cu}_3\text{O}_{(7-x)}$  coated conductors," *Supercond. Sci. Tech.*, vol. 18, pp. 1168-1175, 2005.
- [125] G. Ehrlich and F. Hudda, "Atomic View of Surface Self Diffusion," *J. Chem. Phys.*, vol. 44, no. 3, p. 1039, 1966.
- [126] J. Amar, F. Family and P.-M. Lam, "Dynamic scaling of the island size distribution and percolation in a model of submonolayer MBE," *Phys. Rev. B*, vol. 50, pp. 8781-8797, 1994.
- [127] R. W. Eason *et al*, "Multi-beam pulsed laser deposition for advanced thin-film optical waveguides," *Journal of Physics D: Applied Physics*, vol. 47, no. 3, 034007, 2014.
- [128] C. Vittoria, "Fabrication of ferrite films using laser deposition". US Patent 5,227,204, 27 August 1991.
- [129] C. A. Carosella *et al*, "Pulsed laser deposition of epitaxial  $\text{BaFePO}_4$  thin films," *J. Appl. Phys.*, vol. 71, no. 10, pp. 5107-5110, 1992.
- [130] Y. Y. Song *et al*, "Optimized pulsed laser deposited barium ferrite thin films with narrow ferromagnetic resonance linewidths," *J. Appl. Phys.*, vol. 94, no. 8, pp. 5103-5110, 2003.
- [131] X. H. Liu *et al*, "Barium ferrite ( $\text{BaFe}_{12}\text{O}_{19}$ ) thin films prepared by pulsed laser deposition on MgO buffered Si substrates," *Appl. Phys. A*, vol. 80, no. 3, pp. 611-614, 2005.

- [132] Z. Chen *et al*, "Structure and Magnetism of Ba-Hexaferrite Films Grown on Single Crystal 6-H SiC With Graduated Interfacial MgO Buffer Layers," *IEEE Transactions on Magnetism*, vol. 42, no. 10, pp. 2855-2857, 2006.
- [133] M. Khaleeq-ur-Rahman *et al*, "Deposition and characterization of strontium hexaferrite (SrFe<sub>12</sub>O<sub>19</sub>) by PLD technique," *Optics and Laser Technology*, vol. 47, pp. 361-365, 2013.
- [134] S. A. Oliver *et al*, "Properties of pulsed laser deposited scandium-doped barium hexaferrite films," *J. Appl. Phys.*, vol. 85, no. 8, pp. 4630-4632, 1999.
- [135] P. Papakonstantinou *et al*, "Co-Ti substituted Ba-ferrite films prepared by pulsed laser deposition," *J. Magn. Soc. Jpn.*, vol. 19, pp. 177-180, 1995.
- [136] A. L. Geiler *et al*, "Epitaxial growth of PbFe<sub>12</sub>O<sub>19</sub> thin fillms by alternating target laser ablation deposition of Fe<sub>2</sub>O<sub>3</sub> and PbO," *J. Appl. Phys.*, vol. 101, 09M510, 2007.
- [137] A. L. Geiler *et al*, "Alternating target laser ablation deposition of high quality barium hexaferrite thin films from barium monoferrite and hematite targets," *J. Appl. Phys.*, vol. 103, 07B914, 2008.
- [138] J. Goldstein *et al*, *Scanning Electron Microscopy and X-Ray Microanalysis: A Text for Biologists, Materials Scientists, and Geologists*, Springer, 2012.
- [139] C. Hammond, "X-ray diffraction:Contributions of Laue and Bragg," in *The Basics of Crystallography and Diffraction (Third Edition)*, Oxford University Press, pp. 194-202, 2009.
- [140] M. Yasaka *et al*, "X-ray thin film measurement techniques," *The Rigaku Journal*, vol. 26, no. 2, pp. 10-15, 2010.
- [141] R. B. Roof, "INDX, X-Ray Diffraction Powder Pattern Indexing, Trial Unit Cell Testing," *Organisation for Economic Co-Operation and Development, Nuclear Energy Agency*, vol. 41, no. 26, 1989.
- [142] C. Hammond , "Describing lattice planes and directions in crystals," in *The Basics of Crystallography and Diffraction (Third Edition)*, Oxford University Press, 2009, pp. 131-149.
- [143] G. S. Parkinson, "Iron Oxide Surfaces," *Surface Science Reports*, vol. 71, pp. 272-365, 2016.
- [144] C. Hammond, "The Diffraction of X-rays," in *The Basics of Crystallography and Diffraction (3rd Edition)*, Oxford, Oxford University Press, 2009, pp. 215-240.
- [145] J. Divalent and A. Gibaud, "Specular Reflectivity form Smooth and Rough surfaces," in *X-ray and Neutron Reflectivity: Principles and Applications*, Berlin, Springer, 2009, pp. 85-131.
- [146] H. Kiessig, "Interferenz von Röntgenstrahlen an dünnen Schichten," *Ann. Phys.*, vol. 402, no. 7, pp. 715-768, 1931.
- [147] Rigaku. software, *Integrated Thin Film Analysis Software GlobalFit (Reflectivity Analysis)*, vol. 26, USA: Rigaku Corp, 2010, pp. 28-29.
- [148] M. Bjorck and G. Andersson, "GenX: an extensible X-ray reflectivity refinement program utilizing differential evolution," *J. Appl. Cryst.*, vol. 40, pp. 1174-1178, 2007.
- [149] S. K. Sinha *et al*, "X-ray and neutron scattering from rough surfaces," *Phys. Rev. B*, vol. 38, no. 4, pp. 2297-2311, 1988.
- [150] K. Seo *et al*, "X-Ray Pole Figure Analysis on Fiber Textured Epitaxial Niobium Films for SRF Cavities," *Proceedings of SRF2009*, vol. TUPPO080, pp. 418-421, 2009.
- [151] J. P. Glusker and K. N. Trueblood, *Crystal Structure Analysis*, New York: Oxford University Press, 1985.
- [152] W. Kim *et al*, "A new method for the identification and quantification of magnetite–maghemite mixture using conventional X-ray diffraction technique," *Talanta*, vol. 94, pp. 343-352, 2012.
- [153] M. M. Can *et al*, "Effect of milling time on the synthesis of magnetite nanoparticles by wet milling," *Materials Science and Engineering B*, vol. 172, pp. 72-75, 2010.

- [154] F. Dubois *et al*, "Raman mapping of corrosion products formed onto spring steels during salt spray experiments. A correlation between the scale composition and the corrosion resistance," *Corrosion Science*, vol. 50, pp. 3401-3409, 2008.
- [155] C. Kittel, "Phonons I: Crystal Vibrations," in *Introduction to Solid State Physics (Eighth Edition)*, John Wiley and sons, 2005, pp. 89-104.
- [156] J. S. Blakemore, "Chapter 2: Lattice Dynamics," in *Solid State Physics (Second Edition)*, Cambridge University Press, 1985, pp. 87-148.
- [157] R. S. Mulliken, "Report on Notation for the Spectra of Polyatomic Molecules," *The Journal of Chemical Physics*, vol. 23, no. 11, pp. 1997-2011, 1955.
- [158] F. A. Cotton, *Chemical Applications of Group Theory (Third Edition)*, New York: Wiley, 1990.
- [159] C. N. Banwell and E. M. McCash, "Raman Spectroscopy," in *Fundamentals of Molecular spectroscopy (Fourth Edition)*, London, McGraw-Hill, 1994, pp. 101-126.
- [160] P. A. Joy *et al*, "The relationship between field-cooled and zero-field-cooled susceptibilities of some ordered magnetic systems," *J. Phys. Condens. Matter*, vol. 10, pp. 11049-11054, 1998.
- [161] G. Woltersdorf, "3.2 Ferromagnetic Resonance," in *Spin-Pumping and Two-Magnon Scattering in Magnetic Multilayers*, Halle, Martin-Luther-Universität, 2001, pp. 46-55.
- [162] R. F. Soohoo, "Chapter 10: Ferromagnetic resonance," in *Magnetic Thin films*, New York, Harper and Row, 1965, pp. 184-204.
- [163] S. Beguhn *et al*, "A new highly sensitive broadband ferromagnetic resonance measurement system with lock-in detection," *Journal of Applied Physics*, vol. 111, no. 7, 07A503, 2012.
- [164] C. Kittel, "On the Theory of Ferromagnetic Resonance Absorption," *Physical Review*, vol. 73, no. 2, pp. 155-161, 1948.
- [165] C. Vittoria, "Phenomenological Theory," in *Magnetics, Dielectrics, and Wave Propagation with MATLAB Codes*, Boca Raton, CRC Press, 2011, pp. 167-228.
- [166] D. E. Sayers *et al*, "New Technique for Investigating Noncrystalline Structures: Fourier Analysis of the Extended X-Ray—Absorption Fine Structure," *Phys. Rev. Lett.*, vol. 27, no. 18, pp. 1204-1207, 1971.
- [167] G. Van Der Laan, "Applications of soft x-ray magnetic dichroism," *Journal of Physics: conference series*, vol. 430, 012127, 2013.
- [168] J. Yano and V. K. Yachandra, "X-ray absorption spectroscopy," *Photosynth. Res.*, vol. 102, pp. 241-254, 2009.
- [169] M. L. Baker *et al*, "K- and L-edge X-ray absorption spectroscopy (XAS) and resonant inelastic X-ray scattering (RIXS) determination of differential orbital covalency (DOC) of transition metal sites," *Coordination Chemistry Reviews*, vol. 345, pp. 182-208, 2017.
- [170] B. N. Figgis, *Introduction to Ligand Fields*, New York: Interscience Publishers, 1966.
- [171] H. A. Bethe, "Splitting of terms in crystals," *Annalen der Physik*, vol. 3, pp. 133-206, 1929.
- [172] G. Racah, "Theory of Complex Spectra. II," *Phys. Rev.*, vol. 62, no. 9, pp. 438-462, 1942.
- [173] T. M. Dunn, D. S. McClure and R. G. Pearson, *Some aspects of crystal field theory*, New York: Harper and Row, 1965.
- [174] B. D. Bhattacharyya, "Jahn-Teller Effect in the Ligand Field Theory of Trigonal Bipyramidal V<sup>4+</sup> Complexes," *Phys. Stat. Sol. b*, vol. 71, pp. 427-433, 1975.
- [175] M. E. Foglio and G. E. Barberis, "Study of Co<sup>2+</sup> in Different Crystal Field Environments," *Brazilian Journal of Physics*, vol. 36, no. 1A, pp. 40-54, 2006.
- [176] G. F. Dionne, "Crystal Electric Fields," in *Magnetic Oxides*, Springer, 2009, pp. 48-72.
- [177] G. Van der Laan *et al*, "Experimental proof of magnetic x-ray dichroism," *Phys. Rev. B*, vol. 34, no. 9, pp. 6529-6531, 1986.

- [178] B. T. Thole *et al*, "X-ray circular dichroism as a probe of orbital magnetization," *Phys. Rev. Lett.*, vol. 68, no. 12, pp. 1943-1946, 1992.
- [179] G. Van der Laan and A. I. Figueroa, "X-ray magnetic circular Dichroism - A versatile tool to study magnetism," *Co-ordination Chemistry Reviews*, vol. 277, pp. 95-129, 2014.
- [180] P. Berkvens *et al*, "Design and practices at four European synchrotron radiation facilities," *Radiation Measurements*, vol. 41, no. 2, pp. 200-205, 2006.
- [181] D. H. Bilderback, P. Elleaume and E. Weckert, "Review of third and next generation synchrotron light sources," *J. Phys. B: At. Mol. Opt. Phys.*, vol. 38, pp. 773-797, 2005.
- [182] N. A. Dyson, "Experimental techniques for the study of x-rays," in *X-rays in atomic and nuclear physics*, London, Longman, 1973, pp. 180-196.
- [183] E. Stavitski and F. M. F. de Groot, "The CTM4XAS program for EELS and XAS spectral shape analysis of transition metal L edges," *Micron*, vol. 41, pp. 687-694, 2010.
- [184] R. D. Cowan, *The Theory of Atomic Structure and Spectra*, Berkeley: University of California Press, 1981.
- [185] P. Carra *et al*, "X-ray circular dichroism and local magnetic fields," *Phys. Rev. Lett.*, vol. 70, no. 5, pp. 694-697, 1993.
- [186] C. T. Chen *et al*, "Experimental Confirmation of the X-Ray Magnetic Circular Dichroism Sum Rules for Iron and Cobalt," *Phys. Rev. Lett.*, vol. 75, no. 1, pp. 152-155, 1995.
- [187] A. J. Meyer and G. Asch, "Experimental  $g'$  and  $g$  values of Fe, Co, Ni and their alloys," *J. Appl. Phys.*, vol. 32, S330, 1961.
- [188] H. D. Young and R. A. Freedman, "Chapter 24: Capacitance and Dielectrics," in *University Physics (12th edition)*, Pearson, 2008, pp. 815-845.
- [189] S. J. Barrington *et al*, "The effect of particulate density on performance of Nd:Gd<sub>3</sub>Ga<sub>5</sub>O<sub>12</sub> waveguide lasers grown by pulsed laser deposition," *Optics Communications*, vol. 185, pp. 145-152, 2000.
- [190] H. M. Christen and E. Eres, "Recent advances in pulsed-laser deposition of complex oxides," *Journal of Physics: Condensed Matter*, vol. 20, no. 26, 264005, 2008.
- [191] R. G. Pearson, "Hard and Soft Acids and Bases," *Journal of the American Chemical Society*, vol. 85, no. 22, pp. 3533-3539, 1963.
- [192] S. Ohashi *et al*, "Compact laser molecular beam epitaxy system using laser heating of substrate for oxide film growth," *Review of Scientific Instruments*, vol. 70, no. 1, pp. 178-183, 1999.
- [193] T. C. May-Smith *et al*, "Design and performance of a ZnSe tetra-prism for homogeneous substrate heating using a CO<sub>2</sub> laser for pulsed laser deposition experiments," *Appl. Opt.*, vol. 47, no. 11, pp. 1767-1780, 2008.
- [194] T. Sato, "Spectral Emissivity of Silicon," *Japanese Journal of Applied Physics*, vol. 6, no. 3, pp. 339-347, 1967.
- [195] A. M. Witternberg, "Total Hemispherical Emissivity of Sapphire," *Journal of the Optical Society of America*, vol. 55, no. 4, pp. 432-435, 1965.
- [196] H. D. Young and R. A. Freedman, "Chapter 17: Temperature and Heat," in *University Physics (12th Edition)*, Pearson, 2008, pp. 596-597.
- [197] R. P. Borges *et al*, "Magnetic and electric "dead" layers in (La<sub>0.7</sub>Sr<sub>0.3</sub>)MnO<sub>3</sub> thin films," *J. Appl. Phys.*, vol. 89, no. 7, pp. 3868-3873, 2001.
- [198] M. Y. Chern, T. W. Lu and W. L. Xu, "(110) oriented indium tin oxide films grown on m- and r-plane sapphire substrates," *Japanese Journal of Applied Physics*, vol. 54, 045503, 2015.
- [199] A. J. Caruana *et al*, "Demonstration of polycrystalline thin film coatings on glass for spin Seebeck energy harvesting," *Phys. Status Solidi RRL*, vol. 10, no. 8, pp. 613-617, 2016.

- [200] C. A. Klient *et al*, "Magnetic Properties of Epitaxial Fe<sub>3</sub>O<sub>4</sub> Films," *J. Phys IV France*, vol. 7, pp. 593-594, 1997.
- [201] P. Prieto *et al*, "Fourfold in-plane magnetic anisotropy of magnetite thin films grown on TiN buffered Si(001) by ion-assisted sputtering," *J. Mater. Chem. C*, vol. 4, p. 7632, 2016.
- [202] T. Suzuki *et al*, "Room-temperature electron spin transport in a highly doped Si channel," *Appl. Phys. Express*, vol. 4, 023003, 2011.
- [203] C. A. Klient, "Structural and magnetic properties of epitaxial magnetite thin films prepared by pulsed laser deposition," *Journal of Magnetism and Magnetic Materials*, Vols. 140-144, pp. 725-726, 1995.
- [204] F. Bertram *et al*, "X-ray diffraction study on size effects in epitaxial magnetite thin films on MgO(001)," *J. Phys. D: Appl. Phys.*, vol. 45, 395302, 2012.
- [205] H. Ellis, Revised Nuffield advanced Science: Book of Data, Harlow: Longman Group Limited, 1984.
- [206] L. Blaney, "Magnetite (Fe<sub>3</sub>O<sub>4</sub>): Properties, Synthesis, and Applications," *Lehigh Review*, vol. 15, no. 5, pp. 33-81, 2007.
- [207] D. Reisinger *et al*, "Epitaxy of Fe<sub>3</sub>O<sub>4</sub> on Si(001) by pulsed laser deposition using a TiN/MgO buffer layer," *Journal of Applied Physics*, vol. 94, no. 3, pp. 1857-1863, 2003.
- [208] L. Du and D. Maroudas, "Current-induced surface roughness reduction in conducting thin films," *Appl. Phys. Lett.*, vol. 110, no. 10, 103103, 2017.
- [209] C. Teichert *et al*, "Comparison of surface roughness of polished silicon wafers measured by light scattering topography, soft-x-ray scattering, and atomic-force microscopy," *Appl. Phys. Lett.*, vol. 66, no. 18, pp. 2346-2348, 1995.
- [210] F. M. Smits, "Measurement of Sheet Resistivities with the Four-Point Probe," *The Bell System Technical Journal*, vol. 37, pp. 711-718, 1958.
- [211] M. B. Heaney, "Electrical Conductivity and Resistivity," in *Electrical Measurement, Signal Processing, and Displays*, Florida, CRC Press, 2003, pp. 7-1.
- [212] E. R. Morris and Q. Williams, "Electrical resistivity of Fe<sub>3</sub>O<sub>4</sub> to 48 GPa: Compression-induced changes in electron hopping at mantle pressures," *Journal of Geophysical Research*, vol. 102, no. B8, pp. 18139-18148, 1997.
- [213] G. A. Samara, "Effect of pressure on the metal-nonmetal transition and conductivity of Fe<sub>3</sub>O<sub>4</sub>," *Phys. Rev. Lett.*, vol. 21, pp. 795-797, 1968.
- [214] G. V. Keller, "Electrical properties of rocks and minerals," in *Handbook of Physical constants*, Boulder, Geological Society of America, 1966, pp. 553-577.
- [215] M. C. Menard *et al*, "Electrochemical discharge of nanocrystalline magnetite: structure analysis using X-ray diffraction and X-ray absorption spectroscopy," *Phys. Chem. Chem. Phys.*, vol. 15, pp. 18539--18548, 2013.
- [216] V. V. Balashev *et al*, "Effect of Oxygen Pressure on the Texture of a Magnetite Film Grown by Reactive Deposition on a SiO<sub>2</sub>/Si(001) Surface," *Physics of the Solid State*, vol. 57, no. 12, pp. 2532-2536, 2015.
- [217] W. L. Zhou *et al*, "Granular growth of Fe<sub>3</sub>O<sub>4</sub> thin films and its antiphase boundaries prepared by pulsed laser deposition," *Journal of Applied Physics*, vol. 89, no. 11, pp. 7398-7400, 2001.
- [218] A. M. Jubb and H. C. Allen, "Vibrational Spectroscopic Characterization of Hematite, Maghemite and Magnetite Thin Films Produced by Vapor Deposition," *ACS Applied Materials and Interfaces*, vol. 2, no. 10, pp. 2804-2812, 2010.
- [219] I. Chamritski and G. Burns, "Infrared and Raman Active Phonons of Magnetite, Maghemite and Hematite: A Computer Simulation and Spectroscopic Study," *J. Phys. Chem. B*, vol. 109, pp. 4965-4968, 2005.

- [220] S. H. Shim and T. S. Duffy, "Raman spectroscopy of Fe<sub>2</sub>O<sub>3</sub> to 62 GPa," *American Mineralogist*, vol. 87, pp. 318-326, 2001.
- [221] O. N. Shebanova and P. Lazor, "Raman spectroscopic study of magnetite (FeFe<sub>2</sub>O<sub>4</sub>): a new assignment for the vibrational spectrum," *Journal of Solid State Chemistry*, vol. 174, pp. 424-430, 2003.
- [222] W. Lei *et al*, "Synthesis and magnetic properties of octahedral Fe<sub>3</sub>O<sub>4</sub> via a one-pot hydrothermal route," *Phys. Lett. A*, vol. 381, pp. 314-318, 2016.
- [223] J. B. Moussy *et al*, "Thickness dependence of anomalous magnetic behaviour in epitaxial Fe<sub>3</sub>O<sub>4</sub>(111) thin films: Effect of density of antiphase boundaries," *Phys. Rev. B*, vol. 70, 174448, 2004.
- [224] T. Schemme *et al*, "Magnetic anisotropy related to strain and thickness of ultrathin iron oxide films on MgO(001)," *Matter. Res. Express*, vol. 2, 016101, 2015.
- [225] S. S. Parkin, R. Sigsbee, R. Felici and G. P. Felcher, "Observation of magnetic dead layers at the surface of iron oxide films," *Appl. Phys. Lett.*, vol. 48, pp. 604-606, 1986.
- [226] S. K. Arora *et al*, "Giant magnetic moment in epitaxial Fe<sub>3</sub>O<sub>4</sub> thin films on MgO(100)," *Phys. Rev. B*, vol. 77, 134443, 2008.
- [227] M. Ledinsky *et al*, "Profilometry of thin films on rough substrates by Raman spectroscopy," *Sci. Rep.*, vol. 6, 37859, 2016.
- [228] C. Carmerlingo *et al*, "Evaluation of thin metal film thickness from light attenuation and multi-reflection effects on micro-Raman response," *Thin Solid Films*, vol. 536, pp. 142-146, 2013.
- [229] M. Ziese and H. J. Blythe, "Magnetoresistance of magnetite," *Condens. Matter*, vol. 12, pp. 13-28, 2000.
- [230] R. C. Weast, CRC Handbook of Chemistry and Physics (55th ed.), Cleveland, Ohio: CRC Press, 1974.
- [231] S. Tiwari *et al*, "Oriented growth of Fe<sub>3</sub>O<sub>4</sub> thin films on crystalline and amorphous substrates by pulsed laser deposition," *J. Phys. D: Appl. Phys.*, vol. 40, pp. 4943-4947, 2007.
- [232] A. J. Ying *et al*, "A rigorous comparison of X-ray diffraction thickness measurement techniques using silicon-on-insulator thin films," *J. Appl. Cryst.*, vol. 42, pp. 401-410, 2009.
- [233] S. B. Ogale *et al*, "Magnetotransport anisotropy effects in epitaxial magnetite (Fe<sub>3</sub>O<sub>4</sub>) thin films," *Phys. Rev. B*, vol. 57, no. 13, pp. 7823-7828, 1998.
- [234] D. T. Margulies *et al*, "Anomalous moment and anisotropy behavior in Fe<sub>3</sub>O<sub>4</sub> films," *Phys. Rev. B*, vol. 57, no. 14, pp. 9175-9187, 1996.
- [235] N. B. Manson *et al*, "Second-Order Raman Spectrum of MgO," *Phys. Rev. B*, vol. 3, no. 6, pp. 1968-1972, 1971.
- [236] O. Mauit *et al*, "Ultrathin magnetite in Fe<sub>3</sub>O<sub>4</sub>/MgO superlattices: Investigating the enhanced thin film magnetic moment," *Phys. Rev. B*, vol. 95, 125128, 2017.
- [237] J. M. Coey *et al*, "Magnetoresistance of magnetite," *Appl. Phys. Lett.*, vol. 72, no. 6, pp. 734-736, 1998.
- [238] X. Y. Zhang *et al*, "Observation of growth morphology in pulsed-laser deposited barium ferrite thin films," *Applied Surface Science*, vol. 143, no. 4, pp. 323-327, 1999.
- [239] M. Mohebbi, "Magnetoelectric Hexaferrite Thin Films Growth for Next Generation Device Applications," Northeastern University, Boston, 2013.
- [240] B. Stibbe, "Magnetoelektrische Effekte in multifunktionalen Schichtstrukturen," TECHNISCHE UNIVERSITÄT MÜNCHEN, Munich, 2014.
- [241] Y. N. Wang and J. C. Huang, "Texture analysis in hexagonal materials," *Materials Chemistry and Physics*, vol. 81, pp. 11-26, 2003.

- [242] Z. Chen *et al*, "Structure, magnetic, and microwave properties of thick Ba-hexaferrite films epitaxially grown on GaN/Al<sub>2</sub>O<sub>3</sub> substrates," *Appl. Phys. Lett.*, vol. 96, 242502, 2010.
- [243] R. C. Pullar, M. D. Taylor and A. K. Bhattacharya, "Halide removal from BaM (BaFe<sub>12</sub>O<sub>19</sub>) and SrM (SrFe<sub>12</sub>O<sub>19</sub>) ferrite fibers via a steaming process," *J. Matt. Res.*, vol. 16, no. 11, pp. 3162 - 3169, 2001.
- [244] H. Kojima, *Handbook of Ferromagnetic materials*, vol. 3, pp. 305-392, 1982.
- [245] H. Xuemin *et al*, "The structure, morphology and magnetic properties of Sr-ferrite powder prepared by the molten-salt method," *J. Phys. D*, vol. 47, no. 23, 235002, 2014.
- [246] Y. Guan *et al*, "The effects of Co-Ti co-doping on the magnetic, electrical, and magnetodielectric," *AIP Advances*, vol. 3, 122115, 2013.
- [247] G. Qiang *et al*, "Temperature effect on the magnetic property and ferroelectricity in hexaferrite SrFe<sub>12</sub>O<sub>19</sub>," *Appl. phys. A*, vol. 122, p. 681, 2016.
- [248] O. Kubo *et al*, "Improvement in the temperature coefficient of coercivity for barium ferrite particles," *IEEE Transactions on Magnetics*, vol. 24, no. 6, pp. 2859-2861, 1988.
- [249] R. Tang *et al*, "Room-temperature multiferroic and magnetocapacitance effects in M-type hexaferrite BaFe<sub>10.2</sub>Sc<sub>1.8</sub>O<sub>19</sub>," *Appl. Phys. Lett.*, vol. 109, no. 8, 2016.
- [250] J. Smit and H. P. J. Wijn, "Ferrites: physical properties offerrimagnetic oxides in relation to their technical applications," *Philips Technical Library*, 1959.
- [251] H. B. Lee *et al*, "Heliconical magnetic order and field-induced multiferroicity of the Co<sub>2</sub>Y-type hexaferrite Ba<sub>0.3</sub>Sr<sub>1.7</sub>Co<sub>2</sub>Fe<sub>12</sub>O<sub>22</sub>," *Phys. rev. B*, vol. 86, 094435, 2012.
- [252] G. Srinivasan, "Magnetolectric Composites," *Annu. Rev. Mater. Res.*, vol. 40, pp. 153-178, 2010.
- [253] K. Ebnabbasi, *Microwave Devices Utilizing Magnetolectric Hexaferrite Materials for Next Generation of Communication Systems*, Boston: Northeastern University, 2012.
- [254] J. M. Williams, J. Adetunji and M. Gregori, "Mossbauer spectroscopic determination of magnetic moments of Fe<sup>3+</sup> and Co<sup>2+</sup> in substituted barium hexaferrite, Ba(Co,Ti)<sub>x</sub>Fe<sub>(12-2x)</sub>O<sub>19</sub>," *Journal of Magnetism and Magnetic Materials*, vol. 220, pp. 124-128, 2000.
- [255] D. J. Huang *et al*, "Spin and orbital magnetic moments of Fe<sub>3</sub>O<sub>4</sub>," *Phys. Rev. Lett*, vol. 93, 077204, 2004.
- [256] M. Kallmayer *et al*, "Magnetic moment investigations of epitaxial magnetite thin films," *J. Appl. Phys.*, vol. 103, 07D715, 2008.
- [257] Y. P. Cai *et al*, "Orbital and spin moments of 5 to 11 nm Fe<sub>3</sub>O<sub>4</sub> nanoparticles measured via x-ray magnetic circular dichroism," *J. Appl. Phys.*, vol. 115, 17B537, 2014.
- [258] P. Scherrer, "Bestimmung der Grösse und der inneren Struktur von Kolloidteilchen mittels Röntgenstrahlen," *Nachr. Ges. Wiss. Göttingen*, vol. 26, pp. 98-100, 1918.
- [259] A. P. Roberts, Y. Cui and K. L. Verosub, "Wasp-waisted hysteresis loops: Mineral magnetic characteristics and discrimination of components in mixed magnetic systems," *Journal of Geophysical research*, vol. 100, no. B9, pp. 17909-17924, 1995.
- [260] P. Borisov *et al*, "Growth of M-type hexaferrite thin films with conical magnetic structure," *Appl. Phys. Lett.*, vol. 102, 032902, 2013.
- [261] A. Ataie, I. R. Harris and C. B. Ponton, "Magnetic properties of hydrothermally synthesized strontium hexaferrite as a function of synthesis conditions," *Journal of Materials science*, vol. 30, no. 6, pp. 1429-1433, 1995.
- [262] K. Haneda and A. H. Morrish, "Magnetic properties of BaFe<sub>12</sub>O<sub>19</sub> small particles," *IEEE Transactions on Magnetics*, vol. 25, no. 3, pp. 2597-2601, 1992.
- [263] K. H. Buschow, "chapter 3," in *Handbook of Magnetic Materials*, Oxford, UK, North-Holland, 2011, p. 130.

- [264] D. S. Chrischon *et al*, "FMR linewidth and the crystallization processes in Co-based amorphous microwires," *Journal of Magnetism and Magnetic Materials*, vol. 336, pp. 66-70, 2013.
- [265] A. Hrabec *et al*, "Spin-orbit interaction enhancement in Permalloy thin films by Pt-doping," *Phys. Rev. B (Condensed Matter)*, vol. 93, no. 1, 014432, 2016.
- [266] M. Javed Iqbal, "Physical, electrical and dielectric properties of Ca-substituted strontium hexaferrite (SrFe<sub>12</sub>O<sub>19</sub>) nanoparticles synthesized by co-precipitation method," *Journal of Magnetism and Magnetic Materials*, vol. 322, pp. 1720-1726, 2010.
- [267] I. V. Zavislyak *et al*, "Current-induced nonlinear magnetoelectric effects in strontium hexaferrite," *Phys. Rev. B*, vol. 94, 224419, 2016.
- [268] E. R. Dobrovinskaya, L. A. Lytvynov and V. Pishchik, "Electrical Properties of Sapphire," in *Sapphire: Material, Manufacturing, Applications*, New York, Springer, 2009, pp. 114-119.
- [269] V. J. Folen, G. T. Rado and E. W. Stadler, "Anisotropy of the Magnetoelectric Effect in Cr<sub>2</sub>O<sub>3</sub>," *Phys. Rev. Lett.*, vol. 6, no. 11, pp. 607-608, 1961.
- [270] R. E. Cohen, "Origin of Ferroelectricity in Perovskite Oxides," *Nature*, vol. 358, pp. 136-138, 1992.
- [271] K. A. Muller and H. Burkard, "SrTiO<sub>3</sub>: An intrinsic quantum paraelectric below 4 K," *Phys. Rev. B*, vol. 19, no. 7, pp. 3593-3602, 1979.
- [272] X. Obradors *et al*, "X-ray analysis of the structural and dynamic properties of BaFe<sub>12</sub>O<sub>19</sub> hexagonal ferrite at room temperature," *J. Solid State Chem.*, vol. 56, no. 2, pp. 171-181, 1985.
- [273] J. G. Rensen and J. G. van Wieringen, "Anisotropic Mössbauer fraction and crystal structure of BaFe<sub>12</sub>O<sub>19</sub>," *Solid State Commun.*, vol. 7, pp. 139-1141, 1969.
- [274] Accelrys Inc, *Materials Studio, version 8.0*, San Diego, CA, USA: Accelrys Inc, 2016.
- [275] S. J. Clark *et al*, "First principles methods using CASTEP," *Z. Kristallogr.*, vol. 220, pp. 567-570, 2005.
- [276] M. Probert, *First Principles Materials Modelling*, lecture notes: University of York, 2017.
- [277] J. P. Perdew, K. Burke and M. Ernzerhof, "Generalized Gradient Approximation Made Simple," *Phys. Rev. Lett.*, vol. 77, no. 18, pp. 3865-3868, 1996.
- [278] O. P. Aleshko-Ozhevskii, M. K. Faek and I. I. Yamzin, "A Neutron Diffraction Study of the Structure of Magnetoplumbite," *Soviet Physics - Crystallography*, vol. 14, no. 3, pp. 367-369, 1969.
- [279] R. Tang *et al*, "Room temperature magnetodielectric effects in epitaxial hexaferrite BaFe<sub>10.2</sub>Sc<sub>1.8</sub>O<sub>19</sub> thin film," *Appl. Phys. Lett.*, vol. 110, 242901, 2017.
- [280] P. S. Wang and H. J. Xiang, "Room-Temperature Ferrimagnet with Frustrated Antiferroelectricity: Promising Candidate Toward Multiple-State Memory," *Phys. Rev. X*, vol. 4, 011035, 2014.
- [281] J. M. Hu, Z. Li, L. Q. Chen and C. W. Nan, "High-density magnetoresistive random access memory operating at ultralow voltage at room temperature," *Nat. Commun.*, vol. 2, p. 553, 2011.